Bioanalysis: Advanced Materials, Methods, and Devices
Series Editor: Tuan Vo-Dinh

Michael W. Collins
Carola S. König *Editors*

Micro and Nano Flow Systems for Bioanalysis

Springer

Bioanalysis:
Advanced Materials, Methods, and Devices

Series Editor:
Tuan Vo-Dinh
Fitzpatrick Institute for Photonics
Duke University
Durham, NC, USA

For further volumes:
http://www.springer.com/series/8091

Michael W. Collins • Carola S. König
Editors

Micro and Nano Flow Systems for Bioanalysis

Springer

Editors
Michael W. Collins
School of Engineering and Design
Brunel University
London, UK

Carola S. König
Brunel Institute for Bioengineering
Brunel University
London, UK

ISBN 978-1-4614-4375-9 ISBN 978-1-4614-4376-6 (eBook)
DOI 10.1007/978-1-4614-4376-6
Springer New York Heidelberg Dordrecht London

Library of Congress Control Number: 2012951672

Printed on acid-free paper

Springer is part of Springer Science+Business Media (www.springer.com)

Preface

This volume was inspired by a Special Session at the 3rd International Conference on Micro and Nano Flows (MNF2011) held at Thessaloniki, Greece, from 22nd to 24th August, 2011.

The Conference ethos was strongly interdisciplinary, with parallel sessions on both single- and mixed-phase thermofluids in engineering together with fluid flow aspects of biomedicine. The Special Session was in addition to the biomedical stream of presentations. It was entitled *Micro and Nano Flows in Medicine: the way ahead* and involved a number of speakers of international invited status, and covered a comprehensive range of topics from ultra-fine optical measurement methods to multi-scale modelling. Also, there was an overall stress on relevance to clinical practice.

In the process of organising the session one of us (MWC) had email/telephone discussions with Tuan Vo-Dinh, series editor of the Springer US *Bioanalysis: Advanced Materials, Methods and Devices* series. On his invitation and Springer US's approval the current volume was commissioned. This further widened the international spread of authors and would include specific material on "bench-to-bedside" information transfer, otherwise known as translational medicine.

Almost 20 years ago MWC had the privilege of participating in a UK-funded (Engineering and Physical Sciences Research Council) survey study of nanofluid dynamics in medicine. This resulted in the publication of the complete survey in book form (Ciofalo et al., 1999, with prior abbreviated Journal publication as Ciofalo et al., 1996). At that time, it was reasonably straightforward to identify a limited number of international groups working in the area, a "luxury" that the greatly increased worldwide activity has made much more difficult.

Turning to the present, the advances in medical knowledge and understanding have a breathtaking impact, especially when, as here, examples of the various scientific approaches are combined in a single publication. It is made easier for readers to appreciate such advances since they can be identified as taking a limited number of forms. These may be summarised as: non-invasive optical measurement methods, modelling at ultra-fine scales combined with multi-scale methods, and the engineering of micro-devices. Again and again, we will find a focus on the

behaviour of individual cells, and this is, perhaps, what distinguishes fine-scale biomedicine from conventional engineering. While both can involve the transport of individual particles within flowing fluids, in physiology the sheer cellular complexity and the information-rich DNA content set these "particles" apart from their engineering companions.

In more detail, advances in optical measurement methods are strongly ongoing, with a number of chapters in this volume. The key technology of Optical Coherence Tomography (OCT) is addressed in the chapter by Coupland and Halls, including the underlying theory. Conventional Magnetic Resonance Imaging is combined with Surface Enhanced Raman Scattering (MR/SERS Imaging) to enable nanoparticle-based drug delivery systems to be used in cancer diagnosis and therapy (Yigit and Medarova). Atomic Force Microscopy (AFM) has been combined with Dynamic Laser Speckle (DLS) by Chizhik, Drozd and Fomin to inspect and *manipulate* individual cells in living tissue. Again, the theory of DLS is given. Finally, a combination of micro Particle Image Velocimetry and Particle Tracking Velocimetry (micro-PIV/PTV), employing a Spinning Disk Confocal Microscope (SDCM) is used by Lima et al. to investigate the fine details of blood flow. Illuminating records of the movement and collisions of individual red and white blood cells are given. In conclusion, it is worth pointing out that appreciation of developments in optical methods can be gained from the trade/research journals *Laser Focus World* and *BioOptics World,* published by Penn Well. The latter journal, subtitled *Advances in lasers, optics and imaging for the life sciences,* will provide information and inspiration and in fact originally helped to drive our interest in this area.

Turning to modelling, there is again a challenge to focus on individual particles (usually red blood cells) which the Lattice Boltzmann method handles rather handsomely (Melchionna et al.). But such a focus is not the whole answer, because it is not just the detailed biomedical behaviour that we need to understand, but the way in which that behaviour impacts on the higher scales of vessel and organ. This is the rationale behind the multi-scale concept, the scales involving time as well as space. Melchionna et al. explain how LB methods on the one hand can address the microscale nature of the Endothelial Surface Layer (ESL) and on the other is especially suitable for large-scale complex blood vessels. Another endothelial-scale problem is addressed by Fu, namely the possibility of metastasis of tumours via the blood stream, involving penetration through the endothelial cleft. Finally, a fully multi-scale approach is used by Perfahl et al. in their particularly comprehensive analysis of angiogenesis and tumour growth.

Before leaving (the experiments of) optical methods and (the mathematics of) modelling, the interaction between the two should be noted. As shown by Coupland and Halls and by Chizhik, Drozd and Fomin, a high level of mathematics is involved in explaining the optical effects. Conversely, Melchionna et al. use Multi-detector Computed Tomography (MDCT) data to define their three-dimensional blood vessel geometries.

The third feature of advances in fine-scale biomedical studies is the use of engineering in microfluidics devices able to isolate and manipulate individual cells. The key objective is to avoid physical contact with the cell membranes. This may be done with an inertial force field (Tanaka et al.), or by the use of magnetic (Lewpiriyawong and Yang) or electric (Medoro, 2011) fields. The very definition of the performance indicates the complexity and challenge that such devices represent.

In terms of applications almost all the above focus on cancer. In the cardiovascular field, a cardiopulmonary surgeon and a microcirculation specialist, Karagounis and Pries, respectively unite to describe the surgical implications of advances in understanding of microflows. Also, Nayak et al. discuss the effects of low shear stress on the regulation of endothelial activation and subsequent vascular inflammation.

The final important topic is that of translational medicine, addressed in considerable detail by Bradshaw Pierce and Tan. Whereas the traditional approach to nanoscale biomedical processes is via fluid dynamics (Ciofalo et al., 1996), in fact as scales reduce, transport is a better description. Even more precisely, given the way in which cancer cells change genetically, the transport is that of *information* rather than of just physical particles. There is little doubt that this is where the action is. The two EU-funded reports which have only just anticipated this volume (Shublaq, 2012a, b) make this clear. There are other keywords. So we read (Shublaq, 2012a) "... personalised medicine, the idea of using the genotype of a patient (or of a tumour), or the phenotype ... to select the right drug at the right time. This is seen as a top priority in Europe and worldwide."

We now make some concluding comments. Firstly, the international spread of authors is represented not only by the range of chapters, but by the multi-centre character of individual chapters. This, of course, is a reflection of the interdisciplinary nature of the subject. For Perfahl et al. four countries and four Universities are involved, and for Lima et al. the corresponding numbers are two and three. The chapter by Tanaka et al. from Japan involved two universities with four departments.

In drawing this Preface to a close, we as editors would like to express our deep gratitude to Springer US: to Sara Kate Heukerott for her unfailing help and efficiency and to David Packer for his consistent support. It goes without saying that we wish to thank every author involved and to compliment them on the achievements and quality of their research. These chapters represent the inspiration, dedication and skill of a worldwide activity: we hope that the volume will correspondingly inform and inspire its readers.

London, UK

Michael W. Collins
Carola S. König

References

Ciofalo M, Hennessy TR, Collins MW (1996) Modelling nanoscale fluid dynamics and transport in physiological flows, Med Eng Phys 18(6):437–451

Ciofalo M, Hennessy TR, Collins MW (1999) Nanoscale fluid dynamics in physiological processes. A review study, advances in computational bioengineering 2. WIT Press, Southampton

Medoro G (2011) Detection and isolation of circulating cancer cells with single-cell resolution: a successful Lab-on-a-chip device. Proceedings of the 3rd International Conference on Micro and Nano Flows, Thessaloniki, Greece, 22–24 Aug 2011

Shublaq N (2012a) Strategic report for translational systems biology and bioinformatics in the European Union, EU INBIOMEDvision Consortium, ICT-270107. http://www.inbiomedvision.eu

Shublaq N (2012b) Strategic report on genotype-phenotype resources in the European Union, EU INBIOMEDvision Consortium, ICT-270107. http://www.inbiomedvision.eu

Contents

List of Contributors

T. Alarcón Centre de Recerca Matemàtica, Campus de Bellaterra, Barcelona, Spain

Massimo Bernaschi IAC-CNR, Institute for Computation "M. Picone", National Research Council, Rome, Italy

Mauro Bisson IAC-CNR, Institute for Computation "M. Picone", National Research Council, Rome, Italy

H.M. Byrne Department of Computer Science, Oxford Centre for Collaborative Applied Mathematics, University of Oxford, UK

T. Chen H. Lee Moffitt Cancer Center & Research Institute, Tampa, FL, USA

Sergei Chizhik A.V. Likov Heat and Mass Transfer, Institute of the National Academy of Sciences of Belarus, Minsk, Belarus

Jeremy M. Coupland Department of Mechanical and Manufacturing Engineering, Loughborough University, UK

Lizaveta Drozd A.V. Likov Heat and Mass Transfer, Institute of the National Academy of Sciences of Belarus, Minsk, Belarus

V. Estrella H. Lee Moffitt Cancer Center & Research Institute, Tampa, FL, USA

Paul C. Evans Department of Cardiovascular Science, Sheffield University Medical School, Sheffield University, UK

Nikita Fomin A.V. Likov Heat and Mass Transfer, Institute of the National Academy of Sciences of Belarus, Minsk, Belarus

Bingmei M. Fu Department of Biomedical Engineering, The City College of The City University of New York, NY, USA

R.A. Gatenby H. Lee Moffitt Cancer Center & Research Institute, Tampa, FL, USA

R.J. Gillies H. Lee Moffitt Cancer Center & Research Institute, Tampa, FL, USA

Ian Halliday MERI, Sheffield Hallam University, UK

Justin A.T. Halls Brunel Institute for Bioengineering, Brunel University, Uxbridge, UK

Yohsuke Imai School of Engineering, Tohoku University, Sendai, Japan

Takuji Ishikawa School of Engineering, Tohoku University, Sendai, Japan

Vasilios A. Karagounis Cardiothoracic Vascular Surgery, Panorama, Greece

Uday Kishore Biosciences, Centre for Infection, Immunity and Disease Mechanisms, School of Health Sciences and Social Care, Brunel University, London, UK

Carola S. König Brunel Institute for Bioengineering, Brunel University, London, UK

A. Lapin Center for Systems-Biology, University of Stuttgart, Germany

Nuttawut Lewpiriyawong School of Mechanical and Aerospace Engineering, Nanyang Technological University, Singapore

Rui Lima DTM, ESTiG/IPB, Braganca Polytechnic, Portugal

CEFT/FEUP, Porto University, Portugal

M.C. Lloyd H. Lee Moffitt Cancer Center & Research Institute, Tampa, FL, USA

P.K. Maini Centre for Mathematical Biology, Mathematical Institute, Department of Biochemistry, Oxford Centre for Integrative Systems Biology, University of Oxford, UK

Noriaki Matsuki Department Biomedical Engineering, Okayama University of Science, Japan

Zdravka Medarova Molecular Imaging Laboratory, Athinoula A. Martinos Center for Biomedical Imaging, Massachusetts General Hospital and Harvard Medical School, Charlestown, MA, USA

Simone Melchionna IPCF-CNR, Institute for Physico-Chemical Processes, National Research Council, Rome, Italy

Annapurna Nayak Centre for Infection, Immunity and Disease Mechanisms, Biosciences, School of Health, Sciences and Social Care, Brunel University, London, UK

Centre for Biotechnology and Bioinformatics, School of Life Sciences, Jawaharlal Nehru, Institute for Advanced Studies, Secunderabad, Andhra Pradesh, India

Keiko Numayama-Tsuruta School of Biomedical Engineering, Tohoku University, Sendai, Japan

M.R. Owen Centre for Mathematical Medicine and Biology, School of Mathematical Sciences, University of Nottingham, UK

H. Perfahl Center for Systems-Biology, University of Stuttgart, Germany

Erica L. Bradshaw Pierce Department of Pharmaceutical Science, Skaggs School of Pharmacy, University of Colorado Anschutz Medical Campus, Aurora, CO, USA

Giuseppe Pontrelli IAC-CNR, Institute for Computation "M. Picone", National Research Council, Rome, Italy

Axel R. Pries Department of Physiology and CCR, Charité-Universitätsmedizin Berlin, Germany

M. Reuss Center for Systems-Biology, University of Stuttgart, Germany

Tim J. Spencer MERI, Sheffield Hallam University, UK

Sauro Succi IAC-CNR, Institute for Computation "M. Picone", National Research Council, Rome, Italy

Aik Choon Tan Division of Medical Oncology, Department of Medicine, School of Medicine, University of Colorado Anschutz Medical Campus, Aurora, CO, USA

Department of Biostatistics and Informatics, Colorado School of Public Health, University of Colorado Anschutz Medical Campus, Aurora, CO, USA

University of Colorado Cancer Center, University of Colorado Anschutz Medical Campus, Aurora, CO, USA

Tatsuya Tanaka School of Engineering, Tohoku University, Sendai, Japan

Hironori Ueno International Advanced Research and Education Organization, Tohoku University, Sendai, Japan

Takami Yamaguchi School of Biomedical Engineering, Tohoku University, Sendai, Japan

Chun Yang School of Mechanical and Aerospace Engineering, Nanyang Technological University, Singapore

Mehmet V. Yigit Molecular Imaging Laboratory, Athinoula A. Martinos Center for Biomedical Imaging, Massachusetts General Hospital and Harvard Medical School, Charlestown, MA, USA

Takefumi Yoshimoto School of Engineering, Tohoku University, Sendai, Japan

Chapter 1
Iron Oxide Nanoparticles and Derivatives for Biomedical Imaging and Application in Cancer Diagnosis and Therapy

Mehmet V. Yigit and Zdravka Medarova

Abstract Imaging-capable nanoparticulate contrast agents for cancer diagnosis and small RNA-based tumor therapy have been an emerging field in molecular imaging and pharmaceutical sciences. One example of such agents includes magnetic nanoparticles (MN), which have traditionally been utilized as contrast agents for Magnetic Resonance Imaging. The probes typically consist of a dextran-coated superparamagnetic iron oxide core (for MRI), labeled with Cy5.5 dye (for near-infrared in vivo optical imaging), coated with targeting-peptides for receptor-mediated uptake by specific cell types and conjugated to synthetic small interfering RNA (siRNA) molecules as therapeutic agents. The potential of these nanoparticles as MRI contrast agents for tumor imaging and delivery modules for small interfering RNA has been investigated. Furthermore, the feasibility of combining the imaging and delivery capabilities of these nanoparticles for the tracking of siRNA bioavailability has been explored. The versatile functionalization potential of MN has allowed controlling properties of the agents, such as uptake mechanism and target organ distribution. The tumoral accumulation of MN-siRNA results in a remarkable level of target-gene down-regulation. Repeated treatment with MN-siRNA targeting the tumor-specific anti-apoptotic gene, birc5, leads to the induction of apoptosis in the tumors and an overall reduction in tumor growth rate. Bioconjugated MNs were also used for biosensing application for several metabolically important compounds and processes. A second generation of nanoparticles, which combine the capability for high-resolution MRI with detection by ultrasensitive surface enhanced Raman scattering has been tested in silico and in vivo. Different types of magnetic nanoparticles have been used for therapy of cancer by Magnetic Fluid Hyperthermia.

M.V. Yigit • Z. Medarova (✉)
Molecular Imaging Laboratory, Athinoula A. Martinos Center for Biomedical Imaging, Massachusetts General Hospital and Harvard Medical School, Charlestown, MA 02129, USA
e-mail: zmedarova@partners.org

M.W. Collins and C.S. König (eds.), *Micro and Nano Flow Systems for Bioanalysis*, Bioanalysis 2, DOI 10.1007/978-1-4614-4376-6_1,

1.1 Introduction

Iron oxide nanoparticles have been of interest for biomedical applications due to their functional versatility. Concrete applications include cellular therapy, biosensing, tissue repair, drug delivery, hyperthermia therapy, MRI, magnetofection, etc. [11] The literature includes numerous reports describing the synthesis of iron oxide nanoparticles via physical and chemical methods. Among them, wet chemistry procedures have been widely used, as size, composition, magnetic properties, and shapes are more controllable with this method [12]. Iron oxides are generally prepared by co-precipitation of Fe^{2+} and Fe^{3+} salts in an aqueous solution. The anionic salt content (chlorides, nitrates, sulfates, etc.), the Fe^{2+} and Fe^{3+} ratio, pH and the ionic strength in the aqueous solution are key elements in controlling the size of the particles [28]. One important step in the synthesis is to prevent the oxidation of the synthesized nanoparticles and protect their magnetic properties, which is generally established by carrying out the reaction in an oxygen free environment (under N_2) [10]. The co-precipitation process is generally done in the presence of a surface coating in order to prevent the agglomeration of the iron oxides into microparticles during the synthesis. There have been several surface coating materials used for stabilizing iron oxide nanoparticles, among which there are synthetic and natural polymers, such as polyethylene glycol (PEG), dextran, polyvinylpyrrolidone (PVP), fatty acids, polypeptides, chitosin, gelatin, etc. [11].

1.2 Biomedical Applications of Iron Oxide Nanoparticles

The majority of iron oxide nanoparticles are intended for biomedical applications. Their use as contrast agents for MRI is particularly attractive, due to their high sensitivity of detection [3]. MRI is a clinically approved noninvasive medical imaging method, which allows the collection of three-dimensional information from the body with excellent tissue contrast. Iron oxide nanoparticles have been used to observe different in vivo biological events, MRI including determining the fate of transplanted pancreatic islets [6,20], tumor progression [22] or lymph node metastasis [13], etc.

Establishing target specific contrast agents for MRI presents a great opportunity for detecting disease at the initial stages when therapeutic intervention has the highest chances of success. This is possible because molecular targeting of the contrast would accomplish the detection of the early phenotypic changes that define the pathology. Combining diagnosis and therapy would be even more interesting, because it would allow the assessment of therapeutic efficacy as a function of drug delivery. It is possible to impart all of these functionalities to iron oxide nanoparticles by having different ligands attached to the surface of the nanoparticles.

There are several methods of preparing iron oxide nanoparticles but the focus of this chapter is on cross-linked dextran coated superparamagnetic iron oxides, whose

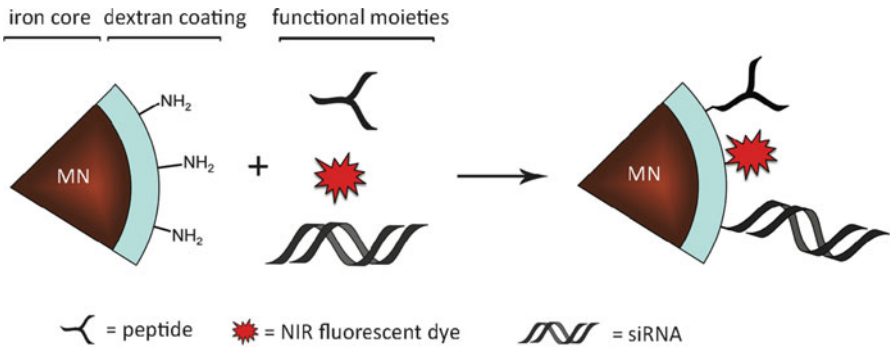

Fig. 1.1 Superparamagnetic iron oxide nanoparticles coated with dextran serve as templates for conjugation of several molecular moieties. In this example, magnetic nanoparticles are conjugated to a tumor targeting peptide, NIR fluorescent dye (cy5.5), and siRNA

precursor is a clinically approved contrast agent [14]. The iron oxide nanoparticles discussed in this chapter have a ~5 nm superparamagnetic iron oxide core. They are coated with dextran, which is a biodegradable and biocompatible polymer. The dextran surface is further cross-linked using several chemical processes to introduce amine groups for functionalization. Multiple moieties including targeting peptides [17], aptamers [33,34], NIR fluorescent dyes [26], therapeutic materials [31], etc. can be conjugated to iron oxide nanoparticles through amine terminals and bifunctional linkers, Fig. 1.1.

1.3 Multifunctional Cancer Imaging with Iron Oxide Nanoparticles

Cancer diagnosis by nanotechnology is an emerging field. Detecting cancer noninvasively (a feature of nanotechnology) benefits the patient in obvious and subtle ways. Alternatively, surgical methods may produce high morbidity and are completely unnecessary for the patient who does not have the disease. Noninvasive imaging of cancer with high sensitivity is crucial and achievable, as an inherent property of magnetic nanoparticles. Moreover, a slight modification of the nanoparticle to include a therapeutic moiety offers the possibility of combining diagnosis with an initial drug delivery step.

There are two main approaches in imaging the disease with magnetic nanoparticles. The first is passive-targeted imaging in which the nanoparticles reach the malignant tissues due to the mechanical properties of the nanoparticles, their size, and the physical properties of the surface coating such as charge and hydrophobicity [24]. The second, active-targeted imaging approach, incorporates a targeting moiety into the nanoparticle, which facilitates cellular uptake by malignant cells [29].

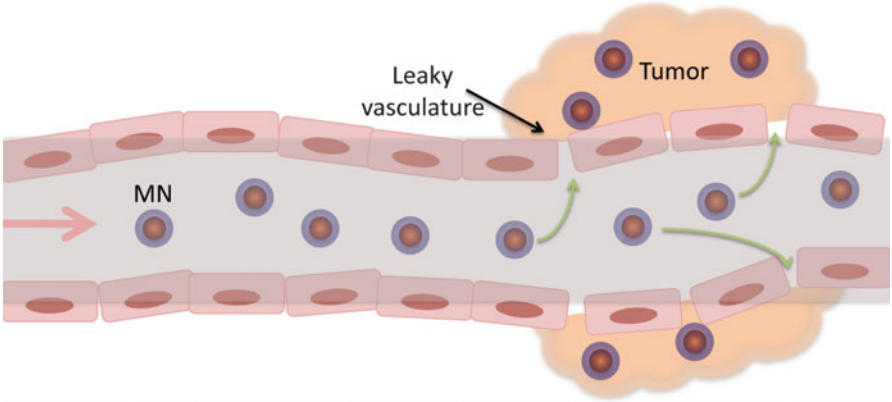

Fig. 1.2 A scheme of passive targeting with magnetic nanoparticles (MN) through the leaky tumor vasculature

An alternate method of imaging biological phenomena with nanoparticles utilizes the magnetic relaxation switching (MRS) property of iron oxide nanoparticles. In this method the nanoparticle-target molecule assembly increases the ability to change T2 relaxation time. Such a change makes these nanoparticles a better T2 contrast agent. Consequently cancer-related biomaterials could be detected by MRI.

1.3.1 Passive-Targeted Imaging

Even though this approach does not involve cellular specificity, it has been used successfully in clinical trials [24]. Vascular permeability plays a key role in the passive targeting strategy employed in delivering the iron oxide nanoparticles to tumor tissues. Nanoparticles are synthesized without any targeting group attached. The nanoparticles penetrate the tumor mass after passing through the leaky vasculature and in most cases are retained in the tumor mass. On the other hand, normal vasculature has low leakiness and normal tissues have a tightly packed structure, which presents a barrier to nanoparticles attempting to penetrate healthy tissues, Fig. 1.2.

For both passive targeting and active targeting it is important to have the nanoparticles circulate a long time in the blood stream, avoiding phagocytosis. Macrophages eliminate foreign materials in the body, once recognized, and therefore decrease the tumor uptake of the nanoparticles. Therefore, it is important to prevent phagocytosis by (1) using a hydrophilic coating like PEG or dextran, (2) limiting the size of the nanoparticles to between 30 and 50 nm, which in most cases is optimum for passive targeting [30]. With such approaches it is often possible to utilize passive targeting for cancerous tumors. Small iron oxide nanoparticles have been used for the

passive targeting of different cancer types such as prostate, bladder, penile, and testicular cancer as well as renal neoplasm [24].

Non-invasive imaging is the central rationale for using unconjugated iron oxide nanoparticles. Passive targeting has been used to assess the extent of lymph node metastasis in prostate cancer patients in clinical studies using lymphotropic superparamagnetic nanoparticles [13]. These studies have shown that with these magnetic nanoparticles, detection of small metastases or otherwise undetectable metastases (by other noninvasive means) is now possible by high-resolution MRI. There are very mild side effects associated with these nanoparticles. Even the patients within high-risk groups such as cardiovascular, renal, and hepatic diseases tolerated the injected dosage well. Severe side effects were uncommon.

1.3.2 Active-Targeted Imaging

Active targeting is expected to improve upon the passive targeting approach and increase the specificity of cellular uptake. Active targeting is achieved by conjugation of anti-receptor molecules to the nanoparticle surface. Binding then induces prolonged interaction of nanoparticles with cancer cell surfaces and results in elevated cellular uptake. The targeting ligand selected for the nanoparticles could be a peptide, protein and its derivatives, an aptamer, or a small molecule like folate. This strategy has been studied extensively and is being expanded as new surface receptors for different cancer types are identified. Different cancer types such as breast cancer, glioblastoma, ovarian cancer, liver cancers and so on have been imaged using the targeted imaging method [4]. Even though studied extensively in in vitro laboratory situations, application in clinical studies can be impeded due to the additional synthetic and purification steps. A select group of reports on targeted imaging are now discussed to better familiarize the readers with this approach.

In one study Weissleder and coworkers were able to show that it is possible to image transgene expression in vivo by MRI using an active-targeted imaging method [32]. The group studied an engineered transferrin receptor (ETR) expressing cell line (ETR positive) and ETR negative gliosarcoma cells. They were able to show that the ETR positive cells tended to take up the probe 500 % more efficiently in cell culture than ETR negative cells. The nanoparticles used for this study were dextran coated superparamagnetic nanoparticles conjugated to human holo-transferrin proteins, which specifically target transferrin. The group implanted ETR positive and negative cells to the right and left flank of nude mice, respectively. After the tumors developed, the probe was injected and imaged by T2-weighted MRI. The MRI results demonstrated that the nanoparticles preferentially accumulated in ETR positive tumors.

In another study Moore and coworkers used synthetic peptides conjugated to iron oxide nanoparticles to image adenocarcinoma cells in vivo [23]. The cellular target in this study was the underglycosylated mucin-1 (uMUC-1) antigen, which is a transmembrane molecule overexpressed by most human epithelial cancer cells. A synthetic peptide EPPT was conjugated to the nanoparticles covalently as a

targeting ligand, which was derived from a monoclonal antibody (ASM2) raised against human epithelial cancer cells. The peptide showed a remarkable affinity for uMUC-1. The nanoparticles were further conjugated to a near infrared dye (cy5.5) to gather additional information about tumor specific accumulation by in vivo optical imaging. The authors tested several uMUC-1 positive human cancer cells from different organs in order to gather broader information about interaction between the conjugated nanoparticles and the transmembrane molecule including nanoparticle uptake both in vitro and in vivo. In vitro cell binding assays indicated that the uMUC-1 positive cells had a greater nanoparticle uptake (attributed to the interaction with EPPT). In vivo, mice were implanted with uMUC-1 positive and negative tumor cells in the right and left flanks to evaluate and compare the probe uptake by several different human adenocarcinomas. The results showed that indeed the uMUC-1 positive cells tended to take up the probe to a greater extent than the antigen-negative cells. These results were confirmed by in vivo magnetic resonance and optical imaging.

In another study Kumar et al. showed that myristoylated polyarginine peptide (MPAP)-functionalized iron oxide nanoparticles showed a significant uptake by orthotopically implanted gliomas in mice [16]. Gliomas are very aggressive and progress very quickly. Detection of brain cancer at early stages of development is important to fight the disease. In this study, the authors were able to specifically target U-87 human glioma cells and identify each tumor using in vivo MRI. In this type of brain tumor the blood brain barrier becomes leaky and has pores as large as 100 nm. Exploiting the leakiness of the vasculature and utilizing a cationic membrane translocation peptide (MPAP), a significant nanoparticle passage was achieved into the tumor interstitium and then into the tumor cells.

1.3.3 Magnetic Relaxation Switching

Magnetic Relaxation Switching (MRS) is an event where the magnetization efficacy of nanoparticles changes as their state of dispersity changes. When iron oxide nanoparticles aggregate they become more efficient at changing the T2 relaxation time of the neighboring protons and when they go from an aggregated to a dispersed state they return back to their initial magnetization. This property of magnetic nanoparticles has been used to detect several target molecules via magnetic relaxation switching. The target could be a physiologically relevant material such as a virus, protein, metal ions or other indicators of biological events [25,36].

In one study, telomerase activity in malignant cells was investigated by MRS [9]. Telomerase activity is elevated in many malignancies and is believed to play a significant role in tumorigenesis. Detection of telomerase activity is important in following cancer development, designing telomerase inhibitors, adjusting treatment dosage, and understanding enzymatic functions and levels. The authors designed magnetic nanoparticles that bind to telomerase-associated repeat units (TTAGGG), forming small clusters of assembled magnetic nanoparticles depending upon the

presence of elevated telomerase activity in malignant cells. Such assemblies cause a change in T2 relaxation time, which can be detected by benchtop NMR relaxometers. In the absence of such a binding event, the nanoparticle assembly does not form, and therefore, a change in T2 is not observed. The assay detects telomerase activity with high sensitivity.

Additional biochemical studies were conducted to establish the potential of MRS in detecting cancer related biological compounds. For example in one proof of principle study, nanoparticles were conjugated with adenosine aptamer and assembled into clusters [33]. After administration of adenosine, the nanoparticles disassembled, with binding to adenosine and a concomitant increase in T2. In another study the nanoparticles were conjugated to thrombin aptamers and after binding thrombin the nanoparticles assembled and decreased T2, as imaged by MRI [34].

In a different study detection of biologically relevant calcium ions was achieved by using the MRS properties of magnetic nanoparticles [1]. Calcium has an important role as a second messenger in cellular pathways and its detection is important in investigating neural network activity in the brain. In this study, the nanoparticles were conjugated to calmodulin, a calcium binding protein. The nanoparticles then assembled upon binding to intracellular calcium ions. With this clustering event, the T2 decrease was fivefold greater and detectable by MRI. This outcome suggests MRS may soon apply to more clinically relevant scenarios.

1.4 Non-invasive MR/SERS Imaging with Gold-Iron Oxide Nanoparticles

Although MRI is a valuable imaging tool due to its high spatial resolution (25–100 μm), it requires microgram to milligram quantities of contrast agent for imaging. Therefore, it suffers from low sensitivity. On the other hand, fluorescence is a sensitive detection method, which suffers from low spatial resolution (2–3 mm) and background auto-fluorescence. Consequently, a multimodal imaging method combining MRI and optical detection with sensitivity equivalent to in vivo fluorescence but without background interference represents a unique advantage. To that purpose, combining surface enhanced Raman scattering (SERS) with MRI was investigated. In SERS, enhanced Raman scattering signal is detected from molecules absorbed on rough metal surfaces such as gold and silver. SERS is particularly valuable, since it is highly sensitive (two orders of magnitude brighter than quantum dots) and the background interference is minimal. The advantage of SERS over other optical methods is reflected in its capability for spectroscopic detection and ultra-high sensitivity suitable for identification of single molecules under certain conditions. It has been shown that in order to obtain an in vivo SERS signature, intravenous or intramuscular administration of as little as 50 fmol of SERS active gold nanoparticles is enough to obtain a distinguishing SERS signal from deep tissues or from tumor xenografts [27].

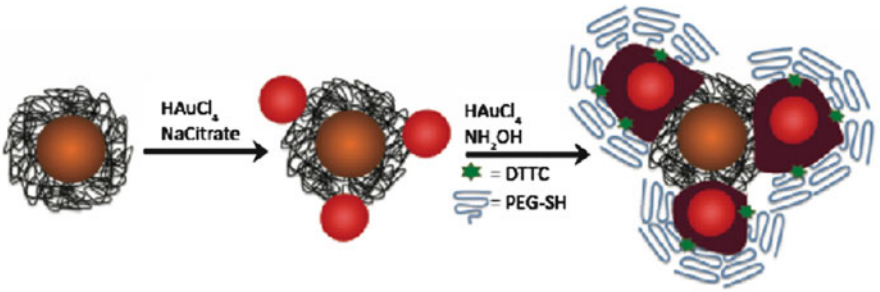

Fig. 1.3 Schematic representation of the synthesis of a SERS and MRI active contrast agent, AuMN-DTTC. The process involves sequential reduction of gold onto the parental MN, expansion of the gold seeds, and incorporation of DTTC and PEG onto the gold seeds

Yigit et al. synthesized MRI-active superparamagnetic iron oxide nanoparticles, stably complexed with gold nanoparticles (AuMN-DTTC). The gold nanoparticles serve as a template for a Raman active dye molecule to generate a surface-enhanced Raman scattering (SERS) effect (Fig. 1.3). The synthesized probe was tested for its utility as a T2 weighted MRI contrast agent and a SERS active contrast agent [35].

In vivo MR imaging of mice injected intramuscularly with the probe revealed that AuMN-DTTC indeed could be detected by MRI. SERS measurements using a portable Raman system showed a distinct SERS signal associated with the injection site [35].

This agent presents novel opportunities for noninvasive imaging. By combining the two modalities, it could allow the high-resolution, high-sensitivity in vivo detection of biological processes.

1.5 siRNA Therapeutics with Iron Oxide Nanoparticles

RNA interference is a powerful cellular process, which has been explored extensively for therapeutic applications. Administration of synthetic small interfering RNA molecules (siRNAs) into cellular compartments for degrading disease-causing mRNAs has shown dramatic therapeutic effects. Due to their initial success and future potential there are several siRNA-based preclinical and clinical trials for various diseases [15]. The biggest hurdles facing in vivo siRNA therapy are protection from nuclease degradation of the siRNA molecules in the circulation, their delivery to tissues of interest and intercellular uptake. Nanoparticles serve as a suitable platform to address these questions. Bioconjugation of siRNA molecules to nanoparticles not only results in successful delivery of the siRNA payload into the cellular environment but also protects them from nuclease degradation [7]. Recently there has been a successful phase I clinical trial of a targeted siRNA–nanoparticle conjugate for targeting solid tumors [5]. In addition to

delivery, it is important to image the bioavailability of the siRNA noninvasively. There are several examples of probes synthesized and tested to address this goal.

In one example, the probe consists of magnetic nanoparticles (for MRI) tagged with Cy5.5 dye (for NIRF imaging) and conjugated to a synthetic siRNA duplex targeting green fluorescent protein (GFP). The probe was tested in GFP-expressing tumors as a model system [21]. The probe was further conjugated to myristoylated polyarginine peptide (MPAP), which acts as a membrane translocation vector for increased uptake in tumor cells. First, in vitro experiments using green fluorescent protein (GFP) or control red fluorescent protein (RFP)-expressing tumor cells confirmed that GFP was down-regulated, whereas RFP expression remained constant. The in vivo studies showed that after systematic intravenous administration of the probe, accumulation was observed in tumors. Tumor uptake was confirmed by MRI and in vivo optical imaging (Fig. 1.4). The expression of GFP in the GFP-expressing tumor cells was reduced, whereas RFP expression was not affected in the RFP-expressing tumors, indicating that the effect was specific. These results were confirmed by in *vivo* optical imaging and quantitative RT-PCR.

In a more clinically relevant scenario, the nanoparticles carried siRNA to the antiapoptotic gene *birc5*, which encodes Survivin. Survivin is an important therapeutic target because it is a member of the inhibitor of apoptosis protein family, which shows tumor-restricted expression in most human neoplasms. The synthesized probe was administered intravenously into breast tumor-bearing mice twice a week for 2 weeks. MRI studies before and after probe administration revealed that the probe accumulated in tumor cells, which was also confirmed by in vivo optical imaging.

The specific silencing of *birc5* was confirmed by RT-PCR. As a result, a noticeable increase in tumor-associated levels of apoptosis and necrosis was observed. These results demonstrated the applicability of the siRNA-conjugated nanoparticles as multifunctional therapeutic and imaging agents (Fig. 1.5).

In a similar scenario, in order to improve the bioavailability of the siRNA complex to tumor cells, the nanoparticles were conjugated to the MUC-1 specific EPPT peptide, instead of MPAP. This modification increases the overall nanoparticle availability in tumor cells [17]. Studies with the targeted probe revealed that the contrast agents were taken up by tumor cells *in vivo* resulting in an overall slower tumor growth due to specific silencing of *birc5* by the siRNA-functionalized probe.

This technology has far-reaching implications. By bringing imaging and therapy together, it can be applied to a wide range of diseases, which can be treated using intervention at the level of gene expression.

1.6 Magnetic Fluid Hyperthermia

Magnetic fluid hyperthermia (MFH) is based on the following principle: the superparamagnetic core absorbs the energy from an alternating external magnetic field and converts it into thermal energy. This causes the nanoparticles to heat up by magnetic hysteresis losses or Néel relaxation. The cells containing these

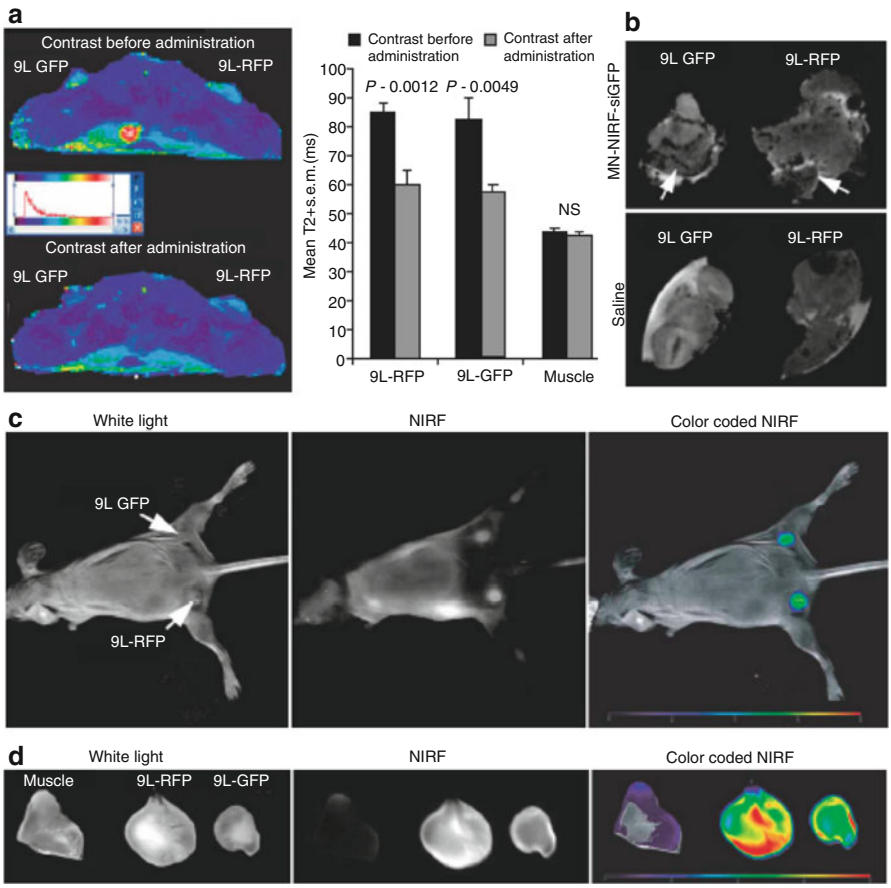

Fig. 1.4 (**a**) In vivo MR imaging of mice bearing bilateral 9L-GFP and 9L-RFP tumors before and 24 h after MN-NIRF-siGFP administration. A significant drop in T2 relaxivity was observed in the tumors. (**b**) Ex vivo high-resolution MR images of excised tumors. (**c**) In vivo NIRF optical imaging of tumor-bearing mice. The fluorescence signal associated with the tumors confirmed the delivery of the MN-NIRF-siGFP probe to tumor tissues. (**d**) Ex vivo NIRF optical imaging showed a significantly higher fluorescence in tumors than in muscle tissues (reprinted from [21] with permission from Nature Publishing Group)

heat-generating nanoparticles undergo cell death when the temperature exceeds their physiological tolerance. This event was first investigated in 1957 by Gilchrist et al. where an external magnetic field was used to heat up tissues containing magnetic nanoparticles [8]. Considering the fact that tumor cells are more sensitive to temperature and that they uptake the magnetic nanoparticles more readily compared to nonmalignant cells, a directed thermal change via magnetic nanoparticles is a promising way to eradicate cancerous cells.

There have been numerous advances in the field of MFH. In vivo studies have been performed in mice, rats, rabbits and dogs and for different types of cancers, including

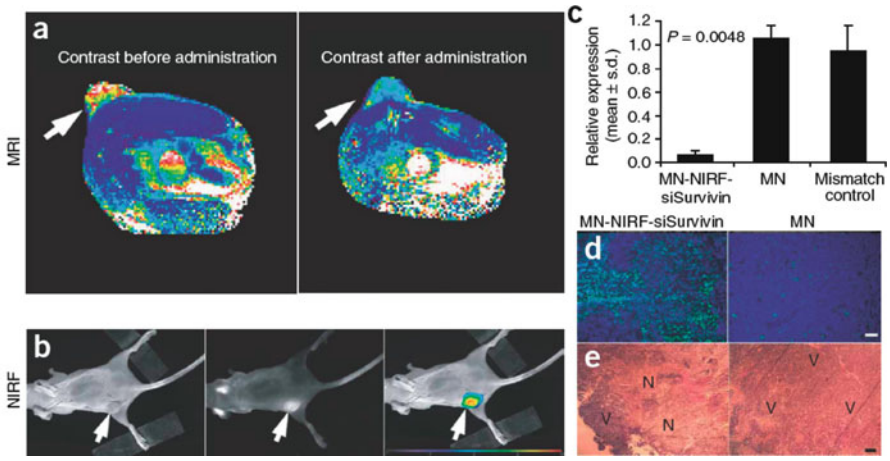

Fig. 1.5 Therapeutic MN-siSurvivin delivery. (**a**) In vivo MRI of mice bearing subcutaneous LS174T human colorectal adenocarcinoma (*arrows*). The significant drop in T2 relaxation times observed after administration of the nanoparticles indicated probe delivery. (**b**) The delivery of the probe to tumors was confirmed by the high-intensity NIRF signal on in vivo optical images of mice after injection of nanoparticles (*left*, white light; *middle*, NIRF; *right*, color-coded overlay). (**c**) Quantitative RT-PCR analysis of survivin expression in LS174T tumors after injection of magnetic nanoparticles conjugated to anti-Survivin siRNA. (**d**) Apoptotic rates in tumor tissues. Note distinct areas with a high density of apoptotic nuclei (*green*) in tumors treated with probe (*left*), which were not observed in tumors treated with the control magnetic nanoparticles (right). (**e**) H&E staining of frozen tumor sections revealed considerable eosinophilic areas of tumor necrosis (N) in tumors treated with probe (*left*). Tumors treated with magnetic nanoparticles were devoid of necrotic tissue (*right*). Purple hematoxiphilic regions (V) indicate viable tumor tissues. Scale bar, 50 μm (reprinted from [21] with permission from Nature Publishing Group)

prostate, brain, etc. [18]. In a recent study, authors injected porphyrin functionalized bimagnetic nanoparticles targeting drug resistant melanoma in mice [2]. Porphyrin functionalization is important because the constant need for porphyrins by cancer cells due to their elevated sugar metabolism results in higher porphyrin uptake by tumor cells. With the targeting porphyrin group on the surface of the nanoparticles, the uptake by healthy cells is minimized. In vivo, mice carrying a subcutaneous melanoma xenograft were used. After intratumoral injection of nanoparticles and the application of alternating magnetic field (AMF) pulses, the authors observed an 11 °C increase in temperature in the tumors and a significant decrease in tumor size. After intravenous injection of the nanoparticles, the tumor size also decreased dramatically, representing a more clinically relevant treatment scenario.

This approach has also been applied clinically. Patients with recurrent glioblastoma multiforme were treated with hyperthermia using magnetic nanoparticles as heat generating probes [19]. Currently the only hyperthermia method that is considered involves local injection of nanoparticles into the tumor, which then is exposed to an external alternating magnetic field [18]. This approach, however, can be made more specific by incorporating targeting moieties into the nanoparticles.

1.7 Summary

Iron oxide nanoparticles hold great promise for many biomedical applications. However, there are still some issues that need to be resolved before successful clinical application of these nanoparticles for true molecular imaging. First, the toxicity associated with the nanoparticles has to be addressed carefully before any clinical applications. Some of the iron oxide nanoparticle derivatives can induce several toxic effects, such as inflammation, the formation of apoptotic bodies, impaired mitochondrial function, generation of reactive oxygen species and chromosomal damage. Better control of the size distribution and minimizing nonspecific uptake by other organs has to be achieved for better clinical outcome.

Iron oxide nanoparticles are gathering much attention since they have potential applications in drug delivery and noninvasive imaging. Therefore, therapy and diagnosis can be achieved by one system. Due to this dual property, it is possible to deliver image-guided therapy by combining two functionalities (diagnosis and therapy) in clinical studies.

References

1. Atanasijevic T, Shusteff M, Fam P, Jasanoff A (2006) Calcium-sensitive MRI contrast agents based on superparamagnetic iron oxide nanoparticles and calmodulin. Proc Natl Acad Sci U S A 103:14707–14712
2. Balivada S, Rachakatla R, Wang H, Samarakoon T, Dani R, Pyle M, Kroh F, Walker B, Leaym X, Koper O, Tamura M, Chikan V, Bossmann S, Troyer D (2010) A/C magnetic hyperthermia of melanoma mediated by iron(0)/iron oxide core/shell magnetic nanoparticles: a mouse study. BMC Cancer 10:119
3. Bulte JW, Kraitchman DL (2004) Iron oxide MR contrast agents for molecular and cellular imaging. NMR Biomed 17:484–499
4. Cole AJ, Yang VC, David AE (2011) Cancer theranostics: the rise of targeted magnetic nanoparticles. Trends Biotechnol 29:323–332
5. Davis ME, Zuckerman JE, Choi CH, Seligson D, Tolcher A, Alabi CA, Yen Y, Heidel JD, Ribas A (2010) Evidence of RNAi in humans from systemically administered siRNA via targeted nanoparticles. Nature 464:1067–1070
6. Evgenov NV, Medarova Z, Dai G, Bonner-Weir S, Moore A (2006) In vivo imaging of islet transplantation. Nat Med 12:144–148
7. Ferrari M (2010) Vectoring siRNA therapeutics into the clinic. Nat Rev Clin Oncol 7:485–486
8. Gilchrist RK, Medal R, Shorey WD, Hanselman RC, Parrott JC, Taylor CB (1957) Selective inductive heating of lymph nodes. Ann Surg 146:596–606
9. Grimm J, Perez JM, Josephson L, Weissleder R (2004) Novel nanosensors for rapid analysis of telomerase activity. Cancer Res 64:639–643
10. Gupta AK, Curtis ASG (2004) Lactoferrin and ceruloplasmin derivatized superparamagnetic iron oxide nanoparticles for targeting cell surface receptors. Biomaterials 25:3029–3040
11. Gupta AK, Gupta M (2005) Synthesis and surface engineering of iron oxide nanoparticles for biomedical applications. Biomaterials 26:3995–4021
12. Gupta AK, Wells S (2004) Surface-modified superparamagnetic nanoparticles for drug delivery: preparation, characterization, and cytotoxicity studies. IEEE Trans NanoBiosci 3:66–73

13. Harisinghani MG, Barentsz J, Hahn PF, Deserno WM, Tabatabaei S, van de Kaa CH, de la RJ, Weissleder R (2003) Noninvasive detection of clinically occult lymph-node metastases in prostate cancer. N Engl J Med 348:2491–2499
14. Josephson L, Tung C-H, Moore A, Weissleder R (1999) High-efficiency intracellular magnetic labeling with novel superparamagnetic-tat peptide conjugates. Bioconjug Chem 10:186–191
15. Kim DH, Rossi JJ (2007) Strategies for silencing human disease using RNA interference. Nat Rev Genet 8:173–184
16. Kumar M, Medarova Z, Pantazopoulos P, Dai G, Moore A (2010) Novel membrane-permeable contrast agent for brain tumor detection by MRI. Magn Reson Med 63:617–624
17. Kumar M, Yigit M, Dai G, Moore A, Medarova Z (2010) Image-guided breast tumor therapy using a small interfering RNA nanodrug. Cancer Res 70:7553–7561
18. Laurent S, Dutz S, Hafeli UO, Mahmoudi M (2011) Magnetic fluid hyperthermia: focus on superparamagnetic iron oxide nanoparticles. Adv Colloid Interface Sci 166:8–23
19. Maier-Hauff K, Ulrich F, Nestler D, Niehoff H, Wust P, Thiesen B, Orawa H, Budach V, Jordan A (2011) Efficacy and safety of intratumoral thermotherapy using magnetic iron-oxide nanoparticles combined with external beam radiotherapy on patients with recurrent glioblastoma multiforme. J Neurooncol 103:317–324
20. Medarova Z, Evgenov NV, Dai G, Bonner-Weir S, Moore A (2006) In vivo multimodal imaging of transplanted pancreatic islets. Nat Protoc 1:429–435
21. Medarova Z, Pham W, Farrar C, Petkova V, Moore A (2007) In-vivo imaging of siRNA delivery and silencing in tumors. Nat Med 13:372–377
22. Medarova Z, Rashkovetsky L, Pantazopoulos P, Moore A (2009) Multiparametric monitoring of tumor response to chemotherapy by noninvasive imaging. Cancer Res 69:1182–1189
23. Moore A, Medarova Z, Potthast A, Dai G (2004) In vivo targeting of underglycosylated MUC-1 tumor antigen using a multimodal imaging probe. Cancer Res 64:1821–1827
24. Mouli SK, Zhao LC, Omary RA, Thaxton CS (2010) Lymphotropic nanoparticle enhanced MRI for the staging of genitourinary tumors. Nat Rev Urol 7:84–93
25. Perez JM, Simeone FJ, Saeki Y, Josephson L, Weissleder R (2003) Viral-induced self-assembly of magnetic nanoparticles allows the detection of viral particles in biological media. J Am Chem Soc 125:10192–10193
26. Pittet MJ, Swirski FK, Reynolds F, Josephson L, Weissleder R (2006) Labeling of immune cells for in vivo imaging using magnetofluorescent nanoparticles. Nat Protoc 1:73–79
27. Qian X, Peng XH, Ansari DO, Yin-Goen Q, Chen GZ, Shin DM, Yang L, Young AN, Wang MD, Nie S (2008) In vivo tumor targeting and spectroscopic detection with surface-enhanced Raman nanoparticle tags. Nat Biotechnol 26:83–90
28. Sjogren CE, Briley-Saebo K, Hanson M, Johansson C (1994) Magnetic characterization of iron oxides for magnetic resonance imaging. Magn Reson Med 31:268–272
29. Storm G, Belliot SO, Daemen T, Lasic DD (1995) Surface modification of nanoparticles to oppose uptake by the mononuclear phagocyte system. Adv Drug Deliver Rev 17:31–48
30. Torchilin VP, Trubetskoy VS (1995) Which polymers can make nanoparticulate drug carriers long-circulating? Adv Drug Deliver Rev 16:141–155
31. Wang P, Yigit MV, Medarova Z, Wei L, Dai G, Schuetz C, Moore A (2011) Combined small interfering RNA therapy and in vivo magnetic resonance imaging in islet transplantation. Diabetes 60:565–571
32. Weissleder R, Moore A, Mahmood U, Bhorade R, Benveniste H, Chiocca EA, Basilion JP (2000) In vivo magnetic resonance imaging of transgene expression. Nat Med 6:351–354
33. Yigit MV, Mazumdar D, Kim HK, Lee JH, Odintsov B, Lu Y (2007) Smart "turn-on" magnetic resonance contrast agents based on aptamer-functionalized superparamagnetic iron oxide nanoparticles. Chembiochem 8:1675–1678
34. Yigit MV, Mazumdar D, Lu Y (2008) MRI detection of thrombin with aptamer functionalized superparamagnetic iron oxide nanoparticles. Bioconjug Chem 19:412–417

35. Yigit MV, Zhu L, Ifediba MA, Zhang Y, Carr K, Moore A, Medarova Z (2011) Noninvasive MRI-SERS imaging in living mice using an innately bimodal nanomaterial. ACS Nano 5:1056–1066
36. Zhao M, Josephson L, Tang Y, Weissleder R (2003) Magnetic sensors for protease assays. Angew Chem Int Ed 42:1375–1378

Chapter 2
Inertial Migration of Cancer Cells in a Microfluidic Device

Tatsuya Tanaka, Takuji Ishikawa, Keiko Numayama-Tsuruta, Yohsuke Imai, Hironori Ueno, Takefumi Yoshimoto, Noriaki Matsuki, and Takami Yamaguchi

Abstract The circulating tumor cell (CTC) test is used to evaluate the condition of breast cancer patients by counting the number of cancer cells in peripheral blood samples. Although microfluidic systems to detect or separate cells using the inertial migration effect may be applied to this test, the hydrodynamic forces acting on cancer cells are incompletely understood. In this chapter, we explain the inertial migration of cancer cells in microchannels. We also explain fabrication techniques of microchannels used in the experiments. By measuring the cell migration probability, we examined the effects of cell deformability and variations in cell size on the inertial migration of cancer cells. The results clearly illustrate that cancer cells can migrate towards equilibrium positions in the similar manner with rigid spheres. These results will be important for the design of microfluidic devices for the CTC test.

T. Tanaka (✉) • T. Ishikawa • Y. Imai • T. Yoshimoto
School of Engineering, Tohoku University, 6-6-01 Aoba, Sendai 980-8579, Japan
e-mail: tatsuya@pfsl.mech.tohoku.ac.jp

K. Numayama-Tsuruta • T. Yamaguchi
School of Biomedical Engineering, Tohoku University, 6-6-01 Aoba, Sendai 980-8579, Japan

H. Ueno
International Advanced Research and Education Organization, Tohoku University, 6-6-01 Aoba, Sendai 980-8579, Japan

N. Matsuki
Department of Biomedical Engineering, Okayama University of Science, 1-1 Ridai-cho, Okayama 700-0005, Japan

M.W. Collins and C.S. König (eds.), *Micro and Nano Flow Systems for Bioanalysis*, Bioanalysis 2, DOI 10.1007/978-1-4614-4376-6_2,

2.1 Introduction

The incidence of breast cancer is increasing in many developed countries. In its diagnosis, it is crucial to detect metastasis or cancer recurrence at an early stage. The circulating tumor cell (CTC) test has been widely adopted for evaluating the prognosis of breast cancer [3,6,7]. In this test a patient's condition is assessed by counting the number of cancer cells in a peripheral blood sample. For this purpose, it is necessary to distinguish cancer cells from other blood cells, and the accuracy of the CTC test is strongly dependent on the precision of cell identification.

Microfluidic devices for cell separation have received much attention. These devices can be classified into two groups based on whether the method of separation is active or passive [2]. While in active separation an external field is involved, such as would be caused by magnetic or electric means, in passive separation an external force is not needed. Passive separation devices have a number of advantages compared with active separation alternatives; these include miniaturization, inexpensive production cost, and easy handling of the device. Examples of passive cell separation methods are the pillar structures method [18,21], hydrodynamic filtration [23,24], and biomimetic separation [11,19]. However, despite their high separation efficiency, devices using such methods are unsuitable for the CTC test because of their low throughput. To overcome this difficulty, a passive cell separation method has been investigated which involves inertial migration.

Segre and Silbergerg [17] originally described the inertial migration process in 1962. When the Reynolds number of a particle is not too small, the inertial force on it generates a drift velocity perpendicular to the streamline. Hence, a group of particles flowing in a channel will move towards the sidewalls, and eventually the particles will be aligned passively at specific positions. Microfluidic devices using inertial migration have been proposed for separating various rigid particles [1,5,16]. The throughput of this method is very high, because the inertial effect becomes significant only at high velocities. The time required for particle separation is often much shorter than that of other methods, and forms its major advantage.

Recently, some groups have succeeded in applying the inertial migration effect to the detection or separation of different types of living cells. Kuntaegowadanahalli et al. [12] developed a five-loop Archimedean spiral microchannel and separated SH-SY5Y neuroblastoma cells (~15 μm in diameter) from C6 rat glioma cells (~6 μm in diameter) in a dilute cell suspension (volume fraction, ~0.05%). In addition to inertial migration forces, their microfluidic device used the Dean force generated by the centrifugal effect. The separation efficiency exceeded 80%, with a high throughput of 1×10^6 cells/min. Hur et al. [9] demonstrated how cells flowing through channels could be aligned three-dimensionally via the inertial migration effect. As they focused on cells at a specific depth, the effects of cell overlap and out-of-focus motion were ignored. Their device allowed red blood cells and leukocytes to be counted with high sensitivity via image analysis. Using a similar approach to Kuntaegowadanahalli et al. [12], Carlo et al. [4] applied the inertial

force effect to isolate platelets from other blood cells in a dilute suspension, enriching the relative number of platelets by 100-fold. These examples illustrate the potential of applying inertial migration to the development of a microfluidic device for the CTC test.

If cancer cells could be separated from blood cells using the inertial migration effect, this would facilitate the development of a microfluidic device for the CTC test. To this end, we have recently studied the inertial migration of cancer cells in a straight microchannel [22], which is introduced in this chapter. In Sect. 2.2, we briefly explain the basic mechanism of inertial migration. Section 2.3 describes the fabrication of a polydimethylsiloxane (PDMS) microchannel, for the sake of readers who are not familiar with microfluidics. We explain the preparation of cancer cells in Sect. 2.4, particularly for readers who have no experience of cell culturing. Section 2.5 gives the results of initial experiments using rigid spheres: these enable the efficiency of inertial migration to be demonstrated. Section 2.6 presents experimental results using cancer cells, thus showing how inertial migration may be applied to them. The results given in Sects. 2.5 and 2.6 are mainly from Tanaka et al. [22], and further details such as the effects of red blood cells on the migration of cancer cells can be found in that paper. This chapter focuses on the fundamental principles of the inertial migration of cancer cells in a microchannel.

2.2 Mechanism of Inertial Migration

Figure 2.1a shows the principles governing the inertial migration of particles flowing in a tube. The particles are subject to drag and inertial lift forces. The drag force (F_D) drives particles along their streamlines, while the shear-induced inertial lift force (F_{IL}) drives them away from the channel center and toward the sidewalls. The particle Reynolds number (Re_p) is a key factor in inertial migration, being defined as $\mathrm{Re_p} = \rho d^2 \dot{\gamma}/\mu$, where d is the diameter of a particle, $\dot{\gamma}$ the shear rate, and ρ and μ the density and viscosity respectively. It represents the ratio of the inertial force to the viscous force acting on the particles. When $Re_p \ll 1$, inertial migration does not occur, and the particles follow the streamlines. When Re_p is not negligibly small, inertial force acts on the particles, and they tend to drift from the streamlines. When particles come close to the wall, the wall-induced inertial lift force (F_{WL}) appears in addition to F_{IL}. These two forces act in opposite directions, and the particles tend to migrate towards equilibrium positions, where the magnitudes of the two inertial forces are balanced.

These equilibrium positions depend mainly on the channel geometry and Re_p (Fig. 2.1b). In a cylindrical channel with moderate Re_p, particles align in an annulus at a radius of about $0.6R$, where R is the channel wall radius [17]. The radius of the equilibrium annulus increases with increasing Re_p because of the increase in F_{IL} [14,15]. For a channel with a square cross-section, particles tend to align near the wall, and the equilibrium positions form the sides of a small square (cf. Fig. 2.1b). For a channel with a rectangular cross-section, the equilibrium positions are near

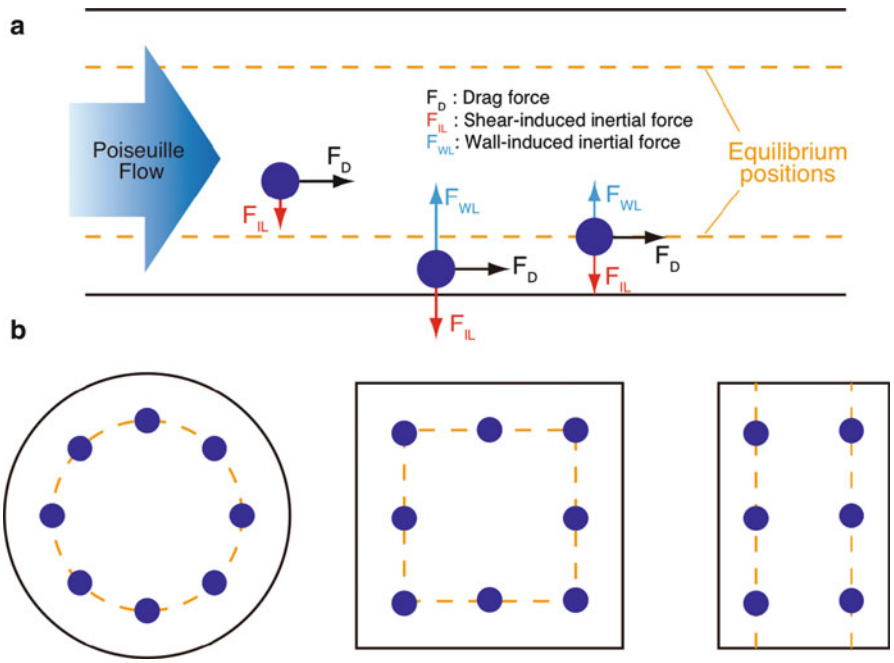

Fig. 2.1 The principle of the inertial migration of particles: (**a**) mechanism of the migration of particles toward their equilibrium positions and (**b**) the equilibrium positions in different channel geometries

the walls of the longer sides [1], because a greater shear rate acts on the particles along the narrower dimension. In terms of particle separation, a rectangular channel is preferable because the number of equilibrium positions is reduced and it is easier to guide particles toward a collecting outlet in a microfluidics device.

The migration length (L_m), i.e., the channel length required for the migration of rigid spheres, is obtained by considering the balance of forces between the shear-induced migration force and the viscous drag force. Bhagat et al. [1] derived L_m as

$$L_m = \frac{3\pi\mu}{2\rho U}\left(\frac{W}{a}\right)^3, \tag{2.1}$$

where U is the average velocity in the channel, W the half-width of the channel, and a the radius of a rigid sphere. When the channel length is much larger than L_m, most of the particles migrate to equilibrium positions. Consequently, L_m is one of the most important parameters in the design of a microchannel for particle separation. In Sect. 2.5, we show that (2.1) is a good approximation for describing the migration of rigid spheres. In Sect. 2.6, we show that (2.1) does not precisely predict the migration of cancer cells, as the L_m for cancer cells is longer than the value for rigid spheres.

2.3 Fabrication of a Polydimethylsiloxane Microchannel

A standard soft lithography technique is widely used for fabricating microchannels such as those with a stenosis [8] or with a bifurcation and confluence [10]. Here, as an example, we outline the fabrication procedure using photoresist SU-8 and polydimethylsiloxane (PDMS). SU-8, an epoxy-based photoresist, is widely used for fabricating channel molds. It can sustain structures with high aspect ratios, so that vertical sidewalls can be built easily. PDMS is a polymeric silicone with excellent material properties for making microfluidic devices. Its good optical transparency, good biocompatibility, accurate replication of fine and complex geometries, high thermal stability, and low cost make PDMS one of the most popular materials for microfluidic devices.

Figure 2.2 is a schematic of the procedure used for fabricating the microchannel. First (Step 1, Fig. 2.2) to enhance the adhesiveness of the photoresist on the wafer, the surface of a silicon wafer was cleaned using piranha solution, which is a mixture of sulfuric acid and hydrogen peroxide, to remove organic residues. After the substrate was washed with deionized water to remove all traces of the cleaning solution, the photoresist (SU-8 2075; Kayaku MicroChem, Tokyo, Japan) was applied to the silicon wafer with a spin coater. The thickness of the photoresist was controlled by adjusting the revolving speed of the spin coater (Step 2). Then, the wafer was glued to a photomask on which the channel geometry had been drawn. Finally, the wafer was exposed to ultraviolet light (Step 3) completing the silicon mold with the microchannel pattern (Step 4).

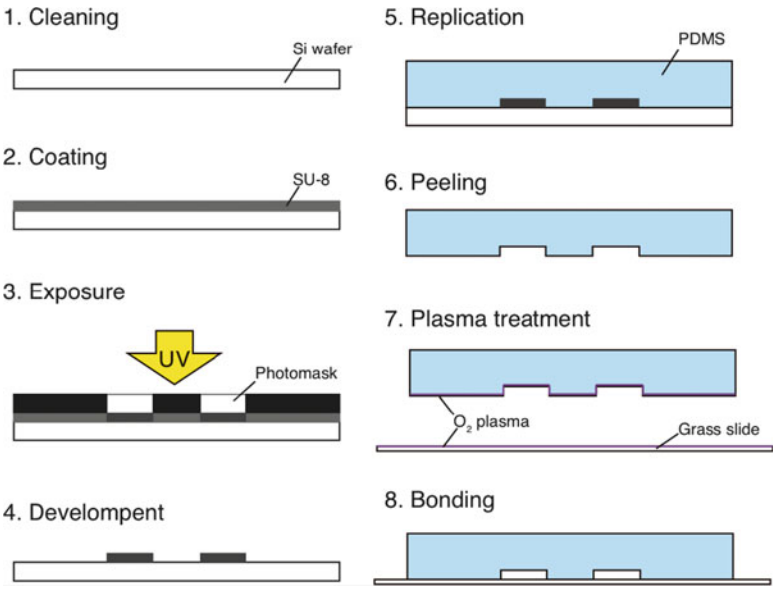

Fig. 2.2 Procedure for fabricating a PDMS microchannel

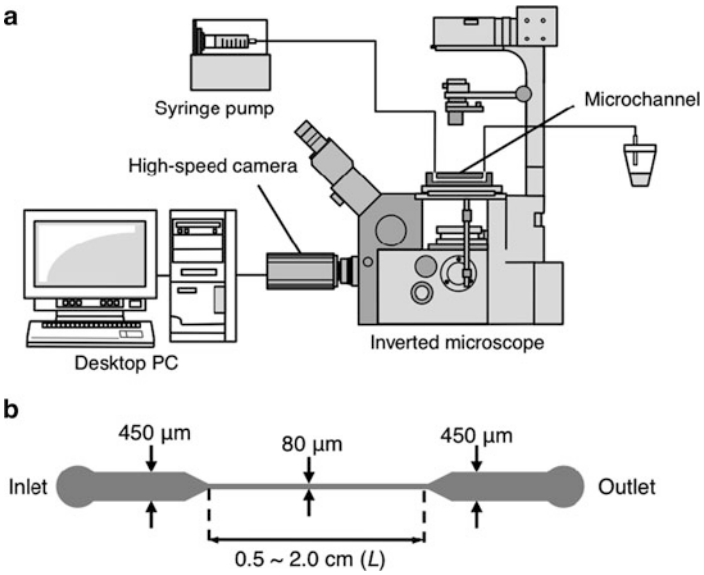

Fig. 2.3 Experimental setup: (**a**) schematic representation of the experimental setup; and (**b**) Geometry of PDMS microchannel. The height of the channel is 220 µm [22]

PDMS (Silpot 184; Dow Corning, Midland, MI) was prepared (Step 5) by mixing the base compound and curing agent at a weight ratio of 10:1. After removing the bubbles created during mixing, the mixture was poured on the master mold and cured by baking for about 40 min at 85°C. The PDMS was peeled (Step 6) from the master, and the fluidic ports used as the inlets and outlets of the fluidic device were created using a biopsy punch (Kai Industries, Gifu, Japan). For channels with very fine patterns, it is sometimes difficult to peel the PDMS channel from the master mold. In such cases, mold release agents are useful. Finally, to prevent fluid leakage from the gap between the PDMS and glass slide, an oxygen plasma treatment was applied (Step 7) to irreversibly bind (Step 8) the PDMS to the glass. Each step is straightforward, although special facilities are necessary, including a clean room and photolithography equipment. Alternatively, a private company may be contracted to fabricate the PDMS microchannel. In Sects. 2.5 and 2.6, we use a simple microchannel (cf. Fig. 2.3b) made using this technique.

2.4 Cell Preparation and Working Fluids

This section explains the preparation of cells and sample fluids used to perform the experiments in Sects. 2.5 and 2.6. The poorly differentiated human breast cancer cell line MDA-MB-231 was used. The cells in RPMI 1640 (Invitrogen,

Carlsbad, CA) with 10% fetal bovine serum (Thermo Fisher Scientific, Waltham, MA) and 1× antibiotic–antimycotic solution (Invitrogen) were cultured in 25-cm^2 tissue culture flasks at 37°C under 5% CO_2 (cf. [10]). For the experiments, cells were grown to 80–90% confluence, dissociated by the addition of 0.25% trypsin–EDTA (Invitrogen), harvested, and washed twice with Dulbecco's phosphate-buffered saline (PBS; Invitrogen).

Two different fluid samples were used in Sects. 2.5 and 2.6, respectively: a dilute suspension of 15-μm-diameter rigid spheres (FluoSpheres polystyrene microspheres; Invitrogen) in PBS and a dilute suspension of cancer cells (MDA-MB-231) in PBS. The concentrations of the rigid spheres and cancer cells were about 1×10^5 particles or cancer cells per milliliter. The density and viscosity at 25°C were 1.05×10^3 kg/m^3 and 1.15×10^{-3} Pa s, respectively.

2.5 Inertial Migration of Rigid Spheres in a Microchannel

The experimental setup for studying the inertial migration of rigid spheres is shown in Fig. 2.3a. The experimental apparatus consisted of an inverted microscope (IX71; Olympus, Tokyo, Japan) and a high-speed camera (Phantom v7.1; Vision Research, Wayne, NJ). A microchannel was placed on the stage, and the sample was injected using a syringe pump (IC 3101; KI Scientific, Holliston, MA). Images of the rigid spheres, taken with the high-speed camera, were recorded on a desktop computer.

A schematic of the PDMS microchannel is shown in Fig. 2.3b. A strong inertial force was induced on the particles flowing in the narrow test section, where Re_p was large. The test section of the channel was 80 μm wide, 220 μm high, and 1.0 cm long. To facilitate image analysis, the width of the microchannel was increased to 450 μm upstream and downstream from the test section.

The behavior of rigid spheres was observed upstream and downstream from the test section. A syringe pump was used to control the flow rate within the range 64-256 μL/min, corresponding to a Re_p of 0.16–0.62. To analyze particle behavior, the probability density of the width position from the center was calculated using the following equation:

$$P_i = \left(\sum_{j=1}^{M} n_{i,j} \right) \Bigg/ \left(\sum_{j=1}^{M} \sum_{i=1}^{N} n_{i,j} \right) \tag{2.2}$$

where P_i is the probability density at section i, M is the total number of frames recorded at 40-ms intervals, and $n_{i,j}$ is the number of particles in section i at frame j. The half-width of the channel was split into 50 sections (i.e., $n = 50$), and each was 4.5 μm wide. To calculate the probability density, at least 100 particles were counted in each experiment.

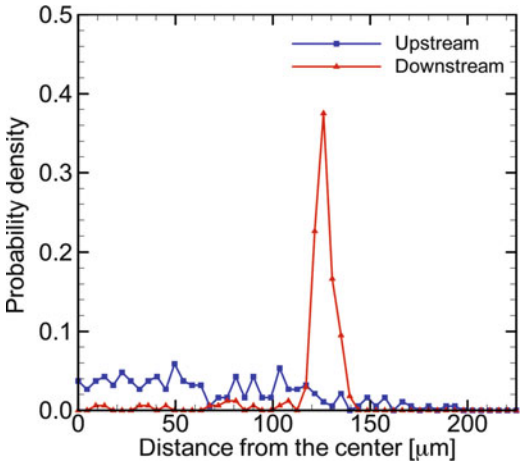

Fig. 2.4 Probability density of the width position of rigid spheres at the upstream and the downstream of the test section with $Re_p = 0.622$. The sidewall is located 225 μm from the center [22]

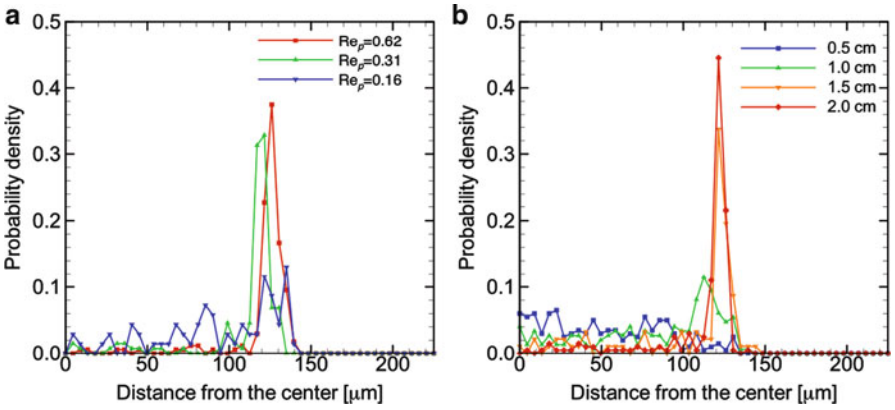

Fig. 2.5 Probability density of the width position of rigid spheres at the downstream of the test section: (**a**) effect of particle Reynolds number Re_p ($L = 1.0$ cm); and (**b**) effect of the channel length L ($Re_p = 0.16$) [22]

Figure 2.4 shows the probability density of the width position of rigid spheres upstream and downstream, with $Re_p = 0.62$. The probability density upstream was relatively uniform, while that downstream peaked around 125 μm from the center (i.e., 100 μm from the sidewall). This result was consistent with that of Bhagat et al. [1], who reported that particles migrated to about $0.4W$ from the sidewalls, where W is the half-width of the test section. The effects of Re_p and the length of the test section on the migration of rigid spheres are shown in Fig. 2.5.

When $Re_p = 0.16$, the migration of rigid spheres was not clearly observed (Fig. 2.5a). When $Re_p = 0.31$ and 0.62, inertial migration of particles toward equilibrium positions was observed. As Re_p increased, the peak of the probability density became larger. The migration of rigid spheres was not significant when $L = 0.5$ or 1.0 cm, whereas migration was apparent when $L = 1.5$ or 2.0 cm (Fig. 2.5b). These results indicate that the migration of rigid spheres occurs due to an inertial effect and that large values of Re_p and L are necessary to achieve strong migration of the spheres. These findings were consistent with those of previous studies [1,5,16]. For $Re_p = 0.16$, the migration length (L_m) was 1.3 cm. For $L = 0.5$ or 1.0 cm, the channel length was shorter than L_m ($L < L_m$). When $L = 1.5$ or 2.0 cm, the channels had adequate length ($L > L_m$). Our experimental results demonstrate that the migration length (L_m) calculated using (2.1) correctly describes the migration of rigid spheres.

2.6 Motion of Cancer Cells in a Microchannel

Next, the migration of cancer cells was compared with that of rigid spheres. Figure 2.6 shows the probability density of the width position of cancer cells upstream and downstream, with $Re_p = 0.62$. Like the rigid spheres, cancer cells displayed a relatively homogeneous probability density upstream, whereas a large peak, around 115 μm from the center (i.e., 110 μm from the wall), was observed downstream. Compared with the rigid spheres, the maximum probability density of the cancer cells was not as high and the probability density function slightly blunter.

The effects of Re_p and L on the probability density of cancer cells are shown in Fig. 2.7. The peak in the probability density increased with Re_p (Fig. 2.7a).

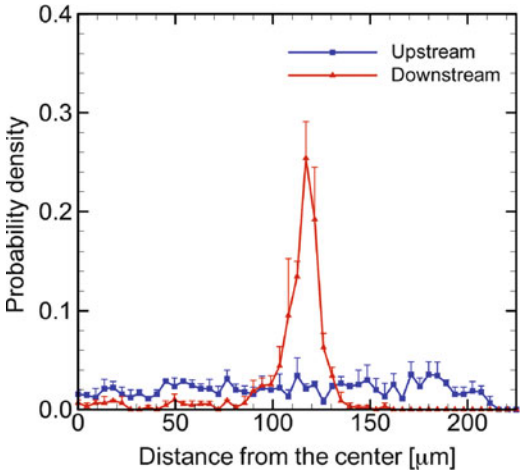

Fig. 2.6 Probability density of the width position of cancer cells at the upstream and the downstream of the test section with $Re_p = 0.62$. *Error bars* indicate standard deviations. The sidewall is located 225 μm from the center [22]

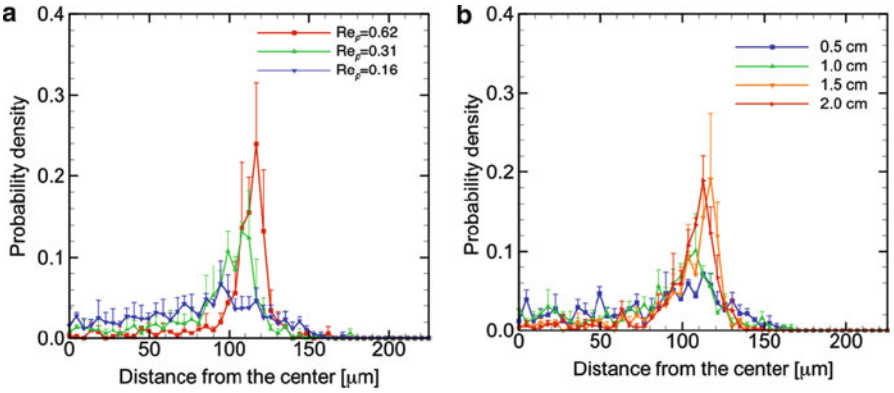

Fig. 2.7 Probability density of the width position of cancer cells at the downstream of the test section: (**a**) effect of particle Reynolds number Re_p ($L = 1.0$ cm); and (**b**) effect of the channel length L ($Re_p = 0.31$). *Error bars* indicate standard deviations [22]

For $Re_p = 0.16$, cancer cell migration was not clearly observed, as for rigid spheres (*cf.* Fig. 2.5a). For $L = 1.5$ and 2.0 cm (Fig. 2.7b), obvious migration of cancer cells was seen. These basic tendencies were the same for the rigid spheres and cancer cells.

To quantify the differences in migration properties between the rigid spheres and cancer cells, we normalized the experimental results using the migration length L_m (2.2). To quantify the migration strength, the maximum probability densities of six sections, $PD_{6,\,max}$, were calculated using the following equation:

$$PD_{6,max} = \left[\sum_{i}^{i+5} P_i\right]_{max}, \quad (i = 1 - 45) \tag{2.3}$$

where max indicates the maximum value. A large value of $PD_{6,\,max}$ indicates that large numbers of rigid spheres or cancer cells were focused in a narrow band in the width direction.

Figure 2.8 shows the correlation between L/L_m and $PD_{6,\,max}$. All of the results are plotted in the figure, covering the experimental conditions $Re_p = 0.16$–0.62 and $L = 0.5$–2.0 cm. The results differed markedly between the rigid spheres and cancer cells; the cancer cells required a greater channel length than the rigid spheres to reach the equilibrium state.

Two possible factors might have affected the migration length of cancer cells as compared with rigid spheres: their deformability and their variation in size.

Firstly, to estimate the effect of cell deformability, we introduced the capillary number, defined as $Ca = \mu\dot{\gamma}/E$, where E is Young's modulus. At a large capillary number, cells undergo marked deformation owing to high shear stress, whereas when Ca is small, cells maintain their original shape. Young's modulus for typical breast cancer cells is about 10^2 Pa [13,20], and the fluid viscosity is of the order of 10^{-3} Pa s.

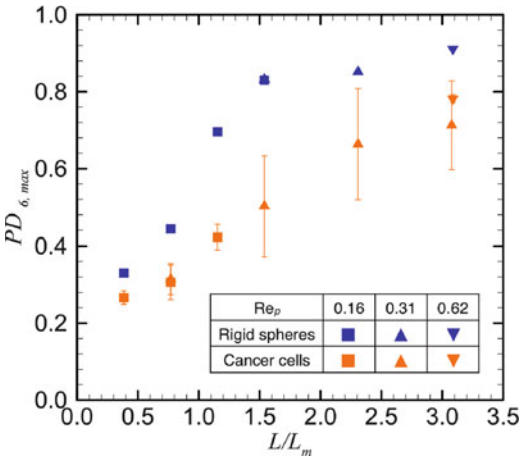

Fig. 2.8 Correlations between $PD_{6,max}$, defined by (2.3), and the normalized channel length L/L_m. The figure contains all experimental data under the conditions of $Re_p = 0.16$–0.62 and $L = 0.5$–2.0 cm. *Error bars* indicate standard deviations [22]

Consequently, Ca becomes greater than unity only when the shear rate $\dot{\gamma}$ exceeds $10^5\ s^{-1}$. In the present study, the average $\dot{\gamma}$ at the highest flow rate ($Re_p = 0.62$) was about $1.2 \times 10^4\ s^{-1}$. Therefore, the effect of cell deformability can be neglected. This was confirmed by the overlapping results of $PD_{6,max}$ obtained for different values of Re_p, which are plotted on a single curve in Fig. 2.8.

The other factor that might have affected the migration length of cancer cells compared with rigid spheres is the size variation of the cancer cells. The migration length L_m, given by (2.1), is proportional to a^{-3}, where a is the particle radius. Consequently, a small variation in cancer cell size results in a large difference in migration length. For example, the migration length of a cancer cell with radius a_0 is double that of a cancer cell with radius $1.26a_0$. The diameter distribution of cancer cells, measured using a cell counter (Vi-CELL XR cell viability analyzer; Beckman Coulter, Brea, CA), showed that the average cell diameter was about 15 μm, with a standard deviation of ~4.3 μm. In general, the size distribution of cancer cells can be expressed by the Gaussian profile of the probability density function (PDF) as

$$\mathrm{PDF}(d) = \frac{1}{\sqrt{2\pi}\sigma} \exp\left(-\frac{(d-d_0)^2}{2\sigma^2}\right), \tag{2.4}$$

where d is the diameter, d_0 is the average diameter, and σ is the standard deviation. The cumulative distribution function (CDF) in this case is

$$\mathrm{CDF}(d) = \frac{1}{2}\left[1 + \mathrm{erf}\left(\frac{d-d_0}{\sqrt{2\sigma^2}}\right)\right] \tag{2.5}$$

When $d = d_0$, CDF = 0.5. Therefore, half of the cancer cells have a migration length L_m greater than that of the rigid spheres. By substituting $d_0 = 15$ μm and $\sigma = 4.3$ μm into (2.5), it can be shown that for 18% of the cancer cells, the migration length is more than double that of the rigid spheres.

2.7 Conclusion

In this chapter we introduce our recent study of inertial migration of cancer cells in a microchannel [22]. The basic mechanism of inertial migration, fabrication of a PDMS microchannel, and the cancer cell preparation are all described. The inertial migration of both rigid spheres and cancer cells was convincingly observed in the microchannel. The migration of cancer cells in a dilute suspension was not as strong as that of rigid spheres, and the channel length required for cancer cell migration was roughly double that for the rigid spheres. The low efficiency of cell migration was attributable mainly to the size variation of the cancer cells. These results have important implications for the design of a microfluidic device for separating targeted cells from other cells.

Acknowledgments This study was supported by Grants-in-Aid for Scientific Research (S) from the Japan Society for the Promotion of Science. We also acknowledge support from the 2007 Global COE Program "Global Nano-Biomedical Engineering Education and Research Network Centre."

References

1. Bhagat AAS, Kuntaegowdanahalli SS, Papautsky I (2009) Inertial microfluidics for continuous particle filtration and extraction. Microfluid Nanofluid 7:217–226
2. Bhagat AAS, Bow H, Hou HW et al (2010) Microfluidics for cell separation. Med Biol Eng Comput 48:999–1014
3. Budd GT, Cristofanilli M, Ellis MJ et al (2006) Circulating tumor cells versus imaging-predicting overall survival in metastatic breast cancer. Clin Cancer Res 12:6403–6409
4. Carlo DD, Edd JF, Irimia D et al (2008) Equilibrium separation and filtration of particles using differential inertial focusing. Anal Chem 80:2204–2211
5. Carlo DD (2009) Inertial microfluidics. Lab Chip 9:3038–3046
6. Cristofanilli M, Budd GT, Ellis MJ et al (2004) Circulating tumor cells, disease progression, and survival in metastatic breast cancer. N Engl J Med 351:781–791
7. Cristofanilli M, Hayes DF, Budd GT et al (2005) Circulating tumor cells: a novel prognostic factor for newly diagnosed metastatic breast cancer. J Clin Oncol 23:1420–1430
8. Fujiwara H, Ishikawa T, Lima R et al (2009) Red blood cell motions in high-hematocrit blood flowing through a stenosed microchannel. J Biomech 42:838–843
9. Hur SC, Tse HTK, Carlo DD (2010) Sheathless inertial cell ordering for extreme throughput flow cytometry. Lab Chip 10:274–280

10. Ishikawa T, Fujiwara H, Matsuki N et al (2011) Asymmetry of blood flow and cancer cell adhesion in a microchannel with symmetric bifurcation and confluence. Biomed Microdevices 13:159–167
11. Jain A, Munn LL (2011) Biomimetic postcapillary expansions for enhancing rare blood cell separation on a microfluidic chip. Lab Chip 11:2941–2947
12. Kuntaegowadanahalli SS, Bhagat AAS, Kumar G et al (2009) Inertial microfluidics for continuous particle separation in spiral microchannels. Lab Chip 9:2973–2980
13. Lee GYH, Lim CT (2007) Biomechanics approaches to studying human disease. Trends Biotechnol 25:111–118
14. Matas JP, Morris JF, Guazzelli E (2004) Inertial migration of rigid spherical particles in Poiseuille flow. J Fluid Mech 515:171–195
15. Matas JP, Morris JF, Guazzelli E (2009) Lateral force on a rigid sphere in large-inertia laminar pipe flow. J Fluid Mech 621:59–67
16. Park JS, Song SH, Jung HI (2009) Continuous focusing of microparticles using inertial lift force and vorticity via multi-orifice microfluidic channels. Lab Chip 9:939–948
17. Segre G, Silberberg A (1962) Behavior of macroscopic rigid spheres in Poiseuille flow. Part 2. Experimental results and interpretation. J Fluid Mech 14:136–157
18. Sethu P, Sin A, Toner M (2006) Microfluidic diffusive filter for apheresis (leukopheresis). Lab Chip 6:83–89
19. Shevkoplyas SS, Yoshida T, Munn LL et al (2005) Biomimetic autoseparation of leukocytes from whole blood in a microfluidic device. Anal Chem 77:933–937
20. Suresh S (2007) Biomechanics and biophysics of cancer cells. Acta Mater 55:3989–4014
21. Tan SJ, Yobas L, Lee GYH et al (2009) Microdevice for the isolation and enumeration of cancer cells from blood. Biomed Microdevices 11:883–892
22. Tanaka T, Ishikawa T, Numayama-Tsuruta K et al (2011) Inertial migration of cancer cells in blood flow in microchannels. Biomed Microdevices. doi:10.1007/s10544-011-9582-y
23. Yamada M, Kano K, Tsuda Y et al (2007) Microfluidic devices for size-dependent separation of liver cells. Biomed Microdevices 9:637–645
24. Zheng S, Liu JQ, Tai YC (2008) Streamline-based microfluidic devices for erythrocytes and leukocytes separation. J Microelectromech Syst 17:1029–1038

Chapter 3
3D Multiscale Modelling of Angiogenesis and Vascular Tumour Growth

H. Perfahl, H.M. Byrne, T. Chen, V. Estrella, T. Alarcón, A. Lapin, R.A. Gatenby, R.J. Gillies, M.C. Lloyd, P.K. Maini, M. Reuss, and M.R. Owen

Abstract We present a three-dimensional, multiscale model of vascular tumour growth, which couples nutrient/growth factor transport, blood flow, angiogenesis, vascular remodelling, movement of and interactions between normal and tumour cells, and nutrient-dependent cell cycle dynamics within each cell. We present computational simulations which show how a vascular network may evolve and

---

The chapter is based on Perfahl et al., 2011, *Multiscale Modelling of Vascular Tumour Growth in 3D: The Roles of Domain Size and Boundary Conditions*. PLoS ONE 6(4): e14790. doi:10.1371/journal.pone.0014790

H. Perfahl (✉) • A. Lapin • M. Reuss
Center for Systems-Biology, University of Stuttgart, Stuttgart, Germany
e-mail: perfahl@ibvt.uni-stuttgart.de; lapin@ibvt.uni-stuttgart.de; reuss@ibvt.uni-stuttgart.de

H.M. Byrne
Oxford Centre for Collaborative Applied Mathematics, Department of Computer Science, University of Oxford, Oxford, UK
e-mail: helen.byrne@maths.ox.ac.uk

T. Chen • V. Estrella • R.A. Gatenby • R.J. Gillies • M.C. Lloyd
H. Lee Moffitt Cancer Center & Research Institute, Tampa FL 33612, USA
e-mail: tingan.chen@moffitt.org; veronica.estrella@moffitt.org; robert.gatenby@moffitt.org; robert.gillies@moffitt.org; mark.lloyd@moffitt.org

T. Alarcón
Centre de Recerca Matemàtica, Campus de Bellaterra, Barcelona, Spain
e-mail: talarcon@crm.cat

P.K. Maini
Centre for Mathematical Biology, Mathematical Institute and Oxford Centre for Integrative Systems Biology, Department of Biochemistry, University of Oxford, Oxford, UK
e-mail: maini@maths.ox.ac.uk

M.R. Owen
Centre for Mathematical Medicine and Biology, School of Mathematical Sciences, University of Nottingham, Nottingham, UK
e-mail: markus.owen@nottingham.ac.uk

M.W. Collins and C.S. König (eds.), *Micro and Nano Flow Systems for Bioanalysis*, Bioanalysis 2, DOI 10.1007/978-1-4614-4376-6_3,

interact with tumour and healthy cells. We also demonstrate how our model may be combined with experimental data, to predict the spatio-temporal evolution of a vascular tumour.

3.1 Introduction

Angiogenesis marks an important turning point in the growth of solid tumours. Avascular tumours rely on diffusive transport to supply them with the nutrients they need to grow, and, as a result, they typically grow to a maximal size of several millimetres in diameter. Growth stops when there is a balance between the rate at which nutrient-starved cells in the tumour centre die and the rate at which nutrient-rich cells on the tumour periphery proliferate. Under low oxygen, tumour cells secrete angiogenic growth factors that stimulate the surrounding vasculature to produce new capillary sprouts that migrate towards the tumour, forming new vessels that increase the supply of nutrients to the tissue and enable the tumour to continue growing and to invade adjacent healthy tissue. At a later stage, small clusters of tumour cells may enter the vasculature and be transported to remote locations in the body, where they may establish secondary tumours and metastases [12].

In more detail, the process of angiogenesis involves degradation of the extracellular matrix, endothelial cell migration and proliferation, capillary sprout anastomosis, vessel maturation and adaptation of the vascular network in response to blood flow [29]. Angiogenesis is initiated when hypoxic cells secrete tumour angiogenic factors (TAFs), such as vascular endothelial growth factor (VEGF) [27, 13]. The TAFs are transported through the tissue by diffusion and stimulate the existing vasculature to form new sprouts. The sprouts migrate through the tissue, responding to spatial gradients in the TAFs by chemotaxis. When sprouts connect to other sprouts or to the existing vascular network via anastomosis, new vessels are created. Angiogenesis persists until the tissue segment is adequately vascularised. The diameter of perfused vessels changes in response to a number of biomechanical stimuli such as wall shear stress (WSS) and signalling cues such as VEGF [31, 26]. For example, vessels which do not sustain sufficient blood flow will regress and be pruned from the network [10, 28].

Tumour growth and angiogenesis can be modelled using a variety of approaches (for reviews, see [18, 35]). Spatially averaged models can be formulated as systems of ordinary differential equations (ODEs) (see [8, 7]). Alternatively, a multiphase approach can be used to develop a spatially structured continuum model that describes interactions between tumour growth and angiogenesis and is formulated as a mixed system of partial differential equations (PDEs) [9]. Alternatively, a 2D stochastic model that tracks the movement of individual endothelial cells to regions of high VEGF concentration is introduced in [6]. Following [6], McDougall and co-workers [19] have developed a model for angiogenesis and vascular adaptation in which the tissue composition is static and

attention focusses on changes in the vasculature. This framework has been extended by Stéphanou et al. [33] to produce 3D simulations of angiogenesis and vascular adaptation. More recently, Macklin et al. [17] coupled a multiphase model to a discrete model of angiogenesis that accounts for blood flow, non-Newtonian effects and vascular remodelling. The models are coupled in two ways: via hydrostatic pressure which is generated by the growing tumour and acts on the vessels and via oxygen which is supplied by the vessels and stimulates growth. Lloyd et al. [16] have developed a model for neoplastic tissue growth which accounts for blood and oxygen transport and angiogenic sprouting. The strain (local deformation) in the tumour tissue is assumed to be an increasing function of the local oxygen concentration. In separate work, Owen et al. [20], building on the work of Alarcón and co-workers [1, 2, 3, 4], proposed a 2D multiscale model for vascular tumour growth which combines blood flow, angiogenesis, vascular remodelling and tissue scale dynamics of multiple cell populations as well as the subcellular dynamics (including the cell cycle) of individual cells. More recently, this framework was extended by Owen et al. [21] to analyse synergistic anti-tumour effects of combining a macrophage-based, hypoxia-targeted, gene therapy with chemotherapy.

While several two-dimensional models of angiogenesis consider tumour growth, few groups account for vascular tumour growth in three space-dimensions. In an extension to work by Zheng at al. [37], Frieboes et al. [14] couple a mixture model to a lattice-free continuous-discrete model of angiogenesis [24] to study vascular tumour growth. However, the effects of blood flow and vascular remodelling are neglected. Lee et al. [15] studied tumour growth and angiogenesis, restricting vessel sprouting to the tumour periphery and surrounding healthy tissue. They incorporated vessel dilation and collapse in the tumour centre and analysed the micro-vessel density within the tumour. Building on work by Schaller and Meyer-Hermann [30], Drasdo et al. [11] developed a lattice-free model for 3D tumour growth and angiogenesis that includes biomechanically induced contact inhibition and nutrient limitation. However, they do not consider an explicit cell cycle model, they neglect the effects of flow-induced vascular remodelling and they ignore interactions between normal and tumour cells. Similarly, Shirinifard et al. [32] present a 3D cellular Potts model of tumour growth and angiogenesis in which blood flow and vascular remodelling are neglected, as are the cell cycle and competition between normal and tumour cells.

In this chapter, we present a 3D multiscale model of angiogenesis and vascular tumour growth, based on Owen et al. [20]. In Sect. 3.2, the mathematical model and the associated computational algorithm are introduced. Computational simulations are presented in Sect. 3.3. There we start by illustrating the growth of a tumour, nested in healthy tissue with two straight initial vessels. We also show how vascular networks derived from experimental data can be integrated in our model.

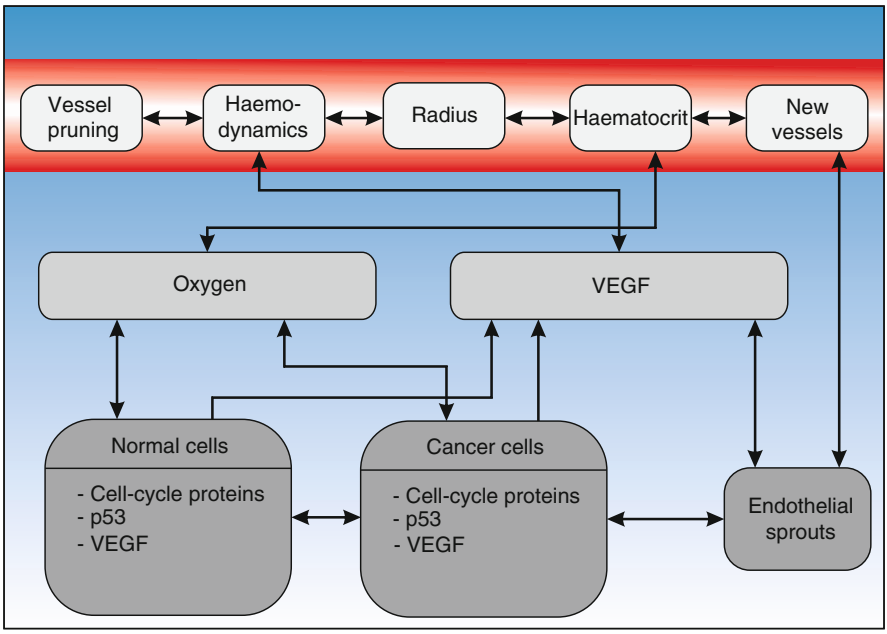

Fig. 3.1 Multiscale model overview (interaction diagram). This figure shows the connections between the different modelling layers. In the subcellular layer, the cell cycle protein concentrations and the p53 and VEGF concentrations are modelled via systems of coupled ordinary differential equations. The local external oxygen concentration influences the duration of the cell cycles. Cells consume oxygen, and produce VEGF in the case of hypoxia. Extracellular VEGF also influences the emergence of endothelial sprouts and their biased random walk towards hypoxic regions. If endothelial sprouts connect to other sprouts or the existing vascular network, new vessels form. Vessel diameter is influenced by the local oxygen concentration and flow-related parameters, such as pressure and wall shear stress. The vascular network delivers oxygen throughout the tissue

3.2 Multiscale Model

The computational model that we use describes the spatio-temporal dynamics of a tumour located in a vascular host tissue. Cells are represented as individual entities (agent-based approach), each with their own cell cycle and subcellular-signalling machinery. Nutrients are supplied by a dynamic vascular network, which is subject to remodelling and angiogenesis. Interactions between the different layers are depicted in Fig. 3.1.

Our model is formulated on a regular grid that subdivides the simulation domain into lattice sites. Each lattice site can be occupied by several biological cells whose movement on the lattice is governed by reinforced random walks, and whose proliferation is controlled by a subcellular cell cycle model. The vascular network consists of vessel segments connecting adjacent nodes on the lattice, with defined

inflow and outflow nodes with prescribed pressures. We also specify the amount of haematocrit entering the system through the inlets. The vessel network evolves via (1) sprouting of tip cells with a probability that increases with the local VEGF concentration, (2) tip cell movement described by a reinforced random walk, and (3) new connections formed via anastomosis. In addition, vessel segments with low WSS for a certain time are pruned away. Elliptic reaction-diffusion equations for the distributions of oxygen and VEGF are implemented on the same spatial lattice using finite difference approximations, and include source and sink terms based on the location of vessels (which act as sources of oxygen and sinks of VEGF) and the different cell types (e.g. cells act as sinks for oxygen and hypoxic cells as sources of VEGF).

In summary, after initialising the system, the diffusible fields, cellular and subcellular states are updated (including cell division and movement), before the vessel network is updated; this process is then repeated until the simulation ends.

A more detailed description of the mathematical model is presented in the following subsections. We start at the smallest spatial scale, namely, the subcellular layer. Then the cellular and diffusible layers are introduced, before the vascular layer. Interactions between these layers are highlighted in the final part of this section where the computational algorithm is presented. The parameter values can be found in Perfahl et al. [22].

3.2.1 Subcellular Layer

Coupled systems of non-linear ODEs are used to model progress through the cell cycle, and changes in expression levels of p53 and VEGF [3]. In practice, the cell cycle can be divided into four phases: during G_1, the cell is not committed to replication, but if conditions are favourable, it may enter the S (synthesis) phase, in which DNA replication takes place. During the G_2 phase, further growth, and DNA and chromatid alignment occur, before the cell divides during M (mitosis) phase. For the cell cycle, we consider the cell mass M and the proteins cycCDK (cyclin-CDK complex), Cdh1 (Cdh1-APC complex), p27 and npRB (non-phoshorylated retinoblastoma protein). The cell cycle model that we use focuses on the G_1-S transition. It extends an earlier model due to Tyson and Novak [36] by accounting for the p27-mediated effect that hypoxia has on the cell cycle [2]. Using square brackets to represent intracellular protein concentrations, we have

$$\frac{\mathrm{d}[\mathrm{Cdh1}]}{\mathrm{d}t} = \frac{(1 + b_3[\mathrm{npRB}])(1 - [\mathrm{Cdh1}])}{J_3 + 1 - [\mathrm{Cdh1}]} - \frac{b_4 M[\mathrm{cycCDK}][\mathrm{Cdh1}]}{J_4 + [\mathrm{Cdh1}]}, \tag{3.1}$$

$$\frac{\mathrm{d}[\mathrm{cycCDK}]}{\mathrm{d}t} = a_4 - (a_1 + a_2[\mathrm{Cdh1}] + a_3[\mathrm{p27}])[\mathrm{cycCDK}], \tag{3.2}$$

$$\frac{\mathrm{d}M}{\mathrm{d}t} = \eta M\left(1 - \frac{M}{M^*}\right), \tag{3.3}$$

$$\frac{\mathrm{d}[\mathrm{p27}]}{\mathrm{d}t} = c_1\left(1 - \chi\frac{M}{M^*}\right) - \frac{c_2 c_{02}}{B + c_{02}}[\mathrm{p27}], \tag{3.4}$$

$$\frac{\mathrm{d}[\mathrm{npRB}]}{\mathrm{d}t} = d_2 - (d_2 + d_1[\mathrm{cycCDK}])[\mathrm{npRB}]; \tag{3.5}$$

where b_3, J_3, b_4, J_4, a_1, a_2, a_3, a_4, η, M^*, c_1, c_2, B, χ, d_1 and d_2 are constants, specified in [22].

In (3.1)–(3.5), when M is small, the cell is maintained in a state corresponding to G_1 for which levels of Cdh1 are high and levels of cycCDK are low. Growth in the cell mass increases Cdh1 degradation and reduces p27 production, so that cycCDK increases. This leads to inhibition of npRB and Cdh1 and, hence, positive feedback on cycCDK. At a certain point, corresponding to the G_1-S transition, the state with high Cdh1 and low CDK is lost, and a state with low Cdh1 and high cycCDK is attained. Finally, when Cdh1 levels are sufficiently low and CDK levels sufficiently high, cell division occurs. The external O_2 concentration c_{02} couples the subcellular and diffusible scales by influencing progress through the cell cycle. Decreasing c_{02} reduces p27 degradation, and the resulting increase in levels of p27 counteracts the effect of the increasing mass on cycCDK. In particular, if c_{02} levels are sufficiently low, the G_1-S transition cannot occur. Further details about the model can be found in [2, 3].

The intracellular concentration of p53 regulates normal cell apoptosis, and that of VEGF controls VEGF release by normal cells. The dynamics of p53 and VEGF are coupled to one another and to the extracellular oxygen concentration, as described by the following differential equations:

$$\frac{\mathrm{d}[\mathrm{p53}]}{\mathrm{d}t} = k_7 - k'_7\frac{c_{02}}{K_{\mathrm{p53}} + c_{02}}[\mathrm{p53}], \tag{3.6}$$

$$\frac{\mathrm{d}[\mathrm{VEGF}]}{\mathrm{d}t} = k_8 + k''_8\frac{[\mathrm{p53}][\mathrm{VEGF}]}{J_5 + [\mathrm{VEGF}]} - k'_8\frac{c_{02}}{K_{\mathrm{VEGF}} + c_{02}}[\mathrm{VEGF}], \tag{3.7}$$

with the constants k_7, k'_7, K_{p53}, k_8, k'_8, k'_8, J_5 and K_{VEGF} (see [22]). The ODEs (3.1)–(3.7) are solved subject to the initial conditions specified in [22], using the open source CVODE library.[1]

[1] https://computation.llnl.gov/casc/sundials/main.html.

Cell death, quiescence and proliferation are determined by a cell's internal protein concentrations. We apply the following rules to identify the different cell states and show their application for a particular cell i (intracellular concentrations of the cell i are denoted by $[\cdot](i)$). In normal cells, cell death occurs if $[\mathrm{p53}](i) > \mathrm{p53}_{\mathrm{THR}}(i)$, where $\mathrm{p53}_{\mathrm{THR}}(i)$ is the maximal threshold they can sustain before undergoing apoptosis, and is given by

$$\mathrm{p53}_{\mathrm{THR}}(i) = \begin{cases} \mathrm{p53}_{\mathrm{THR}}^{\mathrm{high}} \text{ for } \rho_{\mathrm{normal}}(i) > \rho_{\mathrm{THR}} \\ \mathrm{p53}_{\mathrm{THR}}^{\mathrm{low}} \text{ for } \rho_{\mathrm{normal}}(i) \leq \rho_{\mathrm{THR}} \end{cases}. \tag{3.8}$$

We define the set of cells in the neighbourhood of cell i as Θ_i. The normal cell ratio in (3.8) is given by

$$\rho_{\mathrm{normal}}(i) = \frac{\sum_{k \in \Theta_i} \text{ normal cells at site } k}{\sum_{k \in \Theta_i} \text{ normal or cancer cells at site } k}. \tag{3.9}$$

Definition (3.9) accounts for the fact that healthy cells are more likely to die if they live in a tumour environment. This can be caused by the altered microenvironment in tumours. Tumour cells enter quiescence if $[\mathrm{p27}](i) > \mathrm{p27}_e$ or leave quiescence if $[\mathrm{p27}](i) < \mathrm{p27}_l$. If a cancer cell is in quiescence for too long ($> T_{\mathrm{death}}$), the cell dies. It should be noted that cancer cell death is not influenced by p53.

The condition to be satisfied for the proliferation of cells is

$$[\mathrm{Cdh1}](i) < \mathrm{Cdh1}_{\mathrm{THR}} \text{ and } [\mathrm{cycCDK}](i) > \mathrm{cycCDK}_{\mathrm{THR}}. \tag{3.10}$$

The daughter cell is placed in the current location if there is free space; otherwise, it is moved to an empty neighbour location with a high oxygen concentration. If there is no free space in the neighbour CA-cells, the parent cell dies and no daughter is produced.

3.2.2 Cellular Layer

The following section focuses on the creation and movement of new vessels. For a detailed description, see Owen et al. [20]. New sprouts form at site i (which must be a vessel site) with probability $\mathscr{P}_i^{\mathrm{sprout}}$ where

$$\mathscr{P}_i^{\mathrm{sprout}} = \frac{P_{\mathrm{max}}^{\mathrm{sprout}} c_{\mathrm{VEGF}}}{V_{\mathrm{sprout}} + c_{\mathrm{VEGF}}} \Delta t, \tag{3.11}$$

with the timestep size Δt. Since VEGF stimulates sprout formation, the probability of sprouting is assumed to increase with the VEGF concentration, c_{VEGF}. The maximum sprouting probability is $P_{\mathrm{max}}{}^{\mathrm{sprout}}$, and V_{sprout} is a constant. New sprouts

can only emerge if sufficient space is available. Around the base of each sprout, a radius of exclusion is defined, in which new sprouts cannot occur. For the vessel tip cells, we define $\mathscr{P}(i \to j)$ as the probability of moving from i to j, to be

$$\mathscr{P}(i \to j) = \frac{\Delta t D}{d_{ij}^2 \Delta x^2} \frac{(N_\mathrm{m} - N_j)\left(1 + \gamma \frac{c_{\mathrm{VEGF},j} - c_{\mathrm{VEGF},i}}{d_{ij}\Delta x}\right)}{\sum\limits_{k \in \Omega_i} (N_\mathrm{m} - N_k) + N_m - N_i + N_\mathrm{m} M_\mathrm{c}}, \tag{3.12}$$

for $i \neq j \in \Omega_i$. Herein, D represents the cell motility; Δx the CA-lattice size; N_m is the maximal carrying capacity of the cell type attempting to move; N_i is the number of cells; M_c is a constant and $c_{\mathrm{VEGF},\,i}$ the VEGF level at site i γ is the chemotactic sensitivity and Ω_i is the set of sites in the neighbourhood of i, not including i itself. The probabilities are weighted with the distance between lattice site i and j, written as d_{ij}. In the three-dimensional case, Ω_i has at most 26 neighbour elements for each lattice point i. We set the probability to zero if an endothelial cell crosses a vessel. The probability of not moving is

$$\mathscr{P}(i \to i) = 1 - \sum_{\substack{j,k \in \Omega_i \\ j \neq k}} \mathscr{P}(j \to k). \tag{3.13}$$

Whenever a tip cell moves to another location, an endothelial cell remains at the former lattice site. This is equivalent to the snail-trail concept also applied in [5, 34, 23]. A sprout dies if it does not connect to another sprout or the existing vasculature within a certain time period.

3.2.3 Diffusible Layer

The diffusible layer facilitates the coupling between the vascular and subcellular layers. We consider two diffusible components in our model, namely, oxygen and VEGF, and denote their concentrations by c_{VEGF} and c_{02}, respectively. The vascular system acts as an oxygen source, while the normal and tumour cells act as sinks. This behaviour is described by the following, quasi-stationary, reaction-diffusion equation:

$$D_{02}\nabla^2 c_{02} + 2\pi\tilde{R}(t,\mathbf{x})P_{02}(c_{02}^{\mathrm{blood}} - c_{02}) - k_{02}(t,\mathbf{x})c_{02} = 0, \tag{3.14}$$

with the diffusion coefficient of oxygen, D_{02}. In (3.14), the vessel radius indicator function $\tilde{R}$ returns the vessel radius if a vessel is present at position $\mathbf{x}$ and zero otherwise. Equation (3.14) also accounts for the vessel permeability to oxygen (P_{02}), the blood oxygen concentration ${c_{02}}^{\mathrm{blood}}$ and the cell-type-dependent oxygen consumption rate k_{02}. If cells become hypoxic or quiescent, they start to secrete

VEGF, which then can be removed by the vasculature. The concentration of VEGF is determined by

$$D_{\mathrm{VEGF}}\nabla^2 c_{\mathrm{VEGF}} - 2\pi\tilde{R}(t,\mathbf{x})P_{\mathrm{VEGF}}c_{\mathrm{VEGF}} + k_{\mathrm{VEGF}}(t,\mathbf{x}) - \delta_{\mathrm{VEGF}}c_{\mathrm{VEGF}} = 0, \quad (3.15)$$

wherein D_{VEGF} is the diffusion coefficient of VEGF, P_{VEGF} the permeability of the vessels to VEGF, k_{VEGF} the cell-type-dependent VEGF production rate and the decay rate δ_{VEGF}. In our numerical algorithm, (3.14) and (3.15) are discretised with a finite difference scheme, and the resulting sparse linear system of equations is solved with a GMRES-solver.

In case of a non-periodic simulation domain, it is assumed that there is no flux of diffusible substances over the boundary, and thus, homogeneous Neumann boundary conditions are imposed. For simulations in a periodic domain, we apply periodic boundary conditions for the calculation of diffusible substance concentrations.

3.2.4 Vascular Layer

We follow very closely the work of Secomb et al. and refer the reader to [26] for full details. We assume a laminar Poiseuille flow in each vessel. The flux $\dot{Q}_i$ through vessel i is given by

$$\dot{Q}_i = \frac{\pi R_i^4}{8\mu(R_i,H_i)L_i}\Delta P_i, \quad (3.16)$$

where ΔP_i is the pressure difference at the vessel segment i, L_i the vessel length, $\mu(R_i, H_i)$ is the radius R_i and haematocrit H_i dependent blood viscosity [26]. In (3.16), we can identify the resistance of vessel i by $\mathrm{Res}_i = 8\mu(R_i,H_i)L_i/(\pi R_i^4)$. In (3.16), the blood viscosity is defined by

$$\mu(R,H) = \mu_0\mu_{\mathrm{rel}}(R,H), \quad (3.17)$$

where μ_0 is a positive constant,

$$\mu_{\mathrm{rel}}(R,H) = \left[1 + (\mu_{0.45}(R) - 1)\frac{(1-H)^C - 1}{(1-0.45)^C - 1}\left(\frac{2R}{2R-1.1}\right)^2\right]\left(\frac{2R}{2R-1.1}\right)^2, \quad (3.18)$$

$$\mu_{0.45}(R) = 6\mathrm{e}^{-0.17R} + 3.2 - 2.44\mathrm{e}^{-0.06(2R)^{0.645}} \quad (3.19)$$

and

$$C = C(R) = \left(0.8 + \mathrm{e}^{-0.15R}\right)\left(-1 + \frac{1}{1 + 10^{-11}(2R)^{12}}\right) + \frac{1}{1 + 10^{-11}(2R)^{12}}. \tag{3.20}$$

Using (3.16)–(3.20), we can calculate the flux through each vessel segment in terms of the pressure at each junction of the vascular tree. At any node of the vascular network, the total flow into that node must balance the total flow out of that node. With the pressures at each inlet and outlet (P_{in} and P_{out}, respectively) prescribed, we obtain a linear system of equations for the pressures at each vessel node. This system is solved with the direct SuperLU solver.[2]

When updating the vascular network, there are two different timescales of interest, the timescale for flow and the timescale for vascular adaptation. While changes in flow may be rapid, we assume that vascular adaptation occurs on the same timescale as endothelial cell movement and cell division. Consequently, we model the temporal evolution of a vessel segment's radius by applying the following discretised ODEs

$$R(t + \Delta t) = R(t) + \alpha_R \Delta t R(t)(S_{\mathrm{h}} + S_{\mathrm{m}} - k_{\mathrm{s}}), \tag{3.21}$$

where Δt is the timestep size and the updated radius must satisfy the constraint $R_{\min} \leq R\,(t + \Delta t\,) \leq R_{\max}$. The factor α_R that appears in (3.21) relates the stimuli to our timestep size Δt. In the absence of any details on the rate of vascular adaptation (since all previous studies of which we are aware consider quasi-steady state vessel radii), we set $\alpha_R = 3.3 \times 10^{-6}\, min^{-1}$ so that the rate of change of the vessel radius is typically less than 10 % per hour. k_{s} is the shrinking tendency of a vessel which takes into account that vessels tend to regress in the absence of stimuli. S_{h} and S_{m} are haemodynamic and metabolic stimuli for vascular adaptation:

- **Haemodynamic stimulus:**

$$S_{\mathrm{h}} = \log(\tau_{\mathrm{w}} + \tau_{\mathrm{ref}}) - k_p \log((\tau(P)), \tag{3.22}$$

with the WSS

$$\tau_{\mathrm{w}} = \frac{R\Delta P}{L}, \tag{3.23}$$

the constant reference WSS τ_{ref} and the corresponding set point pressure of the WSS $\tau(P\,)$, described by the empirical function

$$\tau(P) = 100 - 86 \exp\left(-5000[\log(\log P)]^{5.4}\right). \tag{3.24}$$

[2] http://crd.lbl.gov/~xiaoye/SuperLU/.

- **Metabolic stimulus:**

$$S_{\mathrm{m}} = k_m(c_{\mathrm{VEGF}}) \log\left(\frac{\dot{Q}_{\mathrm{ref}}}{\dot{Q}H + a\dot{Q}_{\mathrm{ref}}} + 1\right), \tag{3.25}$$

with

$$k_m(c_{\mathrm{VEGF}}) = k_m^0\left(1 + k_m^{\mathrm{VEGF}} \frac{c_{\mathrm{VEGF}}}{V_0 + c_{\mathrm{VEGF}}}\right), \tag{3.26}$$

where $\dot{Q}_{\mathrm{ref}}$, a, ${k_m}^0$, ${k_m}^{\mathrm{VEGF}}$ and V_0 are parameters. $\dot{Q}_{\mathrm{ref}}$ is a reference flow, and the term $a\dot{Q}_{\mathrm{ref}}$ (where a is a small parameter) in the denominator of (3.25) is introduced to avoid extreme vessel dilation in poorly perfused vessels (and hence, S_{m} differs slightly from the original model [20, 25]).

In addition to being created, new vessels can also be removed by pruning. If a vessel is exposed to a WSS that is below a threshold (${\tau_{\mathrm{w}}}^{\mathrm{crit}}$) for a certain time ($T_{\mathrm{prune}}$), we remove that vessel from the system. In general, the vascular adaptation algorithm includes the following steps. First, the vessel radii evolve according to (3.21). Then we calculate the flows in the network. In contrast to the previous model [20], the evolution of the radius is considered separately and is not iterated until a steady state is reached.

3.2.5 Computational Algorithm

The basis of our model is a regular grid that subdivides the simulation domain into cellular automaton lattice sites. Each lattice site can be occupied by several biological cells and vessels. Figure 3.1 shows the high degree of coupling between the different spatial scales. We enumerate the main steps below:

1. **Initialisation** *(vascular and cellular layers)* We specify an initial vascular network as a system of straight pipes with fixed inflow and outflow nodes and prescribed pressures. We also prescribe the amount of haematocrit that enters through each inlet, and the initial location of the different cell types in the cellular automaton domain.
2. **Update cells, oxygen and VEGF** *(diffusible, cellular and subcellular layers)*
   - **Calculation of oxygen concentration** *(diffusible layer)* The reaction-diffusion equation (3.14) is used to calculate the quasi-stationary oxygen concentration $c_{02}(t, \mathbf{x})$ in the simulation domain. Oxygen consumption by normal and cancer cells is included in (3.14) via sink terms, assuming first-order kinetics. On the other hand, perfused blood vessels deliver oxygen to the tissue and thus account for oxygen sources.

- **Calculation of cell cycle, p53 and VEGF ODEs** *(subcellular layer)* The subcellular layer is coupled to its local environment via the oxygen concentration. Oxygen drives the cell cycle of individual cells, whose current state is described by the time-dependent concentrations of the proteins Cdh1, cycCDK, p27, npRB and the cell mass M. Internal p53 and VEGF concentrations are also considered. All subcellular variables are modelled by the coupled systems of non-linear ODEs (3.1)–(3.7).
- **Check for cell division** *(cellular layer)* Cells divide if their Cdh1 and cycCDK concentrations are under, respectively, over a predefined threshold [see (3.10)].
- **Cell movement** *(cellular layer)* Vascular tip cells perform a biased random walk through the tissue. The probability of moving in a certain direction is influenced by the local VEGF gradient and cell densities [see (3.12)]. The motility of normal and cancer cells is also included via (3.12).
- **Calculation of VEGF concentration** *(diffusible layer)* Quiescent tumour cells and hypoxic normal cells produce VEGF, and so contribute to the source term in the reaction-diffusion equation (3.15) for the VEGF concentration $c_{\mathrm{VEGF}}(t, \mathbf{x})$. VEGF is removed by the vascular system.
- **Check for cell quiescence** *(cellular layer)* Tumour cells enter or leave a quiescent state depending on the internal cell p27 concentration, which is described in (3.4). Oxygen is the external factor that influences the level of p27.
- **Check for cell death** *(cellular layer)* Normal cells die if their subcellular p53 concentration exceeds a threshold value. If a normal cell is surrounded by a high number of tumour cells, then its p53 threshold for cell death is reduced [see (3.8)]. This models the degradation of a tumour's environment by tumour cells. Tumour cells die if they are quiescent for a certain period of time; unlike normal cells, their death is not influenced by p53.

3. **Update vasculature** *(cellular and vascular layer)* The vascular system continually remodels and evolves in response to external and internal stimuli:

   - **Check for new tip cells** *(cellular layer)* A raised VEGF concentration in the tissue stimulates the vasculature to form new sprouts. The probability that new sprouts emerge is specified by (3.11) and is an increasing function of the local extracellular VEGF concentration.
   - **Check for anastomosis** *(cellular layer)* New vessels are formed if sprouts connect to other sprouts or to the pre-existing vascular network.
   - **Vessel pruning** *(vascular layer)* Vessels that are underperfused ($\tau_{\mathrm{w}} < \tau_{\mathrm{w}}^{\mathrm{crit}}$) for a certain period of time (T_{prune}) are removed from the vascular network.
   - **Calculation of radius adaptation** *(vascular layer)* The vessel radii are updated at each timestep according to (3.21). The change in vessel radii is influenced by haemodynamic and metabolic stimuli as well as the general tendency of vessels to shrink [see (3.22)–(3.25)].

- **Calculation of pressures and flows within vasculature** *(vascular layer)* Poiseuille's flow (3.16) is considered in each branch of the vascular network, and the pressure at each node is calculated by applying conservation of mass. The haematocrit is assumed to split symmetrically at bifurcations.

In 1, the successive cellular automaton model is initialized. Then 2 and 3 are carried out on each time interval Δt until the final simulation time is reached.

3.3 Simulations

The results from a typical simulation, showing the development of a tumour and its associated network of blood vessels, are depicted in Fig. 3.2. Simulations were performed on a 50 $\times$50 $\times$50 lattice with spacing 40 μm, which corresponds to a 2 mm $\times$2 mm $\times$2 mm cube of tissue. For the following simulations, each lattice site can be occupied by at most one cell (either normal or cancerous), which implies that, for the grid size used (40 μm), the tissue is not densely packed. A small tumour was implanted at $t = 0$ h in a population of normal cells perfused by two parallel parent vessels with countercurrent flow (i.e. the pressure drops and hence flows are in opposite directions). Initially, insufficient nutrient supply in regions at distance from the vessels causes widespread death of the normal cells. The surviving tumour cells reduce the p53 threshold for death of normal cells, which further increases the death rate of the normal cells and enables the tumour to spread. Initially, due to inadequate vascularisation, most of the tumour cells are quiescent and secrete VEGF which stimulates an angiogenic response. After a certain period of time, the quiescent cells die and only a small vascularised tumour remains, encircling the upper vessel. The tumour expands preferentially along this vessel, in the direction of highest nutrient supply. Diffusion of VEGF throughout the domain stimulates the formation of new capillary sprouts from the lower parent vessel. When the sprouts anastomose with other sprouts or existing vessels, the oxygen supply increases, enabling the normal cell population to recover. Because the tumour cells consume more oxygen than normal cells and they more readily secrete VEGF under hypoxia, VEGF levels are higher inside the tumour, and the vascular density there is much higher than in the healthy tissue. The tumour remains localised around the upper vessel until new vessels connect the upper and lower vascular networks. Thereafter, the tumour cells can spread to the lower region of the domain until eventually the domain is wholly occupied by cancer cells and their associated vasculature.

As a further step, we document preliminary results of a vascular tumour growth simulation for which the initial vascular geometry was taken from multiphoton fluorescence microscopy (a detailed description of the experimental setting can be found in [22]). The aim here is to integrate the mathematical model with in vivo

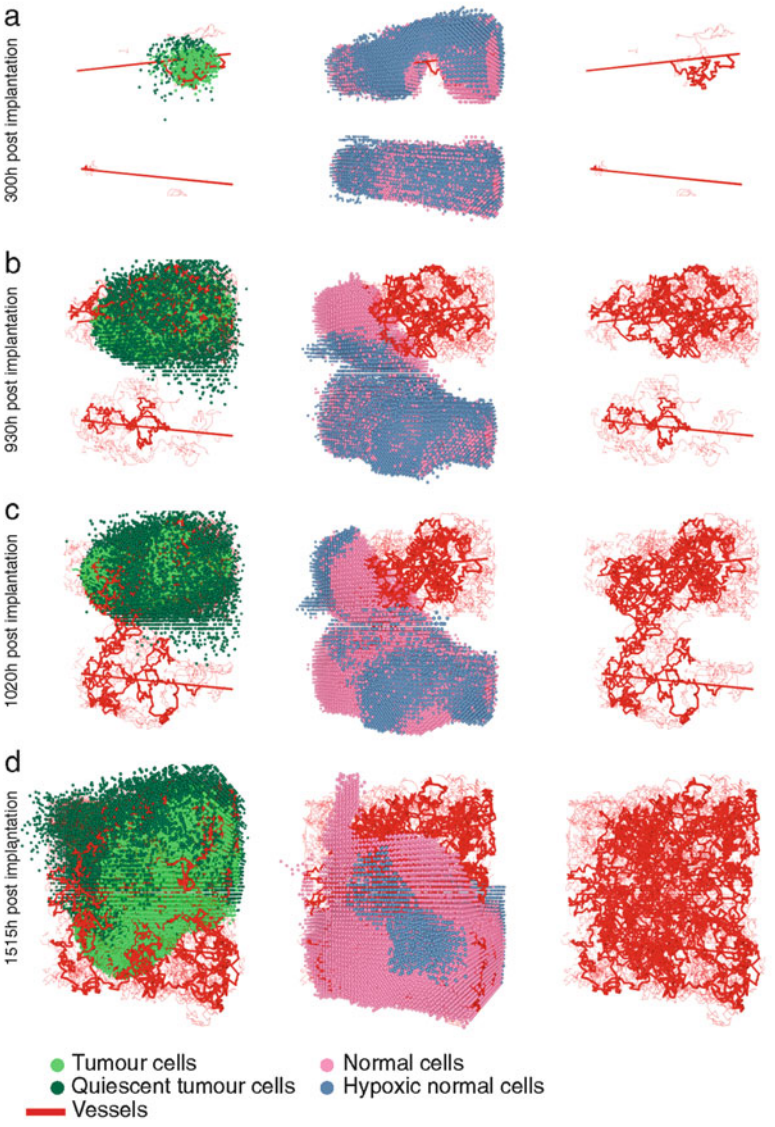

Fig. 3.2 Tumour growth in healthy tissue. The tumour cells and vasculature are depicted in the *left column*, the vasculature and normal cells in the *middle column* and the vessel network in the *right column*. The figure shows a realisation of a $50 \times 50 \times 50$ domain with a cube of tumour cells implanted in healthy tissue initially with two straight vessels

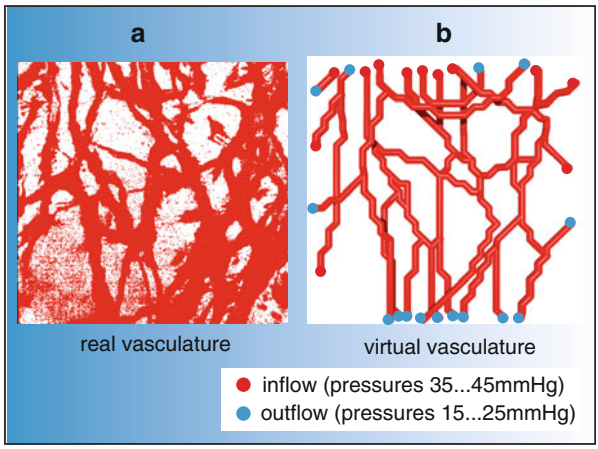

Fig. 3.3 Image reconstruction. We reconstructed the vascular network by applying the following strategy. 3D multiphoton fluorescence microscopy images (**a**) taken from mouse models in vivo formed the basis of our geometrical reconstruction. Based on the data, we reconstructed the vascular graph model that describes the connectivity of the vascular network. (**b**) We assigned inflow (*red points*) and outflow (*blue points*) nodes at various pressures in order to obtain a persistent and stable network. The vascular graph is characterised by the spatial coordinates of the nodes and the connections between them

experimental data. Experimental data defining a vascular network associated with a tumour were obtained by implanting a tumour construct comprising a central core of human breast cancer cells surrounded by rat microvessel fragments, embedded in a collagen matrix into a mouse dorsal window chamber. The cancer cells and rat microvascular cells express different fluorescent proteins so that, following implantation, the tumour and its vascular network can be visualised.

We used experimental data to reconstruct the vascular graph model, locating nodes in the vessel centres and connecting them by edges. We embed the vascular system into healthy tissue and then simulate vessel adaptation until a steady state is reached. This example provides proof of concept.

Currently in the computational models, the vasculature is embedded in a healthy tissue into which a small tumour is implanted and its evolution is studied. A projection of a 3D image set of the tissue is presented on the left-hand side of Fig. 3.3, while the virtual reconstruction is shown on the right-hand side. In Fig. 3.4, we observe that the tumour expands radially into the surrounding healthy tissue which it degrades by decreasing the p53 death threshold for normal cells. Normal cells in the lower left and right corners of the simulation domain (first column) are exposed to low oxygen (hypoxia), and hence produce VEGF which induces an angiogenic response in our model. While the new vessel in the lower left corner is persistent and increases in radius, the vessel in the lower right corner is pruned back. In this case, pruning occurs because the new blood vessel connects vessels from the initial network that have similar pressures. In general, the normal cells are adequately nourished by oxygen as only a few hypoxic cells can be

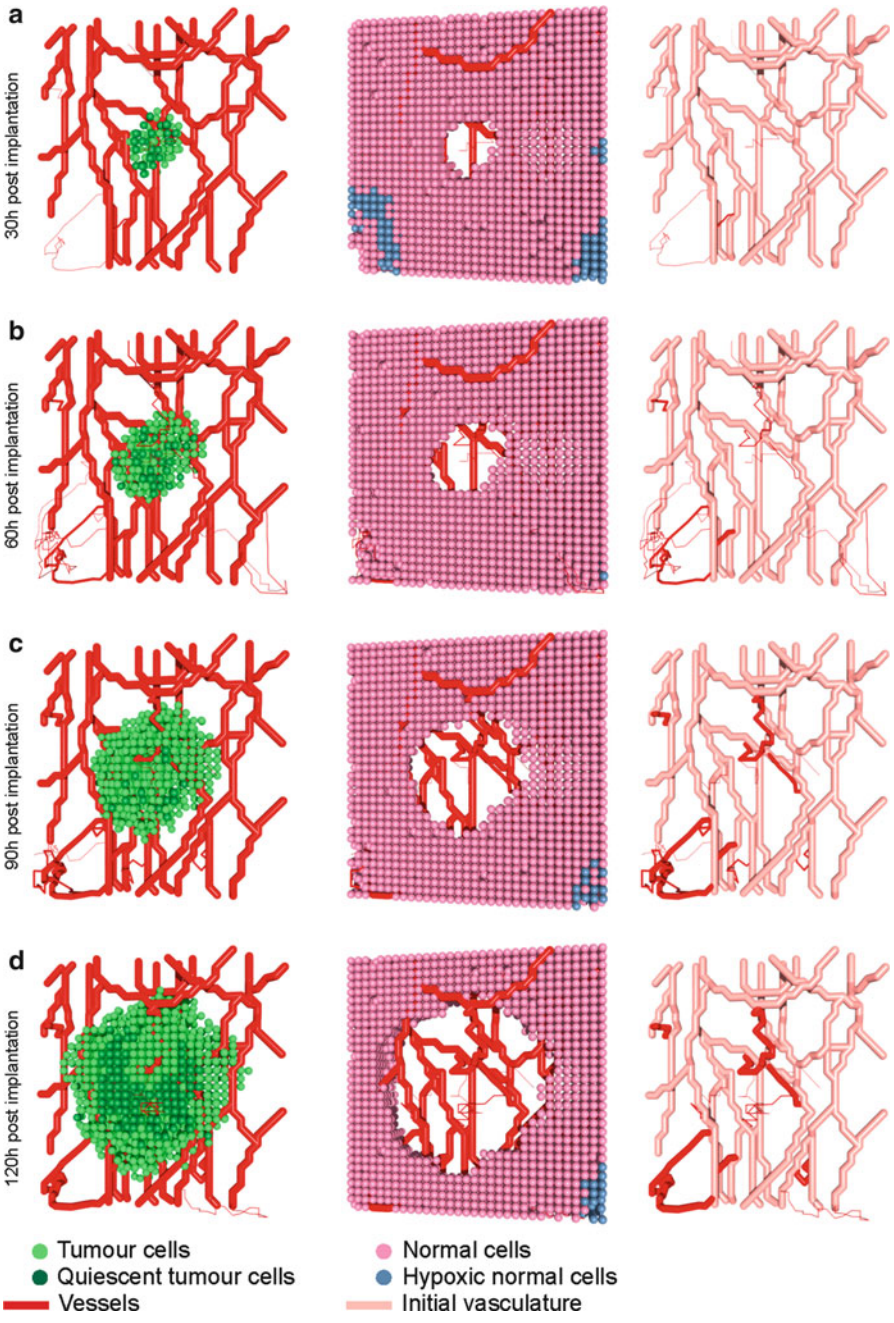

Fig. 3.4 Proof of concept: tumour growth in an experimentally derived vascular network. (**a –d**) show the computed temporal evolution of a tumour in a real vascular network embedded in normal tissue. As initial condition, we have taken a vascular network from multiphoton fluorescence

observed in simulations with normal cells only. In contrast, we find a high percentage of quiescent cancer cells in all states of tumour growth, leading to further angiogenesis in our simulations (see Fig. 3.4). The dark red vessels in row 3 indicate new vessels that develop after tumour implantation. In conclusion, our model with the chosen parameter values predicts an increase in the vascular density following tumour implantation.

3.4 Conclusions

In this chapter we have presented a multiscale model of vascular tumour growth and angiogenesis. After the introduction, the mathematical model was presented in Sect. 3.2 where we gave a detailed description of the mathematical models on the different length scales. Finally, we introduced the computational algorithm that we use to simulate the model. In the third section, simulation results were shown. We started by considering the growth of a tumour nested in healthy tissue initially perfused by two straight and parallel vessels and then studied the evolution of cells and the vascular system. As proof of concept, we then used an experimentally derived vessel network to initialise a simulation of tumour growth and angiogenesis. To the best of our knowledge, this is the first time this has been done—Secomb, Pries and co-workers (e.g. [31, 26]) have used such networks to study structural adaptation alone. Our work paves the way for further research which will be more closely linked with experimental data. In particular, it would be of great interest to compare our model simulations with experimental data from two or more time points. The first time point defining the initial conditions for the simulations and data from later time points used to test the model's predictive power or to estimate parameter values. We would not expect to obtain a detailed match at later time points, since we simulate a stochastic system, but we would expect agreement between experimental and simulated values for certain characteristics, such as vessel volume fractions and the distributions of vessel radii and segment lengths.

One problem is the large number of parameters contained in multiscale models such as ours. This makes it nontrivial to parametrise them. One strategy would be to start by parametrising small and well-defined submodels independently of each other. In this way, it should then be possible to determine whether coupling the submodels together gives physiologically realistic results or if additional effects have to be incorporated. Another important issue is determining the influence that each system parameter has on the simulation results. This could be established by performing a comprehensive parameter sensitivity analysis. Such knowledge would

Fig. 3.4 (continued) microscopy and embedded it in a $32 \times 32 \times 6$ cellular automaton domain. In the *first column*, the tumour expands radially, and degrades the healthy tissue (*second column*). The predicted adaptations of the vascular system are shown in the *third column* where the experimentally derived network is shown in *light red*, while the new vessels are coloured in *red*

enable us to identify those biophysical mechanisms that dominate the system dynamics and to use this information to derive simpler models which exhibit the same behaviour. Unfortunately, simulations are very time-consuming—the simulation shown in Fig. 3.2 takes several days on a desktop computer, and then several realisations of the Monte Carlo simulation have to be carried out for a statistical analysis. Therefore, future optimisations and the parallelisation of the computer programme are essential. One also has to investigate to which extent the models are overdetermined, meaning that changes in different parameters lead to the same pattern in the simulations.

Beside these limitations, multiscale models build promising frameworks for future developments. They enable us to investigate how processes operating on different space and time scales interact and to study the effect that such interactions have on the overall system dynamics. They also enable researchers in different areas to link and couple their models. To simplify this model exchange, model interfaces have to be defined and standardised. Equally, multiscale models can be used to develop and parametrise simpler continuum models that can be solved more efficiently. Most current multiscale models generate qualitatively accurate and meaningful results, and, therefore, they can be applied to identify sensitive mechanisms that then stimulate biological experiments.

Acknowledgements HMB, MRO and HP acknowledge financial support by the Marie Curie Network MMBNOTT (Project No. MEST-CT-2005-020723). RAG and PKM acknowledge partial support from NIH/NCI grant U54CA143970. HP, AL and MR thank the BMBF—Funding Initiative FORSYS Partner: "Predictive Cancer Therapy". In vivo window chamber work was funded in part by Moffitt Cancer Center PS-OC NIH/NCI U54CA143970. This publication was based on work supported in part by Award No. KUK-C1-1013-04, made by King Abdullah University of Science and Technology (KAUST).

References

1. Alarcón T, Byrne HM, Maini PK (2003) A cellular automaton model for tumour growth in an inhomogeneous environment. J Theor Biol 225:257–274
2. Alarcón T, Byrne HM, Maini PK (2004) A mathematical model of the effects of hypoxia on the cell-cycle of normal and cancer cells. J Theor Biol 229(3):395–411
3. Alarcón T, Byrne HM, Maini PK (2005) A multiple scale model for tumor growth. Multiscale Model Sim 3:440–475
4. Alarcón T, Owen MR, Byrne HM, Maini PK (2006) Multiscale modelling of tumour growth and therapy: The influence of vessel normalisation on chemotherapy. Comput Math Method M7(2-3):85–119
5. Anderson ARA (2005) A hybrid mathematical model of solid tumour invasion: The importance of cell adhesion. Math Med Biol 22:163–186
6. Anderson ARA, Chaplain MAJ (1998) Continuous and discrete mathematical models of tumor-induced angiogenesis. Bull Math Biol 60(5):857–899
7. Arakelyan L, Vainstein V, Agur Z (2002) A computer algorithm describing the process of vessel formation and maturation, and its use for predicting the effects of anti-angiogenic and anti-maturation therapy on vascular tumor growth. Angiogenesis 5(3):203–14

8. Arakelyan L, Merbl Y, Agur Z (2005) Vessel maturation effects on tumour growth: validation of a computer model in implanted human ovarian carcinoma spheroids. Eur J Cancer 41 (1):159–167
9. Breward CJW, Byrne HM, Lewis CE (2003) A multiphase model describing vascular tumour growth. Bull Math Biol 65:609–640
10. Clark ER (1918) Studies on the growth of blood-vessels in the tail of the frog larva - by observation and experiment on the living animal. Am J Anat 23(1):37–88
11. Drasdo D, Jagiella N, Ramis-Conde I, Vignon-Clementel I, Weens W (2010) Modeling steps from a benign tumor to an invasive cancer: Examples of intrinsically multi-scale problems. In: Chauviere A, Preziosi L, Verdier C (eds) Cell mechanics: From single scale-based models to multiscale modeling. Chapman & Hall/CRC, pp 379–417
12. Folkman J (1971) Tumour angiogenesis – therapeutic implications. New Engl J Med 285:1182–1186
13. Folkman J, Klagsburn M (1987) Angiogenic factors. Science 235:442–447
14. Frieboes HB, Lowengrub JS, Wise S, Zheng X, Macklin P, Bearer E, Cristini V (2007) Computer simulation of glioma growth and morphology. Neuroimage 37(S1):59–70
15. Lee DS, Rieger H, Bartha K (2006) Flow correlated percolation during vascular remodeling in growing tumors. Phys Rev Lett 96(5):058,104–4
16. Lloyd BA, Szczerba D, Rudin M, Székely G (2008) A computational framework for modelling solid tumour growth. Phil Trans R Soc A 366:3301–3318
17. Macklin P, McDougall S, Anderson AR, Chaplain MAJ, Cristini V, Lowengrub J (2009) Multiscale modelling and nonlinear simulation of vascular tumour growth. J Math Biol 58:765–798
18. Mantzaris N, Webb SD, Othmer HG (2004) Mathematical modelling of tumour angiogenesis: A review. J Math Biol 49:111–187
19. McDougall SR, Anderson ARA, Chaplain MAJ (2006) Mathematical modelling of dynamic adaptive tumour-induced angiogenesis: Clinical implications and therapeutic targeting strategies. J Theor Biol 241(3):564–89
20. Owen MR, Alarcón T, Maini PK, Byrne HM (2009) Angiogenesis and vascular remodelling in normal and cancerous tissues. J Math Biol 58:689–721
21. Owen M, Stamper I, Muthana M, Richardson G, Dobson J, Lewis C, Byrne H (2011) Mathematical modeling predicts synergistic antitumor effects of combining a macrophage-based, hypoxia-targeted gene therapy with chemotherapy. Cancer Res 71(8):2826
22. Perfahl H, Byrne H, Chen T, Estrella V, Alarcón T, Lapin A, Gatenby R, Gillies R, Lloyd M, Maini P, et al (2011) Multiscale modelling of vascular tumour growth in 3d: The roles of domain size and boundary conditions. PloS one 6(4):e14,790. doi:10.1371/journal.pone.0014790
23. Plank MJ, Sleeman BD (2003) A reinforced random walk model of tumour angiogenesis and anti-angiogenic strategies. Math Med Biol 20(2):135–181
24. Plank M, Sleeman B (2004) Lattice and non-lattice models of tumour angiogenesis. Bull Math Biol 66(6):1785–1819
25. Pries AR, Secomb TW, Gaehtgens P (1998) Structural adaptation and stability of microvascular networks: Theory and simulations. Am J Physiol 275(2 Pt 2):H349–H360
26. Pries A, Reglin B, Secomb T (2001) Structural adaptation of microvascular networks: Functional roles of adaptive responses. Am J Physiol 281:H1015–H1025
27. Pugh C, Rattcliffe P (2003) Regulation of angiogenesis by hypoxia: Role of the hif system. Nature Med 9:677–684
28. Resnick N, Yahav H, Shay-Salit A, Shushy M, Schubert S, Zilberman L, Wofovitz E (2003) Fluid shear stress and the vascular endothelium: For better and for worse. Progr Biophys Mol Biol 81:177–199
29. Risau W (1997) Mechanisms of angiogenesis. Nature 386:871–875
30. Schaller G, Meyer-Hermann M (2005) Multicellular tumor spheroid in an off-lattice Voronoi-Delaunay cell model. Phys Rev E 71:1–16

31. Secomb TW, Hsu R, Beamer NB, Coull BM (2000) Theoretical simulation of oxygen transport to brain by networks of microvessels: Effects of oxygen supply and demand on tissue hypoxia. Microcirculation 7:237–247
32. Shirinifard A, Gens JS, Zaitlen BL, Poplawski NJ, Swat M (2009) 3D Multi-Cell simulation of tumor growth and angiogenesis. PLoS ONE 4(10):e7190. doi:10.1371/journal.pone.0007190
33. Stéphanou A, McDougall SR, Anderson ARA, Chaplain MAJ (2005) Mathematical modelling of flow in 2d and 3d vascular networks: Applications to anti-angiogenic and chemotherapeutic drug strategies. Math Comp Modelling 41(10):1137–1156
34. Stokes CL, Lauffenburger DA (1991) Analysis of the roles of microvessel endothelial cell random motility and chemotaxis in angiogenesis. J Theor Biol 152(3):377–403
35. Tracqui P (2009) Biophysical models of tumour growth. Rep Prog Phys 72(5):056,701
36. Tyson JJ, Novak B (2001) Regulation of the eukaryotic cell cycle: Molecular antagonism, hysteresis, and irreversible transitions. J Theor Biol 210:249–263
37. Zheng X, Wise SM, Cristini V (2005) Nonlinear simulation of tumor necrosis, neovascularization and tissue invasion via an adaptive finite-element/level set method. Bull Math Biol 67(2):211–259

Chapter 4
Microvascular Permeability and Tumor Metastasis

Bingmei M. Fu

Abstract Angiogenesis and microvascular hyperpermeability are two critical processes for tumor growth and metastasis. Although various anti-angiogenic therapies have been postulated to inhibit tumor growth and intravasation since the early 1970s, strategies targeting at microvascular hyperpermeability to prevent tumor cell adhesion and extravasation have not been well developed. The vascular endothelium forming the microvessel wall and the glycocalyx layer at its surface are the principal barriers to, and regulators of, the material exchange between circulating blood and body tissues. The cleft between adjacent endothelial cells (interendothelial cleft) is the principal pathway for water and solute transport through the microvessel wall in health. It is also suggested to be the pathway for high molecular weight plasma proteins, leukocytes, and tumor cells across microvessel walls in disease. Thus this review first introduces the mathematical models for transport of water and solutes through the interendothelial cleft. These models, combined with the experimental results from in vivo animal studies and electron microscopic observations, are used to evaluate the role of the endothelial surface glycocalyx, the junction strand geometry in the interendothelial cleft, and the surrounding extracellular matrix and tissue cells, as the determinants of microvascular transport. The second part of the review demonstrates how changes in microvascular permeability and blood flow affect tumor cell adhesion in in vivo and in vitro model systems. The role of integrin signaling during tumor cell adhesion is also discussed.

B.M. Fu (✉)
Department of Biomedical Engineering, The City College of the City University of New York, 160 Convent Avenue, New York, NY 10031, USA
e-mail: fu@ccny.cuny.edu

M.W. Collins and C.S. König (eds.), *Micro and Nano Flow Systems for Bioanalysis*, Bioanalysis 2, DOI 10.1007/978-1-4614-4376-6_4,

4.1 Introduction

The microvascular bed is the primary location where water and nutrients are exchanged between circulating blood and body tissues. The microvessel walls consist mainly of endothelial cells (Fig. 4.1a). Under normal conditions, the cleft between endothelial cells (interendothelial cleft) is widely believed to be the principal pathway for transport of water and hydrophilic solutes (such as glucose, amino acids, vitamins, and hormones) across the capillary wall [57]. Direct and

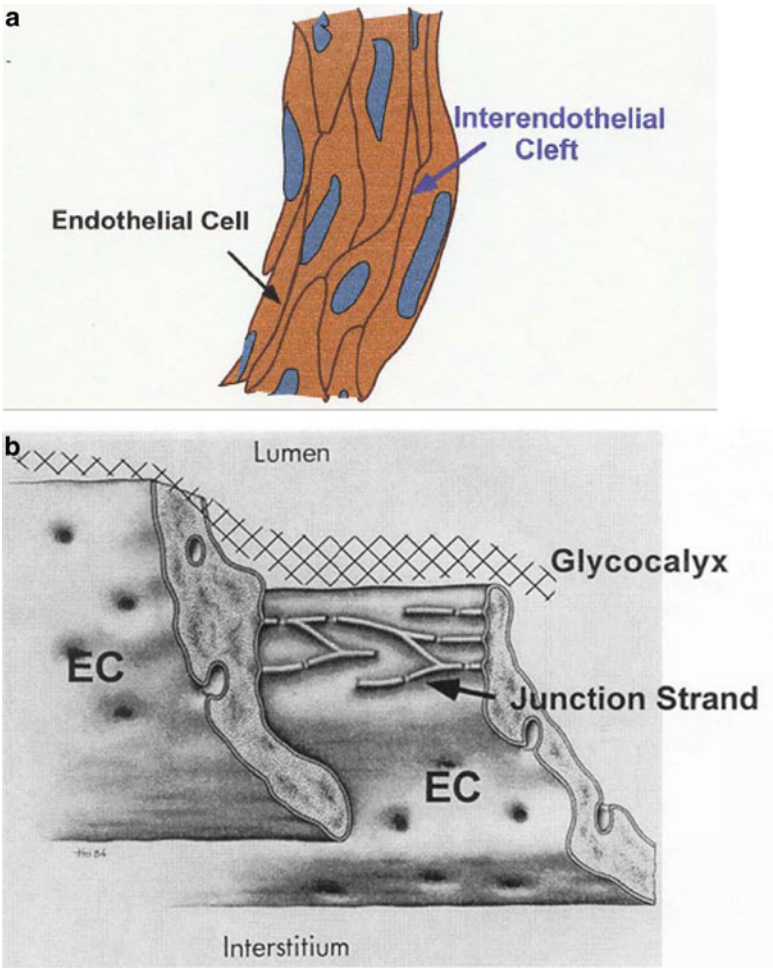

Fig. 4.1 (**a**) A typical mesenteric post-capillary venule of diameter 30 μm, whose wall consists of endothelial cells. The gap between adjacent endothelial cells is called interendothelial cleft. (**b**) Ultrastructural organization of junction strands in the interendothelial cleft and the endothelial surface glycocalyx. Revised from Bundgaard [13]

indirect evidence indicates that there are junctional strands with discontinuous leakages [13] and fiber matrix components [57,72] at the endothelial surface (Fig. 4.1b). It has been concluded that the transport of proteins or other macromolecules is through vesicle shuttle mechanisms [65]. In disease, large gaps are formed in the microvessel endothelium to allow the passage of plasma proteins and cells such as blood cells and tumor cells. Microvascular permeability is a quantitative measure of how permeable the microvessel wall is to all kinds of substances including water and solutes with a variety of sizes. Under healthy conditions, the microvessel wall maintains a normal permeability to water and small solutes for the material exchange during our body's metabolic processes. By contrast, in disease, the integrity of the vessel wall structure can be destroyed and much larger particles such as proteins, leukocytes, and tumor cells can transfer through the wall. It is the effect of transvascular pathways at the vessel wall and their structural barriers that determines and regulates the microvascular permeability. Therefore, we first introduce basic information about transport across microvessels.

4.2 Microvascular Permeability and Transport Across Microvessels

The endothelial cells lining the microvessel walls provide the rate-limiting barrier to extravasation of plasma components of all sizes from electrolytes to proteins. To date, four primary pathways have been observed in the wall of a microvessel by using electron microscopy: intercellular clefts, transcellular pores, vesicles, and fenestra (Fig. 4.2). Microvessels of different types and in different tissues may have different primary transvascular pathways. Under different physiological and pathological conditions, the primary pathway can be changed for the same microvessel (summarized in [57]).

Interendothelial (Intercellular) Cleft. The cleft between adjacent endothelial cells is widely believed to be the principal pathway for water and hydrophilic solute transport through the microvessel wall under normal physiological conditions. The interendothelial cleft is also suggested to be the pathway for the transport of high molecular weight plasma proteins, leukocytes, and tumor cells across microvessel

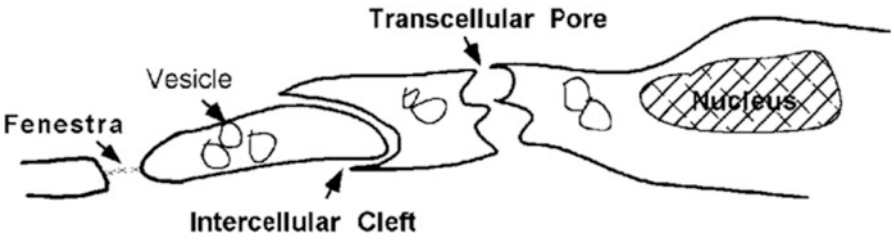

Fig. 4.2 Schematic depiction of various transvascular pathways in the microvessel wall

walls in disease. Direct and indirect evidence (summarized in [57]) indicates that there are tight junction strands with discontinuous leakages and fiber matrix components (glycocalyx layer) [18] at the endothelial surface. These structural components of the microvessel wall form the barrier between the blood stream and body tissues, which maintains the normal microvessel permeability to water and solutes. Variations in permeability are caused by the changes in these structural components.

The molecular basis for the passage of molecules at the level of the breaks in tight junctions is more likely to be the localized absence of cell–cell contacts with corresponding loss of a closely regulated molecular sieve as suggested by Fu et al. [28] and Michel and Curry [57]. Thus the junction break–surface matrix model suggests independent mechanisms to regulate the permeability properties of the microvessel wall. The junction break size and frequency are likely to involve regulation of cell–cell attachment via occludin and other junction proteins including the cadherin-associated junctions [22]. On the other hand, the regulation of glycocalyx density and organization is likely to involve interaction of the molecules forming the cell surface with the cytoskeleton, and with circulating plasma proteins. Some of the cellular mechanisms underlying these interactions are reviewed in [22,57]. Under physiological and pathological conditions, microvessel permeability can be regulated acutely and chronically by mechanisms that are currently in the process of being understood.

A serial section electron microscopy study on frog and rat mesenteric capillaries by Adamson et al. [1] demonstrated that the junction strand was interrupted by infrequent breaks that, on average, were 150 nm long, spaced 2–4 μm apart along the strand, and which accounted for up to 10 % of the length of the strand under control conditions. At these breaks, the space between adjacent endothelial cells (average ~20 nm) was as wide as that in regions of the cleft between adjacent cells with no strands. The luminal surfaces of endothelial cells (ECs) lining the vasculature are coated with a glycocalyx of membrane-bound macromolecules composed of sulfated proteoglycans, hyaluronic acid, sialic acids, glycoproteins, and plasma proteins that adhere to this surface matrix [64,67,68,78]. The thickness of this endothelial surface glycocalyx (ESG) has been observed to range from less than 100 nm to 1 μm for the microvessels in different tissues and species by using different preparation and observing methods [17,50,33,53,57,72,80,82,87]. Although the ESG thickness varies, its density and organization have been reported to be the same among different tissues and species. The glycocalyx fiber radius is ~6 nm and gap spacing between fibers ~8 nm [6,72].

Vesicles. Cytoplasmic vesicular exchange, which behaves like a shuttle bus, is presumed to be the major pathway for transport of plasma proteins and large molecules under normal physiological conditions [65].

Transcellular Pores. In response to local tissue injury or inflammation, additional transport pathways for large molecules may be opened (transcellular pores) and existing pathways made less restrictive. The response is complex, and varies among different animals, organs, and tissues [58].

Fenestrae. Fenestrae usually exist in fenestrated microvessels (in the kidney) instead of a continuous microvessel endothelium. In some fenestrated microvessels, there exists a very thin membrane of ~25 nm thick, diaphragm, which covers the fenestra. Fenestrated endothelia have higher hydraulic conductivities and are more permeable to small ions and molecules than are continuous endothelia. However, their permeability to plasma proteins is about the same [57].

4.2.1 Transport Coefficients

The abovementioned ultrastructural study using electron microscopy and other methods shows that the microvessel wall behaves as a passive membrane for water and hydrophilic solute transport [57]. The membrane transport properties are often described by the Kedem–Katchalsky equations derived from the theory of irreversible thermodynamics,

$$J_s = PRT\Delta C + (1 - \sigma_f)CJ_v \tag{4.1}$$

$$J_v = L_p(\Delta p - \sigma_d RT\Delta C) \tag{4.2}$$

where J_s and J_v are the solute and total volumetric fluxes; ΔC and Δp are the concentration and pressure difference across the membrane: $L_{p,}$ the hydraulic conductivity, describes the membrane permeability to water, P, the diffusive permeability, describes the permeability to solutes, σ_f is the solvent drag or ultrafiltration coefficient that describes the retardation of solutes due to membrane restriction, and $\sigma_{d,}$ the reflection coefficient, describes the selectivity of membrane to solutes. In many transport processes, σ_f is equal to σ_d and thus we often use σ, the reflection coefficient, to represent both of them [57]. R is the universal gas constant and T is the absolute temperature.

4.2.2 Determination of Microvascular Transport Coefficients

All of the permeability measurements have been interpreted in terms of $L_{p,}$ P and σ, which are measured experimentally on intact whole organisms (including human subjects), on perfused tissues and organs, on single perfused microvessels, and on monolayers of cultured microvascular endothelial cells. Different experimental preparations have their advantages and disadvantages. Although measurements made on the intact regional circulation of an animal subject (usually using radioactive isotope labeled tracers) suffer from uncertainties surrounding the exchange surface area of the microvessel wall and the values of the transvascular differences

in pressure and concentration, they usually involve minimal interference with the microvessels themselves. These studies can provide valuable information concerning microvascular exchange under basal conditions. At the other extreme are measurements on single perfused vessels. The hydraulic conductivity L_p and reflection coefficient σ have been measured using the Landis technique and the solute diffusive permeability P using quantitative fluorescence microscope photometry. Both of these techniques are described in detail in [57]. The surface area of the microvessel can be measured directly, as also can the difference in pressure and concentration across the vessel walls. The disadvantages of the single vessel preparation are (1) that they have direct interference with the vessels involved, and (2) that they are usually restricted to a small number of convenient vessel types (e.g., mesenteric vessels on a two dimensional translucent tissue). Direct interference with a vessel, whether it is exposure to light or micromanipulation, might be expected to increase permeability. However, this concern was allayed when it was shown that L_p and P for potassium ions in single muscle capillaries were similar to values based on indirect measurements on the intact muscle microcirculation [57].

Although the rapid growth of endothelial cell biology is largely a result of experiments on cultured endothelial cells in vitro (in dishes), there are limitations to the use of monolayers of cultured endothelial cells for gaining direct information about vascular permeability. In general, the in vitro permeability to albumin is two to ten times larger than that from the in vivo (in live animals) measurement. Although the monolayers of cultured endothelial cells do not completely reflect the permeability characteristics of microvascular endothelium in vivo, they are the most accessible and convenient models for studying the molecular mechanisms by which the microvascular permeability is regulated. The techniques for measuring endothelial monolayer permeability to water and solutes are described in [5,14,47].

4.3 Transport Models for the Interendothelial Cleft

4.3.1 1D Models

Prior to the late 1980s, there were two major 1D theories which attempted to correlate cleft structure with the large amount of experimental data for L_p, P, and σ—the pore–slit and the fiber matrix theory. In microvessels with a continuous endothelium, the principal pathway for water and solutes lies between the endothelial cells through the interendothelial cleft. 1D pore–slit models were developed in terms of the ultrastructure of the cleft.

In the pore–slit theory, the permeability properties of the microvessel wall can be described in terms of flow through water-filled cylindrical pores or rectangular slits through the vessel wall. A Poiseuille type viscous flow was assumed in the pore/slit to describe the resistance to water flow, with the characteristic Reynolds number for the flow of the order of 10^{-8}. The resistance to solute diffusion can be

described in terms of the additional drag on a spherical molecule moving within the pore relative to movement in free solution, and the selectivity of the membrane in terms of steric exclusion at the pore entrance [57].

In the fiber matrix theory, the principal hypothesis to describe the molecular filter of the transvascular pathway is based on the presence of a glycocalyx layer at the endothelial cell surface. Using the stochastic theory of Ogston et al. [61], Curry and Michel [19] described the solute partition coefficient and the restricted solute diffusion coefficient in terms of the fraction of the matrix volume occupied by fibers and the fiber radius. The partition coefficient is defined as the space available to a solute of radius a relative to the space available to water with $a = 0$. In fact, their expressions for the effective diffusivity of a solute only consider the steric exclusion of solutes by the fiber array; they do not include the hydrodynamic interactions between the fibers and the diffusing solute, which are important when the solute size is comparable to the gap spacing between fibers. Using two alternative approaches, Philips et al. [63] calculated the effects of hydrodynamic interactions on the hindered transport of solid spherical macromolecules in ordered or disordered fibrous media. One approach was a rigorous "Stokesian-dynamics" method or generalized Taylor dispersion theory [10,11], via which local hydrodynamic coefficients can be calculated at any position in a fibrous bed. But detailed information about the fiber configuration needs to be given. The other approach was an effective medium theory based on Brinkman's equation. Comparing predicted results with the experimental data for transport of several proteins in hyaluronic acid solutions, they found that the use of Brinkman's equation was in good agreement with more rigorous methods for a homogeneous fiber matrix, as summarized in [57].

A simplified model of the endothelial surface glycocalyx (ESG) has been used by Squire et al. [72], Sugihara-Seki [75], and Sugihara-Seki et al. [76], in which the core proteins in the ESG were assumed to have a circular cylindrical shape and to be aligned in parallel to form a hexagonal arrangement based on recent detailed structural analyses of the ESG. They analyzed the motion of solute and solvent to estimate the filtration reflection coefficient as well as the diffusive permeability of the ESG. Later, Zhang et al. [90] studied osmotic flow through the ESG using a method developed by Anderson and Malone [4] for osmotic flow in porous membranes. Instead of a rigorous treatment of the hexagonal geometry of the cylinders, they adopted an approximation in which the geometry is replaced by an equivalent fluid annulus around each cylinder and estimated the osmotic reflection coefficient of the ESG. Further, Akinaga et al. [3] examined the charge effect on the osmotic flow for membranes with circular cylindrical pores by extending the formulation of osmotic flow developed by Anderson and Malone [4].

4.3.2 3D Models

1D models, used until 1984, were based on random section electron microscopy. Bundgaard [13] was the first to attempt to reconstruct the 3D junction strand

ultrastructure using serial section electron microscopy. Later, Ward et al. [83] examined the 3D features of the junction strands of rat cardiac capillaries by using a goniometric tilting technique. Based on the study of Bundgaard [13] and Ward et al. [83], Tsay and Weinbaum [79] and Weinbaum et al. [84] proposed a basic 3D model for the interendothelial cleft. Their 3D treatments showed that 1D models are a poor description of a cleft with infrequent large breaks since the solute will be confined to small wake-like regions on the downstream side of the junction strand discontinuities and thus not fill the wide part of the cleft. The prediction in Weinbaum et al. [85] as to the likely geometry of the large pores in the junction strand was confirmed by the serial section electron microscopic study on frog mesenteric capillaries in Adamson and Michel [2] . According to these new experimental results, a modified combined junction-orifice-fiber entrance layer model (described in Fig. 4.3), which included a large orifice-like junctional break with the width $2d$ and height $2B$, spaced $2D$ apart, a finite region of fiber matrix components (with the thickness L_f) at the entrance of the cleft and very small pores or slits (with the height $2b_s$) in the continuous part of the junction strand, was developed by Fu et al. [28]. Using this combined junction-orifice-fiber entrance layer model it was predicted that in order to provide an excellent fit for the hydraulic conductivity and the diffusive permeability data for solutes of size ranging from potassium to albumin for frog mesenteric capillaries, there should be a significant fiber layer at the luminal side of the endothelium, together with large infrequent breaks of ~150 nm and a continuous small slit of several nm in the junction strand in the interendothelial cleft. Due to the similarity in morphological wall structure of microvessels in different tissues [57], this 3D model can be easily adapted to explain the permeability data in other types of microvessels [46,48,52,89]. Fu et al. [27] in another work described a new approach to explore junction strand structure. The time dependent diffusion wake model in Fu et al. [27] provided a new interpretation of labeled tracer studies to define the permeability pathways for low molecular weight tracers which depend on the time dependent filling of the extravascular space.

In Fu et al. [26] a time dependent convective-diffusion wake model for high molecular weight tracers was proposed to design experiments that could test for the location of the molecular filter. Combined with the experimental results, this model confirmed the role of the ESG as the primary molecular filter to large molecules and particles. Hu and Weinbaum [42] also showed that coupling of water flow to albumin flux on the tissue side of the ESG could give rise to a nonuniform distribution of albumin concentration and a corresponding nonuniform distribution of effective osmotic pressure. A similar model for oncotic pressures opposing filtration across rat microvessels [1] further confirms the hypothesis that colloid osmotic forces opposing filtration across non-fenestrated continuous capillaries are developed across the ESG and that the oncotic pressure of interstitial fluid does not directly determine fluid balance across the microvascular endothelium.

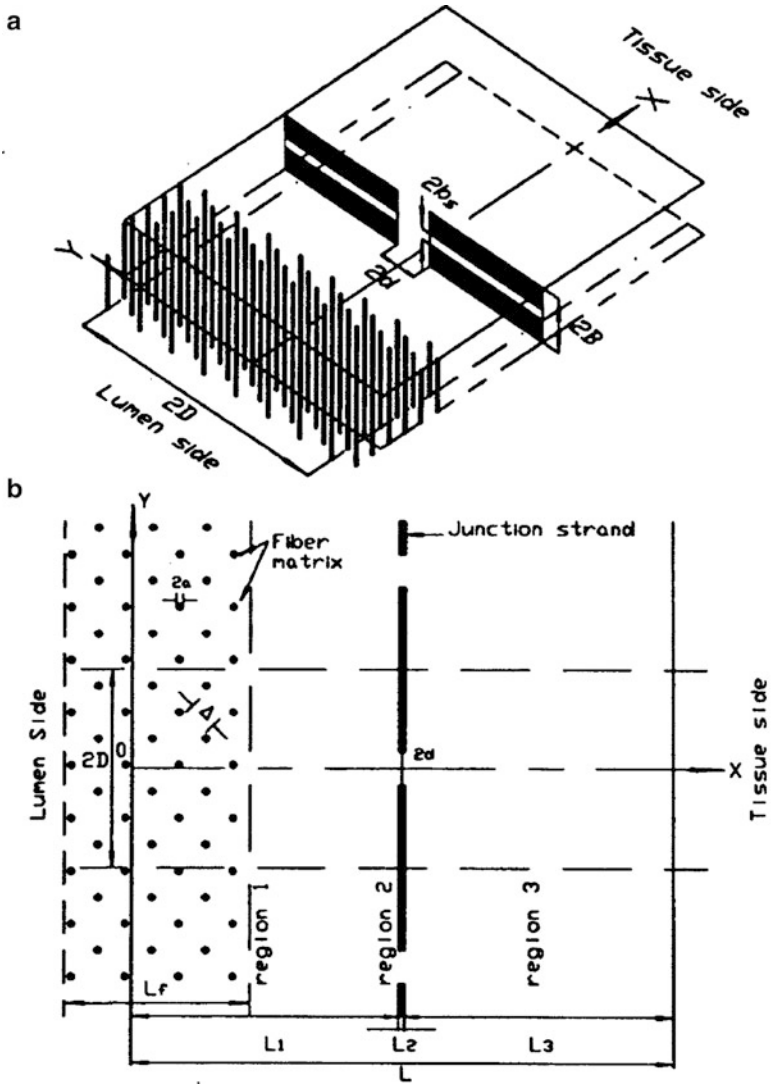

Fig. 4.3 (**a**) 3D sketch of the junction-orifice-matrix entrance layer model for the interendothelial cleft. 2B is the width of the cleft. Large junction breaks observed in Adamson et al. [1] are $2d \times 2B$, while the small continuous slit in the junction strand is $2b_s$. (**b**) plane view of the model. Junction strand with periodic openings lies parallel to the luminal front of the cleft. L_2, depth of pores in junction strand. L_1 and L_3, depths between junction strand and luminal and abluminal fronts of the cleft, respectively. $2D$, distance between adjacent large junction breaks. At the entrance of the cleft on luminal side, cross-bridging structures are represented by a periodic square array of cylindrical fibers. a, radius of these fibers, Δ, gap spacing between fibers, and L_f, thickness of entrance fiber layer. The fiber matrix (surface glycocalyx) carries negative charge due to its molecular composition. The charge density of the surface glycocalyx is in the range of 20–30 mEq/L for mesenteric and brain microvessels. Revised from Fu et al. [27–29], Li and Fu [46], and Yuan et al. [88]

4.3.3 Charge Effects of the Endothelial Surface Glycocalyx

Due to the composition of the ESG, it carries a negative charge [57,88] and it would affect the permeability and selectivity of the microvessel wall to water and solutes. Previously, a simple 1D Donnan-type model had been proposed to describe the charge effect on microvessel permeability [57]. It was based on a Donnan equilibrium distribution of ions, which exists as a result of retention of negative charges on the capillary membrane. Later, an electrochemical model was proposed by Damiano and Stace [20] for the transport of charged molecules through the capillary glycocalyx without considering transport through the cleft region. To investigate the charge selectivity on microvessel permeability, Fu et al. [29] extended the 3D junction-orifice-fiber matrix model developed by Fu et al. [28] for the interendothelial cleft to include a negatively charged glycocalyx layer at the entrance of the interendothelial cleft. Both electrostatic and steric exclusions on charged solutes are considered at the interfaces of the glycocalyx layer between the vessel lumen and between the endothelial cleft. The effect of electrostatic interactions between charged solutes and the matrix on solute transport is also described within the glycocalyx layer. Their model can successfully explain the observations in [57]. Recently, an electrodiffusion-filtration model has been developed to describe the transport of negatively charged macromolecules, bovine serum albumin, across venular microvessels in frog mesentery [15]. A very interesting prediction is that the convective component of albumin transport is greatly diminished by the presence of a negatively charged glycocalyx. Most recently, Li and Fu [46] have developed a model for the charge effect of the ESG and the basement membrane between the endothelium and astrocyte foot processes on the transport across the blood–brain barrier.

Bhalla and Deen [9] studied the effects of charge on osmotic reflection coefficients of macromolecules in porous membranes. Sugihara-Seki et al. [77] proposed an electrostatic model to predict the effects of surface charge on the osmotic reflection coefficient of charged spherical solute across the ESG, based on the combination of low-Reynolds-number hydrodynamics and a continuum description of the electric double layers. The ESG was assumed to consist of identical circular cylinders with a fixed surface charge, aligned parallel to each other so as to form an ordered hexagonal arrangement. Their model predicts that the charge of the ESG contributes significantly to the microvessel reflection coefficient to albumin, which was reported in Michel and Curry [57].

4.4 Microvascular Hyperpermeability and Tumor Metastasis

The danger of cancer is organ failure caused by metastatic tumors that are derivedfrom the primary tumor [73]. One critical step in tumor metastasis is adhesion of primary tumor cells to the endothelium forming the microvascular

wall in distant organs. Understanding this step may lead to new therapeutic concepts for tumor metastasis targeting tumor cell arrest and adhesion in the microcirculation. Microvascular hyperpermeability due to compromised microvessel wall integrity by inflammatory agents and cytokines is one factor that increases tumor cell adhesion to the microvessel endothelium.

4.4.1 VEGF Effect on Microvascular Integrity

Vascular endothelial growth factors (VEGFs) are a family of cytokines that act to increase the delivery of nutrients to tissue by three distinct mechanisms: (a) endothelial cell growth, migration, and new blood vessel formation (angiogenesis) [21], (b) increased blood flow (by vasodilatation) [8], and (c) increased vascular permeability to water and solutes [7,21,30,31,40,66,86]. Combining in vivo permeability measurement and a mathematical model for the interendothelial transport, Fu et al. [29] predicted that the acute effects of VEGF on microvascular integrity are widened gap opening of the interendothelial cleft and partial degradation of the ESG. Longer term effects of VEGF include the formation of gaps between adjacent endothelial cells in venular microvessels [56], vesiculovascular organelle pathways [25], transcellular pores [25,59], and fenestra [25,66]. Fu et al. [32] also found that the VEGF-induced microvascular hyperpermeability can be abolished by enhancing intracellular levels of adenosine 3′,5′-cyclic monophosphate (cAMP), which strengthens the microvessel integrity by increasing the number of junction strands in the cleft between endothelial cells forming the microvessel wall.

4.4.2 VEGF Effect on Tumor Cell Adhesion

Previous studies have found that many cancer cells express VEGF to a high degree [45], while the microvascular endothelium has abundant VEGF receptors including VEGFR2 (KDR/Flk-1) [55]. VEGFR2 has been implicated in normal and pathological vascular endothelial cell biology [62]. Recently, it has been shown that ectopic administration of VEGF enhances the adhesion and transmigration of human breast cancer MDA-MB-231 cells across a monolayer of human brain microvascular endothelial cells under a static condition in vitro [45]. In addition, VEGF enhances the adhesion of malignant MDA-MB-435 cells and ErbB2-transformed mouse mammary carcinomas to intact rat mesenteric microvessels under flow in vivo [69] (Fig. 4.4).

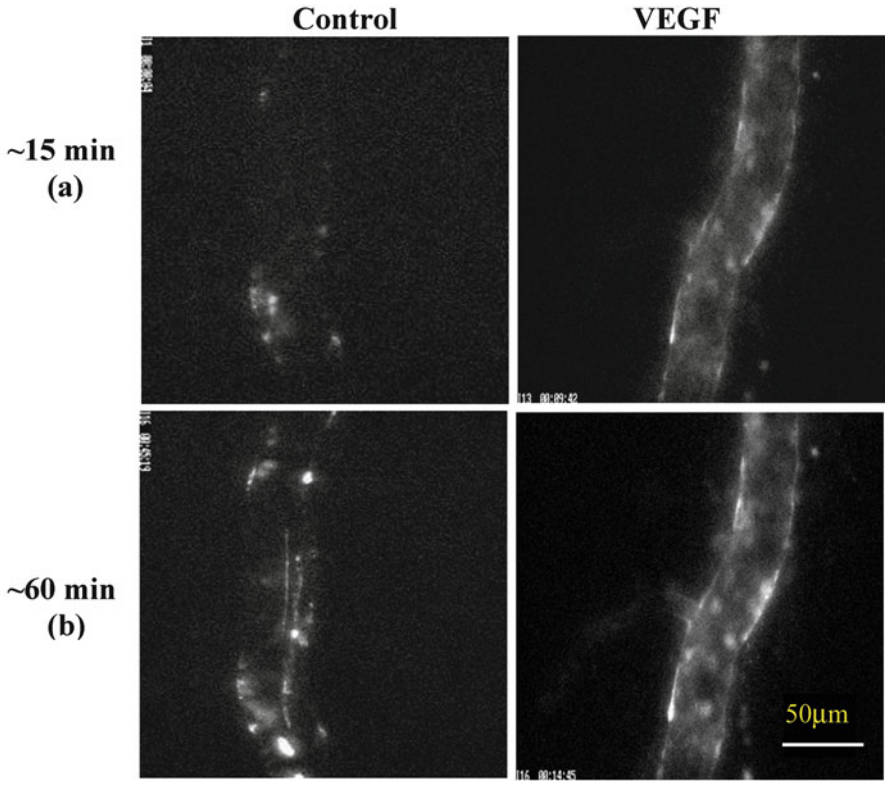

Fig. 4.4 Photomicrographs showing in vivo MDA-MB-435s tumor cell adhesion to a single perfused microvessel under control with 1%BSA Ringer perfusate and under treatment with 1 nM VEGF perfusate after (**a**) ~15 min and (**b**) ~60 min perfusion. The perfusion velocity is ~1,000 μm/s, which is the mean normal flow velocity in post-capillary venules. Bright spots indicate adherent tumor cells labeled with fluorescence. From Shen et al. [69]

4.4.3 Integrin Signaling, Cell Adhesion Molecules, and Tumor Metastasis

Although the nonspecific trapping due to the friction between the tumor cells and the narrow part of microvasculature is found to be responsible for the initial tumor cell arrest [34,37,43,54], the cell adhesion molecules are required for the adhesion in larger microvessels and transmigration [12,24,34–36,41,45,49,69–71,73]. The integrins are a family of signaling and cell adhesion receptors, which attach cells to the extracellular matrix (ECM) and in some cases to other cells, and cooperate with growth factor and cytokine receptors to regulate cell behavior. Signals elicited by integrins enable tumor cells to survive, proliferate, and migrate independently of positional constraints [38], and adhere [24]. The α6β4 integrin is a laminin-5 receptor and was originally described as a "tumor-specific" protein,

because of its apparent upregulation in multiple metastatic tumor types [35]. The β4 integrin is unique among integrins, because the cytoplasmic portion of the β4 subunit is 1,017 amino-acid-long and possesses distinctive adhesive and signaling functions [35]. Upon binding of the ectodomain of β4 to the basement membrane protein laminin-5, the cytoplasmic portion of β4 interacts with the keratin cytoskeleton to promote the assembly of hemidesmosomal adhesions [51]. In addition, β4 activates intracellular signaling autonomously as well as by associating with multiple receptor tyrosine kinases (RTKs), including the EGFR, ErbB2, Met, and Ron [38,60]. Deletion of the β4 signaling domain delayed mammary tumor onset and inhibited primary tumor growth. The tumors arising in mutant mice were significantly more differentiated histologically as compared to control tumors. In addition, primary tumor cells expressing signaling-defective β4 displayed a reduced proliferative rate and invasive ability and underwent apoptosis when deprived of matrix adhesion. Finally, upon injection in the tail vein of nude mice, the mammary tumor cells expressing mutant β4 exhibited reduced ability to metastasize to the lung [39].

Most recently, Fan et al. [24] have examined the adhesion of ErbB2-transformed mammary tumor cells to mouse brain microvascular endothelial monolayer. They found that integrin β4 signaling does not exert a direct effect on adhesion to the endothelium or the underlying basement membrane. Rather, it enhances ErbB2-dependent expression of VEGF by tumor cells. VEGF in turn partially disrupts the tight and adherent junctions that maintain the adhesion between endothelial cells, enabling tumor cells to intercalate between endothelial cells and extend projections reaching the underlying exposed basement membrane, and enabling adhesion to occur between cell adhesion molecules (e.g., integrins) and ECM proteins (e.g., laminins).

4.4.4 Reducing Tumor Cell Adhesion by Enhancing Microvessel Wall Integrity

In addition to blocking the cell adhesion molecules at the surface of tumor and endothelial cells or in the ECM, e.g., integrins, ICAM-1, P-selectins, junctional adhesion molecules, and laminins, Shen et al. [69] measured cancer cell adhesion after pretreatment of cells with the antibody blocking VEGF, and pretreatment of the microvessel with VEGF receptor (KDR/Flk-1) inhibitor, SU1498. They found that anti-VEGF and SU1498 almost completely abolished the adhesion of malignant MDA-MB-435s to vascular endothelium in vivo. In an in vitro experiment, Fan et al. [24] showed that although VEGF receptor (KDR/Flk-1) inhibitor SU1498 did not decrease the basal permeability of a microvascular endothelial monolayer, nor tumor cell adhesion under the normal permeability conditions. It, however, abolished microvascular hyperpermeability induced by VEGF as well as increasing tumor cell adhesion (Fig. 4.5).

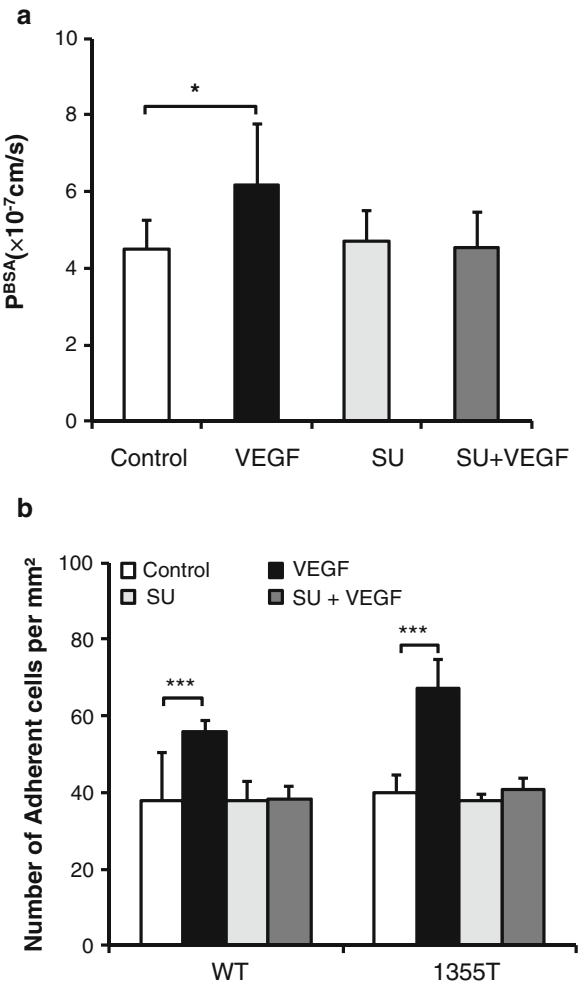

Fig. 4.5 Effects of VEGF and the endothelial VEGF receptor (KDR/Flk-1) inhibitor SU-1498 on (**a**) Permeability of the bEnd3 monolayer to albumin ($n = 6$) and (**b**) WT and 1355 T tumor cell adhesion. Permeability and adhesion were measured after 1 h control and VEGF treatment. For inhibition by SU-1498, the bEnd3 monolayer was pretreated with SU-1498 for 30 min. From Fan et al. [24]

4.4.5 Tumor Cell Adhesion in the Microcirculation

In vitro static adhesion assays have been utilized to investigate tumor cell adhesion to endothelial cells [23,45] and to extracellular matrix (ECM) proteins [39]. Tumor cell adhesion has also been investigated using flow chambers [16,36,71] or artificial blood vessels [12] to address flow effects. Direct injection of tumor cells into the circulation has enabled the observation of tumor cell metastasis in target organs after sacrificing the animals [70], while intravital microscopy has been used to observe the interactions between circulating tumor cells and the microvasculature both in vivo and ex vivo [34,37,43,54,69,74].

Tumor cell extravasation is a dynamic process in which tumor cell adhesion to the vascular endothelium and transendothelial migration occurs under flow

conditions. Therefore, the geometry of the microvasculature and the local hydrodynamic factors, along with the cell adhesion molecules at the tumor cell and endothelial cell should play a crucial role in tumor cell adhesion and extravasation. Tumor cells are exposed to flow while (a) circulating from the primary tumor, (b) arresting on the downstream vascular endothelium, and (c) transmigrating into the secondary target organ. Investigations of the role of shear flow in tumor cell adhesion and extravasation will contribute to the understanding of the complex process of tumor metastasis. Tumor cell extravasation would normally occur in the microvasculature where shear forces are relatively low (like in post-capillary venules) although of sufficient magnitudes to activate cell surface receptors and alter vascular cell function. During tumor cell extravasation there are significant changes in the structure and function of both tumor and endothelial cells. For example a significant rearrangement of the cell cytoskeleton is required in both the tumor cells during migration [44] and in the endothelial cells as the barrier function is altered [81]. The extravasation of tumor cells also induces endothelial cell remodeling [43].

In an in vitro flow chamber study, Slattery et al. [71] found that the shear rate, rather than the shear stress, plays a more significant role in PMN (polymorphonuclear neutrophils)-facilitated melanoma adhesion and extravasation. β2 integrins/ICAM-1 adhesion mechanisms were examined and the results indicate LFA (lymphocyte function-associated)-1 and Mac-1 (CD11b/CD18) cooperate to mediate the PMN-EC (endothelial cell)–melanoma interactions under shear conditions. In addition, endogenously produced IL-8 contributes to PMN-facilitated melanoma arrest on the EC through the CXC chemokine receptors 1 and 2 (CXCR1 and CXCR2) on PMN [49,71].

4.5 Summary and Future Study

Although transport across the endothelium is a classic problem that has been investigated for more than several decades, the fundamental questions related to the structure–transport function of the microvessel wall and the interaction between the circulating cells and the cells forming the wall still remain unclear. With the help of mathematical models for more accurate interpretations and predictions, new techniques involving transgenic animals with fluorescent proteins expressed endothelial cells and circulating blood and tumor cells, new fluorescent dyes for labeling the structural components of transvascular pathways, intravital and electron microscopy, and new developments in molecular biology and biochemistry will lead to more fascinating discoveries in this field.

One problem is the development of models for dynamic water and solute transport through multi-transvascular pathways including intercellular, transcellular, fenestral, and vesicle routes. They are important for predicting the malfunction in the transvascular process in disease. Another problem is to create transvascular models for cells such as leukocytes and cancer cells. The transport of cells is crucial in many physiological and pathological processes including inflammatory response and tumor metastasis.

Acknowledgments The author would like to thank the support from NSF CBET 0754158, and NIH CA153325-01 and CA137788-01.

References

1. Adamson RH, Lenz JF, Zhang X, Adamson GN, Weinbaum S, Curry FE (2004) Oncotic pressures opposing filtration across non-fenestrated rat microvessels. J Physiol 557:889–907
2. Adamson RH, Michel CC (1993) Pathways through the inter-cellular clefts of frog mesenteric capillaries. J Physiol 466:303–327
3. Akinaga T, Sugihara-Seki M, Itano T (2008) Electrical charge effect on osmotic flow through pores. J Phys Soc Jpn 77:053401
4. Anderson JL, Malone DM (1974) Mechanism of osmotic flow in porous membranes. Biophys J 14:957–982
5. Antonetti DA, Wolpert EB, DeMaio L, Harhaj NS, Scaduto RC Jr (2002) Hydrocortisone decreases retinal endothelial cell water and solute flux coincident with increased content and decreased phosphorylation of occludin. J Neurochem 80:667–677
6. Arkill KP, Knupp C, Michel CC, Neal CR, Qvortrup K, Rostgaard J, Squire JM (2011) Similar endothelial glycocalyx structures in microvessels from a range of mammalian tissues: evidence for a common filtering mechanism? Biophys J 101:1046–1056
7. Bates DO, Curry FE (1996) Vascular endothelial growth factor increases hydraulic conductivity of isolated perfused microvessels. Am J Physiol 271(40):H2520–H2528
8. Bates DO, Heald RI, Curry FE, Williams B (2001) Vascular endothelial growth factor increases Rana vascular permeability and compliance by different signalling pathways. J Physiol 533(Pt. 1):263–272
9. Bhalla G, Deen WM (2009) Effects of charge on osmotic reflection coefficients of macromolecules in porous membranes. J Colloid Interface Sci 333:363–372
10. Brandy JF, Bossis G (1988) Stokesian dynamics. Annu Rev Fluid Mech 20:111
11. Brenner H, Adler PM (1982) Dispersion resulting from flow through spatially periodic media: II Surface and intraparticle transport. Phil Trans R Soc Lond A 307(149):149–200
12. Brenner W, Langer P, Oesch F, Edgell CJ, Wieser RJ (1995) Tumor cell-endothelium adhesion in an artificial venule. Anal Biochem 225:213–219
13. Bundgaard M (1984) The three-dimensional organization of tight junctions in a capillary endothelium revealed by serial-section electron microscopy. J Ultmstruct Res 88:1–17
14. Cancel LM, Fitting A, Tarbell JM (2007) In vitro study of LDL transport under pressurized (convective) conditions. Am J Physiol 293:H126–H132
15. Chen B, Fu BM (2004) An electrodiffusion-filtration model for effects of surface glycocalyx on microvessel permeability to macromolecules. ASME J Biomech Eng 126:614–624
16. Chotard-Ghodsnia R, Haddad O, Leyrat A, Drochon A, Verdier C, Duperray A (2007) Morphological analysis of tumor cell/endothelial cell interactions under shear flow. J Biomech 40:335–344
17. Constantinescu A, Spaan JA, Arkenbout EK, Vink H, Vanteeffelen JW (2011) Degradation of the endothelial glycocalyx is associated with chylomicron leakage in mouse cremaster muscle microcirculation. Thromb Haemost 105(5):790–801
18. Curry FE, AdamsonRH (2012) Endothelial glycocalyx: permeability barrier and mechanosensor. Ann Biomed Eng 40(4):828–39
19. Curry FE, Michel CC (1980) A fiber matrix model of capillary permeability. Microvasc Res 20:96–99
20. Damiano ER, Stace TM (2002) A mechano-electrochemical model of radial deformation of the capillary glycocalyx. Biophys J 82:1153–1175

21. Dvorak HF, Brown LF, Detmar M, Dvorak AM (1995) Vascular permeability factor/vascular endothelial growth factor, microvascular hyperpermeability, and angiogenesis. Am J Pathol 146:1029–1039
22. Drenckhahn D, Ness W (1997) The endothelial contractile cytoskeleton. In: Born GVR, Schwartz CJ (eds) Vascular endothelium: physiology, pathology and therapeutic opportunities. Schattauer, Stuttgart, pp 1–15
23. Earley S, Plopper GE (2006) Disruption of focal adhesion kinase slows transendothelial migration of AU-565 breast cancer cells. Biochem Biophys Res Commun 350:405–412
24. Fan J, Cai B, Zeng M, Hao Y, Giancotti FG, Fu BM (2011) Integrin β4 signaling promotes mammary tumor cell adhesion to brain microvascular endothelium by inducing ErbB2-medicated secretion of VEGF. Ann Biomed Eng 39(8):2223–2241
25. Feng D, Nagy JA, Payne K, Hammel I, Dvorak HF, Dvorak AM (1999) Pathways of macromolecular extravasation across microvascular endothelium in response to VPF/VEGF and other vasoactive mediators. Microcirculation 6(1):23–44
26. Fu B, Curry FE, Adamson RH, Weinbaum S (1997) A model for interpreting the tracer labeling of interendothelial clefts. Ann Biomed Eng 25:375–397
27. Fu BM, Curry FE, Weinbaum S (1995) A diffusion wake model for tracer ultrastructure-permeability studies in microvessels. Am J Physiol 269(38):H2124–H2140
28. Fu BM, Weinbaum S, Tsay RY, Curry FE (1994) A junction-orifice-fiber entrance layer model for capillary permeability: application to frog mesenteric capillaries. ASME J Biomech Eng 116:502–513
29. Fu BM, Chen B, Chen W (2003) An electrodiffusion model for effects of surface glycocalyx layer on microvessel solute permeability. Am J Physiol 284:H1240–H1250
30. Fu BM, Shen S (2003) Structural mechanisms of vascular endothelial growth factor (VEGF) on microvessel permeability. Am J Physiol 284(6):H2124–H2135
31. Fu BM, Shen S (2004) Acute VEGF effect on solution permeability of mammalian microvessels in vivo. Microvasc Res 68(1):51–62
32. Fu BM, Shen S, Chen B (2006) Structural mechanisms in the abolishment of VEGF-induced microvascular hyperpermeability by cAMP. ASME J Biomech Eng 128(3):313–328
33. Gao L, Lipowsky HH (2010) Composition of the endothelial glycocalyx and its relation to its thickness and diffusion of small solutes. Microvasc Res 80:394–401
34. Gassmann P, Kang ML, Mees ST, Haier J (2010) In vivo tumor cell adhesion in the pulmonary microvasculature is exclusively mediated by tumor cell-endothelial cell interaction. BMC Cancer 10:177
35. Giancotti FG (2007) Targeting, integrin beta4 for cancer and anti-angiogenic therapy. Trends Pharmacol Sci 28:506–511
36. Giavazzi R, Foppolo M, Dossi R, Remuzzi A (1993) Rolling and adhesion of human tumor cells on vascular endothelium under physiological flow conditions. J Clin Invest 92:3038–3044
37. Glinskii OV, Huxley VH, Glinsky GV, Pienta KJ, Raz A, Glinsky VV (2005) Mechanical entrapment is insufficient and intercellular adhesion is essential for metastatic cell arrest in distant organs. Neoplasia 7(5):522–527
38. Guo W, Giancotti FG (2004) Integrin signalling during tumour progression. Nat Rev Mol Cell Biol 5:816–826
39. Guo W, Pylayeva Y, Pepe A, Yoshioka T, Muller WJ, Inghirami G, Giancotti FG (2006) Beta 4 integrin amplifies ErbB2 signaling to promote mammary tumorigenesis. Cell 126:489–502
40. Hippenstiel S, Krull M, Ikemann A, Risau W, Clauss M, Suttorp N (1998) VEGF induces hyperpermeability by a direct action on endothelial-cells. Am J Physiol 18:L678–L684
41. Hood JD, Cheresh DA (2002) Role of integrins in cell invasion and migration. Nat Rev Cancer 2:91–100
42. Hu X, Weinbaum S (1999) A new view of Starling's Hypothesis at the microstructural level. Microvasc Res 58:281–304

43. Kienast Y, von Baumgarten L, Fuhrmann M, Klinkert WE, Goldbrunner R, Herms J, Winkle F (2010) Real-time imaging reveals the single steps of brain metastasis formation. Nat Med 16(1):116–122
44. Lauffenburger DA, Horwitz AF (1996) Cell migration: a physically integrated molecular process. Cell 84:359–369
45. Lee TH, Avraham HK, Jiang S, Avraham S (2003) Vascular endothelial growth factor modulates the transendothelial migration of MDA-MB-231 breast cancer cells through regulation of brain microvascular endothelial cell permeability. J Biol Chem 278:5277–5284
46. Li G, Fu BM (2011) An electro-diffusion model for the blood–brain barrier permeability to charged molecules. ASME J Biomech Eng 133(2):0210
47. Li G, Simon M, Shi Z, Cancel L, Tarbell JM, Morrison B, Fu BM (2010) Permeability of endothelial and astrocyte cocultures: in vitro blood–brain barrier models for drug delivery. Ann Biomed Eng 38(8):2499–2511
48. Li G, Yuan W, Fu BM (2010) A model for water and solute transport across the blood–brain barrier. J Biomech 43(11):2133–2140
49. Liang S, Slattery MJ, Dong C (2005) Shear stress and shear rate differentially affect the multistep process of leukocyte-facilitated melanoma adhesion. Exp Cell Res 310(2):282–292
50. Lipowsky HH (2011) The endothelial glycocalyx as a barrier to leukocyte adhesion and its mediation by extracellular proteases. Ann Biomed Eng 40(4):840–848
51. Litjens SH, de Pereda JM, Sonnenberg A (2006) Current insights into the formation and breakdown of hemidesmosomes. Trends Cell Biol 16:376–383
52. Liu Q, Mirc D, Fu BM (2008) Mechanical mechanisms of thrombosis in intact bent microvessels of rat mesentery. J Biomech 41:2726–2734
53. Long DS, Smith ML, Pries AR, Ley K, Damiano ER (2004) Microviscometry reveals reduced blood viscosity and altered shear rate and shear stress profiles in microvessels after hemodilution. Proc Natl Acad Sci U S A 101:10060–10065
54. Mook ORF, Marle J, Vreeling-Sindelarova H, Jongens R, Frederiks WM, Noorden CJK (2003) Visualisation of early events in tumor formation of eGFP-transfected rat colon cancer cells in liver. Hepatology 38:295–304
55. Mukhopadhyay D, Nagy JA, Manseau EJ, Dvorak HF (1998) Vascular permeability factor/vascular endothelial growth factor-mediated signaling in mouse mesentery vascular endothelium. Cancer Res 58(6):1278–1284
56. McDonald DM, Thurston G, Baluk P (1999) Endothelial gaps as sites for plasma leakage in inflammation. Microcirculation 6(1):7–22
57. Michel CC, Curry FE (1999) Microvascular permeability. Physiol Rev 79(3):703–761
58. Michel CC, Neal CR (1997) Pathways through microvascular: endothelium or normal and increased permeability. In: Born GVR, Schwartz CJ (eds) Vascular endothelium: physiology, pathology and therapeutic opportunities. Schattauer, Stuttgart, pp 37–48
59. Michel CC, Neal CR (1999) Openings through endothelial cells associated with increased microvascular permeability. Microcirculation 6(1):45–62
60. Moasser MM, Basso A, Averbuch SD, Rosen N (2001) The tyrosine kinase inhibitor ZD1839 ("Iressa") inhibits HER2-driven signaling and suppresses the growth of HER2-overexpressing tumor cells. Cancer Res 61:7184–7188
61. Ogston AG, Preston BN, Wells JD (1973) On the transport of compact particles through solutions of chain-polymers. Proc R Soc Lond A 333:297–316
62. Olsson AK, Dimberg A, Kreuger J, Claesson-Welsh L (2006) VEGF receptor signalling—in control of vascular function. Nat Rev Mol Cell Biol 7(5):359–371
63. Phillips RJ, Deen WM, Brady JF (1990) Hindered transport in fibrous membranes and gels: Effect of solute size and fiber configuration. J Colloid Interf Sci 139(2):363–373
64. Reitsma S, Slaaf DW, Vink H, van Zandvoort MA, Oude Egbrink MG (2007) The endothelial glycocalyx: composition, functions, and visualization. Pflugers Archiv Eur J Physiol 454:345–359

65. Renkin EM (1988) Transport pathways and processes. In: Simionescu N, Simionescu M (eds) Endothelial cell biology. Plenum, New York, pp 51–68
66. Roberts WG, Palade GE (1995) Increased microvascular permeability and endothelial enestration induced by vascular endothelial growth factor. J Cell Sci 108:2369–2379
67. Salmon AH, Neal CR, Sage LM, Glass CA, Harper SJ, Bates DO (2009) Angiopoietin-1 alters microvascular permeability coefficients in vivo via modification ofendothelial glycocalyx. Cardiovasc Res 83(1):24–33
68. Salmon AH, Satchell SC (2012) Endothelial glycocalyx dysfunction in disease: albuminuria and increased microvascular permeability. J Pathol 226(4):562–574
69. Shen S, Fan J, Cai B, Lv Y, Zeng M, Hao Y, Giancotti FG, Fu BM (2010) Vascular endothelial growth factor enhances mammary cancer cell adhesion to endothelium *in vivo*. J Exp Physiol 95:369–379
70. Schluter K, Gassmann P, Enns A, Korb T, Hemping-Bovenkerk A, Holzen J, Haier J (2006) Organ-specific metastatic tumor cell adhesion and extravasation of colon carcinoma cells with different metastatic potential. Am J Pathol 169:1064–1073
71. Slattery MJ, Liang S, Dong C (2005) Distinct role of hydrodynamic shear in leukocyte-facilitated tumor cell extravasation. Am J Physiol 288:C831–C839
72. Squire JM, Chew M, Nneji G, Neal C, Barry J, Michel CC (2001) Quasi-periodic substructure in the microvessel endothelial glycocalyx: a possible explanation for molecular filtering? J Struct Biol 136:239–255
73. Steeg PS, Theodorescu D (2008) Metastasis: a therapeutic target for cancer. Nat Clin Pract Oncol 5(4):206–219
74. Steinbauer M, Guba M, Cernaianu G, Köhl G, Cetto M, Kunz-Schugart LA, Gcissler EK, Falk W, Jauch KW (2003) GFP-transfected tumor cells are useful in examining early metastasis in vivo, but immune reaction precludes long-term development studies in immunocompetent mice. Clin Exp Metastasis 20:135–141
75. Sugihara-Seki M (2006) Transport of spheres suspended in the fluid flowing between hexagonally arranged cylinders. J Fluid Mech 551:309–321
76. Sugihara-Seki M, Akinaga T, Itano T (2008) Flow across microvessel walls through the endothelial surface glycocalyx and the interendothelial cleft. J Fluid Mech 601:229–252
77. Sugihara-Seki M, Akinaga T, Itano T (2010) Effects of electric charge on osmotic flow across periodically arranged circular cylinders. J Fluid Mech 664:174–192
78. Tarbell JM, Pahakis MY (2006) Mechanotransduction and the glycocalyx. J Intern Med 259:339–350
79. Tsay R, Weinbaum S (1991) Viscous flow in a channel with periodic cross-bridging fibers of arbitrary aspect ratio and spacing. J Fluid Mech 226:125–148
80. van den Berg BM, Vink H, Spaan JA (2003) The endothelial glycocalyx protects against myocardial edema. Circ Res 92:592–594
81. van Hinsbergh VW, Nieuw Amerongen GP (2002) Intracellular signalling involved in modulating human endothelial barrier function. J Anat 200:549–560
82. Vink H, Duling BR (1996) Identification of distinct luminal domains for macromolecules, erythrocytes, and leukocytes within mammalian capillaries. Circ Res 79:581–589
83. Ward BJ, Bauman KF, Firth JA (1988) Interendothelial junctions of cardiac capillaries in rats: their structure and permeability properties. Cell Tissue Res 252:57–66
84. Weinbaum S, Tsay R, Curry FE (1992) A three-dimensional junction-pore-matrix model for capillary permeability. Microvasc Res 44:85–111
85. Weinbaum S, Tarbell JM, Damiano ER (2007) The structure and function of the endothelial glycocalyx layer. Annu Rev Biomed Eng 9:121–167
86. Wu HM, Huang Q, Yuan Y, Grange HJ (1996) VEGF induces NO dependent hyperpermeability in coronary venules. Am J Physiol 40:H2735–H2739
87. Yen WY, Cai B, Zeng M, Tarbell JM, Fu BM (2012) Quantification of the endothelial surface glycocalyx on rat and mouse blood vessels. Microvasc Res 83(3):337–346

88. Yuan W, Li G, Zeng M, Fu BM (2010) Modulation of the blood–brain barrier permeability by plasma glycoprotein orosomucoid. Microvasc Res 80(1):148–157
89. Yuan W, Lv Y, Zeng M, Fu BM (2009) Non-invasive method for the measurement of Solute Permeability of Rat Pial Microvessels. Microvasc Res 77:166–173
90. Zhang X, Curry FE, Weinbaum S (2006) Mechanism of osmotic flow in a periodic fiber array. Am J Physiol 290:H844–H852

Chapter 5
Micro Flows in the Cardiopulmonary System: A Surgical Perspective

Vasilios A. Karagounis and Axel R. Pries

Abstract Micro-flows in different organs—i.e., the flow of blood through the smallest vessels, the microcirculation—differ in a number of aspects from blood flow in larger vessels. Most prominently, the vessels of the microcirculation exhibit diameters which are comparable in diameter to the size of red blood cells. In addition to these hemorheological differences, the vessels of the microcirculation exhibit the largest fraction of the overall inner vessel surface which is covered by the endothelium. This chapter focuses on the heart and the lung addressing phenomena in the microcirculation, including the no reflow phenomenon, coronary microvascular dysfunction in the heart and the hypoxic pulmonary vasoconstriction in the lung.

5.1 The Heart

The blood flow is delivered to the heart through large epicardial conductance vessels (1–3 mm in size) and then into the myocardium by penetrating arteries leading a plexus of capillaries. The bulk of the resistance to coronary flow is in the penetrating arterioles (140 down to 20 μm in size). Because the heart is metabolically very active, there is a high density of capillaries such that there is approximately one capillary for every myocyte, with an intercapillary distance at rest of approximately 17 μm [22].

V.A. Karagounis (✉)
Cardiothoracic Vascular Surgery, PO Box 819, Panorama Thessaloniki 55236, Greece
e-mail: pouliana50@hotmail.com

A.R. Pries
Department of Physiology and CCR, Charité - Universitätsmedizin Berlin, Charité, Arnimallee 22, Berlin 14195, Germany
e-mail: axel.pries@charite.de

M.W. Collins and C.S. König (eds.), *Micro and Nano Flow Systems for Bioanalysis*, Bioanalysis 2, DOI 10.1007/978-1-4614-4376-6_5,

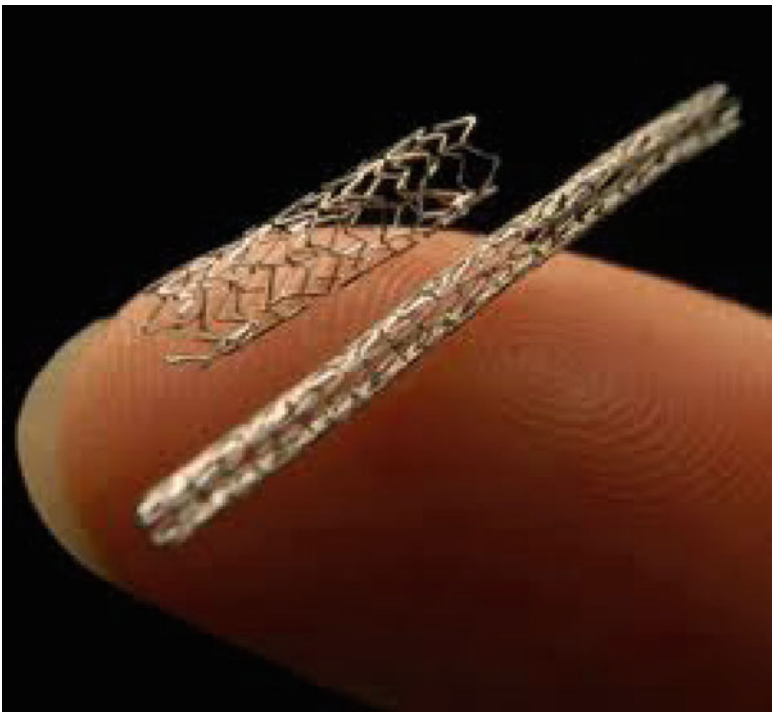

Fig. 5.1 Coronary artery stents

Atherosclerotic disease primarily affects the large conductance vessels of the heart. The hemodynamic effect that a coronary artery stenosis has upon blood flow may be considered in terms of Poiseuille's law, which describes the resistance (R) of a viscous fluid to laminar flow through a cylindrical tube. Resistance is inversely proportional to the fourth power of the radius (r) and directly proportional to the length (L) of the narrowing, and viscosity of the fluid (μ). By Poiseuille's law a 1-cm, 80% stenosis has a resistance that is 16 times as high as the resistance of a 1-cm, 60% stenosis. Similarly, if this stenosis progresses to a 90% stenosis, the resistance is 256 times as great as the resistance of a 60% stenosis [6,10]

$$R = 8\mu \mathrm{L}/\pi r^4$$

Placement of coronary artery stents (Figs. 5.1 and 5.2) or coronary artery bypass (Fig. 5.3) reestablish the coronary blood flow and decrease the probability of myocardial infarction. However, this approach is only addressing the patency of large vessels and there is increasing evidence that the microcirculation plays a very relevant role in the pathophysiology of myocardial perfusion states with increased flow resistance.

Fig. 5.2 Right coronary angiogram before (*left*) and after stent deployment (*right*)

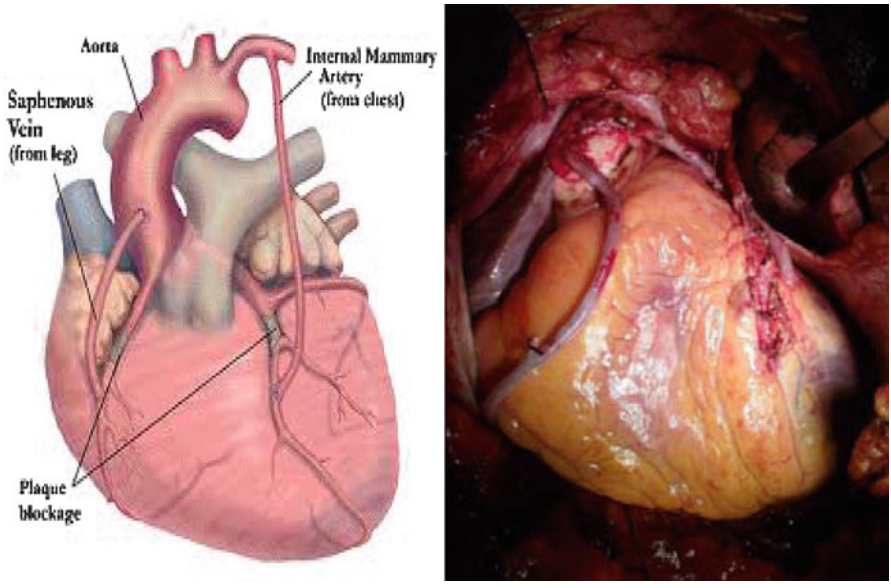

Fig. 5.3 Coronary artery bypass with left internal mammary artery to the left anterior descending coronary artery and saphenous vein graft to the right coronary artery

In a variable proportion of patients presenting with ST-segment elevation myocardial infarction, ranging from 5 to 50%, primary percutaneous coronary intervention (PCI) achieves epicardial coronary artery reperfusion but not myocardial reperfusion, a condition known as “no-reflow.” Of note, no-reflow is

associated with a worse prognosis at follow-up. The phenomenon has a multifactorial pathogenesis including: distal embolization, ischemia–reperfusion injury, and individual predisposition of coronary microcirculation to injury. Several therapeutic strategies have been tested for the prevention and treatment of no-reflow. In particular, thrombus aspiration before stent implantation prevents distal embolization during stent deployment and has been recently shown to improve myocardial perfusion and clinical outcome as compared with the standard procedure. However, it is conceivable that the relevance of each pathogenetic component of no-reflow is different in different patients, thus explaining the occurrence of no-reflow despite the use of mechanical thrombus aspiration [14].

Another term used to indicate reduced microvessel flow, commonly occurring following percutaneous coronary interventions (PCI), is Microvascular obstruction (MVO) which may lead to myocardial injury, and is an independent predictor of adverse outcome. Severe MVO may manifest angiographically as reduced flow in the patent upstream epicardial arteries, a situation that is termed, as mentioned above, "no-reflow." Microvascular obstruction can be broadly categorized according to the duration of myocardial ischemia preceding PCI. In "interventional MVO" (e.g., elective PCI), obstruction typically involves myocardium that was not exposed to acute ischemia before PCI. Conversely "reperfusion MVO" (e.g., primary PCI for acute myocardial infarction) occurs within a myocardial territory that was ischemic before the coronary intervention. Interventional and reperfusion MVO have distinct pathophysiological mechanisms and may require individualized therapeutic approaches. Interventional MVO is triggered predominantly by downstream embolization of atherosclerotic material from the epicardial vessel wall into the distal microvasculature. Reperfusion MVO results from both distal embolization and ischemia–reperfusion injury within the subtended ischemic tissue. Management of MVO and no-reflow may be targeted at different levels: the epicardial artery, microvasculature, and tissue [8]

The no-reflow phenomenon, being inadequate myocardial perfusion of a given coronary segment, without angiographic evidence of mechanical vessel obstruction, after PCI, is difficult to understand and treat due to the large variability between patients and the experimental difficulties in assessing the different interacting processes at tissue level, such as ischemic injury, reperfusion injury, distal embolization, susceptibility of microcirculation to injury, which contribute to no reflow [15,18]. Increasingly, however, techniques to analyze microvascular function in experiments and in patients are developed [17]. For the clinical routine, approaches based on catheterization, including the index of microvascular resistance (IMR, a measure of microvascular function), and the fractional flow reserve (FFR, a measure of the epicardial component) have been introduced and used under different conditions [13].

The no-reflow phenomenon is a type of coronary microvascular dysfunction (CMD) occurring with an acute myocardial infarction [5]. The pathogenetic mechanisms of CMD include *structural*: luminal obstruction, vascular wall infiltration, perivascular fibrosis, *functional*: endothelial dysfunction, dysfunction of smooth-muscle cell, autonomic dysfunction *extravascular*: extramural compression. Research

aiming at a better understanding of the pathogenesis of CMD and the development of therapeutic principles is necessarily based on the knowledge of the physiological principles governing microvascular control of myocardial perfusion in healthy subjects.

A condition which is related to CMD is the observation of angina symptoms in patients with normal results in a coronary angiogram, often called coronary syndrome X [4,12]. Recent analyses have shown that this condition may have a significant negative influence on prognosis for cardiac events. This condition is specifically prevalent in women [21].

CMD is also linked to non cardiac diseases with well known microvascular implications. For example, diabetes mellitus (DM) strongly affects the microvascular system (arterioles, capillaries, venules). Also, the viscosity of the blood is increased in hyperglycemia, with concomitant increase in resistance of the microvasculature, leading to stasis and thrombosis of capillaries. Coronary heart disease events and mortality are greater in patients with DM.

5.2 The Lung

Airflow is delivered to the lungs through bronchi, into bronchioles and then into alveoli where the oxygen and carbon dioxide exchange takes place with the pulmonary capillaries. A mean number of 480 million alveoli with a mean diameter of 200 μm are found in human lungs [16]. The adequacy of gas exchange in the lungs is determined by the balance between pulmonary ventilation and capillary blood flow [3,7,11]. This balance is commonly expressed as the ventilation–perfusion (V/Q) ratio. A perfect match between ventilation and perfusion ($V/Q = 1$), which corresponds to normal arterial oxygenation, is the reference point for defining the abnormal patterns of gas exchange [1].

A V/Q ratio above 1.0 describes the condition where ventilation is excessive relative to capillary blood flow, with resultant hypoxemia and hypercapnia. The excess ventilation, known as *dead space ventilation*, does not participate in gas exchange with the blood [2]. Dead space ventilation increases when the alveolar–capillary interface architecture is destroyed such as in emphysema (Figs. 5.4 and 5.5)

A V/Q ratio below 1.0 describes the condition where capillary blood flow is excessive relative to ventilation. The excess blood flow, known as *intrapulmonary shunt,* does not participate in pulmonary gas exchange, with resultant also hypoxemia and hypercapnia [1]. The fraction of the cardiac output that represents intrapulmonary shunt is known as the *shunt fraction* [7,11,2]. Intrapulmonary shunt fraction increases when small airways are occluded, such as in asthma, when alveoli are filled with fluid, such as in acute respiratory distress syndrome (ARDS) (Figs. 5.6 and 5.7). The main functional mechanism to combat perfusion ventilation mismatch is the so-called hypoxic pulmonary vasoconstriction (HPV) [19], which leads vasoconstriction of arteriolar vessels supplying regions with low

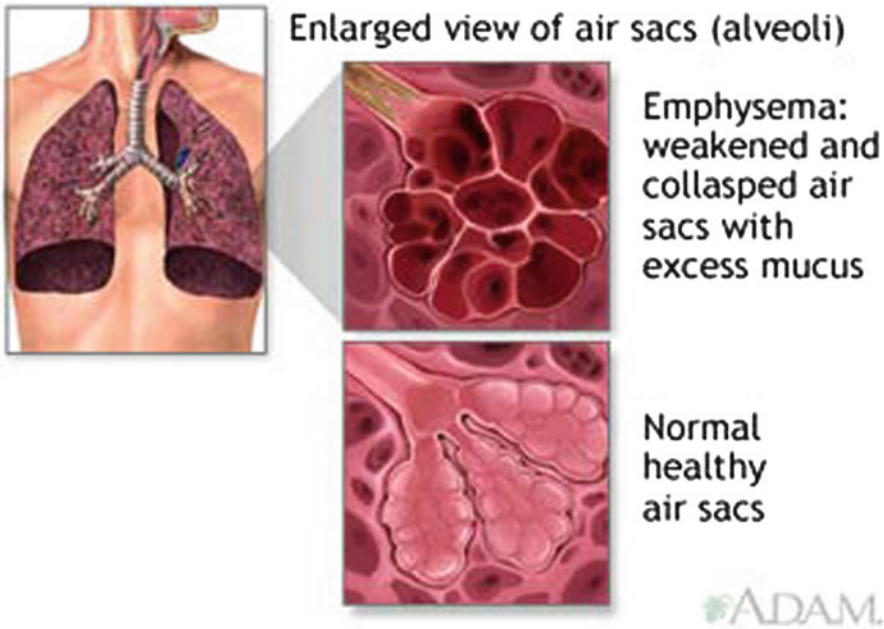

Fig. 5.4 Schematic of normal and emphysematous alveoli

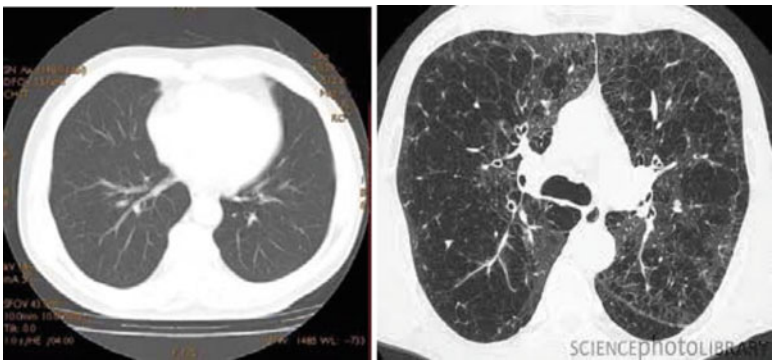

Fig. 5.5 *Left*: CT scan of lung with normal parenchyma. *Right*: CT scan of lung with emphysema

ventilation. Thus, local perfusion is matched to local ventilation. The assessment of such mechanisms and their relation to the microvascular flow properties in the living lung are still very difficult. However, major advances with respect to experimental approaches have been made [9,20] suggesting that the amount of information about pulmonary micro-flows and their clinical application will increase substantially in the near future.

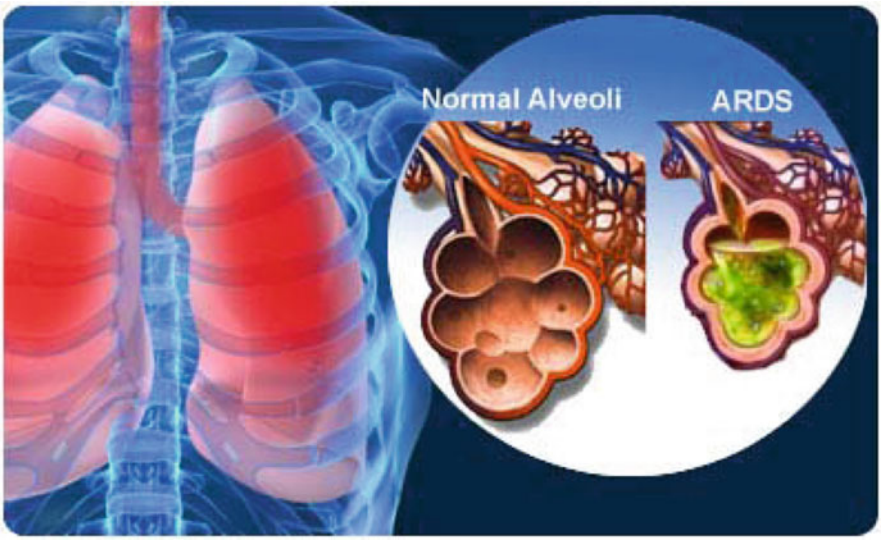

Fig. 5.6 Schematic of normal alveoli and ones filled with fluid due to ARDS

Fig. 5.7 *Left*: CT scan of lung with normal parenchyma. *Right*: CT scan of lung with fluid filled alveoli due to ARDS

References

1. Marino PL (2007) Hypoxemia and hypercapnia. In: Marino PL (ed) The ICU book. Lippincott Williams & Wilkins, Philadelphia, PA, pp 367–383
2. D'Alonzo GE, Dantzger DR (1983) Mechanisms of abnormal gas exchange. Med Clin North Am 67:557–571
3. Buohuys A (1964) Respiratory dead space. In: Fenn W, Rahn H (eds) Handbook of physiology: respiration. American Physiological Society, Bethesda, MD, pp 699–714

4. Bugiardini R, Badimon L, Collins P, Erbel R, Fox K, Hamm C, Pinto F, Rosengren A, Stefanadis C, Wallentin L, Van de WF (2007) Angina, "normal" coronary angiography, and vascular dysfunction: risk assessment strategies. PLoS Med 4:e12
5. Camici PG, Crea F (2007) Coronary microvascular dysfunction. N Engl J Med 356:830–840
6. Chien S, Usami S, Skalak R (1984) Blood flow in small tubes. In: Renkin EM, Michel CC (eds) Handbook of physiology, section 2: the cardiovascular system, vol IV, The microcirculation. American Physiological Society, Bethesda, MD, pp 217–249
7. Dantzger DR (1991) Pulmonary gas exchange. In: Dantzger DR (ed) Cardiopulmonary critical care, 2nd edn. WB Saunders, Philadelphia, PA, pp 25–43
8. Jaffe R, Dick A, Strauss BH (2010) Prevention and treatment of microvascular obstruction-related myocardial injury and coronary no-reflow following percutaneous coronary intervention: a systematic approach. JACC Cardiovasc Interv 3:695–704
9. Kuebler WM (2011) Real-time imaging assessment of pulmonary vascular responses. Proc Am Thorac Soc 8:458–465
10. Katritsis D, Choi MJ, Webb-Peploe MM (1991) Assessment of the hemodynamic significance of coronary artery stenosis: theoretical considerations and clinical measurements. Prog Cardiovasc Dis 34(1):69–88
11. Lanken PN (1995) Ventilation–perfusion relationship. In: Grippi MA (ed) Pulmonary pathophysiology. JB Lippincott, Philadelphia, PA, pp 195–210
12. Melikian N, de BB, Fearon WF, MacCarthy PA (2008) The pathophysiology and clinical course of the normal coronary angina syndrome (cardiac syndrome X). Prog Cardiovasc Dis 50:294–310
13. Melikian N, Vercauteren S, Fearon WF, Cuisset T, MacCarthy PA, Davidavicius G, Aarnoudse W, Bartunek J, Vanderheyden M, Wyffels E, Wijns W, Heyndrickx GR, Pijls NH, de BB (2010) Quantitative assessment of coronary microvascular function in patients with and without epicardial atherosclerosis. EuroIntervention 5:939–945
14. Niccoli G, Burzotta F, Galiuto L, Crea F (2009) Myocardial no-reflow in humans. J Am Coll Cardiol 54:281–292
15. Niccoli G, Kharbanda RK, Crea F, Banning AP (2010) No-reflow: again prevention is better than treatment. Eur Heart J 31:2449–2455
16. Ochs M, Nyengaard JR, Jung A, Knudsen L, Voigt M, Wahlers T, Richter J, Gundersen HJG (2004) The number of alveoli in the human lung. Am J Respir Crit Care Med 169:120–124
17. Pries AR, Habazettl H, Ambrosio G, Hansen PR, Kaski JC, Schachinger V, Tillmanns H, Vassalli G, Tritto I, Weis M, de WC, Bugiardini R (2008) A review of methods for assessment of coronary microvascular disease in both clinical and experimental settings. Cardiovasc Res 80:165–174
18. Rezkalla SH, Dharmashankar KC, Abdalrahman IB, Kloner RA (2010) No-reflow phenomenon following percutaneous coronary intervention for acute myocardial infarction: incidence, outcome, and effect of pharmacologic therapy. J Interv Cardiol 23:429–436
19. Sylvester JT, Shimoda LA, Aaronson PI, Ward JP (2012) Hypoxic pulmonary vasoconstriction. Physiol Rev 92:367–520
20. Tabuchi A, Mertens M, Kuppe H, Pries AR, Kuebler WM (2008) Intravital microscopy of the murine pulmonary microcirculation. J Appl Physiol 104:338–346
21. Vaccarino V, Badimon L, Corti R, de WC, Dorobantu M, Hall A, Koller A, Marzilli M, Pries A, Bugiardini R (2011) Ischaemic heart disease in women: are there sex differences in pathophysiology and risk factors? Position paper from the working group on coronary pathophysiology and microcirculation of the European Society of Cardiology. Cardiovasc Res 90:9–17
22. Vinten-Johansen J, Zhao ZQ, Guyton RA (2003) Cardiac surgical physiology. In: Cohn LH, Edmunds LH Jr (eds) Cardiac surgery in the adult. McGraw-Hill, New York, pp 53–84

Chapter 6
Regulation of Endothelial Activation and Vascular Inflammation by Shear Stress

Annapurna Nayak, Carola S. König, Uday Kishore, and Paul C. Evans

Abstract Atherosclerosis is a multifactorial disorder caused by genetic and environmental factors such as cholesterol, obesity, hypertension, diabetes, and smoking and is the primary cause of morbidity and mortality worldwide. Blood flow is known to exert shear stress on the vascular endothelium. Atherosclerotic lesions occur predominantly at sites of low shear, whereas regions of the vasculature exposed to high shear are protected. Low shear stress leads to activation of endothelial cells which in turn can initiate inflammation. Shear stress can also modulate several signalling pathways mediated by the activated endothelial cells. The molecules involved in these signalling pathways can be atheroprotective or atherogenic. The aim of this chapter is to discuss the effects of low shear stress on the regulation of endothelial activation and subsequent vascular inflammation.

A. Nayak
Centre for Infection, Immunity and Disease Mechanisms, Biosciences, School of Health Sciences and Social Care, Brunel University, London, UK

Centre for Biotechnology and Bioinformatics, School of Life Sciences, Jawaharlal Nehru Institute for Advanced Studies, Secunderabad, Andhra Pradesh, India

C.S. König
Brunel Institute for Bioengineering, Brunel University, London, UK

U. Kishore
Centre for Infection, Immunity and Disease Mechanisms, Biosciences, School of Health Sciences and Social Care, Brunel University, London, UK

P.C. Evans (✉)
Department of Cardiovascular Science, Sheffield University Medical School, Sheffield University, Sheffield, UK
e-mail: Paul.Evans@sheffield.co.uk

M.W. Collins and C.S. König (eds.), *Micro and Nano Flow Systems for Bioanalysis*, Bioanalysis 2, DOI 10.1007/978-1-4614-4376-6_6,

Abbreviations

MKP-1	Mitogen activated protein kinase phosphatase 1
KLF2	Kruppel like factor 2
Nrf2	Nuclear factor erythroid 2-related factor 2
VCAM-1	Vascular cell adhesion molecule-1
PECAM-1	Platelet-endothelial cell adhesion molecule-1
ICAM-1	Intracellular cell adhesion molecule-1
MCP-1	Monocyte chemoattractant protein 1
JNK	c-Jun N-terminal kinase
ATF2	Activating transcription factor 2
NF-κB	Nuclear factor κ-light-chain-enhancer of activated B cells
NOS	Nitric oxide

6.1 Introduction

Inflammation of vascular tissues is induced in response to harmful stimuli such as chemicals, pathogens or injury. Vascular inflammation involves the recruitment of leukocytes, also known as white blood cells (monocytes, macrophages, dendritic cells, neutrophils, and lymphocytes) to the site of injury. The vascular system is lined with a monolayer of endothelial cells termed as the endothelium. This monolayer of cells performs various functions such as acting as a mechanical barrier and an anticoagulant, maintaining an anti-inflammatory environment, facilitating physiological control of vasoregulation, and modulating vascular permeability. Endothelial infiltration by circulating leukocytes is comprised of a multistep process that involves rolling of the leukocytes on the endothelium, attachment of the leukocytes to the endothelium, and transmigration of the leukocytes across the endothelial cells lining the blood vessel walls [1]. These processes are mediated by several different receptors called selectins, addressins, and integrins on the leukocytes and their subsequent interaction with adhesion molecules expressed on the surface of the endothelial cells. The adhesion molecules on endothelial cells include E-selectin, intracellular cell adhesion molecule-1 ICAM-1 (CD54), and vascular cell adhesion molecule-1 VCAM-1 [2,4].

The location of endothelial cells within the vascular endothelium is such that they are constantly exposed to mechanical forces such as pressure, circumferential stretch or tension and shear stress. Shear stress is a biomechanical quantity that is determined by factors such as blood flow velocity, vessel geometry and local fluid viscosity. Shear stress may be computationally estimated using fluid dynamics models. The numerical calculation of wall shear stress has been the topic of numerous studies, both in relation to larger scale flow features such as flow detachment and recirculation zones (e.g., [26]) as well as on significantly smaller scales (e.g., [24]). Particularly the study of the role of nitric oxide and the development of atherosclerotic plaque has been well studied in the past (e.g., [23]).

In a biomedical context shear stress is typically expressed in units of dynes/cm^2. Physiological arterial-level shear stress is variable, due to anatomical variation and pulsatility, but is approximately >15 dynes/cm^2 [18]. The magnitude of the shear stress may also be estimated in most of the vasculature by Poiseuille's law which states that shear stress is proportional to blood flow viscosity, and inversely proportional to the third power of the internal radius [13]. A change in the physiological amount of shear stress has been implicated in the pathogenesis of cardiovascular diseases. As pointed out by Cunningham and Gotlieb, three aspects of the way in which shear stress affects the endothelial surface can be distinguished. First, *laminar flow* gives the straightforward steady Poiseuille's flow effect (averaged over the physiological pulsatory cycle). Second, *oscillatory flow,* expresses cycle-to-cycle variations, which are normally zero or very low. Third, there are local regions of disrupted flow comprising separation, recirculation and reattachment [9]. Indeed in a combined numerical and in vitro study it was demonstrated that oscillatory low shear stress present in recirculation zones can lead to a significant activation of endothelial cells by enhancing ICAM-1 expression [34].

Shear stress, or rather, lower levels of shear stress have long been associated with the development of atherosclerosis. Atherosclerosis is a multifactorial disorder caused by genetic and environmental factors such as cholesterol, obesity, hypertension, diabetes, and smoking. It is the primary cause of morbidity and mortality worldwide. The pathogenesis of atherosclerosis involves biochemical and biomechanical changes in the arterial walls. Atherosclerosis is a chronic inflammatory disease that involves complex interactions between various modified lipoproteins, monocyte-derived macrophages, T lymphocytes, endothelial cells, and smooth muscle cells [25]. Atherosclerotic lesions occur predominantly in areas such as inner curvatures of the coronary arteries where there is lower shear stress compared to the average physiological shear stress levels and also in areas that demonstrate bifurcations where the shear stress is oscillatory [6,22].

At physiological levels of shear stress, the endothelial cells elongate and orient themselves parallel to the direction of the flow [17]. However, at lower levels of shear stress, the endothelial cells are found to being more rounded in shape [17]. Interestingly, such a rounded endothelial cell morphology has been observed in atherosclerotic lesions, and this is consistent with the finding that atherosclerosis develops at branches and bends that are exposed to lower levels of shear stress [6,22].

6.2 Signalling Pathways Involved in Shear Stress Mediated Endothelial Activation and Inflammation

Dysfunction of endothelial cells has been believed to be one of the main factors in initiating the pathogenesis of atherosclerosis [25]. This dysfunction in turn can lead to changes in gene expression by the endothelial cells. Various signalling pathways have been implicated in being upregulated or downregulated following endothelial

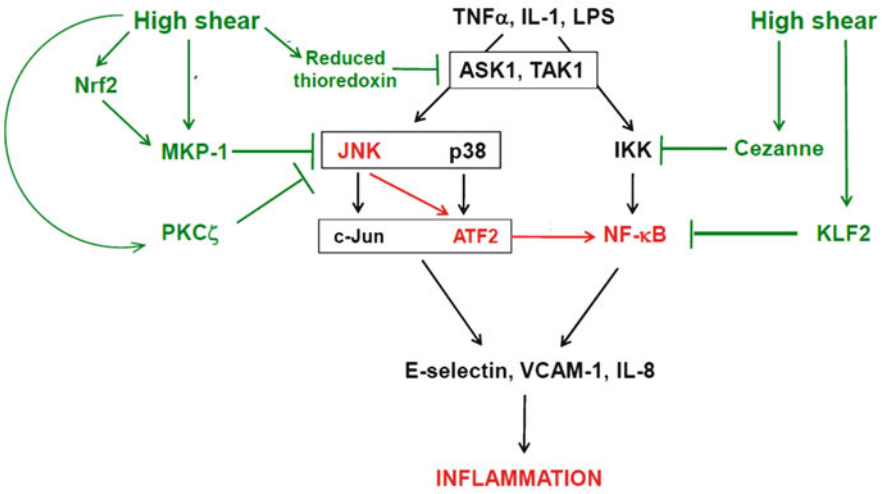

Fig. 6.1 Illustration of various signalling pathways that are involved in the pathogenesis of atherosclerosis due to differential levels of shear stress. High, laminar shear is atheroprotective and induces expression of anti-inflammatory factors such as MKP-1, Nrf2, Cezanne, and KLF2. The expression of these anti-inflammatory factors can down regulate the activation of inflammatory pathways. Low, oscillatory shear stress on the other hand induces the JNK-ATF2 –NF-KB pathway that in turn leads to recruitment of inflammatory leukocytes modulated by the expression of E-selectin and VCAM-1

activation by lower levels of shear stress. Upregulation of pro-inflammatory signalling molecules such as JNK, p38, and NF-κB are implicated in the pathogenesis of atherosclerosis whilst upregulation of Nrf2, KLF2, and MKP-1 and activation of eNOS is more atheroprotective. The inflammatory mechanisms that are involved in atherosclerosis and modulated by shear stress are hence explained in detail (Fig. 6.1).

6.2.1 Mitogen Activated Protein Kinase Phosphatase 1

Mitogen activated protein kinase phosphatase 1 (MKP-1) belongs to the family of dual specificity protein phosphatases that are ubiquitously located within the body and is upregulated by various extracellular stimuli [29]. This early gene is upregulated in vascular and nonvascular cells by an array of factors that include heat shock [14], oxidative stress [14], pro-inflammatory cytokines such as tumor necrosis factor-α (TNF-α) [31], lipopolysaccharides (LPS) from bacteria [28], peptide ligands such as thrombin [5], and growth factors such as vascular endothelial growth factors [15]. A primary function of MKP-1 is to inactivate the mitogen activated protein kinase (MAPK) by dephosphorylation of p38 and JNK at specific tyrosine and threonine residues. Shear stress controls the expression of MKP-1 by

endothelial cells. For instance, MKP-1 is over expressed in regions of vascular endothelium subject to laminar unidirectional high shear stress. These regions are termed atheroprotective regions as they do not exhibit any signs of developing atherosclerosis. The consequence of MKP-1 expression by these endothelial cells is that it negatively regulates the JNK and p38 pathways and thus hampers inflammation [36]. On the other hand, it also suppresses VCAM-1 expression [36] which promotes the recruitment of leukocytes to the vessel walls. Thus, high shear stress can prove to be atheroprotective in that it protects arteries from induction of persistent endothelial expression of MKP-1, which in turn, suppresses the activities of p38 and JNK [36]. Prior studies revealed that MKP-1 exerts anti-inflammatory effects in EC by inhibiting the expression of adhesion molecules and chemokines [5,31,36]. MKP-1 also suppresses the activation of macrophages and their capacity to produce the pro-atherogenic cytokine TNFα [7]. In addition, MKP-1 can be induced by low density lipoprotein (LDL) [19] and cyclic strain in smooth muscle cells [16] and reduces their proliferation. Thus, MKP-1 may exert anti-atherogenic effects in vascular endothelium by suppressing EC activation and also influence lesion development by regulating macrophage physiology and smooth muscle cell accumulation. Hence more research has to be carried out with respect to MKP-1 expression in regions that are susceptible to low, oscillatory shear stress and exploitation of this expression to yield therapeutic benefits.

6.2.2 Nuclear Factor Erythroid 2-Related Factor 2

Nuclear factor erythroid 2-related factor 2 (Nrf2) is a member of the "cap 'n' collar" family of basic leucine zipper transcription factors that is important in protecting cells against oxidative damage by reactive oxygen species (ROS) [3]. Nrf2 plays an important role in the protection of endothelial cells via antioxidant response element (ARE)-mediated gene expression of phase II detoxification antioxidant proteins. Both types of shear stress, laminar and oscillatory, have shown to increase the expression of Nrf2. However, stabilization of Nrf2 and expression of genes modulated by Nrf2 is only induced by laminar shear stress. In studies on human umbilical vein endothelial cells (HUVEC), induction of Nrf-2 regulated genes such as heme oxygenase 1, NAD(P)H quinone oxidoreductase1, glutamate-cysteine ligase modifier subunit, and ferritin heavy chain is carried out by laminar shear stress [32,33]. The regulation of these genes is inhibited when treated with Nrf2 siRNA. Laminar shear stress has been observed to induce gene expression of cytoprotective enzymes for glutathione biosynthesis and detoxification which are regulated by Nrf2. Laminar shear stress might activate Nrf2 via a phosphoinositol 3-kinase/Akt-dependent signalling pathway [10].

Following activation by laminar shear stress, Nrf2 acts in an anti-inflammatory manner similar to that of MKP-1. Nrf2 is constitutively active in endothelial cells in atheroprotected regions and has been observed to reduce the proinflammatory activities of p38 MAP kinase by inactivating it [35]. Nrf2 also suppresses the

VCAM-1 expression. The other manner in which Nrf2 controls endothelial activation is by reducing MKK3/6 signaling to p38 and by enhancing the activity of MKP-1. The mechanism behind the MKK3/6 suppression by Nrf2 is likely to involve redox regulation too because ASK1, a MAP kinase that acts upstream from MKK3/6, is known to be inhibited by reduced forms of glutathione and thioredoxin [35]. Further evidence suggests that Nrf2 can enhance the catalytic activity of MKP-1 by promoting a reducing environment via the induction of multiple antioxidants. Thus, it is proposed that laminar shear stress suppresses endothelial cell activation at atheroprotected sites by inducing MKP-1 and by simultaneously enhancing MKP-1 activity via activation of Nrf2 [35].

Interestingly, in regions of low shear stress that are more susceptible to atherosclerosis, Nrf2 seems to be expressed in a nonactive form and is incapable of suppressing the pro-inflammatory milieu that follows the formation of atherogenic lesions [35]. In addition to these observations, HUVEC challenged with laminar shear stress and simultaneously treated with Nrf2 siRNA (that will interefere with the expression of biologically active Nrf2) showed an upregulation of expression of adhesion molecules and chemokines (Takabe et al. 2011). In the same study, arterial endothelial cells isolated from Nrf2 deficient mice also demonstrated a similar result. The collective observation from the above studies suggest that Nrf2 might be an important therapeutic candidate to suppress inflammation in the vascular endothelium, as it can inhibit expression of adhesion molecules and recruitment of chemokines.

6.2.3 *Kruppel-like Factor*

Kruppel-like factor (KLF2) is an endothelial transcription factor, the expression of which is specifically induced by laminar shear stress [21]. It is an anti-inflammatory transcription factor that aids in maintaining the atheroprotective phenotype of vascular endothelial cells. KLF2 induces the expression of atheroprotective endothelial nitric oxide (eNOS) and thrombomodulin whilst downregulating the expression of pro-atherogenic MCP-1 and endothelin [11]. KLF2 also inhibits the expression of VCAM-1 and E-selectin, and thus, it suppresses the initiation of the inflammatory cascade that precedes the rolling and adhesion of inflammatory cells [27].

6.2.4 *JNK-NF-κB Pathway*

The nuclear factor κ-light-chain-enhancer of activated B cells (NF-κB) family of transcription factors regulates vascular inflammation by inducing adhesion proteins and other proinflammatory molecules in vascular endothelial cells [30]. There are five different subunit forms of NF-κB and the RelA/p50 heterodimer is the most

abundant form of NF-κB found in vascular endothelial cells. RelA expression is preferentially found in athero-susceptible regions of the arteries [8]. The low, oscillatory shear stress that is exerted in these regions initiate the signalling pathway that induces the expression of RelA [8]. Murine studies that involved the exposure of vascular endothelial cells to low levels of shear stress exhibited an enhanced activation of the mitogen activated protein kinase JNK1 and a downstream transcription factor ATF2 [8]. Simultaneously, the expression of RelA was also observed to be increased in the vascular endothelium. However, when JNK1 was genetically abrogated, activation of ATF2 was hindered and RelA expression was also reduced in the murine vascular endothelium. These observations indicated that low, oscillatory shear stress influences ATF2 and RelA activity through a JNK1-dependent mechanism [8]. The important roles JNK isoforms play in cardiovascular injury and disease have been demonstrated previously. This is supported by animal studies that have revealed that JNK can be activated in arteries in response to injury, during the development of aneurysms or in atherosclerotic lesions [37]. Other studies also report that the gene transfer of a dominant negative form of JNK1 reduced neointimal formation in injured arteries [12] and genetic deletion of JNK2 reduced foam cell formation and EC dysfunction in hypercholesterolemia [20].

Thus, the JNK-ATF2-NK-κB signalling pathway might be a key role in promoting inflammation in the vascular endothelium during atherosclerosis influenced by low, oscillatory shear stress.

6.3 Conclusion

Laminar shear stress is vital in maintaining vascular homeostasis and preventing atherosclerosis. Low, oscillatory shear stress can activate vascular endothelial cells through different inflammatory mechanisms. This activation can lead to recruitment of leukocytes that can lead to the development of atherogenic lesions. By comparing and contrasting the gene expression of various molecules in regions of laminar shear stress and oscillatory shear stress, the relationship between blood flow and development of atherogenesis can be understood more clearly. The conclusion from these studies are that high, laminar shear stress is atheroprotective and does not activate endothelial cells whereas low, oscillatory shear stress is pro-atherogenic and can initiate the activation of vascular endothelial cells, thus leading to inflammation seen in the pathogenesis of atherosclerosis. Therefore, the control of shear stress can be of potential therapeutic interest in the treatment of atherosclerosis and other diseases where fluctuations of shear stress can play a role in the pathogenesis.

References

1. Abbas AB, Lichtman AH (2009) Basic immunology. Elsevier, Philadelphia, PA
2. Alon R, Kassner PD, Carr MW, Finger EB, Hemler ME, Springer TA (1995) The integrin VLA-4 supports tethering and rolling in flow on VCAM-1. J Cell Biol 128:1243–1253
3. Andrews NC, Erdjument-Bromage H, Davidson MB, Tempst P, Orkin SH (1993) Erythroid transcription factor NF-E2 is a haematopoietic-specific basic-leucine zipper protein. Nature 362:722–728
4. Campbell JJ, Qin S, Bacon KB, Mackay CR, Butcher EC (1996) Biology of chemokine and classical chemoattractant receptors: differential requirements for adhesion-triggering versus chemotactic responses in lymphoid cells. J Cell Biol 134:255–266
5. Chandrasekharan UM, Yang L, Walters A, Howe P, DiCorleto PE (2004) Role of CL-100, a dual specificity phosphatase, in thrombin-induced endothelial cell activation. J Biol Chem 279:46678–46685
6. Cheng C et al (2006) Atherosclerotic lesion size and vulnerability are determined by patterns of fluid shear stress. Circulation 113(23):2744–2753
7. Chi HB et al (2006) Dynamic regulation of pro- and anti-inflammatory cytokines by MAPK phosphatase 1 (MKP-1) in innate immune responses. Proc Natl Acad Sci U S A 103:2274–2279
8. Cuhlmann S et al (2011) Disturbed blood flow induces RelA expression via c-Jun N-terminal kinase 1: a novel mode of NF-κB regulation that promotes arterial inflammation. Circ Res 108:950–959
9. Cunningham KS, Gotlieb AI (2005) The role of shear stress in the pathogenesis of atherosclerosis. Lab Invest 85(1):9–23
10. Dai G, Vaughn S, Zhang Y, Wang ET, Garcia-Cardena G, Gimbrone MA Jr (2007) Biomechanical forces in atherosclerosis-resistant vascular regions regulate endothelial redox balance via phosphoinositol 3-kinase/Akt-dependent activation of Nrf2. Circ Res 101:723–733
11. Dekker RJ et al (2005) Endothelial KLF2 links local arterial shear stress levels to the expression of vascular tone-regulating genes. Am J Pathol 167:609–618
12. Izumi Y et al (2001) Gene transfer of dominant-negative mutants of extracellular signal-regulated kinase and c-Jun NH2-terminal kinase prevents neointimal formation in balloon-injured rat artery. Circ Res 88:1120–1126
13. Kamiya A, Bukhari R, Togawa T (1984) Adaptive regulation of wall shear stress optimizing vascular tree function. Bull Math Biol 46:127–137
14. Keyse SM, Emslie EA (1992) Oxidative stress and heat shock induce a human gene encoding a protein-tyrosine phosphatase. Nature 359:644–647
15. Kinney CM, Chandrasekharan UM, Mavrakis L, DiCorleto PE (2008) VEGF and thrombin induce MKP-1 through distinct signaling pathways: role for MKP-1 in endothelial cell migration. Am J Physiol Cell Physiol 294:C241–C250
16. Lai KH, Wang H, Lee WS, Jain MK, Lee ME, Haber E (1996) Mitogen-activated protein kinase phosphatase-1 in rat arterial smooth muscle cell proliferation. J Clin Invest 98:1560–1567
17. Levesque MJ, Nerem RM (1985) The elongation and orientation of cultured endothelial cells in response to shear stress. J Biomech Eng 107:341–347
18. Malek AM, Alper SL, Izumo S (1999) Hemodynamic shear stress and its role in atherosclerosis. JAMA 21(282):2035–2042
19. Metzler B, Li CH, Hu YH, Sturm G, Ghaffari-Tabrizi N, Xu QB (1999) LDL stimulates mitogen-activated protein kinase phosphatase-1 expression, independent of LDL receptors, in vascular smooth muscle cells. Arterioscler Thromb Vasc Biol 19:1862–1871
20. Osto E et al (2008) c-Jun N-terminal kinase 2 deficiency protects against hypercholesterolemia-induced endothelial dysfunction and oxidative stress. Circulation 118:2073–2080

21. Parmar KM et al (2006) Integration of flow-dependent endothelial phenotypes by Kruppel-like factor 2. J Clin Invest 116:49–58
22. Pedersen EM et al (1999) Distribution of early atherosclerotic lesions in the human abdominal aorta correlates with wall shear stresses measured in vivo. Eur J Vasc Endovasc Surg 18:328–333
23. Plank MJ, Wall DJN, David T (2007) The role of endothelial calcium and nitric oxide in the localisation of atherosclerosis. Math Biosci 207:26–39
24. Pontrelli G et al (2011) Modelling wall shear stress in small arteries using the Lattice Boltzmann method: influence of the endothelial wall profile. Med Eng Phys 33:832–839
25. Ross R (1999) Atherosclerosis—an inflammatory disease. N Engl J Med 340(2):115–126
26. Shanmugavelayudam SK, Rubenstein DA, Yin W (2010) Effect of geometrical assumptions on numerical modeling of coronary blood flow under normal and disease conditions. J Biomech Eng 132:061004
27. SenBanerjee S et al (2004) KLF2 Is a novel transcriptional regulator of endothelial proinflammatory activation. J Exp Med 199:1305–1315
28. Stawowy P, Goetze S, Margeta C, Fleck E, Graf K (2003) LPS regulate ERK1/2-dependent signaling in cardiac fibroblasts via PKC-mediated MKP-1 induction. Biochem Biophys Res Commun 303:74–80
29. Sun H, Charles CH, Lau LF, Tonks NF (1993) MKP-1 (3CH134), an immediate early gene product, is a dual specificity phosphatase that dephosphorylates MAP kinase in vivo. Cell 75:487–493
30. Van der Heiden K, Cuhlmann S, Luong LA, Zakkar M, Evans PC (2010) Role of nuclear factor kappaB in cardiovascular health and disease. Clin Sci (Lond) 118:593–605
31. Wadgaonkar R et al (2004) Regulation of c-Jun N-terminal kinase and p38 kinase pathways in endothelial cells. Am J Respir Cell Mol Biol 31:423–431
32. Warabi E et al (2004) Effect on endothelial cell gene expression of shear stress, oxygen concentration, and low-density lipoprotein as studied by a novel flow cell culture system. Free Radic Biol Med 37:682–694
33. Warabi E et al (2007) Shear stress stabilizes NF-E2-related factor 2 and induces antioxidant genes in endothelial cells: role of reactive oxygen/nitrogen species. Free Radic Biol Med 42:260–269
34. Yin W, Shanmugavelayudam SK, Rubenstein DA (2009) 3D numerical simulation of coronary blood flow and its effect on endothelial cell activation. Conf Proc IEEE Eng Med Biol Soc 2009:4003–4006
35. Zakkar M et al (2009) Activation of Nrf2 in endothelial cells protects arteries from exhibiting a proinflammatory state. Arterioscler Thromb Vasc Biol 29:1851–1857
36. Zakkar M et al (2008) Increased endothelial mitogen-activated protein kinase phosphatase-1 expression suppresses proinflammatory activation at sites that are resistant to atherosclerosis. Circ Res 103:726–732
37. Zou YP, Qi Y, Roztocil E, Nicholl SM, Davies MG (2007) Patterns of kinase activation induced by injury in the murine femoral artery. J Surg Res 142:332–334

Chapter 7
Digital Optical and Scanning Probe Microscopy for Inspection and Manipulation of Biocells

Sergei Chizhik, Lizaveta Drozd, and Nikita Fomin

Abstract As biomedical interest has progressed to the study of biological tissues and single cells investigations of the different biomaterials involved require very careful use of fine-scale measurement methods, Atomic Force Microscopy (AFM) and Dynamic Laser Speckle (DLS) being reported here. AFM and DLS are complex experimental systems with the functions of scanning probe and optical microscopy. A special optical system makes it possible to visualize the objects and position the probe within microscale dimensions. AFM is used both for visualization and identification of the local adhesion and viscoelastic properties of biological cells, and for manipulation of the cell by means of varying the load being applied to it. Additional information about cellular activity could be obtained by laser probing via DLS of the living tissues being studied. These techniques, AFM and DLS, greatly enhance the potential for measurements and open a new field of experiments in cell biology. The purpose of this chapter is to show the application of AFM and DLS to studies of biological cells, namely measurement of the motility of general cells in living tissues and the elastic modulus of a single cell membrane, as well as identifying the forces causing membrane damage. The time-space cross-correlation analysis of the temporal evaluation of the dynamic biospeckle patterns is shown to be a means of real time flow visualization of the microcirculation of blood in living tissue. Digital processing of biospeckle pattern records yields 2D maps exhibiting the temporal and spatial variations in subskin blood flow. This could be used for biomedical diagnostic purposes, e.g., for detecting microscale deviations from the normal case. Three methods of evaluating dynamic speckle patterns are described. Both decorrelation and autocorrelation analyses have been realized in real time mode, when a total digital specklegram treatment was performed during the time interval between successive frames (40 ms). Results in the form of 2D maps of subskin blood flux were visualized on the PC monitor with a frequency of 25 Hz.

S. Chizhik • L. Drozd (✉) • N. Fomin
A.V. Likov Heat and Mass Transfer, Institute of National Academy of Sciences of Belarus,
P. Brovki Str. 15, Minsk 220072, Belarus
e-mail: drozd.elizaveta@gmail.com

M.W. Collins and C.S. König (eds.), *Micro and Nano Flow Systems for Bioanalysis*, Bioanalysis 2, DOI 10.1007/978-1-4614-4376-6_7,

7.1 Introduction

Nanobiotechnology and scanning probe microscopy (SPM) are new fields that are of considerable interest to modern medical science. Currently Atomic Force Microscopy (AFM) is widely used in medical and biological research using all varieties of Scanning Probe Microscopy (SPM) [1]. Even without special methods of preparation AFM gives an opportunity to investigate the morphology of the surface of different biological objects with nanoresolution. Also this method allows the analysis of the physical and mechanical properties at micro- and nanoscales. It is one of the instruments that enable spatial images of the surface to be realized with a resolution close to a single atom. AFM has several advantages over optical and scanning electron microscopes. First of all, it allows the receipt of a three-dimensional relief of the sample. And by using AFM a conducting surface is not necessary. Furthermore, the measurements can be made not only in vacuo but also in an atmosphere of air or any other gas, and moreover, even in liquid. For this reason AFM gives wide possibilities for the investigation of organic molecules and living cells [2]. As shown by Burnham and Colton [3], Ueda et al. [4], Ikai and Afrin [5], AFM is currently successfully being used to estimate the local elastic and adhesive properties of the surface.

Additional information about cellular activity in living tissues may be obtained by DLS laser probing. Laser monitoring of living tissue has been widely discussed since the inception of lasers [6]. Coherent light scattered from any diffuse object produces a random granular interference structure some distance away from the object. This structure is called a speckle pattern. Such a pattern can also be observed when a living semi-transparent tissue is illuminated by a laser light. The visible laser light penetrates into the human skin to a depth of about 200–1,000 μm and is multiply scattered by the erythrocytes flowing inside the smallest candelabra capillaries as well as by surrounding tissue. So, an image of the tissue illuminated with laser light differs from an image taken under white light conditions by the speckle pattern that is superimposed on the surface features of the tissue. As the scatterers (erythrocytes) move, the speckles also move and change their shape. The dynamic (time-dependent) biospeckle pattern is formed as a superposition of some moving speckles with different dynamics, including static speckles. These biospeckles play a dual role: as a source of noise in tissue images and as a carrier of useful information about biological or physiological activity of living tissues. The latter include subskin blood flow and general tissue-structure motility, see, e.g., Fercher and Briers [7], Asakura and Takai [8], Briers [9, 10], Okamoto [11], Aizu and Asakura [12].

Modern DLS technique based on computer-aided acquisition and evaluation of dynamic biospeckle patterns extends the methods of cell monitoring, and it allows the derivation of a two-dimensional map of subskin erythrocyte motility in living tissues via statistical analysis of the recorded speckle pattern [13–16].

7.2 Single Biocell Test

Methods for using AFM to study biological objects can be divided into two main groups respectively dealing with high-resolution visualization and evaluation of local mechanical properties (elasticity). A new direction of study is developing in cytology, which investigates "cell nanomechanics."

7.2.1 Cellular Elastography

Elastography is a method of measuring the elastic properties of biological soft tissues [17–21]. Today elastography is widely used in the form of ultrasonic, optical, and magnetic resonance methods, which allow the access and analysis of the information about the mechanical properties of tissues and organs The evaluation of these properties may be applied widely, including in oncology (the detection of size and shape of tumors), in neurology, in traumatology, in transplantology, in dermatology, in anesthesiology, and in sports medicine [22–24]. Moreover, pathophysiological changes in the mechanical properties of the tissues may show up at single cell level, and thanks to AFM this problem can be addressed. Assessment of structural features of the cell surface and the local elastic modulus is of interest from the point of view of both the pharmaceutical treatment of the cells and the dynamics of the mechanical properties. These important aspects relate to cellular migration [25–27], to the process of cytodifferentiation [28, 29], to cellular aging, and to the development of cellular pathology [30, 31].

Another important development in this field is direct AFM measurement of interaction forces between ligands and receptors [32–34]. When a scan of a soft and delicate object like a biological cell is treated in contact mode the surface may be damaged by the probe if the loading force is too large. Deducing a guiding principle for the magnitude of the force required for cell manipulation is valuable for cellular level surgery.

Hemodynamic particles in the investigations reported here are erythrocytes (red blood cells) due to their availability. At the same time, erythrocyte membranes have similar principles of organization as biological membranes. Therefore it is convenient to use them for natural models for cell elastography methods, currently being developed to study the general structural and functional characteristics of membranes [35].

As mentioned in the Introduction, the use of laser light for illumination opens additional possibilities for biotissue monitoring. Coherent light scattered by a biotissue under study produces a random granular interference structure some distance away from the object, which is called a biospeckle pattern [6–8], as in Fig. 7.1 (right). The potential of monitoring biotissues based on speckle pattern analysis will be discussed in Sect. 7.5.

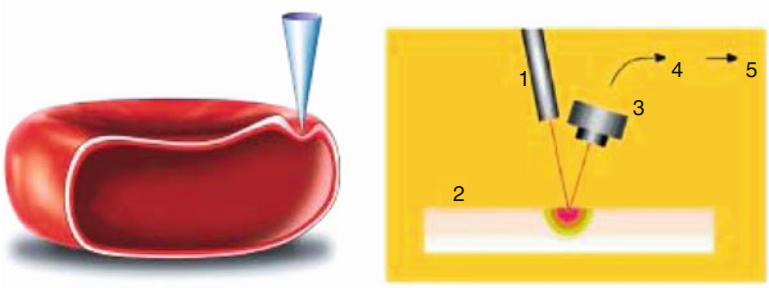

Fig. 7.1 Schematic illustration of AFM tip probing of single erythrocyte in vitro (*left*) and laser inspection of erythrocytes motility in a living tissue in vivo by DLS (*right*): *1* laser; *2* tissue under study; *3* CCD camera; *4* digital frame grabber; *5* PC

The purpose of this section is to explain the possibilities of using AFM and DLS in the study of biological cells, namely, measurement of the general cell motility in living tissue, the elastic modulus of the single cell membrane, as well as identification of the forces causing damage of the membrane. The latter aspect provides information about cutting of the cell membrane, useful in so-called cell surgery.

7.2.2 Force Spectroscopy

The procedure of force spectroscopy constitutes a standard mode of AFM. The method consists in the realization of the contact deformation of a specimen using the probe (Fig. 7.1) and in quantifying the relationship between probe interaction force and distance [3]. We record the cantilever deflection as the sample moves up, reaches the tip, and is retracted. The force curve is obtained by monitoring the movement of the reflected laser beam from the rear of the cantilever. The force curves are the relation between the bend of the cantilever and the position of the probe. Knowing the displacement of the sample in the vertical direction and the amplitude of cantilever bending, it is possible to calculate the total external force that has been applied to it and the resulting deformation of the sample. The force curve is applied to the calculation of Young's modulus (Fig. 7.2, right).

The figure shows the different stages of the indentation process. At the beginning of the force curve recording, the tip is distant from the sample and approaches, but does not contact it (a). Since there is no contact the cantilever deflection is constant. As soon as the tip actually touches the sample, the cantilever moves upward (b). Further, as the tip indents the sample, the cantilever arm moves downward (c). The sample is then retracted displaying a reverse behavior to action (c), as indicated by the curve (d) which shows the deflection during retraction. However, when adhesion between sample and tip occurs, the tip will adhere to the sample beyond the point of contact (e), until it finally breaks free again and the deflection returns to zero (f). The approach curve exactly retraces the pathway to point (e) provided

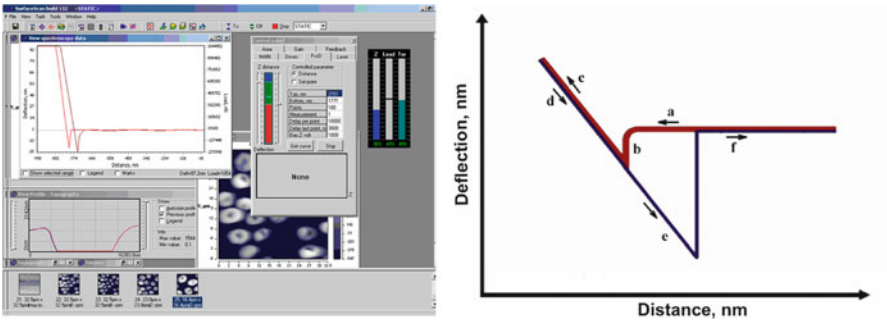

Fig. 7.2 Window of the AFM controlling program, the regime of static force spectroscopy (*left*) and the typical force curve for erythrocytes (*right*)

there is no piezo hysteresis. We have been able to quantify the local elastic properties of the erythrocytes using the force spectroscopy mode. The force curve is obtained by recording the cantilever deflection as the tip is brought into contact at the fixed point and then retracted. The Young's modulus was calculated using the Hertz model describing the elastic deformation of two bodies in contact under load [36]. We consider that the indented sample is assumed to be extremely thick in comparison to the indentation depth. In this case the elastic modulus can be calculated as described earlier [37, 38].

7.3 Methodology of AFM Testing of Cells

7.3.1 Sample's Preparation

Blood used was of healthy persons surveyed in the Republican scientific practical center "Cardiology" (Minsk, Belarus). A drop of venous blood stabilized by heparin was fixed in a 1.5% wt/vol glutaraldehyde solution (Fluka AG). Following fixation for 30 min at room temperature, the blood solution was centrifuged at 1,500 revolutions per minute for 3 min. The supernatant was discarded and the erythrocytes were washed twice in a buffer solution (PBS) and twice in water. The cells were placed on a glass surface and dried at room temperature.

7.3.2 AFM Hardware

AFM researches were carried out using atomic force microscopy NT-206 ("Mi-croTestMachines," Belarus) working in contact mode. Standard cantilevers CSC38 ("MikroMasch" Co., Estonia) with a spring constant of 0.03 N/m were used.

The tip radius was checked using a standard TGT01 silicon grating ("NT-MDT," Russia) and ranged from 40 nm for topography visualization to 60 nm for cell stiffness determination.

7.3.3 Statistical Analysis

The data are presented as mean standard deviation of the mean and analyzed by the Student's *t*-test. A *p*-value of less than 0.05 was considered to be statistically significant.

7.4 Action of Different Forces

The first logical stage in cell manipulation using AFM is the definition of cellular elastic modulus. For the cases of absence or presence of internal organelles in the cell, we have found that this key parameter is respectively independent of or dependent on, the area of indentation. In fact, our earlier researches showed that erythrocyte elasticity modulus did not depend on indentation area [39], and that the values of the modulus in the center and periphery of the cell were the same. Other earlier tests showed that the elasticity modulus did depend on the duration of the loading. Further, it has been shown that the choice of indenter contact velocity is very important in elasticity estimations at the erythrocyte membrane surface. Based on the data we have obtained, it is evident that the estimation of cell membrane properties largely depends on the ratio between the length of the relaxation transitions and the loading duration in the tests [40]. In this work we compared the action of different forces on the cell membrane. In the first series of tests, the erythrocyte elastic modulus was determined for loadings where the cell remained undamaged (Fig. 7.3). In the second series, cell manipulation involved membrane cutting. This could be achieved by subjecting the membrane to certain force regimes. In our experiments four values of load parameters were used, defined non-dimensionally and expressing the load applied to the console. Real values of the load could be determined after calculations on the basis of force spectroscopy data (70, 115, 160, and 190 nN). Figure 7.3 (left) shows scanning results for erythrocytes before and after the loading force is increased from 70 to 115 nN. At this load surface scratching of the erythrocyte membrane occurred, the depth of hollowing being near to 10 nm.

Since the depth is comparable with the thickness of the erythrocyte membrane it means that increasing the load beyond 115 nN can cause the cell membrane to be severed. Figure 7.3 (right) gives AFM images of the erythrocyte before and after the loading force is increased from 115 to 160 nN. At the latter load the erythrocyte was severely damaged and the depth of hollowing was approximately 40 nm. This depth is comparable with the overall thickness of the membrane plus the cytoskeleton.

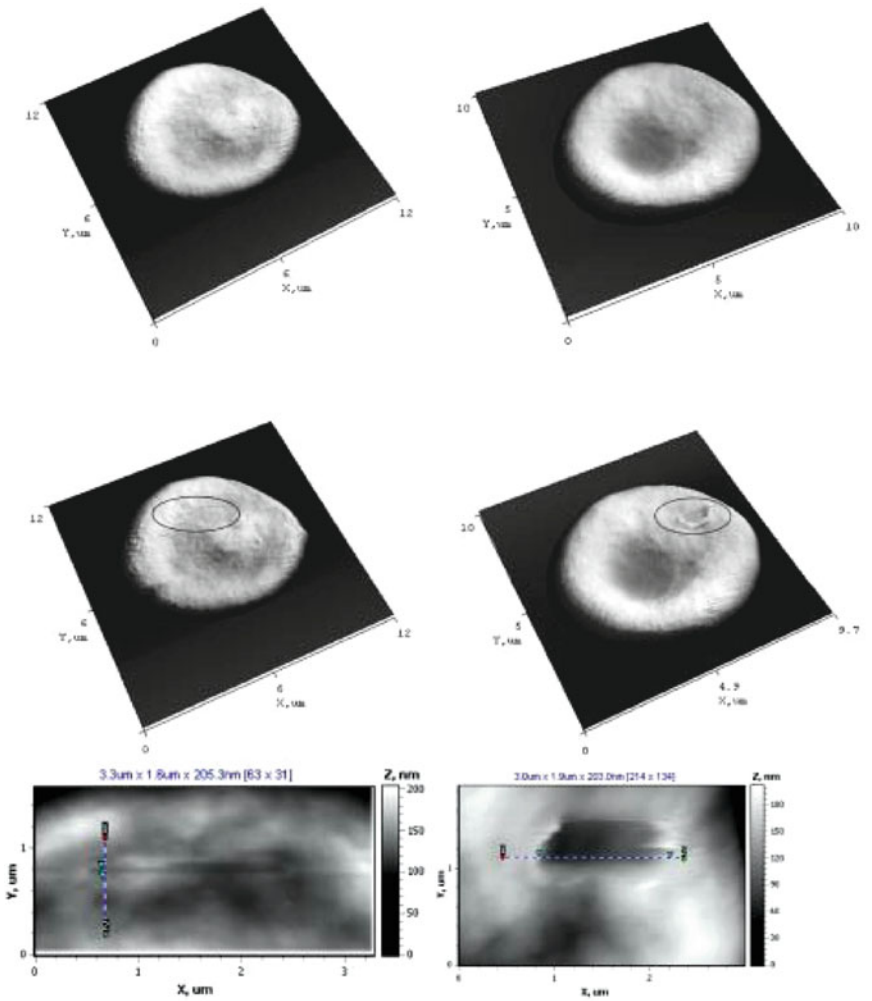

Fig. 7.3 AFM image of erythrocytes. On the *left top-down*: normal cell, scanning area 12.0 × 12.0 μm; erythrocyte after load increase (115 nN), scanning area 12.0 × 12.0 μm; scratch on the cell's surface, scanning area 1.4 × 3.4 μm. On the *right top-down*: normal cell, scanning area 10.0 × 10.0 μm; erythrocyte after load increase (160 nN), scanning area 10.0 × 10.0 μm; hollowing, scanning area 3.0 × 1.9 μm

Using the higher force, then, means the cell may be cut sufficiently strongly to enable the (inner) contents to be investigated.

Also, we calculated the value of the force at the four load parameters. There was a linear dependence between the applied load and the depth of indentation. But the values of maximum forces differed and the range of penetration depths was greater with increasing force and with damage. This is shown in Fig. 7.4

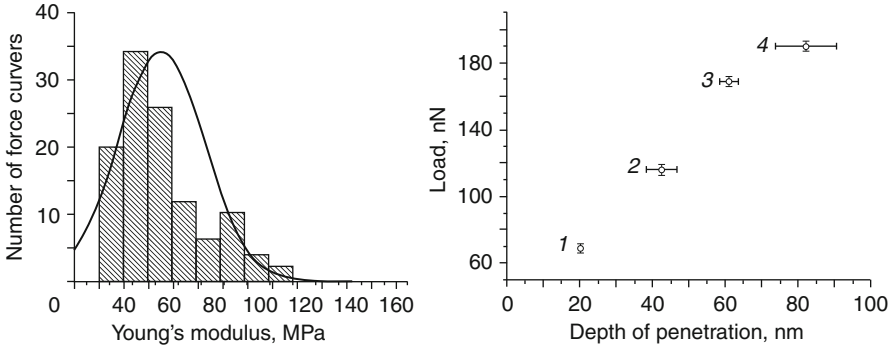

Fig. 7.4 Diagram of the distribution of the modulus of erythrocyte elasticity in healthy persons (*left*) and diagram of the average values of the applying load at maximum of the penetration depth (different loading regime) (*right*): *1*, *2*—action without damage; *3*, *4*—action with damage

(right) where the maximum values of the penetration depth are presented as a function of the average values of the maximum forces reached at the four different loading parameters of 70, 115, 160, and 190 nN. When the force was equal to 20 nN the roughness of the cell surface increased during contact mode scanning. For a loading force between 115 and 160 nN the tip scratched the cell damaging the membrane. And for a force higher than 190 nN the deeper penetration of the tip occurred.

7.5 Elasticity Measurements of Human Cells

In our earlier researches we estimated the elastic modulus of the cells for certain diseases such as diabetes mellitus type II (DM-2) and lung adenocarcinoma [41, 42]. It has been shown that in patients with DM-2 there was a polymorphism of red blood cells (poikilocytosis and anisocytosis). Our results showed no significant differences between the value of rigidity index in patients with DM-2 and healthy persons. The calculated elasticity modulus for erythrocyte membranes in patients with DM-2 was higher than healthy persons by 27.5%. This fact means that in DM-2 patients the deformation of the erythrocyte membrane decreased. Furthermore, while consideration of the integral parameter can only reveal the tendency by investigating the local elasticity then the differences become significant. Also we compared the elastic properties of the erythrocytes for both male and female healthy persons and patients with DM-2. This showed that the value of the erythrocyte elastic modulus (E) in healthy women was lower than in healthy men by 43.5% ($p < 0.001$). E was also significantly lower in women with DM-2 than in men with DM-2 by 48.6% ($p < 0.001$). That is the erythrocytes for both healthy and DM-2 women were

more elastic than for men. At the same time E in men with DM-2 was higher than in healthy males, that is that this pathological condition makes the erythrocytes more rigid.

Turning to lung research, estimation of the difference in mechanical properties between human embryonic fibroblasts cells and the cells of human lung adenocarcinoma cell line (A549) showed that the apparent elastic modulus of human embryonic fibroblasts cells were 1.4 times higher than that of A549 cells at the significance level $p < 0.001$ (260.21 ± 5.84 kPa and 184.31 ± 2.45 kPa, respectively) [42]. Therefore, the membranes of lung cancer cells are more elastic than that of normal fibroblasts, which is in accordance to published data [43, 44]. This result also means that the cytoskeleton structure of cancer cells differs from that of normal cells.

7.6 Blood Flow in the Microcirculation: Laser Monitoring of Biotissues

7.6.1 Biospeckle Pattern Formation

A biospeckle pattern is produced by 3D interference of probing laser coherent light multiply scattered by the erythrocytes flowing inside living tissues, as in Fig. 7.1 (right).

Detailed analysis of multiple scattering on biospeckle formation and its dynamics shows that the time-space cross-correlation analysis of the temporal evaluation of the biospeckle patterns is an effective means of real time flow and stress visualization of a living tissue. Digital processing of biospeckle patterns records yields 2D maps which exhibit the temporal and spatial variations in flowing erythrocytes.

7.6.2 Monitoring of Biotissues by Dynamic Speckle Pattern Analysis

Planar Laser Speckle Photography or Particle Image Velocimetry (PIV) became a standard method for the determination of a fluid velocity map within a selected plane illuminated by a laser beam [13]. However, in many important applications it is difficult to illuminate the area of interest by a thin laser sheet. One of such applications is in vivo subskin blood flux velocimetry, when it is impossible to implement traditional PIV illumination. In such studies one deals with a volume illumination, at least due to the multi-scattering effects and the PIV technique may be combined with speckle photography methods as reported in [13]. Monitoring of the activity of the blood in the microcirculation in living tissues is of considerable importance for many diagnostic purposes. The microcirculation fulfills the function

of thermal and biochemical exchanges and is important, for example, in general physiological thermal regulation. Optical monitoring of the blood flux has an obvious advantage due to its nonintrusive character. Various methods have been used to study blood in the microcirculation by analysis of the light scattered from moving blood; these are based on such optical phenomena as the Doppler effect [6], speckle photography (Fercher and Briers [7], Asakura and Takai [8], Briers [9, 10]), and the dynamic behavior of laser speckles (Fujii et al. [45], Aizu and Asakura [12]). The application of these phenomena is particularly attractive and promising because of the non-invasive character of the measurements (that is without causing any disturbance) and the possibility of implementing these techniques in vivo. In this section real time blood microcirculation monitoring is described. This uses CCD recording of the sequences of the dynamic biospeckle patterns produced when a tissue under study is illuminated with a laser beam with direct digital cross-correlation analysis of the patterns [13, 14].

7.6.3 Biospeckle Dynamics

The dynamics of speckle patterns produced by a moving rough surface have been extensively studied for velocity measurements (e.g., [11, 12]). However, the spatio-temporal properties of biospeckle are essentially different from those of the speckle patterns formed by a moving rough surface due to the effect of the multiple scattering and different velocities of the scatterers. This effect is important for Laser Doppler measurements as well, but the description of the scattered light using speckles has the advantage of including multiple scattering, even if we consider the simplest case of multiple scattering from the "single" rough surface.

For single-point measurements, the intensity fluctuations measured at the point are characterized by the time-correlation length defined by the time at which the normalized temporal autocorrelation function of intensity fluctuations falls to $1/e$. This statistical quantity is inversely proportional to the fluctuating speed of the speckle intensity. Its reciprocal value measures the velocity of a diffuse object at least for the speckles scattered once. A more general description of dynamic speckle patterns is based on the use of multidimensional space-time cross-correlation functions. The normalized cross-correlation function of the fluctuating component $\Delta I = I - <I>$ of the speckle intensity is

$$\gamma\Delta I\left(\mathbf{r_1}, \mathbf{r_2}, t_1, t_2\right) = \frac{\langle \Delta I\left(\mathbf{r}_1, t_1,\right) \cdot \Delta I\left(\mathbf{r_2}, t_2\right)\rangle}{\langle \Delta I\left(\mathbf{r_1}, t_1,\right) > \cdot < \Delta I\left(\mathbf{r_2}, t_2\right)\rangle}. \tag{7.1}$$

The parameter γ, characterizes the mutual correlation of two biospeckle images and varies from 0 to 1. Dynamic speckles have two fundamental motions of speckles. For the first type of the speckle motion called "translation" the speckles move as a whole, and their shape remains unchanged even under considerable

displacement. For the second type of speckle motion, speckles deform, disappear, and reappear without appreciable displacement of their positions. This type of speckle motion is called speckle "boiling." In both cases, the speckle behavior depends not only on the motion of the scatterers but also on the parameters of the optical scheme used for the observation of the speckle. In most cases, the mode of dynamic biospeckle is mixed and speckles both translate and gradually change their structure. One of the main factors characterizing the dynamic behavior of speckle patterns is the shape of the illuminating wavefront. For Gaussian beam illumination, the radius of the beam spot in the object plane, ω, and the radius of the wavefront curvature, ρ, are expressed as functions of the distance z from a position on the beam waist:

$$\omega = \omega_0 \left[1 + \left(\frac{z}{z_0}\right)^2\right]^{1/2}, \quad \rho = z\left[1 + \left(\frac{z}{z_0}\right)^2\right]^{1/2}, \tag{7.2}$$

where $z_0 = \pi{\omega_0}^2/\lambda$ and ω_0 is the spot radius at the beam waist. Two parameters, the correlation time, τ_c, and the lapse time, τ_d, have been introduced by Asakura and Takai [8] to describe the dynamic behavior of speckles composed of both boiling and translation:

$$\gamma\Delta I(\mathbf{r}, \tau) = \exp\left(-\left|\frac{\mathbf{r}}{}\right|^2 r_c^2\right) \exp\left[-\frac{(\tau - \tau_d)^2}{\tau_c^2}\right], \tag{7.3}$$

where $r = r^2 - vecr1$, $\tau = T_2 - T_1$, and the lapse time τ_d depends on (r). Let us consider probing light scattered by a single erythrocyte moving with a constant velocity v. Parameters τ_c, and, τ_d are expressed via parameters of the optical imaging scheme. Thus, for a simple single lens arrangement, they are

$$\tau_c = \frac{1}{|v|}\left[\frac{\sigma_i}{D^2} + \frac{d_i}{r_c^2}\left(\varepsilon\sigma_i - \frac{1}{d_0}\right)^2\right]^{1/2}, \quad \tau_d = \frac{\tau_c^2 d_i^2}{|r_c^2|}\left(\varepsilon\sigma_i - \frac{1}{d_0}\right)vr, \tag{7.4}$$

where d_0 is the distance from the object plane to the imaging lens, d_i is the distance from the lens to the observation plane, $\varepsilon = 1/d_0 + 1/d_i - 1/r$ is a defocusing parameter, D is the imaging lens diameter, and $\sigma = 1 + d_0/\rho$. The dynamic speckle size, $r'c$, is related to a static speckle size parameter $rc = \pi\lambda\ d_i/D$, and the translation distance, rT:

$$r'_c = \frac{r_c^2 + r_T^2}{1 + \sin\Theta(r_T^2/r_c^2)}, \quad r_T = \frac{d_i D}{|\sigma_i}\left(\varepsilon\sigma_i - \frac{1}{d_0}\right) \tag{7.5}$$

with Θ being the angle between the vectors of v and r. Equation 7.5 shows that the correlation time of the intensity fluctuations in speckle pattern is inversely

proportional to the velocity of the erythrocytes creating this speckle pattern. This relationship is widely used for velocity measurements on rough surfaces employing dynamic speckle methods [8]. Both experimental and theoretical investigations show that a similar equation can be used for double and triple scattering from the moving erythrocytes [12]. Numerical investigation of Okamoto and Asakura [11] shows that the value of τ_c increases almost linearly with the increase of the averaged scatterers velocity in the case of multiple scattering as well. Thus, the value of $1/e$ is seen to be proportional to the velocity of scatterers even in more complicated cases, including multiple scattering. However, the relation, similar to (7.5) for such cases, must include many factors like the density of scatterers, and diameters of capillaries. Hence the measurement of the absolute value of the scatterers velocities for such cases needs additional experimental calibration. Consequently, the evolution of the dynamic biospeckle pattern has a more complicated character than in the Speckle Photography technique, where the speckle displacement is always directly proportional to the scatterers displacement in the flow studied. In addition to biospeckle displacement as described above there is the so-called boiling of speckles, i.e., temporal variation of the speckle intensity independent of speckle movement. In the context of addressing such behavior, three methods are now described for the analysis of variations in dynamic speckle patterns.

7.7 Speckle Pattern Analysis

The experimental arrangement at the Belarus State Medical University (BSMU) used for human biotissues monitoring in vivo is shown in Fig. 7.5. A low power He–Ne laser is used as a light source. The laser radiation is transported by

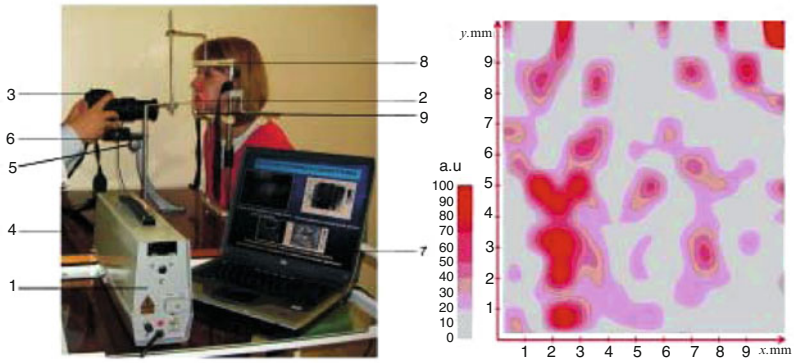

Fig. 7.5 In vivo human tissues monitoring at Belarus State Medical University: *1*—He–Ne laser with power supply; *2*—waveguides for laser beam transportation; *3*—Digital CCD camera of high resolution; *4*—patient table; *5*, *6*—mechanical supports; *7*—PC; *8*, *9*—mechanical supports. On the *right*, example of intensity of subskin blood microcirculation within a tested area in arbitrary units

waveguide to the tissue under study. The scattered light, caused by the erythrocytes moving in the illuminated volume, is collected by the second waveguide and transported onto the CCD matrix where the biospeckle pattern is recorded. Due to the movement of the erythrocytes, the speckles also move, thus forming a dynamic speckle field. The biospeckle patterns are recorded using a high-resolution digital CCD camera with a frame rate of 25 frames/s. The exposure time varies from 1/25 s (for dynamic speckle contrast analysis in a single exposure mode) to 1/1,000 s (for cross-correlation analysis of subsequent frames). Speckle patterns are recorded as a distribution of gray values I(m, n) in digital form for each pixel (m, n) of the CCD matrix. In real time operation the image analysis is performed during the time interval between subsequent (two or more) frames. Three different mathematical approaches are used for the analysis of the resultant biospeckle patterns, as explained below.

7.7.1 Decorrelation of Speckle Patterns

For single-point measurements, the intensity fluctuations at the point are characterized by the time-correlation length defined as the time at which the normalized temporal autocorrelation function of intensity fluctuations falls to $1/e$. This statistical quantity is inversely proportional to the fluctuating speed of the speckle intensity. Its reciprocal value measures the velocity of a diffuse object, at least for speckles scattered once.

A more general description of dynamic speckle patterns is based on the use of multidimensional space-time cross-correlation functions.

The most simple approach is decorrelation analysis. In practice, many parameters are introduced into measurement data to characterize the variations in such speckle patterns quantitatively. Fujii et al. [45], in retinal blood flow measurements, use the average rate of change of speckles termed AD, "the average derivative," and the reciprocal value BR, "the blur rate" of the speckle intensity variations. Oulamara et al. [46] studying the biological activity of botanical specimens by means of biospeckle pattern decorrelation analysis introduce a parameter defined as the decorrelation mean speed (DMS) of the temporal speckle signals. The parameter was computed as an averaged value of the squared difference between the speckle signals, the first being taken as a reference. This parameter is equivalent to the so-called structural function introduced by A.N. Kolmogorov, and widely used for statistical characterization of the intensity of turbulent fluctuations in fluid mechanics [13]. The same parameter is used in our approach [14–16]. The structural function is directly related to the correlation function and defined as

$$D_{k-n} = \frac{\left\langle (I_k - I_n)^2 \right\rangle}{\langle I_k \rangle \langle I_n \rangle}. \tag{7.6}$$

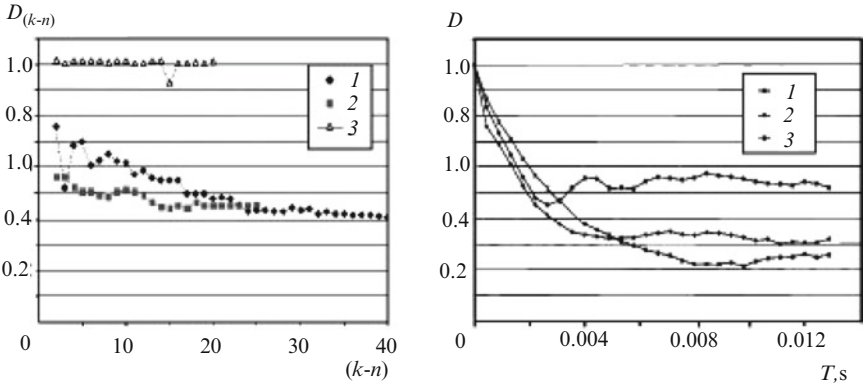

Fig. 7.6 Decorrelation function of the intensity variations in biospeckle patterns formed in laser light scattered from an apple tissue (*1*), human tissue in vivo (*2*), and a fixed ground glass (*3*). On the *x*-axis—numbers of the chosen frames with time interval between subsequent frames equal to 40 ms (*left*). At the *right*—decorrelation functions for three different parts of the human tissue in vivo. *x*-axis shows real time in seconds

To evaluate this function two sequential image maps, *Ik* and *In*, are subsampled. The size of the interrogation window is chosen to be equal to 32 × 32 or 62 × 62 pixels, since such windows contain a sufficient amount (10–100) of speckles for statistical averaging. This gives the possibility of using statistical averaging and to obtain 18 × 18 or 9 × 9 interrogation windows. The total illuminated area is about 2–5 mm in diameter, resulting in the size of interrogation window ranging from 100 × 100 μm to 0.5 × 0.5 mm. The values obtained can be coded either as gray or color variations and displayed at a monitor. Examples of such decorrelation functions obtained in our research are shown in Fig. 7.6.

Two different tissues have been analyzed using this approach. First, Fig. 7.6 shows the decorrelation function variations in biospeckle patterns obtained under illumination of an apple surface by a He–Ne laser.

The speckle movement in such patterns is due to two types of intra-tissue dynamics. There is not only the movement of the chloroplasts and amyloplasts (small particles with a mean size of 1 μm) in the cytoplasm medium of the apple tissue but also the movement of small mineral particles inside the apple cell vacuoles [46]. As the speed of all of these scatterers is less than 1 mm/min^{-1}, there is a clear linear dependence of the evaluated decorrelation function on the time interval between frames. The decorrelation technique was also used in in vivo studies. The speckle pattern variation in this case is due to erythrocyte movement in a living human tissue. The typical speckle patterns for such are shown in Fig. 7.6. Erythrocyte movement can be two orders of magnitude faster than that in an apple tissue, so no linear increase of the structural function with the time interval between successive exposures was evident. Instead, random fluctuations in blood flow velocity were recorded. The values of the decorrelation function obtained are

proportional to the blood flow velocity, but due to the complex processes of light scattering in a living tissue direct experimental calibration is necessary to evaluate absolute levels of velocity.

7.7.2 Contrast Evaluation

The second method is autocorrelation analysis. In this case speckle contrast is evaluated. Each image is interrogated with a window of varying size from 8 × 8 to 50 × 50 and the windows can overlap. The window size $M \times N$ and the extent of overlapping were optimized for each particular optical scheme of the experiment. Contrast is calculated in each window k according to the equation:

$$C_k = \frac{\sigma_{I_k}}{\langle I_k \rangle} = \frac{\sqrt{\langle I_k \rangle^2 - \langle I_k^2 \rangle}}{\langle I_k \rangle}. \\ = \frac{\sqrt{\left[\frac{1}{MN}\sum_{m=1}^{M}\sum_{n=1}^{N} I_k\right]^2 - \frac{1}{MN}\sum_{m=1}^{M}\sum_{n=1}^{N} I_k^2}}{\frac{1}{MN}\sum_{m=1}^{M}\sum_{n=1}^{N} I_k}. \tag{7.7}$$

Color coding of the contrast is used for visualizing the results, this contrast field being displayed on the monitor. An example of such a field is shown in Fig. 7.5 (right). In this case, the speckle field is obtained by laser illumination of the rotating ground glass. When the image corresponds to the part of the ground glass moving with higher velocity, the image is blurred and the contrast is lower. When the contrast of the speckle field is integrated over time it can characterize the mean speckle displacement during the exposure time. As shown by Briers [10] this contrast is inversely proportional to the velocity of scatterers in the interrogation area. The relation between speckle field contrast and relative speckle enlargement (exposure time) was analyzed with the help of a phantom speckle pattern. This phantom was an ideal speckle pattern with a contrast equal to 1. Then mathematical blurring of the speckle pattern was carried out so that the entire window was covered, this giving a contrast value of 0. Contrast was calculated for different relative speckle enlargements and the results of the modeling show nearly linear dependence of the contrast on speckle displacement. Thus, at 50% blurring the contrast was 0.55.

7.7.3 Cross-correlation Analysis

The most general approach in image analysis is cross-correlation analysis. The image is interrogated with small windows as in the approaches above, allowing the

correlation coefficient between the corresponding windows of two subsequent frames to be calculated as:

$$R_{ij}(p,\, q) = \frac{MN}{(M-p)(N-q)} \times \left[\frac{\sum_{m=1}^{M-p} \sum_{n=1}^{N-q} I_i(m,\, n) \cdot I_j(m+p, n+q)}{\sum_{m=1}^{M-p} \sum_{n=1}^{N-q} I_i(m,\, n) \cdot I_j(m,n)} \right]. \tag{7.8}$$

In addition to the common cross-correlation analysis, not only the peak position but also the cross-correlation function at the peak can be evaluated. This latter function value characterizes the decorrelation rate discussed above. Full cross-correlation analysis requires a relatively large interrogation time, and only quasi-real-time operation with a frequency rate of about 5 maps/s can be realized with the hardware currently available.

The information obtained with cross-correlation analysis seems to be a little excessive as it contains the direction of the averaged biospeckle displacement. For such random fields as subskin blood flux it seems that either decorrelation or simple autocorrelation analysis would be sufficient if only the value of the averaged blood flux intensity needs to be extracted.

7.7.4 Efficiency of the Evaluation

The time-space cross-correlation analysis of the temporal evaluation of the dynamic biospeckle patterns is shown to be a means of real time flow visualization of a living tissue blood microcirculation. Digital processing of biospeckle patterns records yields 2D maps exhibiting the temporal and spatial variations in the blood flow. This might be used for biomedical diagnostic purposes to detect, say, a microscale deviation from the normal case. The three methods of evaluation of the dynamic speckle patterns have been tested. Both decorrelation and autocorrelation analysis were realized in a real time mode, when entire treatment of the digital specklegram was performed over the time interval between successive frames (40 ms). Results in the form of 2D maps of subskin blood flux were visualized on the PC monitor at a frequency of 25 Hz.

Full cross-correlation analysis of the dynamic biospeckle pattern needs rather more PC time and, with the hardware currently available, only quasi-real time operation could be achieved at a frequency of about 5 maps/s. The information obtained with cross-correlation analysis seems to be somewhat excessive as it contains the direction of the averaged biospeckle displacement. For random fields such as subskin blood flux it appears that decorrelation or simple autocorrelation analysis would be sufficient when only the value of the averaged blood flux intensity

needs to be extracted. Although the data obtained is seen to be proportional to the velocity of the scatterers, the effect of multiple scattering causes difficulties in obtaining the absolute value of the blood velocity. Therefore, the monitoring reported here is qualitative and the blood flow maps are presented in arbitrary units.

7.8 Conclusions

This investigation reveals the twin potential of AFM for making measurements of the mechanical properties of cells and in performing certain actions on them, combined with DLS for evaluation of erythrocyte motility. There are two main methods for the manipulation of living cells using AFM: by elasticity measurement and direct application of force. We have determined the forces under which the cell membrane may be cut. Further, we have demonstrated the potential of obtaining the quantitative characteristics of cellular mechanical properties for cases of patho-physiological disorders of cells such as diabetes mellitus type II and cancer. These have enabled us to examine how experimental results of force measurements may be used to deduce a guiding principle for the magnitude of forces required for cell manipulation: the objective is to aid cellular level surgery. Quantitative monitoring of erythrocytes motions in living tissues with the use of DLS methods has also been demonstrated. The proposed software makes it possible to recover up to 25,000 motion vectors in a two-dimensional flow region of size 20 $\times$ 30 mm, providing real-time spatial resolution of about 100 μm.

Acknowledgments The authors wish to thank Dr. Serguei Rubnikovich (Belarus Medical State University, Minsk), Dr. Nikolai Bazylev, and Ms. Olga Meleeva (Heat and Mass Transfer Institute) for the help in images treatment and manuscript preparation as well as the National Academy of Sciences and Foundation for Basic Research of Belarus for partial financial support of the work with grants and projects "Energy Efficiency EE 1.6.1," T11MC-023, T10-029.

References

1. Fischer-Cripps AC (2004) Nanoindentation, 2nd edn. Springer, New York
2. Morris VJ, Kirby AR, Gunning AP (1999) Atomic force microscopy for biologists, 2nd edn. Imperial College Press, London
3. Burnham N, Colton RJ (1989) Measuring the nanomechanical properties and surface forces of materials using an atomic force microscope. J Vac Sci Technol A 7:2906–2913
4. Ueda M, Sako Y, Tanaka T, Devreotes P, Yanagida T (2001) Single-molecule analysis of chemotactic signaling in Dictyostelium cells. Science 294:864–867
5. Ikai A, Afrin R (2002) Toward mechanical manipulations of cell membranes and membrane proteins using an atomic force microscope. Cell Biochem Biophys 39:257–277
6. Stern MD (1975) In vivo evaluation of microcirculation by coherent light scattering. Nature 254:56–58

7. Fercher AF, Briers JD (1981) Flow visualization by means of single-exposure speckle photography. Opt Commun 37:326–329
8. Asakura T, Takai N (1986) Statistical properties of dynamic speckles. J Opt Soc Am A 3:1032–1054
9. Briers JD (1993) Speckle fluctuations and biomedical optics: implications and applications. Opt Eng 32:277–283
10. Briers JD (1994) Laser speckle techniques in biology and medicine. SPIE Proc 2083:238–249
11. Okamoto T, Asakura T (1995) The statistics of dynamic speckles. In: Wolf E (ed) Progress in optics, vol XXXIV. Elsevier, Amsterdam, pp 183–248
12. Aizu Y, Asakura T (1996) Bio-speckles. In: Consortini A (ed) Trends in optics. Academic Press, Orlando
13. Fomin N (1998) Speckle photography for fluid mechanics measurements. Springer, Berlin
14. Rubnikovich S, Fomin N (2010) Laser diagnostics and therapy in stomatology (in Russian). National Academic Science, Minsk
15. Fomin N, Fuentes C, Saulnier J-B, Tuhault J-L (2001) Tissue blood flux monitoring by laser speckle photography. Laser Phys 11(4):525–529
16. Bazylev N, Fomin N, Lavinskaya E, Rubnikovich S (2002) Acta Bioeng Biomech 4:510–511
17. Ophir J et al (1991) Elastography: a quantitative method for imaging the elasticity of biological tissues. Ultrason Imaging 13(2):111–134
18. Mansfeld AD, Timanin EM (1995) On the possibility of through measurements of shear viscoelastic parameters of biological tissues. Akust Zhurn 41(3):514–515
19. Gao L et al (1996) Imaging of the elastic properties of tissue a review. Ultrasound Med Biol 22(8):959–977
20. Garra BS et al (1997) Analysis of breast lesions using elastography: initial clinical results. Radiology 202(1):79–86
21. Sarvazyan AP et al (1998) Shear-wave elasticity imaging: a new ultrasonic technology of medical diagnostic. Ultrasound Med Biol 24(9):1419–1435
22. Ophir J et al (1999) Elastography: ultrasonic estimation and imaging of the elastic properties of tissues. Proc Inst Mech Eng H 21(3):203–233
23. Arun T et al (2006) Resolution of axial shear strain elastography. Phys Med Biol 51(20):5245–5257
24. Svensson WE, Amiras D (2006) Breast cancer online (Electronic resource). pp 1–7
25. Sasaki S et al (1998) Elastic properties of living fibroblasts as imaged using force modulation mode in atomic force microscopy. Arch Histol Cytol 61(1):57–63
26. Haga H et al (2000) Time-lapse viscoelastic imaging of living fibroblasts using force modulation in AFM. J Electron Microsc 49(3):473–481
27. Nagayama M, Haga H, Kawabata K (2001) Drastic change of local stiffness distribution correlating to cell migration in living fibroblasts. Cell Motil Cytoskeleton 50(4):173–179
28. Collinsworth AM et al (2002) Apparent elastic modulus and hysteresis of skeletal muscle cells throughout differentiation. Am J Physiol Cell Physiol 283(4):1219–1227
29. Zhang S, Kraus WE, Truskey GA (2004) Stretch-induced nitric oxide modulates mechanical properties of skeletal muscle cells. Am J Physiol Cell Physiol 287(2):292–299
30. Brownell WE et al (2001) Micro- and nanomechanics of the cochlear outer hair cell. Annu Rev Biomed Eng 3:169–194
31. Lieber SC et al (2004) Aging increases stiffness of cardiac myocytes measured by atomic force microscopy nanoindentation. Am J Physiol Heart Circ Physiol 287(2):H645–H651
32. Sako Y, Minoghchi S, Yanagida T (2000) Single-molecule imaging of EGFR signaling on the surface of living cells. Nat Cell Biol 2:168–172
33. Fujiwara T, Ritchie K, Murakoshi H, Jacobson K, Kusumi A (2002) Phospholipids undergo hop diffusion in compartmentalized cell membrane. J Cell Biol 157:1071–1081
34. Byassee TA, Chan WC, Nie S (2000) Probing single molecules in single living cells. Anal Chem 72:5606–5611

35. Kuznetsova TG, Starodubtseva MN, Yegorenkov NI, Chizhik SA, Zhdanov RI (2007) Atomic force microscopy observation of peroxynitrite-induced erythrocyte cytoskeleton reorganization. Micron 38:824–833
36. Hertz H (1881) Ueber den kontakt elastischer koerper. J fuer die Reine Angewandte Mathematik 92:156
37. Chizhik SA, Huang Z, Gorbunov VV, Myshkin NK, Tsukruk VV (1998) Micromechanical properties of elastic polymeric materials as probed by scanning force microscopy. Langmuir 14:2606–2609
38. Lee GYH, Lim CT (2007) Biomechanics approaches to studying human diseases. Trends Biotechnol 25:111–118
39. Drozd ES, Chizhik SA, Konstantinova EE (2009) Probing mechanical and structural properties of the erythrocyte membrane by atomic force microscopy. Russ J Biomech 4(46):22–30
40. Drozd ES, Chizhik SA (2009) Combined atomic force microscopy and optical microscopy measurements as a method of erythrocyte investigation. In: Proceedings of SPIE, vol 7377. SPIE, Bellingham, pp 7370E–7370E-8
41. Drozd ES, Chizhik SA, Kontantinova EE et al (2010) Mechanical characteristics of erythrocyte membranes in patients with type 2 diabetes mellitus. Series of biomechanics, Inst. of Mechanics (Bulg. Acad. of Science). Bulg Soc Biomech 25(3/4):53–60
42. Starodubtseva MN et al (2010) Study of the mechanical properties of single cells as biocomposites by atomic force microscopy. Microsc Sci Technol Appl Educ 22(8):470–477
43. Lekka M et al (1999) Elasticity of normal and cancerous human bladder cells studied by scanning force microscopy. Eur Biophys J 28:312–316
44. Ward K et al (1991) Viscoelastic properties of transformed cells: role in tumor cell progression and metastasis formation. Biorheology 28:301–313
45. Fujii H, Asakura T, Nohira K, Shintomi Y, Ohura T (1985) Blood flow observed by time-varying laser speckle. Opt Lett 1:104–106
46. Oulamara A, Tribillon G, Duvernoy J (1989) Biological activity measurement on botanical specimen surfaces using a temporal decorrelation effect of laser speckle. J Mod Opt 36(2):165–179

Chapter 8
Coherent Microscopy and Optical Coherence Tomography for Biomedical Applications

Jeremy M. Coupland and Justin A.T. Halls

Abstract In recent years the traditional, incoherent methods of optical microscopy have been complemented by coherent imaging methods such as digital holographic microscopy and optical coherence tomography. These methods have the ability to image through distorting media, offer extended contrast enhancement modes such as polarization sensitive and Doppler imaging, and promise varying degrees of 3D imaging capability. Although these techniques might seem quite disparate both in configuration and application, they are similar in many important respects. As coherent, far-field techniques they derive information from the response of the object to a set of optical stimuli and use interferometric methods to record the phase and the amplitude of the elastically scattered field at a distant boundary. Hence, it is only the characteristics of the fields used to illuminate the object and the physical limitations imposed by the optical systems used to measure the response that differentiate the various techniques.

In this chapter, the capabilities of coherent microscopy and optical tomography are compared using linear systems theory. The techniques are characterized in terms of their 3D transfer functions in the frequency domain and their associated 3D point spread functions in the space domain. It is shown that digital holographic techniques that reconstruct images from a single, coherent recording of the scattered field only provide useful 3D information when used to investigate sparse objects such as cells or particles suspended in a transparent fluid. By synthesizing images from multiple recordings of the scattered field using different wavelengths and/or different illuminating wave fronts, the 3D imaging capability of far-field

J.M. Coupland (✉)
Department of Mechanical and Manufacturing Engineering, Wolfson School of Mechanical and Manufacturing Engineering, Loughborough University, Ashby Road, Loughborough, Leicestershire LE11 3TU, UK
e-mail: j.m.coupland@lboro.ac.uk

J.A.T. Halls
Brunel Institute for Bioengineering, Brunel University, Uxbridge, Middlesex UB8 3PH, UK
e-mail: justin.halls@brunel.ac.uk

M.W. Collins and C.S. König (eds.), *Micro and Nano Flow Systems for Bioanalysis*, Bioanalysis 2, DOI 10.1007/978-1-4614-4376-6_8,

optical techniques is extended greatly. In these cases light scattered from different depths can be identified by means of the so-called "coherence gating" or "confocal gating" effects attributed to the source bandwidth and numerical aperture (NA), respectively. These are the methods of optical tomography.

8.1 Introduction

Driven mainly by biomedical applications the optical microscope has been in constant development for over a century. Significant milestones include the imaging theory of Abbe [1], the phase contrast technique introduced by Zernike [2, 3], and the confocal microscope by Minsky [4], which for the first time demonstrated 3D sectioned images. More recently we have witnessed the development of digital holographic microscopy (DHM) and other coherent techniques that have similar 3D capability. In particular, Optical Coherence Tomography (OCT) has produced truly remarkable 3D images of the retina and Doppler OCT has been used to estimate blood flow within tissue [5].

Coherent methods differ from their incoherent counterparts by their ability to record and reconstruct both the phase and amplitude of the scattered field, and for this purpose an interferometer is necessary. Of the 3D imaging methods DHM is the fastest and most straightforward to implement. The simplest set-up uses a point-source in an in-line transmission configuration [6] but many variations are possible including phase stepping, off-axis and backscatter geometries [7–9]. In all these cases the definitive characteristic of DHM is that the 3D scattered field can be estimated from a *single measurement of the scattered field*. In biomedical applications DHM can be used to provide bright field images comparable to those from a conventional microscope even when the image is acquired through a distorting sample container such as a plastic dish. It is also possible to emulate other classical microscopy modes such as dark field, differential interference contrast, and phase and even spiral phase contrast [10, 11]. A comprehensive review of DHM techniques has been published by Ferraro, Wax, and Zelevsky in 2010 [12].

As we explain later, DHM does not provide a true 3D image. This is apparent when it is considered that the 3D field is reconstructed from a measurement of a 2D boundary field and as such the reconstruction must be highly correlated. In the strictest sense, a 3D image can only be synthesized from a sequence of scattered field measurements using multiple source wavelengths, illumination directions or a combination of both.

OCT makes use of a broadband or swept source to measure the response of the object *to light of different wavelengths*. Several variants of the technique are possible but all necessarily collect backscattered light from the object of interest. Early OCT measurements exploited a broadband source with limited coherence to record interference as the object was scanned in the object path of an interferometer [13]. The limited coherence results in a packet of interference fringes that identifies

when the path lengths are balanced and provides a so-called "coherence gate" [14]. In the biomedical field this approach is called time-domain OCT (TD-OCT), although the same approach has been used for many years in optical profilometry where it is most often called Coherence Scanning Interferometry (CSI) [15].

Frequency domain OCT (FD-OCT) obviates the need for mechanical scanning. It offers significantly higher data rates and has found widespread application in ophthalmology where it is routinely used to diagnose retinal disorders. FD-OCT can be implemented using either a swept source (typically a semiconductor laser) or a broad-band source (SLED) together with a multiple-channel spectrometer [16]. In either case, FD-OCT measures the phase and amplitude of the scattered signal as a function of wave number. As we explain later, this signal is directly proportional to the amplitude of individual *spatial frequency components* within the object. Many variations of OCT have been developed including Doppler OCT for flow measurement, polarization-sensitive and spectrally resolved OCT [16]. There are several good introductory sources to this rapidly developing field including, Bouma and Tearney [17] and Drexler and Fujimoto [18]. Brezinski [19] also provides a very accessible introduction to the mathematics and basic principles underlying the technique.

An alternative strategy to 3D imaging is to measure the coherent response of an object *to illumination presented from different directions*. Generally known as Optical Diffraction Tomography (ODT) this approach can be implemented in a similar configuration to DHM using scanning mirrors to provide the necessary illumination conditions. In comparison with OCT, ODT can be used in a forward scatter geometry and biomedical applications include quantitative 3D imaging of refractive index in live cells [20]. It is interesting to note that the mutually aligned laser/pinhole combination of a confocal microscope provides an entirely equivalent image to ODT [21]. Confocal microscopy, however, requires 3D scanning of a single point detector, while ODT exploits a 2D scanning mirror and an area detector. More fundamentally, both ODT and confocal microscopy require illumination and observation optics of high numerical aperture (NA) and depth discrimination by this means is often referred to as a "confocal gate" [18]. The basis of ODT in the context of other tomographic techniques is discussed by Kak and Slaney [22], while confocal microscopy and its implementation is treated by Wilson et al. [23].

The pioneering work of Abbe firmly established the link between the NA and the spatial frequency components which are transmitted by a microscope objective and ultimately define the fidelity of the image. In order to increase the lateral resolution, a large NA is required and consequently the highest resolution 3D imaging microscopes must necessarily exhibit a degree of confocal gating even if coherent recording at multiple wavelengths and coherence gating is also exploited. An example of this is CSI. When implemented using low magnification, small NA objectives, coherence gating dominates and the process is entirely equivalent to TD-OCT. If high magnification, large NA objectives are used, confocal gating dominates and the process is entirely equivalent to laser confocal microscopy. Further information on the principles and practice of CSI is to be found in Leach [24].

It is clear from the above discussions that although 3D microscopy techniques might seem quite disparate both in configuration and application, they are similar in many important respects. With the exception of fluorescent confocal microscopy, elastically scattered light is collected from the object of interest and interferometric methods are used to record the phase and the amplitude of the scattered field. In an abstract sense, all optical techniques derive information from the response of the object to a set of optical stimuli with known spatial and temporal characteristics. Hence, it is only the scanning methods that provide the illuminating fields and those used to record the corresponding responses, which differentiate the various techniques.

In previous papers [21, 25] we have applied scalar diffraction theory to many optical imaging techniques, characterizing them as 3D linear systems. In addition we have also considered image enhancing methods such as phase contrast etc. as 3D linear filtering operations [11]. Although the details of this analysis are beyond the scope of the present chapter, the main results provide a useful insight into their capability. In the following sections the basis of linear imaging theory is presented and the theoretical performance of coherent microscopy and optical tomography is then compared.

8.2 Linear Imaging Theory

The foundations of 3D linear imaging theory were laid by Wolf [26] and Dandliker [27] who considered the reconstruction of the 3D form of an object from holographic recordings. The theory rests on the assumption of weak scattering or the Born approximation [28]. In effect it is assumed that the scattered field is a small perturbation to the field that illuminates the object. This is often the case in flow measurements, for example, where the fluid is usually sparsely seeded with small tracer particles. Although the Born approximation is not strictly justified in dense tissue, linear theory still provides a good estimate of imaging performance as multiple scattering typically raises noise levels in this situation.

According to linear systems theory [21], the process of imaging can be thought of as a filtering operation that is characterized in the space domain by the 3D convolution integral,

$$O(\mathbf{r}) = \int_{-\infty}^{+\infty} H(\mathbf{r} - \mathbf{r}')\ \Delta(\mathbf{r}')\mathrm{d}^3\mathbf{r}' \tag{8.1}$$

where $H(\mathbf{r})$ is the point spread function (PSF) and $\mathrm{d}^3r = \mathrm{d}r'_x\,\mathrm{d}'r_y\,\mathrm{d}'r_z$. The function $\Delta(\mathbf{r})$ represents the object and in this chapter is defined as the refractive index contrast given by,

$$\Delta(\mathbf{r}) = 4\pi^2(1 - n(\mathbf{r})) \tag{8.2}$$

where, $n(\mathbf{r})$ is the refractive index. The PSF can be thought of as the image of an idealized point scattering particle and its size effectively defines the resolution of the system.

In many ways it is more intuitive to characterize the response of optical systems in the spatial frequency domain (k-space or inverse-space) and then go on to calculate the corresponding PSF if required. In this case the transfer function (TF) describes how the individual spatial frequency components that make up the object function are modified by the imaging process. In the frequency domain the 3D convolution of (8.1) can be written, more simply, as the product,

$$\tilde{O}(\mathbf{k}) = \tilde{H}(\mathbf{k})\tilde{\Delta}(\mathbf{k}) \tag{8.3}$$

where tilde represents Fourier transformation such that, $\tilde{H}(k)$, the system TF, is defined as,

$$\tilde{H}(\mathbf{k}) = \int_{-\infty}^{+\infty} H(\mathbf{r}) \exp(2\pi \mathbf{j}\mathbf{k} \cdot \mathbf{r}) \mathrm{d}^3 r \tag{8.4}$$

In the spatial frequency domain it is noted that each point represents a 3D periodic structure or Bragg grating within the object [29]. The 3D structure of a Bragg grating makes it reflect selectively according to both the wavelength, λ, and the angle of incidence. If the incident and reflected waves are represented by the wave vectors k_i and $\mathbf{k}_\mathrm{r}$ $|\mathbf{k}_\mathrm{i}| = |\mathbf{k}_\mathrm{i}| = k_0 = 1/\lambda$ then the vector representing $\mathbf{k}_\mathrm{g}$ is given by,

$$\mathbf{k}_\mathrm{g} = \mathbf{k}_\mathrm{r} - \mathbf{k}_\mathrm{i} \tag{8.5}$$

The reflection process is illustrated in Fig. 8.1a, while the relationship described by (8.5) is represented schematically by the wave vector diagram in Fig. 8.1b.

Under the assumption of weak scattering it can be shown that the amplitude of the reflected wave is directly proportional to the amplitude of the refractive index contrast variation [26]. Consequently it is possible to measure the amplitude of a particular spatial frequency component by measuring the response of the object to appropriately chosen illumination and observation directions. In practice, however, source availability and restrictions in the possible illumination and observation directions limit the spatial frequency content that can be measured. In the following sections, the main methods used in 3D imaging systems are described and compared in terms of PSF and transfer characteristics and their potential as measurement tools for the study of micro- and nano-flow studies are then discussed.

8.3 Digital Holographic Microscopy

Digital Holographic Microscopy (DHM) is the name given to techniques that reconstruct the phase and amplitude of the scattered field from a single, coherent measurement of the light incident on an imaging array. A fundamental requirement

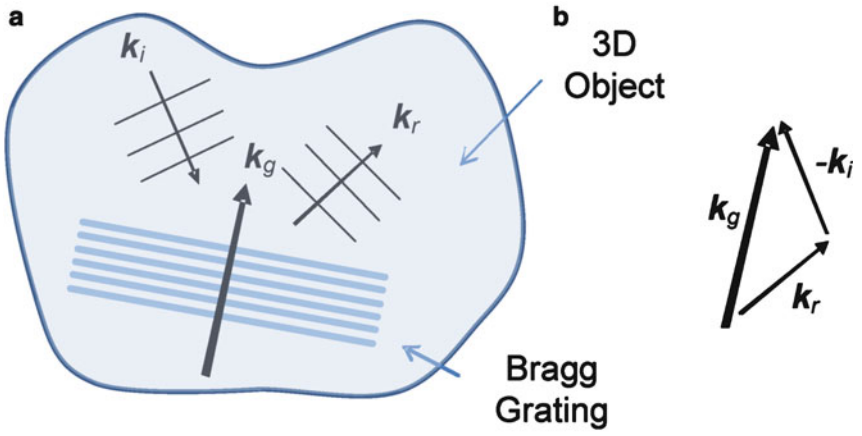

Fig. 8.1 (**a**) Reflection from Bragg gratings within the object and (**b**) the wave vector diagram

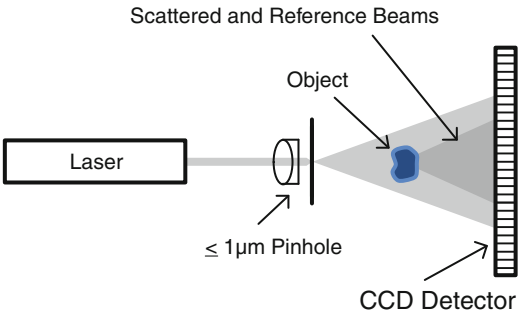

Fig. 8.2 Point-source, in-line digital holography

of DHM is a coherent reference field which is made to interfere with the scattered field. Provided that the phase and amplitude of the reference field is known, that of the object field can be reconstructed.

Point source in-line holographic microscopy is based on the original idea proposed by Gabor [30, 31] in an effort to get away from the limitations imposed by using physical lenses, and more specifically, the very severe limitations of electromagnetic lenses used in electron microscopy. In the configuration shown in Fig. 8.2, the illumination is provided through a pinhole which is less than a wavelength of light in diameter. The pinhole acts a source of spherical wave fronts that expand as they propagate from the pinhole. The expanding nature of the wave fronts provides magnification. If a CCD detector is illuminated by this wave front it will be uniformly exposed, but if a small scattering object is placed in the field, interference between the direct wave front and the scattered wave fronts is recorded by the CCD.

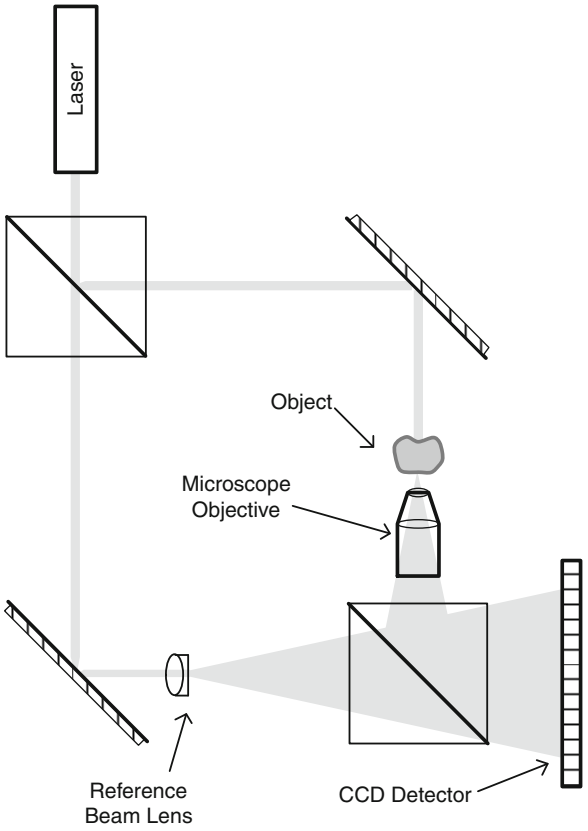

Fig. 8.3 Forward scatter Mach-Zender interferometric DHM configuration

The simplicity of point-source in-line holography is not without limitations, however. First, restrictions must be placed on the distance between object and pinhole in order that the interference is resolved by the CCD. Second, the assumption that the interference is between scattered and unscattered wave fronts is only reasonable for sparse objects that cover a small fraction of the field as there is strictly no direct path from the pinhole to the detector. Finally, there are many problems associated with numerical reconstruction which must include coordinate transformation and nonlinear optimization methods [32]. The limitations of the in-line holographic method can be overcome either by the off-axis holographic configuration originally proposed by Leith and Upatnieks [33] or phase stepping interferometry [7]. For the purpose of DHM the off-axis geometry has the advantage that the phase and amplitude of the scattered field can be recovered from a single interferogram.

An off-axis transmission DHM based on a Mach-Zender interferometer is shown in Fig. 8.3. In this configuration the microscope objective provides the necessary magnification to ensure that the scattered field is resolved by the CCD. The additional wave front curvature introduced by the objective can be eliminated

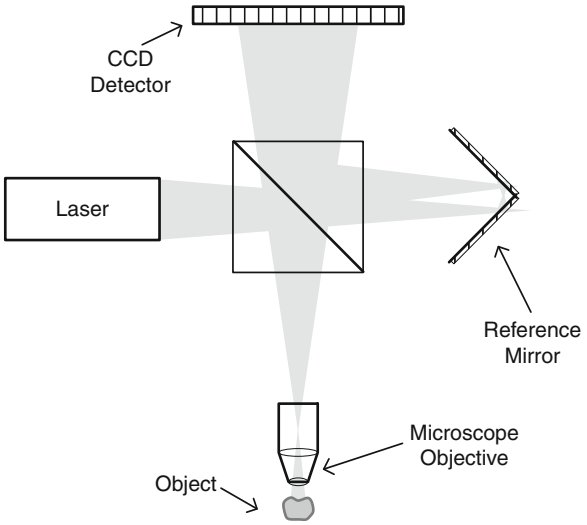

Fig. 8.4 Backscatter Michelson DHM configuration

by introducing a similar lens into the reference arm of the interferometer. The most important aspect of this configuration is the flexibility to add a tilt (or offset) to the reference wave which introduces a carrier frequency to the interference pattern that simplifies numerical reconstruction considerably.

Off-axis DHM can also be implemented in a reflection geometry using a Michelson interferometer configuration as shown in Fig. 8.4. In this arrangement the laser is focused in the back focal plane of the objective such that the object is illuminated by a plane wave. The light scattered from the object passes back through the objective and forms an image at the CCD. As before, the scattered light is mixed with a coherent reference wave of appropriate divergence and tilt such that plane carrier fringes are observed in the intensity recorded by the CCD.

In general terms, DHM and all the other methods of coherent 3D imaging, measure the scattered field at a boundary surface that is far beyond the reach of the evanescent waves that constitute the near-field that surrounds the object. As a consequence, only plane wave components that have the capability to propagate to the boundary (i.e., the far-field) can be measured in this way. Further to this, it is only the plane wave components that propagate within the NA of the objective, that are collected as shown in Fig. 8.5.

Mathematically, the process of reconstructing the scattered field from this limited information can be written as a linear filtering operation. If in the spatial frequency domain the scattered and reconstructed fields are described by the functions, $\tilde{E}^s(\mathbf{k})$ and $\tilde{E}^m(\mathbf{k})$, the DHM reconstruction process can be written as the product [21],

$$\tilde{E}^m(\mathbf{k}) = \tilde{E}^s(\mathbf{k})\tilde{G}_{\mathrm{NA}}(\mathbf{k}) \tag{8.6}$$

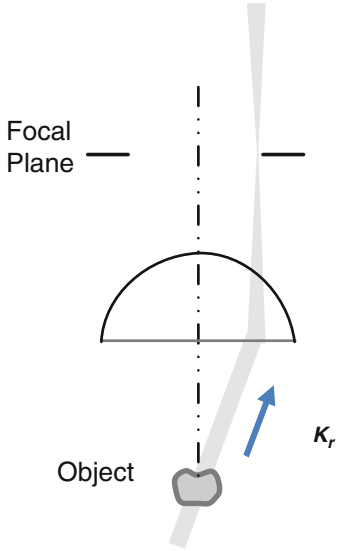

Fig. 8.5 Coherent microscopy configuration

where $\tilde{G}_{\mathrm{NA}}(\mathbf{k})$ represents the wave vectors collected by the system. For the case of a coherent microscope operating at wavelength, λ , the plane wave components collected by the circular aperture can be represented in k-space by wave vectors, $\mathbf{k}_{\mathrm{r}}$ that fall on a spherical shell with a radius equal to the wave number $k_0 = 1/\lambda$. Accordingly $\tilde{G}_{\mathrm{NA}}(\mathbf{k})$ is given by,

$$\tilde{G}_{\mathrm{NA}}(\mathbf{k}) = \frac{j}{4\pi k_{\mathrm{o}}}\delta(|\mathbf{k}| - k_0) \cdot \mathrm{step}\left(\frac{\mathbf{k}\cdot\hat{\mathbf{o}}}{k_{\mathrm{o}}} - \sqrt{1 - N_{\mathrm{A}}^2}\right) \tag{8.7}$$

where N_{A} is the NA of the objective, $\hat{\mathbf{o}}$ is a unit vector in the direction of the viewing axis, and $\delta(x)$ and $\mathrm{step}(x)$ represent the Dirac delta function and Heaviside step function, respectively.

It is clear that (8.3) and (8.6) have identical form; however, it is important to emphasize that the TF, $\tilde{H}(\mathbf{k})$ in (8.3), is applied to the *spectrum of the object function*, $\tilde{\Delta}(\mathbf{k})$, whereas $\tilde{G}_{\mathrm{NA}}(\mathbf{k})$ modifies the *spectrum of the scattered field*, $\tilde{E}^s(\mathbf{k})$. In order to calculate the TF for DHM, $\tilde{H}_{\mathrm{DHM}}(\mathbf{k})$, it is necessary to consider the illumination. From the discussions in Section 2 it is apparent that if the object is illuminated by a plane wave described by the vector k_{i}, $\tilde{H}_{\mathrm{DHM}}(\mathbf{k})$, and $\tilde{G}_{\mathrm{NA}}(\mathbf{k})$ are related such that,

$$\begin{aligned}\tilde{H}_{\mathrm{DHM}}(\mathbf{k}) &= \tilde{G}_{\mathrm{NA}}(\mathbf{k} + \mathbf{k}_{\mathrm{i}}) \\ &= \frac{j}{4\pi k_{\mathrm{o}}}\delta(|\mathbf{k} + \mathbf{k}_{\mathrm{i}}| - k_0) \cdot \mathrm{step}\left(\frac{(\mathbf{k} + \mathbf{k}_{\mathrm{i}})\cdot\hat{\mathbf{o}}}{k_{\mathrm{o}}} - \sqrt{1 - N_{\mathrm{A}}^2}\right)\end{aligned} \tag{8.8}$$

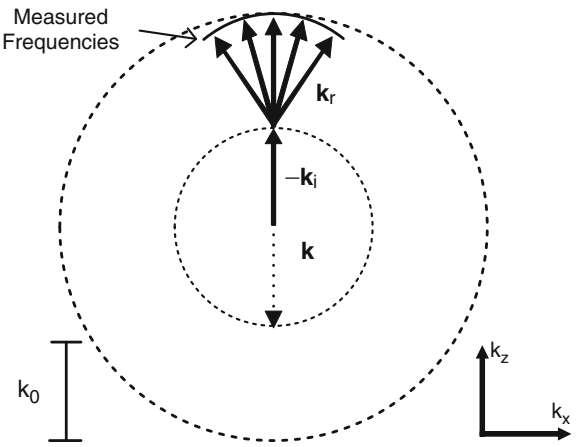

Fig. 8.6 TF of a coherent microscope

A DHM is therefore sensitive to spatial frequencies within the object function that lie on a spherical shell of radius equal to the wave number that is translated from the origin by a vector equal to $-\mathbf{k}_i$. This is illustrated in Fig. 8.6 for the case of axial backscatter illumination, where $\mathbf{k}_i = -k_0\hat{\mathbf{o}}$.

Inverse Fourier transformation of the TF gives the PSF and provides further insight into the imaging process. This has been computed for a back-scatter DHM configuration with NA $= 0.55$ operating at $\lambda = 600$ nm and a section through this distribution is shown in Fig. 8.7.

By definition the PSF of an instrument provides the image of a weakly scattering point object. For DHM it is found that the intensity of the PSF decreases as the square of the distance in the observation direction from its center, in exactly the same way as a focused beam. This means that the total power in any plane perpendicular to the optical axis remains constant and as such a DHM does not produce a 3D image in the strictest sense [5]. Nevertheless, if it is used to investigate sparsely seeded flows, individual particles can be distinguished as bright points in the reconstruction and their 3D position can be measured [34].

A good example of DHM taken from a study of underwater microbiology by Jorge Garcia-Sucerquia et al. [6] is shown in Fig. 8.8. This image is a reconstruction from an in-line hologram.

8.4 Optical Coherence Tomography

Optical Coherence Tomography (OCT) differs fundamentally from DHM because it measures the coherent response of the object *to light of different wavelengths*. Imaging OCT was originally proposed by Huang et al. [13] and has been practiced in many forms. OCT has major applications in opthalmology where it is used extensively to diagnose retinal disorders. For these applications it is convenient to use galvanometer scanning mirrors to scan the retina as shown in the so-called fundus camera illustrated in Fig. 8.9.

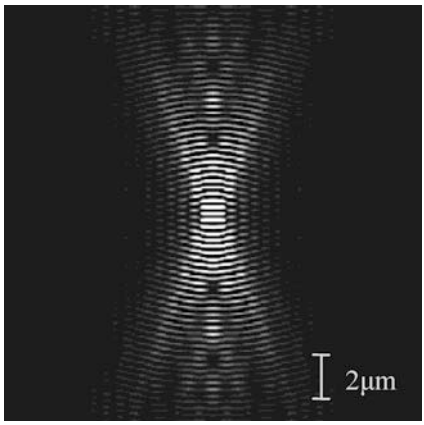

Fig. 8.7 PSF of a coherent microscope (positive real part shown)

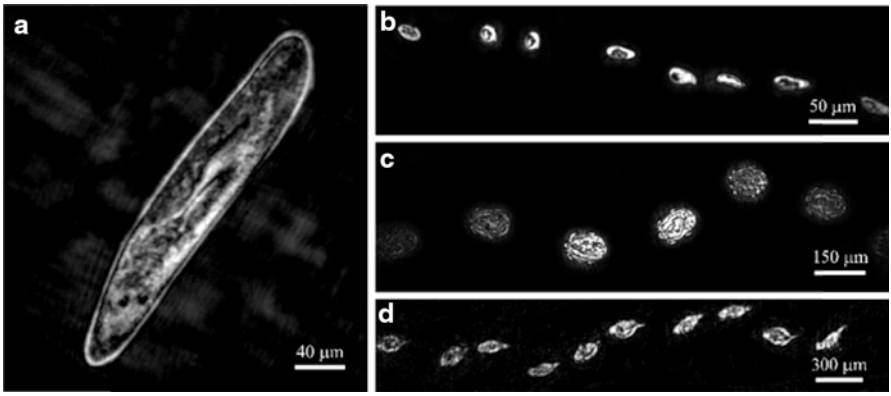

Fig. 8.8 Images taken with underwater DHM. (**a**) Paramecium. (**b–d**) Trajectories of various species swimming through the observation window, with a frame rate of 10 frames/s. (**b**) Ciliate; (**c**), Didinium; (**d**) Rotifer (Reproduced with permission)

The scanning system is connected to the interferometer or OCT engine unit by a fiber optic. Early time domain ophthalmic OCT systems (TD-OCT) used the Michelson interferometer configuration as shown in Fig. 8.10. In this case the interference between object and reference paths is recorded as the depth scan is performed by a mechanically driven mirror. OCT requires a bright light source of limited temporal coherence and super-luminescent diodes, ultrashort pulse and super-continuum lasers have all been used for this purpose [18].

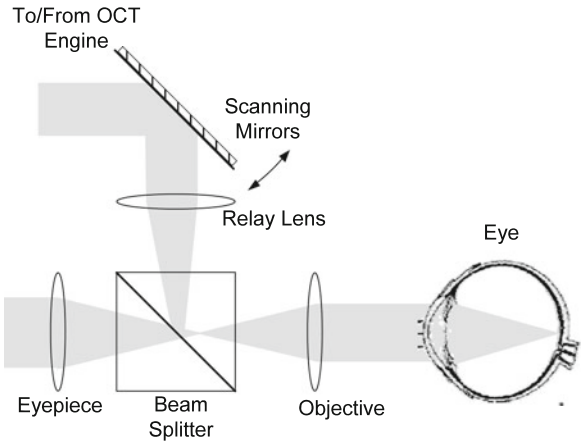

Fig. 8.9 Fundus camera

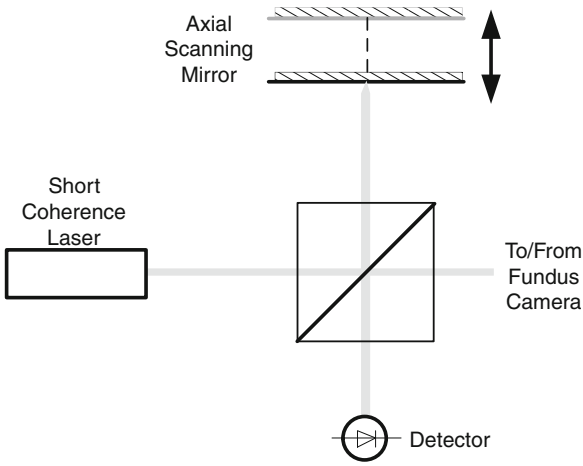

Fig. 8.10 Time domain OCT

With TD-OCT scanning speeds are generally slow. State-of-the-art systems can achieve scan rates up to 8,000 depth scans/s but the reduced sensitivity at these scanning speeds makes retinal imaging impracticable [18]. The need for mechanical scanning is obviated in frequency domain OCT (FD-OCT) and consequently the time necessary to perform a depth scan can be reduced dramatically.

FD-OCT can be implemented using either a tunable source or a white light source together with a spectrometer array as shown in Fig. 8.11. In either case the interference between object and reference paths is recorded as a function of the source frequency (or wave number). In contrast with TD-OCT, the interference signal acquired by FD-OCT has greater modulation and a significantly greater signal to noise ratio (SNR). For this reason FD-OCT is preferred in high speed, high resolution systems.

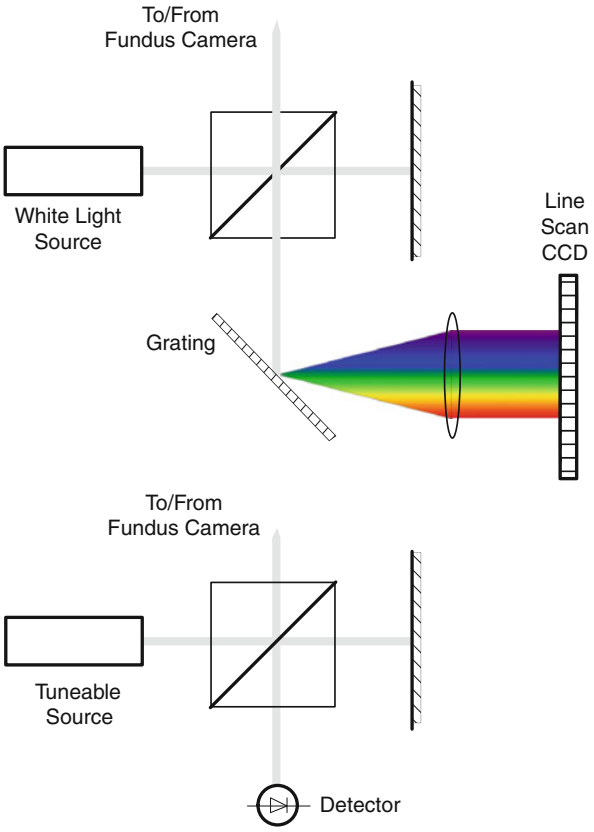

Fig. 8.11 Frequency domain OCT

Although there are many ways to implement OCT they all measure the coherent response of an object when the *wavelength* of the illumination is varied. An FD-OCT system can be considered as the superposition of images from a coherent microscope made at different wavelengths as shown schematically for illumination with four different wave numbers in Fig. 8.12.

In a practical system the illumination wavelength is scanned and if the frame rate of the detector is sufficient, the measured frequencies form a continuum. In this case the TF of the system can be written as the superposition integral [21],

$$\tilde{H}_{\mathrm{OCT}}(\mathbf{k}) = \frac{j}{4\pi}\int_{-\infty}^{+\infty}\frac{S(k_{\mathrm{o}})}{k_{\mathrm{o}}}\delta(|\mathbf{k}+\mathbf{k}_i|-k_0) \cdot \mathrm{step}\left(\frac{(\mathbf{k}+\mathbf{k}_i)\cdot\hat{\mathbf{o}}}{k_{\mathrm{o}}} - \sqrt{1-N_{\mathrm{A}}^2}\right)\mathrm{d}k_0 \tag{8.9}$$

where $S(k_{\mathrm{o}})$ is the source spectrum expressed as a function of wave number. Inverse Fourier transformation of this expression gives the PSF that is shown in Fig. 8.13. For the sake of comparison, the PSF has been computed for a system with the

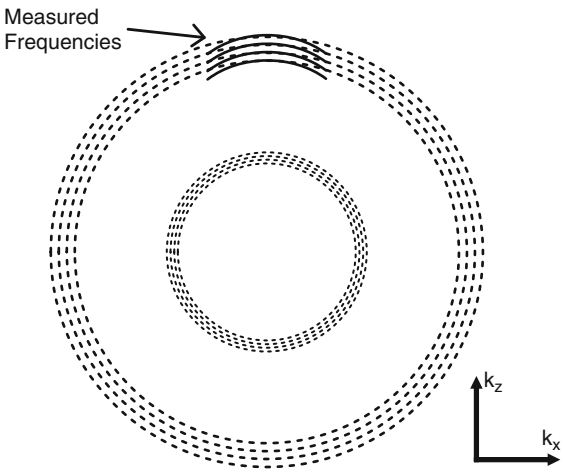

Fig. 8.12 TF of an OCT system

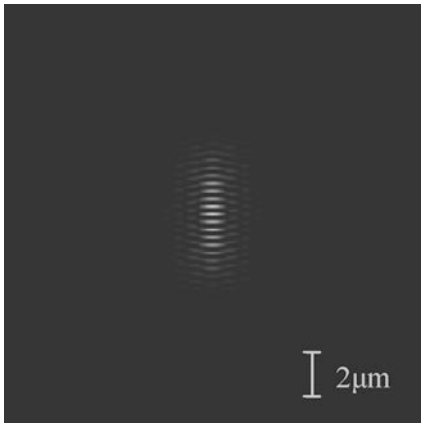

Fig. 8.13 PSF of an OCT system (positive real part shown)

previous NA = 0.55 operating with the same mean wavelength of $\lambda = 600$ nm and a Gaussian spectral distribution with bandwidth of 100 nm (FWHH@$1/e^2$). It can be seen that in comparison with the PSF of DHM shown in Fig. 8.7, the total intensity of the OCT PSF reduces in planes orthogonal to the viewing direction and OCT therefore provides greatly enhanced 3D information. In OCT the extent of the PSF in the axial (i.e., observation) and lateral (perpendicular to the observation) directions are inversely proportional to the source bandwidth and the NA, respectively. It is important to point out that most commercial OCT systems operate with much reduced aperture (NA = 0.01) resulting in a PSF with proportionately larger lateral dimensions.

Fig. 8.14 provides a good example of OCT in medical imaging taken from an in vivo study of human skin by Alex et al. [35]. Depth sections (B-scans) through the surface clearly identify the different layers up to a depth of around 3 mm.

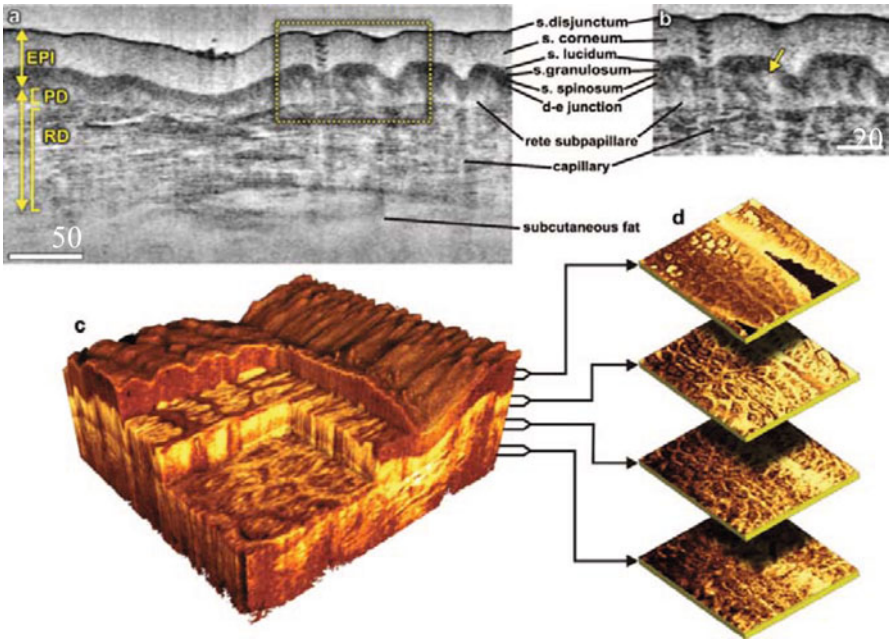

Fig. 8.14 OCT skin images at 1,300-nm (**a**) B-scan of skin above the proximal interphalangeal joint of the middle finger. (**b**) Magnified view of epidermis and dermis (*yellow arrow* points towards the dermal–epidermal junction). (**c**) 3D rendering of the same region reconstructed using 1024 B-scans. (**d**) En face sections of the same (Reproduced with permission)

8.5 Coherence Scanning Interferometry

CSI and confocal microscopy can also be considered to be tomographic techniques and are discussed together in this section because they both provide additional 3D information that is beyond that obtainable using coherent microscopy and OCT. This information is the response of the object to illuminating plane waves *propagating at different angles*. Interestingly, both CSI and confocal microscopy predate coherent microscopy and OCT.

In CSI the object is illuminated by a wide-band distributed source (halogen or LED) through a Mirau interference objective as shown in Fig. 8.15. Interference between the light reflected from a reference surface (within the Mirau objective) and that from the objective is recorded by the CCD as the object is scanned through focus. Considering first the distributed nature of the source, the interference fringes generated by a quasi-monochromatic CSI can be considered to be due to the superposition of coherent recordings made of different plane waves propagating at different angles [21]. The response is illustrated schematically for five different plane wave illuminations in Fig. 8.16.

In practice, if a distributed source and appropriate condenser lenses are used to fill the aperture of the objective, the TF becomes a continuum within the region shown.

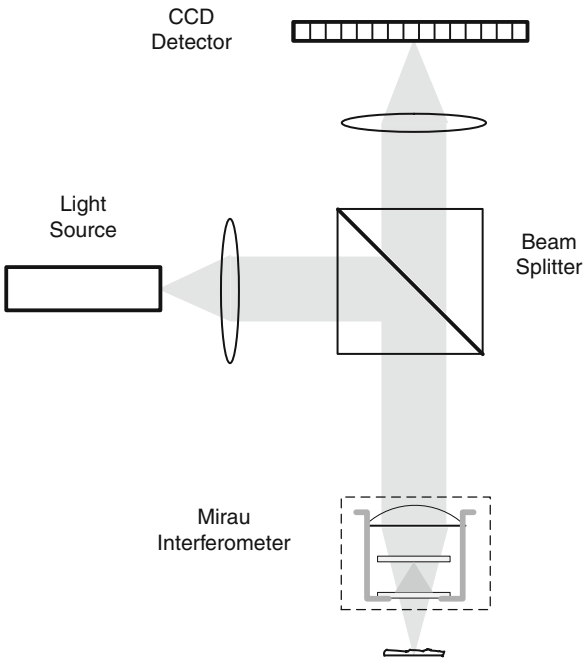

Fig. 8.15 CSI configuration

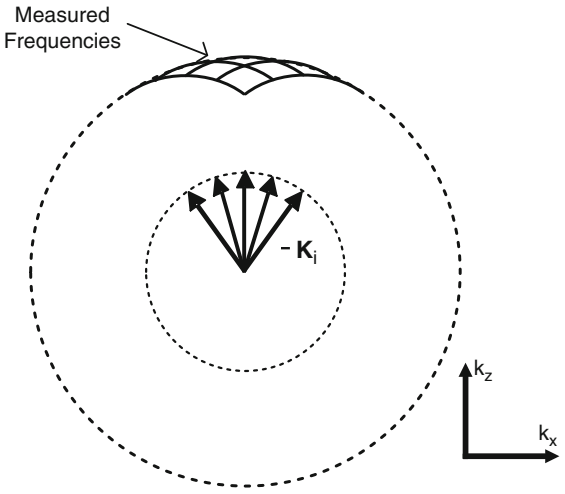

Fig. 8.16 TF of quasi-monochromatic CSI system

If we now consider a polychromatic source the superposition results in the TF shown schematically in Fig. 8.17. In practice a source will have a smooth spectrum and the TF will be a continuum defined by,

$$\tilde{H}_{\mathrm{CSI}}(\mathbf{k}) = \int_{-\infty}^{+\infty} S(k_0)A(\mathbf{k})\mathrm{d}k_0 \tag{8.10}$$

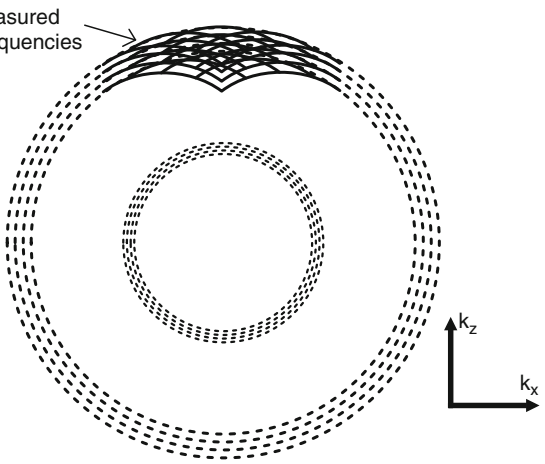

Fig. 8.17 TF of a polychromatic CSI system

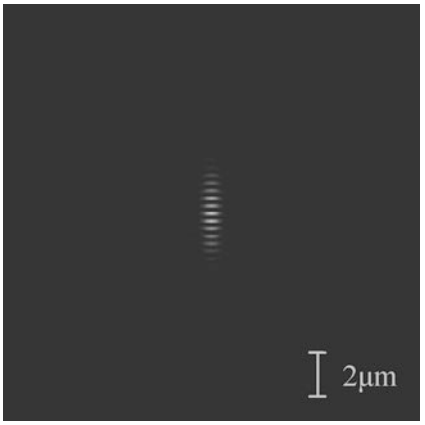

Fig. 8.18 PSF of a CSI system (positive real part shown)

where the function $A(\mathbf{k})$ is defined by the convolution,

$$A(\mathbf{k}) = \int_{-\infty}^{+\infty} \tilde{G}_{\mathrm{NA}}(\mathbf{k}')\tilde{G}_{\mathrm{NA}}(\mathbf{k}-\mathbf{k}')\mathrm{d}^3k' \tag{8.11}$$

For the sake of comparison, the PSF has been computed in Fig. 8.18 for a CSI with NA = 0.55 operating with the same mean wavelength of $\lambda = 600$ nm and a Gaussian spectral distribution with bandwidth of 100 nm (FWHH@$1/e^2$). It can be seen that the lateral dimensions of the PSF are approximately half that of the coherent microscope and the OCT system (Fig. 8.7 and Fig. 8.13) while the axial extent is slightly reduced.

Interestingly, the PSF of a laser confocal microscope (configuration shown in Fig. 8.19) is directly related to that of CSI [21]. In confocal microscopy, however, the detection process is not usually coherent (i.e., not interferometric) and consequently the PSF takes the form of the envelope of the PSF of a quasi-monochromatic CSI of the same NA.

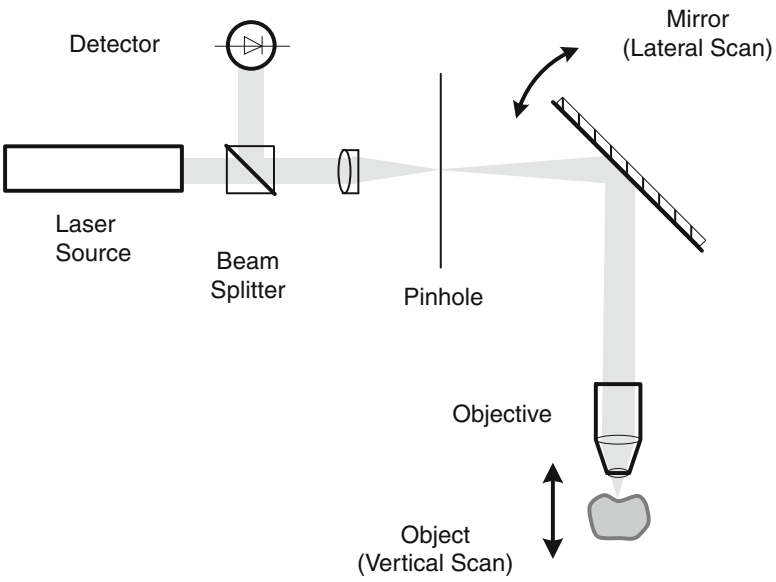

Fig. 8.19 Confocal microscope

From the discussions above it is clear that CSI and confocal microscopy are able to resolve twice the spatial frequency of OCT or DHM. It is also noted that at low NA the axial extent of the PSF for both CSI and OCT is inversely proportional to the source bandwidth. For quasi-monochromatic CSI and confocal microscopy, however, the axial extent is inversely proportional to the squared NA. For broadband CSI systems the axial extent is either bandwidth or NA limited and for typical systems a crossover is observed when NA ≈ 0.3.

8.6 Imaging Performance

In the previous sections we have introduced the methods of coherent microscopy and optical tomography and have characterized their performance in terms of 3D linear imaging theory. The response of the system to spatial frequencies within the object function, or refractive index contrast, is characterized by the TF which, in turn, depends on the aperture of both the illumination and observation optics. The PSF describes the appearance of a point-like object and is the inverse Fourier transform of the TF. The PSF has been calculated for backscatter DHM, OCT, and CSI configurations of equal NA as it provides a useful way to compare the 3D imaging performance of the techniques.

In all the calculated cases the PSF has a cyclic variation in phase along the central axis with a period approximately equal to half the mean wavelength.

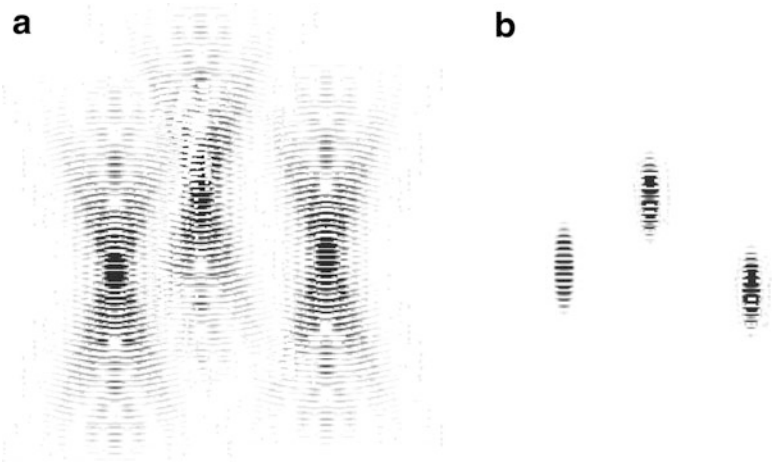

Fig. 8.20 Images of sparse particles using (**a**) DHM and (**b**) OCT

This is a characteristic of the backscatter geometry. A clear distinction between DHM, which uses a single illumination wave and that of the other tomographic techniques that in effect synthesize images from coherent recordings made with either multiple wavelengths and/or multiple illumination directions, is apparent. For the case of DHM (Fig. 8.7), the axial extent of the PSF is considerably greater than the tomographic techniques (Fig. 8.13 and Fig. 8.18). More precisely it can be shown that the total intensity in any plane perpendicular to the central axis of the PSF is equal. The effect of the PSF depends on the application. DHM has been used to measure fluid flow fields in micro-fluidic devices using the technique known as holographic particle image velocimetry (HPIV) [36]. In this application a transparent fluid is sparsely seeded with small particles and images are recorded at two or more instants in time. Since the PSF is by definition the image of a point object it is clear that provided that the particles are sufficiently small their images will take the form of the PSF. As a particle moves, its reconstructed image will move in sympathy and the particle velocity can be deduced by estimating the displacement of its image using correlation for example.

Using the PSFs previously calculated for the DHM and OCT systems a typical image of a sparsely seeded fluid is illustrated in Fig. 8.20. The effect of the PSF is immediately clear. If the particles are separated sufficiently then their images will be distinguishable and their 3D position can be estimated. If the particles are too close, however, the images will overlap, interfere, and become indistinguishable from a uniform background of laser speckle. Analysis shows that an upper limit on the total number of particles that can be identified in this way is proportional to the number of pixels required to record an optimally sampled holographic image [37]. Additional noise sources reduce this limit, however, and typically around 10^4 particles/mm^3 can be identified in practice.

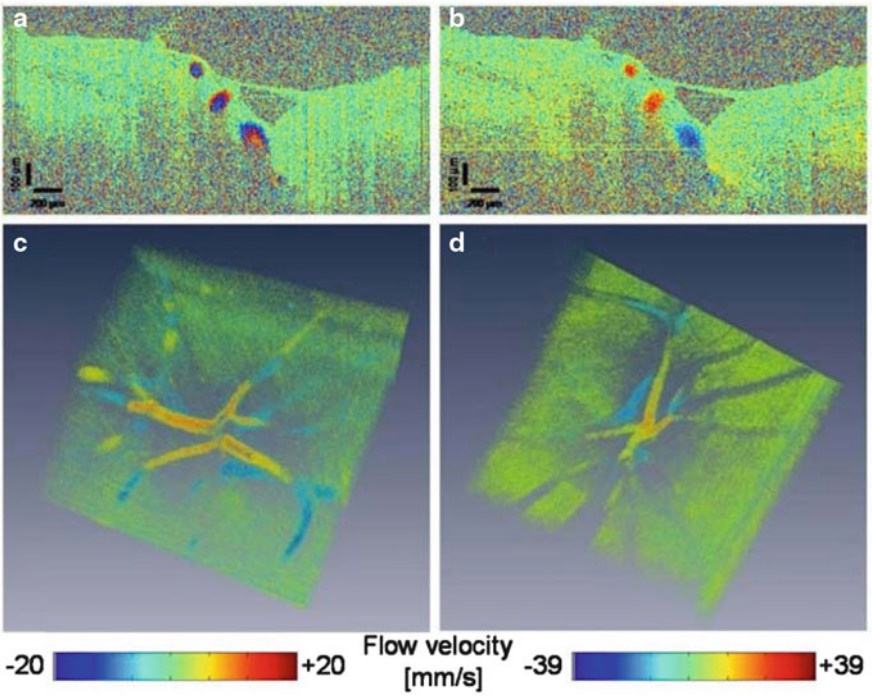

Fig. 8.21 Volumetric Doppler OCT imaging of retinal vasculature. (**a** and **b**) B-scan images close to the optic disk at 100 kHz and 200 kHz, respectively. (**c** and **d**) volumetric images of the retinal arteries and veins branching in the optic disk at 100 and 200 kHz

The PSFs of OCT, CSI and confocal microscopy reduce much more quickly in the axial direction than those of DHM and consequently many more particles can be distinguished per unit volume. The number of particles that can be distinguished is now inversely proportional to the volume of the PSF. From the dimensions of the OCT PSF shown in Fig. 8.13 we might expect around 10^8 particles per mm^3 while a lower NA OCT system (NA = 0.01) might return 10^4 particles per mm^3.

As mentioned previously, if the number concentration is increased the images of particles will overlap and interfere and the image will take on a speckled appearance. With the tomographic techniques, OCT, CSI, and confocal microscopy, it is possible to identify local changes in number density as the speckle will become proportionately brighter or darker. This is not true for the case of DHM, however; the slow decay of the PSF in the axial direction means that any 3D information is lost. For this reason it is necessary to use a tomographic method to image through tissue. As the number concentration or equivalently the scattering coefficient increases, however, the assumption of weak scattering (the Born approximation) breaks down and the effects of multiple scattering are observed. Typically this increases background noise in the reconstruction as a function of depth but can sometimes lead to a significant shadowing effect in low NA tomographic systems [18].

As a final point we note again that when a particle moves, its reconstructed image will move in sympathy. Because the backscatter PSF's have a cyclic phase variation in the axial direction, the phase of the reconstruction at a given point in space will change according to the movement of the surrounding particles in this direction. By measuring the rate of change of phase, or Doppler frequency, the axial velocity of the particles can be deduced. This is the basis of laser Doppler velocimetry that typically exploits a confocal configuration [38] and more recently has been exploited in Doppler OCT [5]. A good example of Doppler OCT showing retinal vasculature by Baumann et al. [37] is presented in Fig. 8.21.

The arterial and venous vessels in the papilla can be clearly distinguished. It is noted, however, that in Fig. 8.21a there appears to be bidirectional flow within the vessels. This is because the individual depth scans are obtained at a rate of 100 kHz which is insufficient to resolve the phase change unambiguously. By increasing the sample rate to 200 kHz the problem is resolved.

8.7 Conclusion and Discussion

This chapter has compared the 3D imaging methods DHM, OCT, CSI, and confocal microscopy with reference to their point spread and transfer characteristics. There is a major distinction between coherent microscopy, that records a single coherent image at a single wavelength, and the other, tomographic, techniques that construct an image from a range of wavelengths and illumination conditions. The tomographic techniques provide superior performance when compared to coherent microscopy but require additional images to be taken with different illumination conditions. This additional information comes at the expense of time and frequently it is necessary to compromise performance.

Although coherent microscopy can only be used to study relatively sparsely seeded flows, it is currently the only flow mapping technique capable of simultaneous whole-field flow measurement. Line transfer CCD cameras and double pulsed laser sources, that are often used in particle image velocimetry, make it possible to record pairs of holograms separated by 1–2 μs at megapixel resolution and at more than 1,000 frame pairs per second. For micro-flow measurement this means a maximum flow velocity of approximately 1–10 m/s depending on the configuration.

To image through scattering media or increase the data density by introducing more seeding particles it is necessary to use a tomographic technique. Doppler OCT is now used routinely, both to image and measure blood flow within the retina. In its original form OCT used a configuration similar to low NA CSI and used a broadband incoherent source. This configuration is referred to as space domain OCT and required slow mechanical scanning. Commercial swept-source OCT systems now exploit fast scanning laser sources to measure the backscattered light scattering along the path of a weakly focused beam. 2D scanning mirrors are required to produce a complete 3D image. Typically the depth scan rate is around 100–200 kHz, and this limits the maximum velocity to around

25–50 mm/s. Although, only the velocity component along the viewing direction is measured and this generally varies with position the 3D flow field can be synthesized from three or more data sets.

The methods of CSI and confocal microscopy have been included in this chapter because of their close relationship to the other techniques. As described in Section 3 both quasi-monochromatic CSI and confocal microscopy derive 3D information by illuminating the object with plane waves from different angles within the NA of the objective. Additionally, broadband CSI exploits spectral information like OCT. According to linear theory, CSI and confocal microscopy will work with more densely seeded flows than DHM and offer significantly better resolution than OCT.

Nevertheless OCT remains the method of choice for in vivo flow measurement for several reasons. Fundamentally, OCT is different from all the other methods. In DHM, CSI and confocal microscopy lateral and depth resolution are coupled as they are proportional to NA and the square of the NA, respectively. In OCT the depth resolution is proportional to the bandwidth of the source and this decoupling allows the PSF of OCT to be tailored to suit different scales. This is exploited in many examples of in vivo imaging since propagation through a rough distorting surface (e.g., the epidermis) generally ruins the fidelity of images with large NA. It is this flexibility, plus the efficiency of swept-source scanning that makes OCT such a powerful tool for biomedical applications.

References

1. Abbe E (1874) A contribution to the theory of the microscope and the nature of microscopic vision. Proc Bristol Nat Soc 1:200–261
2. Zernike F (1942) Phase-contrast, a new method for microscopic observation of transparent objects. Part 1. Physica 9:686–698
3. Zernike F (1942) Phase-contrast, a new method for microscopic observation of transparent objects. Part II. Physica 9:974–986
4. Minsky M (1988) Memoir on inventing the confocal scanning microscope. Scanning 10:128–138
5. Fercher AF, Drexler W, Hitzenberger CK, Lasser T (2003) Optical coherence tomography—principles and applications. Rep Prog Phys 66:239
6. Garcia-Sucerquia J, Xu W, Jericho SK, Klages P, Jericho MH, Kreuzer HJ (2006) Digital in-line holographic microscopy. Appl Opt 45:836–850
7. Zhang T, Yamaguchi I (1998) Three dimensional microscopy with phase-shifting digital holography. Opt Lett 23:1221–1223
8. Cuche E, Marquet P, Depeursinge C (1999) Simultaneous amplitude-contrast and quantitative phase-contrast microscopy by numerical reconstruction of Fresnel off-axis holograms. Appl Opt 38:6994–7001
9. Kuehn J, Montfort F, Colomb T, Rappaz B, Moratal C, Pavillon N, Marquet P, Depeursinge C (2009) Submicrometer tomography of cells by multiple wavelength digital holographic microscopy in reflection. Opt Lett 34:653–655
10. Cuche E, Bevilaqua F, Depeursinge C (1999) Digital holography for quantitative phase-contrast imaging. Opt Lett 24:291–293
11. Lobera J, Coupland JM (2008) Contrast enhancing techniques in digital holographic microscopy. Meas Sci Technol 19:025501

12. Ferraro P, Wax A, Zalevsky Z (2010) Coherent light microscopy. Springer, Berlin
13. Huang D, Swanson EA, Lin CP, Schuman JS, Stinson WG, Chang W, Hee MR, Flotte T, Al E (1991) Optical coherence tomography. Science 254:1178–1181
14. Dresel T, Hausler G, Venzke H (1992) Three-dimensional sensing of rough surfaces by coherence radar. Appl Opt 31:919–925
15. Lee BS, Strand TC (1990) Profilometry with a coherence scanning microscope. Appl Opt 29:3784–3788
16. Schmitt JM (1999) Optical coherence tomography (OCT): a review. IEEE J Sel Top Quant Electron 5:1205
17. Bouma BE, Tearney GJ (2002) Handbook of optical coherence tomography. Marcel Dekker, New York
18. Drexler W, Fujimoto JG (2008) Optical coherence tomography: technology and applications. Proceedings of SPIE the international society for optical engineering, Springer
19. Brezinski M (2006) Optical coherence tomography: principles and applications. Academic, Burlington, MA
20. Lauer V (2002) New approach to optical diffraction tomography yielding a vector equation of diffraction tomography and a novel tomographic microscope. J Microsc 205:165–176
21. Coupland J, Lobera J (2008) Optical tomography and digital holography. Meas Sci Technol 19:070101. doi:10.1088/09570233/19/7/070101
22. Kak AC, Slaney M (1987) Principles of computerized tomography. IEEE, Piscataway, NJ
23. Wilson T (ed) (1990) Confocal microscopy. Academic, San Diego, CA
24. Leach R (2011) Optical measurement of surface topography. Springer, Berlin
25. Ruiz PD, Huntley JM, Coupland JM (2011) Depth-resolved imaging and displacement measurement techniques viewed as linear filtering operations. Exp Mech 51(4):453–465
26. Wolf E (1969) Three-dimensional structure determination of semi-transparent objects from holographic data. Opt Commun 1:153–156
27. Dandliker R, Weiss K (1970) Reconstruction of three-dimensional refractive index from scattered waves. Opt Commun 1:323–328
28. Born M, Wolf E, Bhatia AB (1999) Principles of optics. Cambridge University Press, Cambridge
29. Bragg WL (1913) The diffraction of short electromagnetic waves by a crystal. Proc Cambridge Philos Soc 17:43–57
30. Gabor D (1948) A new microscopic principle. Nature (London) 161:777–778
31. Gabor D (1949) Microscopy by reconstructed wavefronts. Proc Roy Soc Lond Ser A 197:454
32. Jericho MH, Kreuzer HJ (2010) Point source digital in-line holgraphic microscopy. In: Ferraro P, Wax A, Zalevsky Z (eds) Coherent light microscopy. Springer, Berlin, pp 3–30
33. Leith EN, Upatnieks J (1962) Reconstructed wavefronts and communication theory. J Opt Soc Am 52:1123–1130
34. Wormald SA, Coupland JM (2010) On measuring 3D flow within inkjet droplet streams using a digital holographic microscope. J Modern Opt 57(9):700
35. Alex A, Povazay B, Hofer B, Popov S, Glittenberg C, Binder S, Drexler W (2010) Multispectral in vivo three-dimensional optical coherence tomography of human skin. J Biomed Opt 15:026025
36. Coupland JM, Halliwell NA (1992) Particle image velocimetry: three-dimensional fluid velocity measurements using holographic recording and optical correlation. Appl Opt 31:1005–1007
37. Baumann B, Potsaid B, Kraus MF, Liu JJ, Huang D, Hornegger J, Cable AE, Duker JS, Fujimoto JG (2011) Total retinal blood flow measurement with ultrahigh speed swept source/Fourier domain OCT. Biomed Opt Exp 2:1539–1552
38. Durst F, Melling A, Whitelaw J (1981) Principles and practice of laser Doppler anemometry. Academic, London

Chapter 9
Confocal Micro-PIV/PTV Measurements of the Blood Flow in Micro-channels

Rui Lima, Takuji Ishikawa, Yohsuke Imai, and Takami Yamaguchi

Abstract The development of optical experimental techniques has contributed to obtaining explanations of the behaviour of blood flowing in micro-channels. Although past results have been valuable, detailed studies on the flow properties of in vitro blood in micro-channels have been limited by several technical factors such as poor spatial resolution and difficulty in obtaining quantitative detailed measurements at such small scales. In recent years, due to advances in computers, optics, and digital image processing techniques, it has become possible to combine both particle image velocimetry (PIV) and particle tracking velocimetry (PTV) methods with confocal microscopes. As a result, this combination has greatly increased the resolution of conventional micro-PIV/PTV systems and consequently provided additional detailed description on the motion of blood cells not obtainable by traditional methods. In this chapter the most relevant theoretical and technical issues related to both conventional and confocal micro-PIV/PTV methods are discussed. Additionally, the most recent studies on the blood flow behaviour in micro-channels obtained by our confocal micro-PIV/PTV system are also reviewed.

R. Lima (✉)
DTM, ESTiG/IPB, Braganca Polytechnic, C. Sta. Apolonia, Braganca 5301-857, Portugal

CEFT, FEUP, Porto University, R. Dr. Roberto Frias, Porto 4200-465, Portugal
e-mail: ruimec@ipb.pt

T. Ishikawa • Y. Imai
School of Engineering, Tohoku University, 6-6-01 Aoba, Sendai, 980-8579, Japan

T. Yamaguchi
School of Biomedical Engineering, Tohoku University, 6-6-01 Aoba, Sendai 980-8579, Japan

M.W. Collins and C.S. König (eds.), *Micro and Nano Flow Systems for Bioanalysis*, Bioanalysis 2, DOI 10.1007/978-1-4614-4376-6_9,

9.1 Introduction

Human blood is a complex fluid composed mainly of suspended deformable red blood cells (RBCs) within the plasma flow, which are responsible for the supply of oxygen and nutrients to, and removal of carbon dioxide and metabolic wastes from tissues. Phenomena of blood flow in microcirculation depend on several combined effects such as cell deformability, flow shear rates and vessel wall, together with micro-scale biochemical and physiological factors. Since the availability of microscopic techniques scientists have started using optical methods mainly because they are less invasive for measuring the flow field. However, the fact that measurements of blood flow in the microcirculation need to be performed at very small scales has limited the number of flow measurement techniques suitable for this purpose. For instance, MRI and ultrasonography are not suitable for obtaining quantitative flow information in micro-vessels mainly due to their poor spatial resolution. The majority of the works performed in the past to measure blood flow in micro-vessels and micro-channels are double-slit photometry [4,12], video microscopy and image analysis [2,6,13–15,41,43] and laser-Doppler anemometry [5,7,9,16,49]. Recently, the considerable progress in computing capability, optics, high-speed imaging and image processing techniques have made it possible to successfully combine a conventional PIV system with an inverted epifluorescent microscope [19,39,45,51]. This combination, known as micro-PIV, has greatly increased the resolution of conventional PIV; as a result, this technique has gained widespread use to investigate blood flow behaviour in both micro-channels and micro-vessels. Sugii and his co-workers, by using a conventional micro-PIV system, have used red blood cells as tracer markers to measure their velocities in both straight [46] and bifurcated arterioles [40] and they found that the velocity profiles were markedly blunt in the central region. Later they measured both tracer particles and RBCs through a 100 μm glass capillary and they reported that by using in vitro blood with 20% hematocrit (Hct) the velocity profiles were parabolic [47]. More recently, by using liposome tracer particles the blood-plasma velocity has been measured in the beating heart of a chicken embryo [50]. Kim and Lee [18] have analysed the flow behaviour of blood through a circular opaque micro-channel by using an X-ray PIV technique. Their measurements have shown typical non-Newtonian flow characteristics of blood such as yield stress and shear-thinning effects. Generally, most of the findings relating to blood flow dynamics using conventional micro-PIV have yielded conflicting results. In addition, such measurements do not give detailed information on the micro-scale flow behaviour of RBCs in micro-vessels. Hence, there is a need to apply other kinds of optical methods better able to obtain further insight into the complex flow behaviour of blood in the microcirculation.

Recently, the ability to combine both conventional particle image velocimetry (PVI) and particle tracking velocimetry (PTV) systems with a spinning disc confocal microscope (SDCM) has proven an extremely powerful technique to obtain detailed qualitative and quantitative measurements of in vitro blood flowing

through micro-channels. The current chapter will present the most relevant theoretical and technical issues related to both methods and also a comparison between them. Additionally, our most recent confocal micro-PIV/PTV results of blood flow behaviour in both glass and polydimethylsiloxane (PDMS) micro-channels are reviewed.

9.2 PIV/PTV Principles

9.2.1 Calculation Methodology

The principle of calculating several physical parameters (displacement, velocity, shear stress, etc.) related to fluid mechanics is common to both PIV and micro-PIV. The traditional way consists of measuring the displacement of fluorescent tracer particles flowing within the working fluid. However, to measure physiological fluids, such as blood, it is also common to use labelled blood cells as natural tracer particles. By applying a powerful light source, the tracer particles or cells of interest are illuminated and as a result objects with a known time interval (Δt) can be recorded by a high speed camera. By using a short Δt, it can be assumed that the magnitude and direction of the object velocities are constant. As a result, the location of a particle on two consecutive images can be used to estimate its instantaneous velocity as:

$$\vec{u} = \frac{\vec{x}_{t+\Delta t} - \vec{x}_t}{\Delta t} \tag{9.1}$$

$$\vec{v} = \frac{\vec{y}_{t+\Delta t} - \vec{y}_t}{\Delta t} \tag{9.2}$$

where u and v are respectively the velocity components of the particle in the x and y direction. Figure 9.1 shows an overview of the PIV/PTV principle.

The approach used to calculate the velocity of one particle can be extended to the entire flow field of interest. In microfluidics it is common practice to average the instantaneous velocities over a large number of recorded image pairs (N usually greater than 20). Hence, the time-average mean velocity vector of the flow can be defined as

$$\vec{U} = \frac{1}{N} \sum_{t=1}^{N} \vec{u}_t \tag{9.3}$$

$$\vec{V} = \frac{1}{N} \sum_{t=1}^{N} \vec{v}_t \tag{9.4}$$

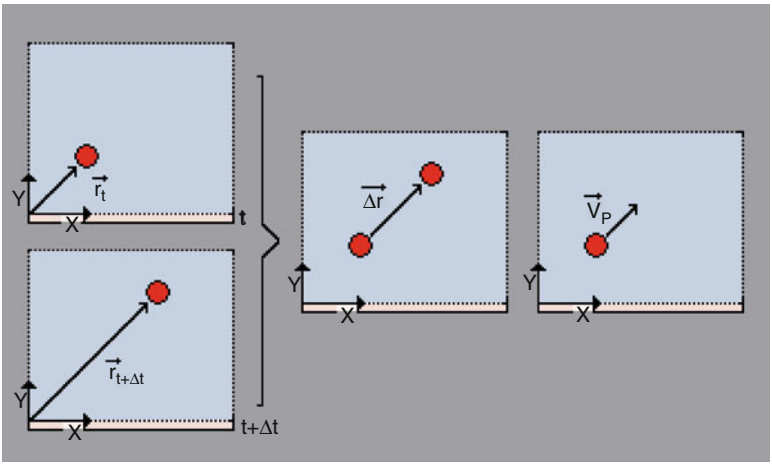

Fig. 9.1 Principle for both PIV and PTV (adapted from [24])

where N is the number of instantaneous velocity measurements, u and v are the time-average mean velocity components of the particle in the x and y directions, respectively.

9.2.2 PIV vs. PTV Methods

The density of trace particles in the images determines the most suitable PIV methodology to calculate the velocity fields. For high concentration of particles, i.e. the interrogation window contains at least three particles, the method is known as high-image-density PIV mode (see Fig. 9.2) [1]. Several researchers consider this method as the most reliable way of determining the velocity field which is estimated by using a statistical technique known as cross-correlation. It is described with much more detail elsewhere [24,27], the overall method being known as PIV cross-correlation, or simply PIV.

In some specific situations such as physiological fluids with high concentrations of cells, the amount of tracer particles captured within the fluid is often low (see Fig. 9.2). One way to overcome the problem of this particular condition is to measure the displacements by tracking individual particles or cells (see Fig. 9.3). This low-image-density PIV methodology is often referred to as particle tracking velocimetry (PTV) or as single particle tracking (SPT) [1,44]. By using this method detailed quantitative information can be obtained on the motion of particles and cells flowing within the working fluid. PTV is, however, limited in its ability to compute automatically particle trajectories, especially when there are multiple collisions of particles or cells. One way to overcome this limitation is by using manual tracking methods.

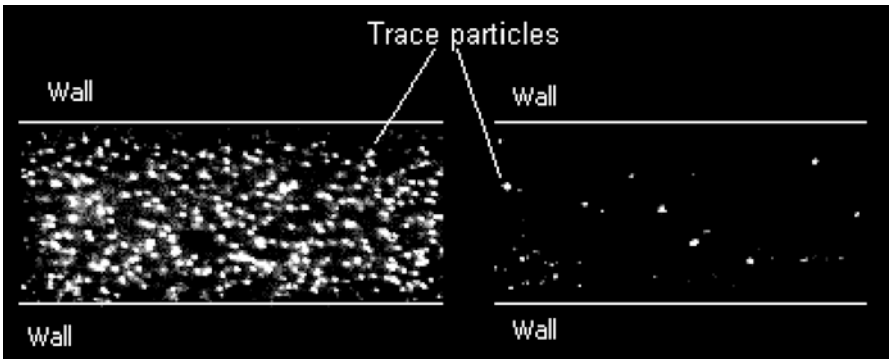

Fig. 9.2 Confocal high density image with pure water (*left image*) and confocal low density image with blood 30 % Hct (*right image*)

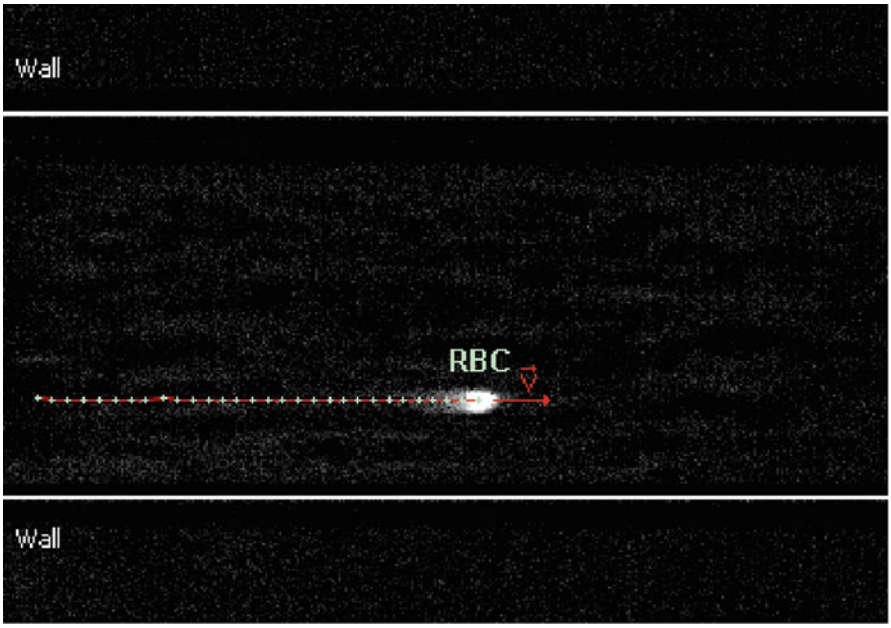

Fig. 9.3 Trajectory of RBC flowing in a micro-channel by using a manual particle tracking technique from ImageJ

9.3 Confocal Micro-PIV/PTV System

9.3.1 Conventional Micro-PIV System

A conventional micro-PIV system consists essentially of a microscope, an objective lens, optical filters, a light source for flow illumination and a high speed camera. Figure 9.4 gives a schematic illustration of a conventional micro-PIV system. Briefly, the light enters the microscope and is reflected 90° upwards by a dichromatic mirror to be transmitted through the objective lens which illuminates the entire flow volume. The objective lens collects the light emitted from the particles which goes back to the dichromatic mirror and to a high speed camera to record the signals from the trace particles. Finally, the recorded images are transferred to a computer to use a PIV post-processing method such as the cross-correlation technique. It is worth mentioning that the resolution of a micro-PIV system is influenced by several factors such as: out-of-focus particle images due to the volume illumination, and density and size of the tracer particles. By using a confocal system, most of the out-of-focus particles can be removed, consequently reducing the errors generated in the velocity field measurements.

9.3.2 Confocal Micro-PIV System

A confocal micro-PIV system consists usually of an inverted microscope combined with a confocal scanning unit (CSU), a high resolution objective lens, a high power

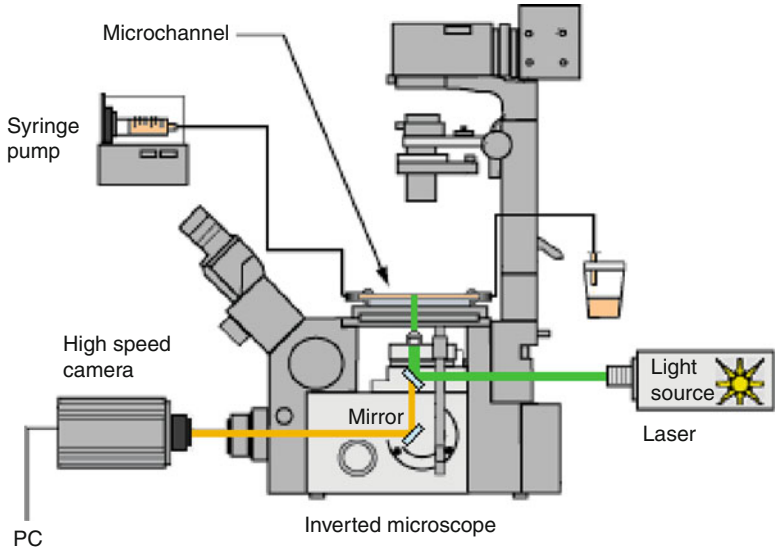

Fig. 9.4 Experimental setup of a conventional micro-PIV system.

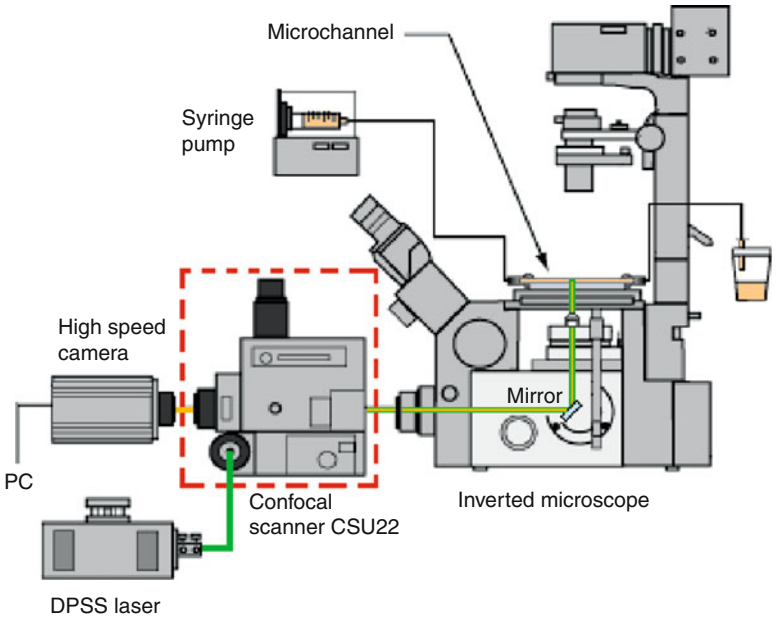

Fig. 9.5 Experimental setup of a confocal micro-PIV system

light source (usually laser) and a high speed camera, as shown in Fig. 9.5. In a confocal system the light enters the CSU and then is conducted to the microscope to illuminate the sample from below the microscope stage. The light emitted from the fluorescent trace particles goes back into the CSU and then to a high-speed camera to capture the confocal images.

9.3.3 Comparison Between Conventional and Confocal Micro-PIV

Figures 9.4 and 9.5 show the main components of both conventional and confocal micro-PIV systems. It is clear that the main difference between the two systems is the existence of a CSU in the confocal system. A study to compare the systems was performed under the same flow conditions. The flow measurements were performed in a 100 μm glass square micro-channel where pure water seeded with 0.15% of tracer particles was pressure driven by means of a syringe pump.

Figure 9.6, clearly demonstrates that by using a CSU it is possible to obtain much clearer image definition of the individual trace particles. Hence, a confocal system reduces the out-of-focus background noise and therefore increases the contrast and definition of an image. By contrast, images recorded by the conventional system were largely blurred, since the out-focus-light reduces contrast and

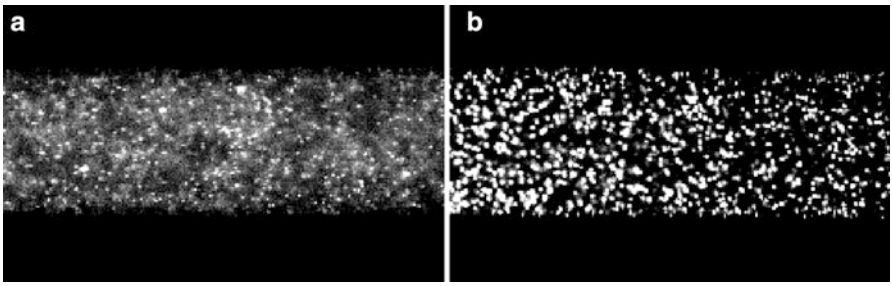

Fig. 9.6 Comparison of particle images from (**a**) conventional and (**b**) confocal micro-PIV system at 20 μm depth for pure water

decreases resolution making it difficult to identify the tracer particles within the flow. Note that the conventional microscopic images were obtained by using an epifluorescent microscope equipped with a mercury lamp and colour filters. These images may be improved by using a more powerful light source, such as a laser or metal halide.

9.4 Confocal Micro-PIV/PTV Measurements and Results

This section shows the most recent studies on blood flow behaviour in micro-channels performed by our confocal micro-PIV/PTV system. The main emphasis is on the confocal micro-PIV/PTV results obtained from both glass and polydimethylsiloxane (PDMS) micro-channels.

9.4.1 Working Fluids, Micro-channels, Experimental Set-up and Image Analysis

Confocal micro-PIV measuements were performed with different working fluids such as physiological saline (PS) with fluorescent trace particles, and in vitro blood containing trace particles and human RBCs with a hematocrit (Hct) up to 20%. Confocal micro-PTV experiments were carried out also with different working fluids such as dextran 40 (Dx-40) containing about 3% Hct up to 35% Hct of human RBCs. For this latter system, rather than employing fluorescent particles labelled RBCs were used to study the flow in micro-channels. A full description of the procedure for labeling human RBCs can be found in Lima et al. [28].

For both confocal systems experiments were performed with different kinds of micro-channels, such as 100-μm and 50-μm circular and square borosilicate glass micro-channels as fabricated by Vitrocom (Mountain Lakes, NJ, USA) [23,25,31]. By using a soft lithographic technique it was also possible to fabricate rectangular

polydimensiloxane (PDMS) micro-channels with complex geometries such as stenoses, bifurcations, confluences and hyperbolic contractions [11,20–22,27,34–36,52,53]. Additionally, by using a wire casting technique [29] it was possible to fabricate 75-μm circular PDMS micro-channels.

Generally both confocal systems used in our flow studies consisted of an inverted microscope (IX71; Olympus, Tokyo, Japan) combined with a confocal scanning unit (CSU22; Yokogawa, Tokyo, Japan), a diode-pumped solid state (DPSS) laser (Laser Quantum Ltd., Stockport, UK) and a high-speed camera (Phantom v7.1;Vision Research, NJ, USA) (as in Fig. 9.5). All the micro-channels were placed on the stage of the microscope where the flow rate of the working fluid was kept constant using a syringe pump (KD Scientific Inc., Holliston, MA, USA). A thermo-plate controller (Tokai Hit, Shizuoka, Japan) was also used: this achieved a surrounding temperature around the micro-channel of about 37 °C. More detailed information about this system can be found elsewhere [23,24,27,28].

All the measurements were digitised and transferred to a computer for evaluation using Phantom camera control software (PH607). The PIV images of the flowing particles were processed and the flow velocity was determined using the cross-correlation PIV method (PivView). A full description and evaluation of the confocal micro-PIV system used in our studies can be found in Lima et al. [23]. For the case of the confocal micro-PTV measurements, series of confocal images were evaluated in Image J [3] using the manual tracking MtrackJ [38] plug-in. Generally, the motions of the labelled RBCs were manually tracked through successive images using the bright centroid criteria available at the MtrackJ. Using this method, it was possible to track labelled RBCs even when two cells were in close proximity. After obtaining a series of x and y positions, data were exported for the determination of several physical quantities such as velocity, radial displacement, and dispersion coefficient.

9.4.2 Confocal Micro-PIV Results

The ability of a confocal micro-PIV system to measure both pure water and diluted suspensions of RBCs was demonstrated by Lima et al. [23]. This study was performed with a square glass micro-channel and it was found that there was good agreement between the measured velocity profiles of pure water and an established analytical solution. Further work was performed by Lima et al. this time to measure both physiological saline (PS) and in vitro blood (20% Hct) in a rectangular PDMS micro-channel [27]. As expected for a long rectangular micro-channel, the velocity profiles were markedly smooth and flat in the centre of the micro-channel (as in Fig. 9.7). However, for the in vitro blood with 20% Hct, small fluctuations in the shape of the ensemble velocity profiles were observed (see Fig. 9.7). Possible reasons for these fluctuations are the interactions between neighbouring RBCs, the formation of a cell-free layer, abrupt increase in the

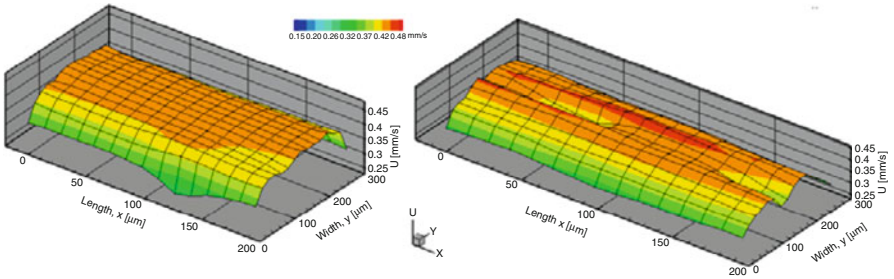

Fig. 9.7 Ensemble velocity profiles with PS (*left image*) and in vitro blood 20 % Hct (*right image*) in a rectangular PDMS micro-channel (from [27])

shear rate in the vicinity of the wall, Hct temporal variation and the light scattered and absorbed from the RBCs.

Lima and his colleagues have performed another study to measure both ensemble and instantaneous velocity profiles for in vitro blood (Hct up to 17%) flowing through a 100-µm square micro-channel [25]. All the measurements were made in the middle plane at a constant flow rate and low Reynolds number ($Re = 0.025$). Although the ensemble velocity profiles were markedly parabolic, some fluctuations in the instantaneous velocity profiles were found to be closely related to the Hct increase. This study has also shown strong evidence that the Root Mean Square (RMS) increases with the Hct increase suggesting that the concentration of RBCs within the plasma flow strongly influences the measurements of the instantaneous velocity fields. Possible reasons for the RMS increase are the motion and interaction of RBCs and the light scattered and absorbed by the RBCs. This latter behaviour seems to be predominant at an Hct value of about 17%. More detailed information about these results can be found in Lima et al. [25].

9.4.3 Confocal Micro-PTV Results

Confocal micro-PIV experiments have shown the ability to measure with good accuracy in vitro blood with Hct up to 9%, in a 100-µm square micro-channel. However, for Hct bigger than 9%, the light absorbed by the RBCs contributes to diminishing the concentration of tracer particles in the recorded confocal images. The low density images become more evident for Hct bigger than 20%, which generates spurious errors in the velocity fields [25]. Therefore, Lima and his colleagues [24,26,28] have applied a new approach, known as confocal micro-PTV, to track the trajectories of individual labelled RBCs at high Hcts. Figures 9.8 and 9.9 show the ability of this confocal method to measure the motion of blood cells at both diluted (3% Hct) and high (20% Hct) suspensions of RBCs, respectively. Additionally, successful measurements were performed in a 75-µm circular PDMS micro-channel as shown in Fig. 9.10.

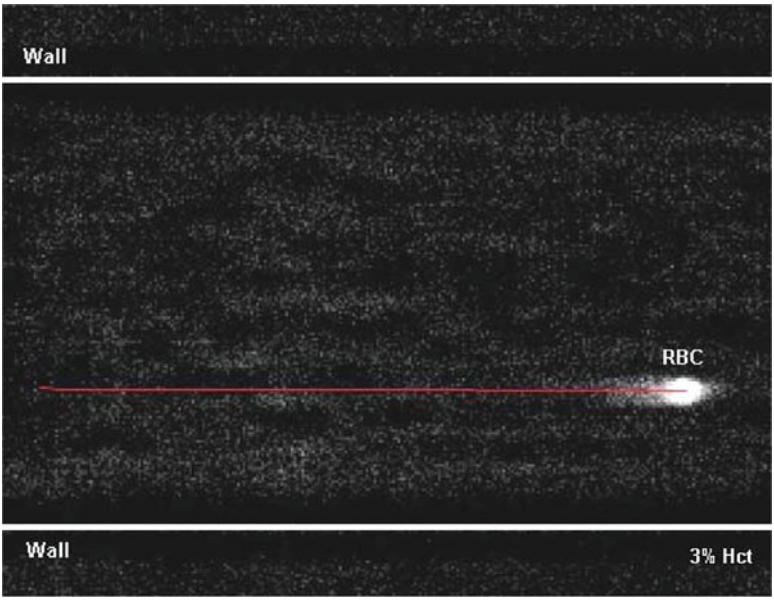

Fig. 9.8 Labelled RBC trajectory at diluted suspensions of cells (3 % Hct) obtained by the proposed confocal micro-PTV system (adapted from [26])

The ability of the confocal system to generate thin in-focus planes has allowed both qualitative and quantitative measurements in flowing blood at concentrated suspensions (up to 35% Hct) of: cell–cell hydrodynamic interaction, RBC orientation and RBC radial dispersion at different depths. Hence, to evaluate the capability of the confocal micro-PTV system to track RBCs, motions of labelled RBCs were followed at several Hcts (3–37%). The measurements of complex micro-rheological events in flowing blood (such as interaction and orientation of blood cells) were performed near the wall of the micro-channel ($z = 20$ μm) with Hct ~ 20% and Re ~0.007.

9.4.3.1 RBC–RBC Interactions in Flowing Blood

The effect of hemodynamic interactions on the motion of RBCs depend on multi-physics factors, such as shear rate, deformability, plasma layer and wall constriction. Figure 9.11 shows the trajectories of two-RBC interactions close to the cell-free layer. This figure shows clearly the radial disturbance effect enhanced by the collision of a neighbouring RBC. The radial displacement (ΔR) of the RBCs increases from two to six times of its initial radial displacement. For the case of RBC1, ΔR continues to increase, due not only to the interaction above but also to others which may occur with neighbouring cells.

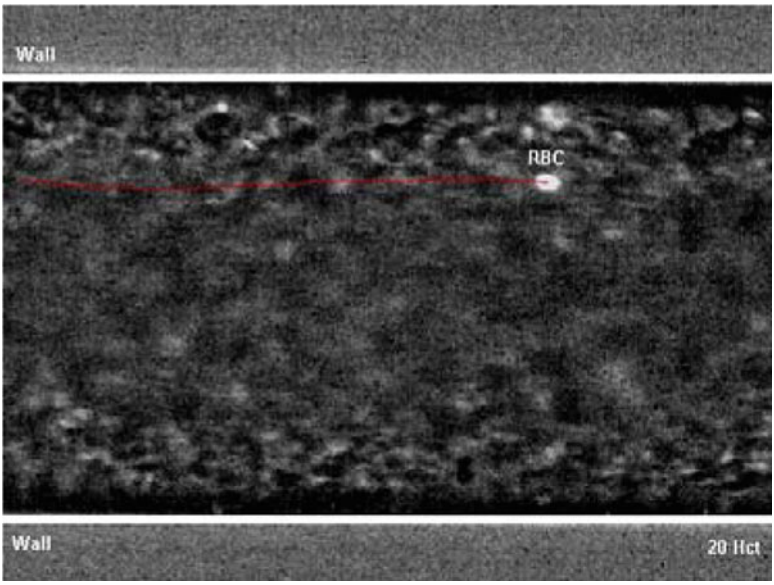

Fig. 9.9 Trajectory of a labelled RBC at high suspensions of cells (20 % Hct) obtained by the proposed confocal micro-PTV system. Experiments were carried out in glass micro-channels (adapted from [26])

9.4.3.2 RBC–WBC Interactions in Flowing Blood

The hemodynamic interaction effect of WBC on the motion of RBCs was also investigated by using confocal micro-PTV. Figure 9.12 shows the interaction of a RBC with the centre upper part of a WBC. Note that the RBC is located in the in-focus plane (high intensity) whereas part of the WBC is under the in-focus plane (lower intensity). It is possible to observe that transversal RBC displacement tends to increase when a collision occurs with a neighbouring WBC.

9.4.3.3 Translational and Rotational Motion of RBCs

The orientation of RBCs was extensively studied at low Hct (values $<1\%$), but this behaviour differed from that for moderate and high Hcts. Figures 9.13 and 9.14 show the orientation of a RBC without and with an interaction, for flow close to the wall of a glass micro-channel. By adjusting the image contrast, it was possible to quantify both translational and rotational motion. The translational motion was measured at the centre of the RBC whereas the rotational was measured along the membrane: these are as shown in Figs. 9.13 and 9.14. The RBC motion without interaction (Fig. 9.13) was measured along the wall of the micro-channel. This RBC did not suffer any interaction with a neighbouring RBC so that its translational radial displacement was almost constant: as a result the RBC rotates as a biconcave

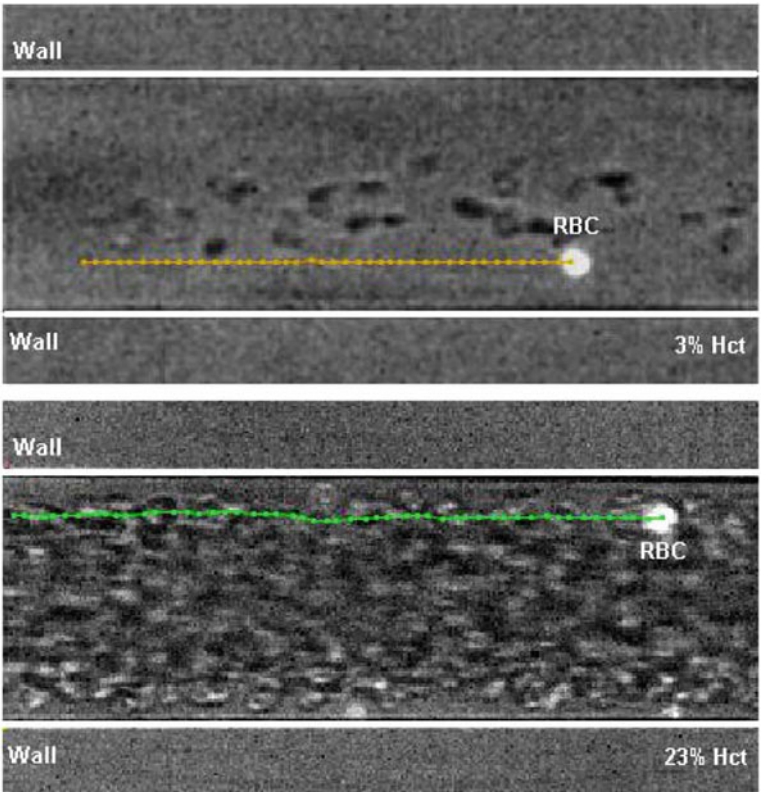

Fig. 9.10 Trajectory of labelled RBCs at low (3 % Hct) and high suspensions of RBCs (23 % Hct) obtained by the proposed confocal micro-PTV system. Experiments were carried out in circular PDMS micro-channel (adapted from [29])

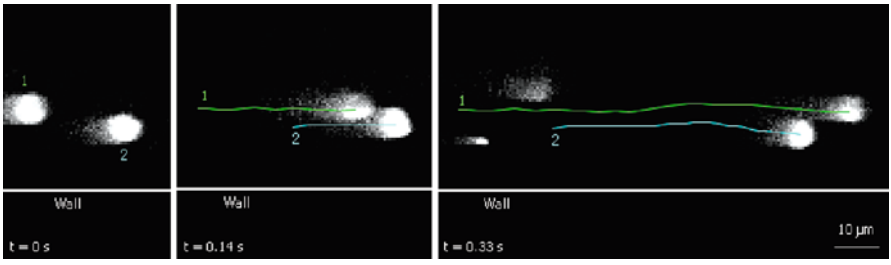

Fig. 9.11 Two-RBC interactions at different time intervals (adapted from [28])

disc in a clockwise direction with periodically varying angular velocity. By contrast, for RBCs that interact with neighbouring cells (Fig. 9.14) both translational and rotational motions change dramatically. In this case the rotation of the RBC is no longer regular and periodic but rather in an erratic manner.

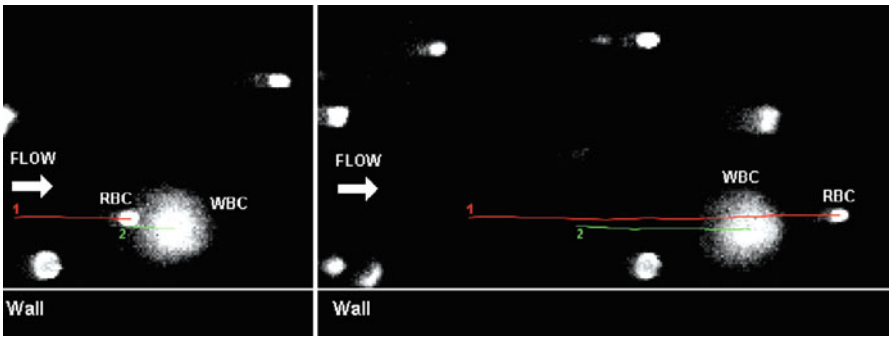

Fig. 9.12 Lateral RBC–WBC interaction at different time intervals (adapted from [32])

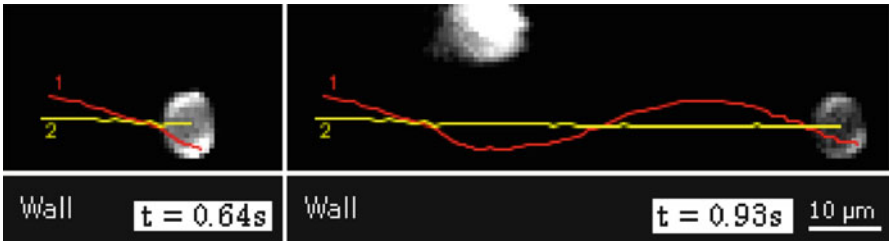

Fig. 9.13 Translational and rotational motion of a RBC rolling on the wall without interaction (adapted from [28])

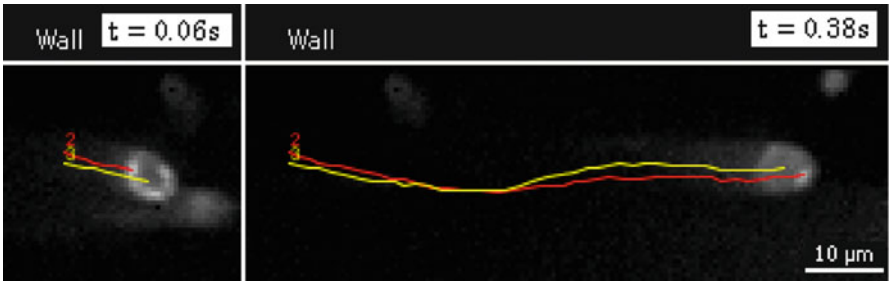

Fig. 9.14 Translational and rotational motion of RBC with interaction (adapted from [28])

9.4.3.4 Effect of Hct on RBC Radial Dispersion

The randomlike transverse motions of RBCs can be analysed by using a radial dispersion coefficient (D_{yy}), given by:

$$D_{yy} = \sum_{t=0}^{n} \frac{\left\langle \left(R_y(t) - R_y(0)\right)^2 \right\rangle}{2t} \tag{9.5}$$

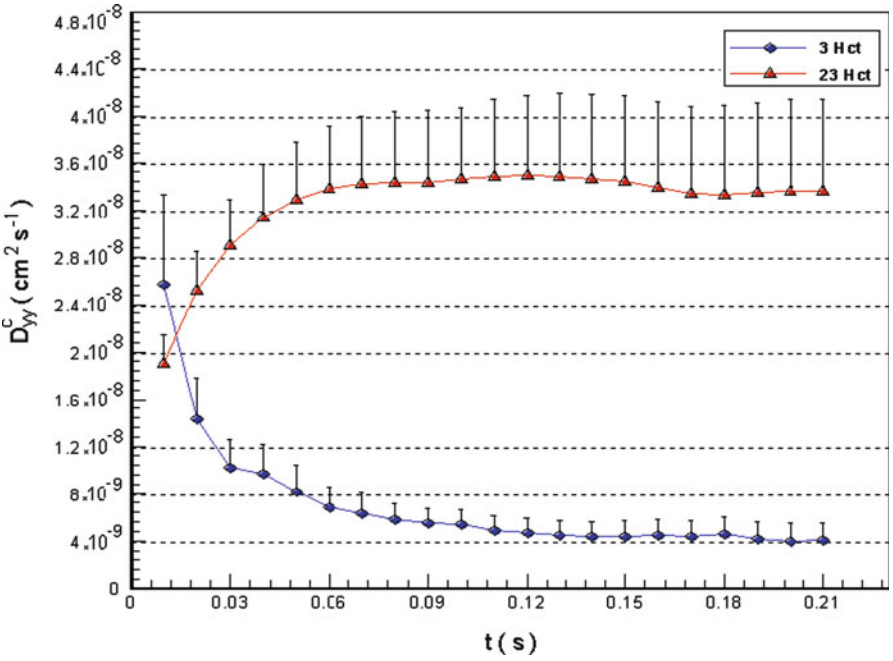

Fig. 9.15 RBCs radial dispersion coefficient (D_{yy}) of 75 μm PDMS circular micro-channel for 3 % Hct and 23 % Hct (adapted from [29])

where R_y and t are the radial displacement and time interval respectively. Hence, in vitro blood with several Hcts was used, the confocal micro-PTV system enabling the paths of hundreds of labelled RBCs to be recorded in the centre plane of 100 and 50 μm glass capillaries and 75 μm PDMS circular micro-channels. The results demonstrated that for RBCs the D_{yy} tends to increase with increasing Hct (as shown in Figs. 9.15 and 9.16). For instance Fig. 9.15 shows clearly that RBCs D_{yy} at Hct of 23% is almost one order magnitude bigger than D_{yy} with 3% Hct.

These research findings are evidence that the RBCs flowing in a crowded environment tend to undergo multi-body collisions which increase the amplitude of the RBC's lateral motion and consequently RBC D_{yy}. Hence, RBCs at high concentrations tend to exhibit higher erratic radial displacement compared to dilute suspensions of RBCs. Additionally, results given in Fig. 9.16 demonstrate that RBC radial dispersion, at both moderate and high Hcts, tends to decrease with the diameter. The main reasons for this are as follows: Hct reduction with diameter (Faharaeus effect) and the constrictive effect of the geometry, the latter limiting the amplitude of the radial displacements of the RBCs. Additional detailed results relating to these data can be found elsewhere [26,28,29].

Very recently, in a study performed by Saadatmand et al. [37] fluid particle diffusion was examined in concentrated suspensions of human RBCs (Hct up to 20%) through a

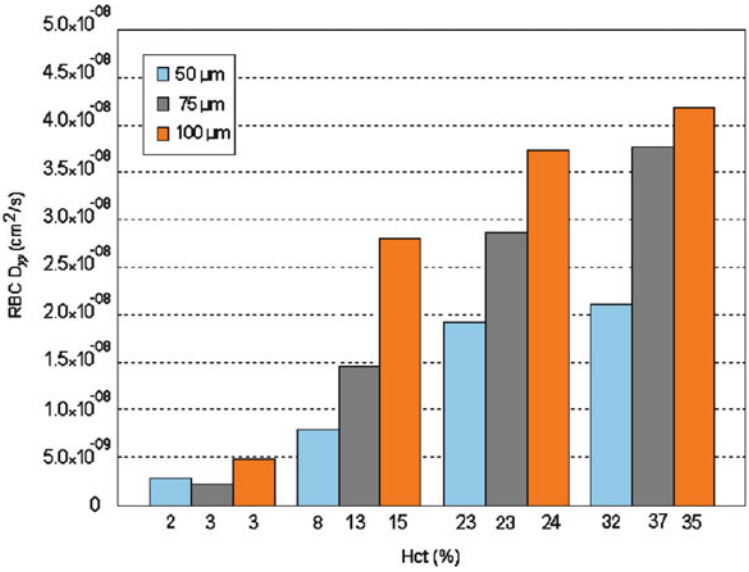

Fig. 9.16 Effect of the microtube geometry on the RBC D_{yy}^{c} (adapted from [29])

capillary tube. The results demonstrated significant enhancement of the particle diffusion, due to a micron-scale flow-field generated by the RBC motions, whereas the dispersion of tracer particles was about 0.7 times that of RBCs. The results also showed that by increasing the flow rate particle dispersion tends to increase almost linearly under constant Hct levels. Moreover, the particle dispersion showed near linear dependency on Hct up to 20%.

9.4.3.5 Effect of Hct on the Cell-free Layer (CFL)

Recent studies have investigated the Hct effect on the cell-free layer (CFL) thickness of both straight circular glass and PDMS micro-channels [8,10,33]. Labelled RBCs flowing near the CFL were tracked manually by using the MtrackJ plugin from Image J. Figure 9.17 gives an example of two trajectories of labelled RBCs flowing at the edge of the CFL. By using MtrackJ, the positions of the tracked RBCs are measured and the average thickness of the CFL is calculated [8,10,30,33].

Examination of Fig. 9.18 reveals an overall enhancement of the CFL thickness as Hct decreases. For the case of the PDMS micro-channel, the CFL thickness decreases almost four fold as Hct is increased from 3 to 37% [30,33]. The results are clear evidence that the CFL thickness tends to reduce as the diameter of the micro-channel decreases.

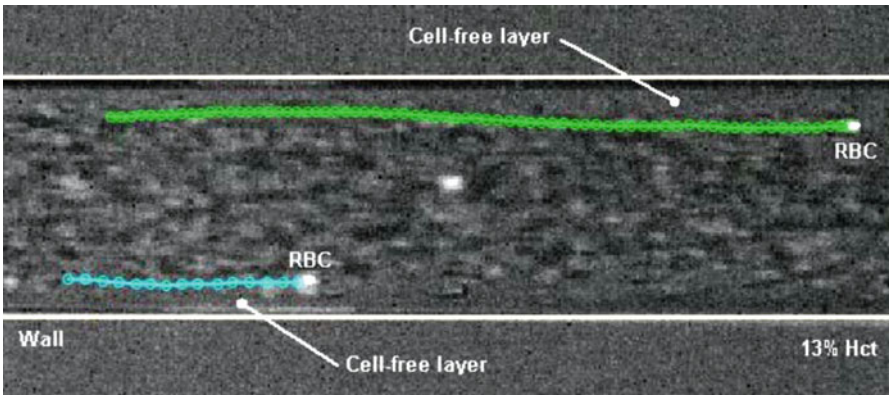

Fig. 9.17 Trajectory of labelled RBCs flowing nearby the cell-free layer (adapted by [29])

9.4.3.6 In Vitro Blood Flow Through Complex Geometries

Past studies on blood flow through glass micro-channels and in micro-vessels have yielded conflicting results with respect to flow resistance and deformability of RBCs [42,48]. However, observed in vivo/in vitro discrepancies have not yet been convincingly explained by the research, which is restricted to straight rigid glass micro-channels. One possible way of understanding observed in vivo/in vitro discrepancies is by using PDMS micro-channels fabricated by a soft lithographic technique [27,34]. By using this kind of technique it is possible to fabricate biomimetic PDMS micro-channels with complex geometries similar to human blood arterioles and capillary networks. In a very recent study performed by Leble et al. [20–22] the effects were investigated of bifurcations (diverging and converging) on the flow behaviour of both fluorescent particles suspended in pure water (PW) and RBCs in concentrated suspensions (14% Hct). A very dominant phenomenon was observed in blood flow behaviour at the region of the converging bifurcation apex. At this region, the formation of a clear triangular CFL was observed, the layer tending to propagate along the centre of the micro-channel. Ishikawa et al. [17] and Leble et al. ([20–22], 2012) give more detailed information about this phenomenon.

Recently, Fujiwara et al., by using a confocal micro-PTV system have investigated the flow behaviour of RBCs in a micro-channel with a stenosis [11]. The influence of a stenosis (70%) on the trajectories of individual RBCs was investigated in a concentrated suspension of up to 20% Hct. For 10% Hct the results indicated that healthy RBC trajectories have a tendency to become asymmetric before and after the stenosis whereas trajectories of particles suspended in pure water tend to be almost symmetric. Furthermore, the influence of the deformability of RBCs on the CFL thickness was also investigated. Fujiwara et al. have demonstrated that deformability plays a crucial role on the asymmetry of the CFL thickness. Generally, they have concluded that the motions of RBCs are strongly influenced not only by RBC deformability but also by the Hct and channel geometry [11].

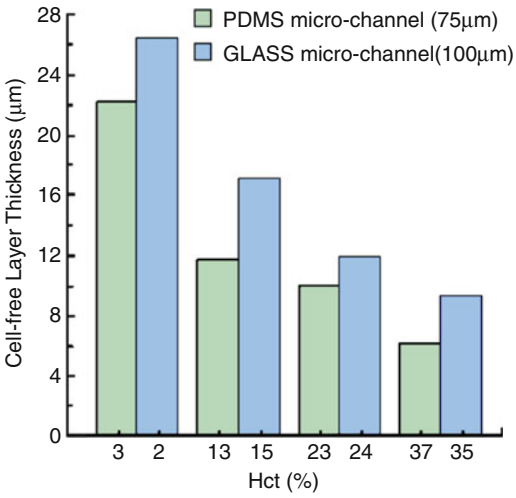

Fig. 9.18 Average thickness of the cell-free layer at different Hcts and diameters [30,33]

9.5 Conclusion and Future Directions

The recent developments in computing, digital image processing techniques and microscopy have made it possible to combine both particle image velocimetry (PIV) and particle tracking velocimetry (PTV) system with confocal microscopes, in so-called confocal micro-PIV/PTV. In this chapter we have presented the most relevant aspects of research using this approach: the theoretical and technical issues for both conventional and confocal micro-PIV/PTV methods and hemodynamic studies in micro-channels are facilitated by using systems based on these methods.

By using a 100-μm square micro-channel, the confocal micro-PIV system has shown good accuracy in measuring blood plasma flow with Hct up to 9%. Nevertheless, for Hct higher than 9%, the light absorbed and scattered by the RBCs contributes to a diminution of the concentration trace particles and as a consequence generates spurious errors in the velocity profiles. This effect becomes much more evident for Hct above 20%. Owing to its optical sectioning ability and consequent improvement of the image contrast and definition, a confocal micro-PTV system was then proposed to track individual blood cells at both low and high Hcts. By using such a system it was indeed found possible to measure cell–cell hydrodynamic interaction, RBC orientation and RBC radial dispersion at different depths and Hcts. Generally, the results suggest that the RBC paths are strongly dependent on the Hct and therefore the RBC dispersion coefficient tends to increase with increase in Hct. In addition, the confocal micro-PTV system has proved to be a powerful tool to obtain further insight into the flow behaviour of blood through complex geometries such as bifurcations, confluences and stenoses. Moreover, by culturing endothelial cells within PDMS microfluidic devices, we expect to develop in the near future a flow system device that closely mimics the in vivo micro-vessel environment.

Acknowledgements The authors acknowledge the financial support provided by: International Doctoral Program in Engineering, from the Ministry of Education, Culture, Sports, Science and Technology of Japan (MEXT), 2007 Global COE Program "Global Nano-Biomedical Engineering Education and Research Network", Japan. Grant-in-Aid for Science and Technology (PTDC/SAU-BEB/108728/2008, PTDC/SAU-BEB/105650/2008 and PTDC/EME-MFE/099109/2008) from the Science and Technology Foundation (FCT) and COMPETE, Portugal. The authors would also like to thank all the colleagues and students for their valuable comments, suggestions and technical assistance throughout this research work.

References

1. Adrian R (1991) Particle-imaging techniques for experimental fluid mechanics. Annu Rev Fluid Mech 23:261–304
2. Alonso C, Pries A, Kiesslich O, Lerche D, Gaehtgens P (1995) Transient rheological behaviour of blood in low-shear tube flow: velocity profiles and effective viscosity. Am J Physiol 268: H25–H32
3. Abramoff M, Magelhaes P, Ram S (2004) Image processing with image J. Biophotonics Int 11:36–42
4. Baker M, Wayland H (1974) On-line volume flow rate and velocity profile measurement for blood in microvessels. Microvasc Res 7:131–143
5. Born G, Melling A, Whitelaw J (1978) Laser Doppler microscope for blood velocity measurement. Biorheology 15:163–172
6. Bugliarello G, Hayden J (1963) Detailed characteristics of the flow of blood *in vitro*. Trans Soc Rheol 7:209–230
7. Cochrane T, Earnshaw J, Love A (1981) Laser Doppler measurement of blood velocity in microvessels. Med Biol Eng Comput 19:589–596
8. Cerdeira T (2009) Estudo do escoamento sanguíneo em microcanais. Final year project, Instituto Politécnico de Bragança (IPB), Portugal (in Portuguese)
9. Einav S, Berman R, Fuhro P, DiGiovanni P, Fine S, Fridman J (1975) Measurement of velocity profiles of red blood cells in the microcirculation by laser Doppler anemometry (LDA). Biorheology 12:207–210
10. Fidalgo C (2010) Estudo da formação da camada de plasma em microcanais. Final year project, Instituto Politécnico de Bragança (IPB), Portugal (in Portuguese)
11. Fujiwara H, Ishikawa T, Lima R, Marsuki N, Imai Y, Kaji H, Nishizawa M, Yamaguchi T (2009) Red blood cell motions in a high hematocrit blood flowing through a stenosed microchannel. J Biomech 42:838–843
12. Gaehtgens P, Meiselman H, Wayland H (1970) Velocity profiles of human blood at normal and reduced hematocrit in glass tubes up to 130 μm diameter. Microvasc Res 2:13–23
13. Goldsmith H (1971) Red cell motions and wall interactions in tube flow. Fed Proc 30 (5):1578–1588
14. Goldsmith H (1971) Deformation of human red cells in tube flow. Biorheology 7:235–242
15. Goldsmith H, Marlow J (1979) Flow behavior of erythrocytes II. Particles motions in concentrated suspensions of ghost cells. J Colloid Interface Sci 71(2):383–407
16. Golster H, Linden M, Bertuglia S, Colantuoni A, Nilsson G, Sjoberg F (1999) Red blood cell velocity and volumetric flow assessment by enhanced high-resolution laser Doppler imaging in separate vessels of hamster cheek pouch microcirculation. Microvasc Res 58:62–73
17. Ishikawa T, Fujiwara H, Matsuki N, Yoshimoto T, Imai Y, Ueno H, Yamaguchi T (2011) Asymmetry of blood flow and cancer cell adhesion in a microchannel with symmetric bifurcation and confluence. Biomed Microdevices 13:159–167

18. Kim GB, Lee SJ (2006) X-ray PIV measurements of blood flows without tracer particles. Exp Fluids 41:195–200
19. Koutsiaris A, Mathioulakis D, Tsangaris S (1999) Microscope PIV for velocity-field measurement of particle suspensions flowing inside glass capillaries. Meas Sci Technol 10:1037–1046
20. Leble V, Dias R, Lima R, Fernandes C, Ishikawa T, Imai Y, Yamaguchi T (2011a) Motions of trace particles and red blood cells in a PDMS microchannel with a converging bifurcation. In: Yamaguchi T, Imai Y, Oliveira MSN, Lima R (eds) Japan-Portugal Nano-BME symposium: proceedings of the 2011 conference, Porto/Braganca, Portugal, pp 29–30
21. Leble V, Lima R, Fernandes C, Dias R (2011b) Flow of red blood cells through a microchannel with a confluence. Proceedings of the Congresso de Métodos Numéricos em Engenharia 2011, CD-ROM paper ID267.pdf, Coimbra, Portugal.
22. Leble V, Lima R, Dias R, Fernandes C, Ishikawa T, Imai Y, Yamaguchi T (2011c) Asymmetry of red blood cell motions in a microchannel with a diverging and converging bifurcation. Biomicrofluidics 5:044120
23. Lima R, Wada S, Tsubota K, Yamaguchi T (2006) Confocal micro-PIV measurements of three dimensional profiles of cell suspension flow in a square microchannel. Meas Sci Technol 17:797–808
24. Lima R (2007) Analysis of the blood flow behavior through microchannels by a confocal micro-PIV/PTV system. PhD (Eng), Bioengineering and Robotics Department, Tohoku University, Sendai, Japan
25. Lima R, Wada S, Takeda M, Tsubota K, Yamaguchi T (2007) *In vitro* confocal micro-PIV measurements of blood flow in a square microchannel: the effect of the haematocrit on instantaneous velocity profiles. J Biomech 40:2752–2757
26. Lima R, Ishikawa T, Imai Y, Takeda M, Wada S, Yamaguchi T (2008) Radial dispersion of red blood cells in blood flowing through glass capillaries: role of heamatocrit and geometry. J Biomech 44:2188–2196
27. Lima R, Wada S, Tanaka S, Takeda M, Ishikawa T, Tsubota K, Imai Y, Yamaguchi T (2008) In vitro blood flow in a rectangular PDMS microchannel: experimental observations using a confocal micro-PIV system. Biomed Microdevices 10(2):153–167
28. Lima R, Ishikawa T, Imai Y, Takeda M, Wada S, Yamaguchi T (2009a) Measurement of individual red blood cell motions under high hematocrit conditions using a confocal micro-PTV system. Ann Biomed Eng 37(8):1546–1559
29. Lima R, Nakamura M, Omori Y, Ishikawa T, Wada S, Yamaguchi T (2009b) Microscale flow dynamics of red blood cells in microchannels: an experimental and numerical analysis. In: Tavares, Jorge (eds) Advances in computational vision and medical image processing: methods and applications, vol. 13. Springer, pp 203–220
30. Lima R, Oliveira M, Cerdeira T, Monteiro F, Ishikawa T, Imai Y, Yamaguchi T (2009c) Determination of the cell-free layer in circular PDMS microchannels. ECCOMAS thematic conference on computational vision and medical image processing, Porto, Portugal
31. Lima R, Oliveira MSN, Ishikawa T, Kaji H, Tanaka S, Nishizawa M, Yamaguchi T (2009d) Axisymmetric PDMS microchannels for in vitro haemodynamics studies. Biofabrication 1(3):035005
32. Lima R, Ishikawa T, Imai Y Yamaguchi T (2010a) Confocal micro-flow visualization of blood cells. Paper 1626. In: Pereira JCF, Sequeira A (Eds) Proceedings of fifth European conference on computational fluid dynamics, ECCOMAS CFD 2010, 14–17 June 2010, Lisbon, Portugal
33. Lima R et al (2010b) Measuring the cell-free layer in circular microchannels. Proceedings of the Sixth World Congress of biomechanics, Singapore
34. Lima R, Fernandes C, Dias R, Ishikawa T, Imai Y, Yamaguchi T (2011) Microscale flow dynamics of red blood cells in microchannels: an experimental and numerical analysis, In: Tavares, Jorge (eds) Computational vision and medical image processing: recent trends, vol. 19 Springer, pp 297–309
35. Lima R, Dias R, Leble V, Fernandes C, Ishikawa T, Imai Y, Yamaguchi T (2012) Flow visualization of trace particles and red blood cells in a microchannel with a diverging and

converging bifurcation. ECCOMAS thematic conference on computational vision and medical image processing, Olhão, Portugal, pp 209–211
36. Lima R, Ishikawa T, Imai Y, Yamaguchi T (2012) Blood flow behavior in microchannels: advances and future trends. In: Dias et al (eds) Single and two-Phase flows on chemical and biomedical engineering, Bentham Science Publishers, Springer (in press)
37. Saadatmand M, Ishikawa T, Matsuki N, Abdekhodaie MJ, Imai Y, Ueno H, Yamaguchi T (2011) Fluid particle diffusion through high-hematocrit blood flow within a capillary tube. J Biomech 44:170–175
38. Meijering E, Smal I, Danuser G (2006) Tracking in molecular bioimaging. IEEE Signal Process Mag 23:46–53
39. Meinhart C, Wereley S, Santiago J (1999) PIV measurements of a microchannel flow. Exp Fluids 27:414–419
40. Nakano A, Sugii Y, Minamiyama M, Niimi H (2003) Measurement of red cell velocity in microvessels using particle image velocimetry (PIV). Clin Hemorheol Microcirc 29:445–455
41. Parthasarathi A, Japee S, Pittman R (1999) Determination of red blood cell velocity by video shuttering and image analysis. Ann Biomed Eng 27:313–325
42. Pries A, Secomb T, Gessner T, Sperandio M, Gross J, Gaehtgens P (1994) Resistance to blood flow in microvessels in vivo. Circ Res 75:904–915
43. Tangelder G, Slaaf D, Muijtjens M, Arts T, Egbrink M, Reneman R (1986) Velocity profiles of blood platelets and red blood cells flowing in arteriols of rabbit mesentery. Circ Res 59:505–514
44. Sbalzarini IF, Koumoutsakos P (2005) Feature point tracking and trajectory analysis for video imaging in cell biology. J Struct Biol 151(2):182–195
45. Santiago J, Wereley S, Meinhart C, Beebe D, Adrian R (1998) A particle image velocimetry system for microfluidics. Exp Fluids 25:316–319
46. Sugii Y, Nishio S, Okamoto K (2002) In vivo PIV measurement of red blood cell velocity field in microvessels considering mesentery motion. Physiol Meas 23:403–416
47. Sugii Y, Okuda R, Okamoto K, Madarame H (2005) Velocity measurement of both red blood cells and plasma of in vitro blood flow using high-speed micro PIV technique. Meas Sci Technol 16:1126–1130
48. Suzuki Y, Tateishi N, Soutani M, Maeda N (1996) Deformation of erythrocytes in microvessels and glass capillaries: effects of erythrocyte deformability. Microcirculation 3:49–57
49. Uijttewaal W, Nijhof E, Heethaar R (1994) Lateral migration of blood cells and microspheres in two-dimensional Poiseuille flow: a laser Doppler study. J Biomech 27:35–42
50. Vennemann P, Kiger K, Lindken R, Groenendijk B, Stekelenburg-de Vos S, Hagen T, Ursem N, Poelmann RE, Westerweel J, Hierk B (2006) In vivo micro particle image velocimetry measurements of blood-plasma in the embryonic avian heart. J Biomech 39:1191–1200
51. Wereley ST, Meinhart CD (2010) Recent advances in micro-particle image velocimetry. Annu Rev Fluid Mech 42:557–576
52. Yaginuma T, Oliveira MSN, Lima R, Dias R, Ishikawa T, Imai Y, Yamaguchi T (2012) Flow visualization of trace particles and red blood cells in a microchannel with a diverging and converging bifurcation, ECCOMAS thematic conference on computational vision and medical image processing, Olhão, Portugal, pp 209–211
53. Yaginuma T, Oliveira MSN, Lima R, Ishikawa T, Yamaguchi T (2011) Red blood cell deformation in flows through a PDMS hyperbolic microchannel. In: Proceedings of TechConnect World 2011—Microtech Conference and Expo 2011, Boston, MA, USA, 2, 505

Chapter 10
The Lattice Boltzmann Method as a General Framework for Blood Flow Modelling and Simulations

Simone Melchionna, Giuseppe Pontrelli, Massimo Bernaschi, Mauro Bisson, Ian Halliday, Tim J. Spencer, and Sauro Succi

Abstract Large-scale simulations of blood flow allow for the optimal evaluation of endothelial shear stress for real-life case studies in cardiovascular pathologies. The procedure for anatomic data acquisition, geometry, and mesh generation are particularly favorable if used in conjunction with the Lattice Boltzmann method and the underlying Cartesian mesh. The methodology allows to accommodate red blood cells in order to take into account the corpuscular nature of blood in multiscale scenarios and its complex rheological response, in particular, in proximity of the endothelium. Taken together, the Lattice Boltzmann framework has become a reality for studying sections of the human circulatory system in physiological conditions.

10.1 Introduction

Blood flow simulations constitute a rapidly growing field for the medical, engineering, and basic sciences communities. The study of blood in the macrovasculature, as much as in capillaries, has deep implications in understanding and prevention of the most common cardiovascular pathologies, with atherosclerosis being perhaps the best known example. Atherosclerosis is responsible for $\sim$ 35% of annual deaths in developed countries, and its development depends on the presence of systemic

S. Melchionna (✉)
IPCF-CNR, Institute for Physico-Chemical Processes, National Research Council, Rome, Italy
e-mail: simone.melchionna@gmail.com

G. Pontrelli • M. Bernaschi •
M. Bisson • S. Succi
IAC-CNR, Institute for Computation "M. Picone", National Research Council, Rome, Italy
e-mail: pontrelli@iac.cnr.it; bernaschi@iac.cnr.it; bisson@iac.cnr.it; succi@iac.cnr.it

I. Halliday • T.J. Spencer
MERI, Sheffield Hallam University, Howard St, Sheffield S1 1WB, UK
e-mail: I.Halliday@shu.ac.uk; T.J.Spencer@shu.ac.uk

M.W. Collins and C.S. König (eds.), *Micro and Nano Flow Systems for Bioanalysis*, Bioanalysis 2, DOI 10.1007/978-1-4614-4376-6_10,

risk factors. The disease results from the accumulation of lipid molecules within the wall of the blood vessels, as well as from enhanced exposure to intramural penetration of nano-sized biological bodies [19]. The build up of the resultant soft tissue and the eventual changes in its consistency leads to serious atherosclerotic pathologies, including catastrophic events such as plaque rupture. Atherosclerotic plaques appear in regions of disturbed blood flow where the local endothelial shear stress (ESS) is low (< 1.0 Pa) or of alternating direction [9]. Hence, plaques tend to form near arterial bifurcations where the flow is always altered compared to unbranched regions [8, 39].

Atherosclerosis primarily affects the coronary arteries, and the evidence that low average ESS has a key role in the disease localization and progression is widely accepted [8, 23, 43, 9]. Predictions of where and how the illness is likely to develop can be obtained by fluid-dynamics simulations as a routine methodology to study blood flow patterns in human arteries. As a matter of fact, the shape and the structure of endothelium play a number of important roles in the vascular system, and its dysfunction may lead to several pathological states, including early development of atherosclerosis [30]. The microscopic shape of the endothelium is defined by the presence of endothelial cells (ECs henceforth), making the arterial wall undulated. This effect becomes more pronounced in small-sized vessels, where the corrugation degree increases. The study of blood flow over a regularly undulating wall made of equally aligned and distributed ECs has been recently carried out in [34] where the variation of wall shear stress over the ECs has been computed. Furthermore, the endothelium is coated by long-chained macromolecules and proteins which form a thin porous layer, called the glycocalyx [44]. The glycocalyx has a *brushlike* structure and a thickness which varies with the vessel diameter, but its average is 100 nm for arterioles. It has several roles: it serves as a transport barrier, to prevent ballistic red blood cell (RBC) interactions with the endothelium, and as a sensor and transducer of mechanical forces, such as fluid shear stress, to the surface of ECs. Actually, it has been recognized that the glycocalyx responds to the flow environment and, in particular, to the fluid stress, but the mechanism by which these proteins sense the shearing forces and transduce mechanical into biochemical signals is still not fully understood [30]. The glycocalyx itself is remodeled by the shearing flow and by the compression exerted by the deformed erythrocytes in capillaries [38]. Flow-induced mechano transduction in ECs has been studied over the years with emphasis on correlation between disturbed flow and atherosclerosis. Recently, some mathematical modelling work has been carried out, using a porous medium to model the endothelial surface layer (ESL henceforth) [1, 42]. However, none of these works includes the effect of the roughness, or wavy nature, of the wall, which should be incorporated for a more realistic description. In the following sections we also present a coarse-grained model that attempts to include some of the basic physical microscale effects of the ESL attached to the EC surface and hence, examine to what extent the wall shear stress may vary due to this layer in addition to the previously examined EC shape and particulate transport.

Simulations of blood flows based on the Lattice Boltzmann (LB) method provide a particularly efficient and flexible framework in handling complex arterial geometries.

In the past, the LB method has been applied to a broad range of fluid-dynamic problems, including turbulence and multiphase flows [41], as well as in blood flow simulations in steady and pulsatile regimes and with non-Newtonian flows through stenoses [32]. A direct benefit of the joint use of simulation and imaging techniques is to understand the connection between fluid-mechanical flow patterns and plaque formation and evolution, with important implications for predicting the course of atherosclerosis and possibly preventing or mitigating its effects, in particular by non-invasively and inexpensively screening large numbers of patients for incipient arterial disease, and to intervene at clinical level prior to the occurrence of a catastrophic event. One option is to obtain the arterial wall shape, plaque morphology, and lumen anatomy from the non-invasive multi-detector computed tomography (MDCT) imaging technique, as in the newest systems with 320-detector rows, a technology that enables 3D acquisition of the entire arterial tree in a single heart beat and high accuracy of nominal resolution of 0. 1 mm [36].

The LB method is particularly flexible for handling complex arterial geometries, since most of its simplicity stems from an underlying Cartesian mesh over which fluid motion is represented. LB is based on moving information along straight-line trajectories, associated with the constant speed of fictitious molecules which characterize the state of the fluid at any instant and spatial location. This picture stands in sharp contrast with the fluid-dynamic representation, in which, by definition, information moves along the material lines defined by fluid velocity itself, usually a very complex space-time-dependent vector field. This main asset has motivated the increasing use over the last decade of LB techniques for large-scale simulations of complex hemodynamic flows [29, 12, 27, 3].

The main aim of this chapter is to show that the inclusion of crucial components such as RBC and the glycocalyx, can be done within a single unified computational framework. This would allow us to reproduce blood rheology in complex flows and geometrical conditions, including the non-trivial interplay between erythrocytes and wall structure. The possibility of embedding suspended bodies in the surrounding plasma and the glycocalyx representation over an undulated endothelial wall addresses major steps forward to model blood from a bottom-up perspective, in order to avoid unnecessary and sometimes wrong assumptions in blood dynamics.

10.2 The Lattice Boltzmann Framework

In the last decade, the LB method has captured increasing attention from the fluid-dynamics community as a competitive computational alternative to the discretization of the Navier–Stokes equations of continuum mechanics. LB is a hydrokinetic approach and a minimal form of the Boltzmann kinetic equation, based on the collective dynamics of fictitious particles on the nodes of a regular lattice. The dynamics of fluid particles is designed in such a way as to obey the basic conservation laws ensuring hydrodynamic behavior in the continuum limit, in which the molecular mean free path is much shorter than typical macroscopic scales [41].

This condition is clearly met in blood flow regimes, together with the Newtonian rheological behavior of blood in large arterial systems. Non-Newtonian rheological models appropriate for simulating blood flow in medium or small-sized arteries, such as the Casson, Carreau, or Carreau-Yasuda models, can be also incorporated within the LB approach [6, 20].

The LB method is based on the collective dynamics of fictitious particles on the nodes of a regular lattice where the basic quantity is $f_p(x,t)$, representing the probability of finding a "fluid particle p" at the mesh location x and at time t and traveling with discrete speed c_p. "Fluid particles" represent the collective motion of a group of physical particles (often referred to as populations). We employ the common three-dimensional 19-speed cubic lattice (D3Q19) with mesh spacing Δx, where the discrete velocities $\mathbf{c}_p$ connect mesh points to first and second neighbors [2]. The fluid populations are advanced in a time step Δt through the following evolution equation:

$$f_p(\mathbf{x}+\mathbf{c}_p\Delta t, t+\Delta t) = f_p(\mathbf{x},t) - \omega(f_p - f_p^{eq})(\mathbf{x},t) + F_p(\mathbf{x},t). \tag{10.1}$$

The right-hand side of (10.1) represents the effect of fluid-fluid molecular collisions, through a relaxation towards a local equilibrium, typically a second-order expansion in the fluid velocity of a local Maxwellian with speed $\mathbf{u}$,

$$f_p^{eq} = w_p\rho\left[1 + \frac{\mathbf{u}\cdot\mathbf{c}_p}{c_s^2} + \frac{\mathbf{uu}:(\mathbf{c}_p\mathbf{c}_p - c_s^2\mathbf{I})}{2c_s^4}\right], \tag{10.2}$$

where $c_s = 1/\sqrt{3}$ is the speed of sound, w_p is a set of weights normalized to unity, and $\mathbf{I}$ is the unit tensor in Cartesian space. The relaxation frequency ω controls the kinematic viscosity of the fluid, $\nu = c_s^2\Delta t\left(\frac{1}{\omega} - \frac{1}{2}\right)$. The kinetic moments of the discrete populations provide the local mass density $\rho(\mathbf{x}, t) = \sum_p f_p(\mathbf{x}, t)$ and momentum $\rho\mathbf{u}(\mathbf{x}, t) = \sum_p \mathbf{c}_p f_p(\mathbf{x}, t)$. The last term F_p in (10.1) represents a momentum source, given by the presence of suspended bodies, if RBCs are included in the model, as discussed in the following sections. In the incompressible limit, (10.1) reduces to the Navier–Stokes equation

$$\begin{aligned} \nabla\cdot\mathbf{u} &= 0, \\ \frac{\partial\mathbf{u}}{\partial t} + (\mathbf{u}\cdot\nabla)\mathbf{u} &= -\frac{1}{\rho}\nabla P + \nu\nabla^2\mathbf{u} + \mathbf{F}, \end{aligned} \tag{10.3}$$

where P is the pressure and $\mathbf{F}$ is any body force, corresponding to F_p in (10.1).

The LB is a low-Mach, weakly compressible fluid solver and presents several major advantages for the practical implementation in complex geometries. In particular, in hemodynamic simulations, the curved blood vessels are shaped on the Cartesian mesh scheme via a staircase representation, in contrast to body-fitted grids that can be employed in direct Navier–Stokes simulations. This apparently crude representation of the vessel walls can be systematically improved by increasing the mesh resolution.

In addition, at the high mesh resolution required to sample low-noise ESS data, the LB method requires rather small time steps (of the order of 10^{-6} s for a resolution of 20 μm).

The wall shear stress, which is central to hemodynamic applications, can be computed via the shear tensor $\sigma(\mathbf{x},t) \equiv \nu\rho(\nabla\mathbf{u} + \nabla\mathbf{u}^T)$ evaluated via its kinetic representation

$$\sigma(\mathbf{x},t) = \frac{-3\nu\omega}{c_S^2}\sum\nolimits_p \mathbf{c}_p\mathbf{c}_p(f_p - f_p^{eq})(\mathbf{x},t). \tag{10.4}$$

The tensor second invariant is the endothelial shear stress or ESS:

$$\mathcal{S}(\mathbf{x}_w,t) = \sqrt{\frac{1}{2}(\sigma:\sigma)(\mathbf{x}_w,t)}, \tag{10.5}$$

where $\mathbf{x}_w$ represents the position of sampling points in close proximity to the mesh wall nodes. $\mathcal{S}(\mathbf{x}_w,t)$ provides a direct measure of the strength of the near-wall shear stress [5]. It is worth mentioning that the ESS evaluation via (10.4) is completely local and does not require any finite-differencing procedure. Thus it is particularly advantageous near boundaries where the computation of gradients is very sensitive to morphological details and accuracy. In order to sample high signal/noise ESS data, the LB mesh needs high spatial resolution, with mesh spacing being as small as $\Delta x \simeq 50$ μm for standard fluid-dynamic simulations, or being as small as $\Delta x \simeq 10$ μm in order to account for the presence of RBCs.

For the multiscale simulations of blood flows, we have developed the MUPHY software [3]. Such simulations in extended arterial systems, are based on the acquisition of MDCT data which are segmented into a stack of slices, followed by a mesh generation from the segmented slices. For a typical coronary artery system, the procedure to build the LB mesh from the MDCT raw data starts from a single vessel, formatted as stacked bi-dimensional contours (slices), with a nominal resolution of 100 μm. In spite of recent technological progress, this resolution is still insufficient, and the inherently noisy geometrical data pose a problem in the evaluation of ESS, a quantity that proves extremely sensitive to the details of the wall morphology. Raw MDCT data present a mild level of geometric irregularities, as shown in Fig. 10.1, that can affect the quality of the LB simulations. For the simulation, we resort to regularize the initial geometry by smoothing the sequence of surface points via a linear filter along the longitudinal direction. Similarly, one could filter out surface points along the azimuthal contour. We have shown that such smoothing is necessary in order to avoid strong artifacts in the simulation results [28]. Even if the precise shape of the vessel is unknown, as it falls within the instrumental indeterminacy, the numerical results converge to a common fluid-dynamic pattern as the smoothing procedure reaches a given level. The regularized geometries are still of great interest because they obey the clinical perception of a smooth arterial system, and, moreover, the smoothing procedure falls within the intrinsic flexibility of the arterial system.

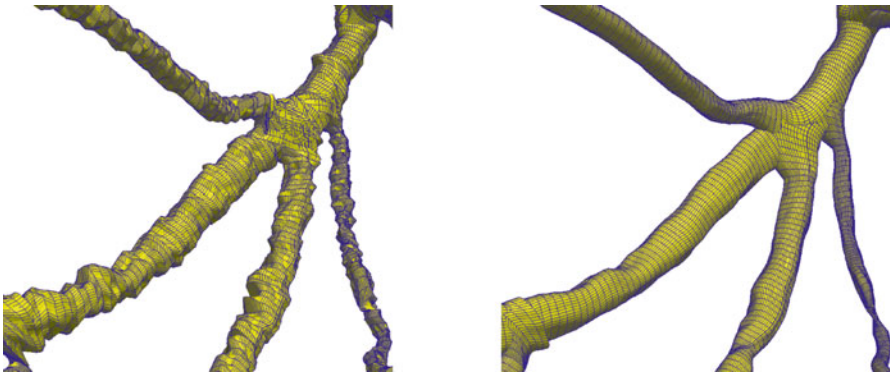

Fig. 10.1 Details of a multi-branched artery as obtained from MDCT (*left*) and after smoothing have been applied as used in simulations (*right*)

When studying coronary arteries as a prototypical system for plaque formation and development, one issue regards the inclusion of deformable vessels in simulation. Whereas larger arteries undergo high deformations, a simple calculation shows that the distensibility index of a coronary artery of sectional area A is $b^{-1} \simeq 1.5$ mmHg. Therefore, the arterial section during a heartbeat has a maximal deformation of $\delta A/A = b\Delta P$, with ΔP the maximal pressure variation over a cardiac cycle. For a pressure jump of 40 mmHg, the deformation is less than 3%, and considering rigid coronary systems does not introduce major artifacts in the computed flow and pressure distributions.

LB allows to impose no-slip boundary conditions at the endothelium by employing the bounce-back method; this consists of reversing at every time step the post-collisional populations pointing toward a wall node, providing first-order accuracy for irregular walls [41]. In the bounce-back method, the points corresponding to the exact no-slip hydrodynamic surface fall at intermediate positions between the external fluid mesh nodes and the nearby wall mesh nodes. Owing to its simplicity, the method handles irregular vessel boundaries in a seamless way, although more sophisticated alternatives with higher-order accuracy are available [4, 21, 17].

In a branched portion of arteries, boundary conditions at the inlet and multiple outlets can be chosen in different ways, typically by following the flow-pressure, pressure-pressure, or flow-flow prescriptions. The first two options are more popular in fluid-dynamic models, and pressure conditions at the outlets reflect the presence of a recipient medium. Even flow-flow conditions have found some applicability, as they can accommodate some type of metabolic autoregulation as encoded by Murray's law [40]. It is worth mentioning that flow-flow conditions can give rise to numerical instabilities in simple pipe flows, as long-lived transients can develop and a certain strain is exhorted on the simulation method. The absence of a peripheral system in real-life simulations can be compensated by using an equivalent RCL circuit at each system outlet, where the auxiliary circuitry introduces an

external viscous dissipation (R), vessel compliance (C), and fluid inertia (L) and compensates for the missing components (lumped parameter model).

In the framework of the LB method, boundary conditions at the inlet and multiple outlets can be imposed as follows. A constant velocity (with plug or parabolic profile) is enforced at the entrance of the main artery, as a way to control the amplitude of the flow. Even if the inlet profiles are not the real ones for irregular geometries, they fulfill the purpose of imposing the total flow rate in the chosen region. The fluid spontaneously and rapidly develops the consistent profile already at a short distance downstream. A constant pressure is imposed on the several outlets of the main artery, as well as on the outlet of all secondary branches (of the order of 10 in typical coronary systems). This leaves the simulation with the freedom of creating an appropriate velocity profile in the outlet regions, and building up a pressure drop between the inlet and the several outlets. The Zou-He method [46] is used to implement both the velocity inlet and the pressure outlets. This method exploits information streamed from fluid bulk nodes onto boundary cells and imposes a completion scheme for particle populations which are unknown because their neighboring nodes are not part of the fluid domain. The boundary cells are treated as normal fluid cells where to execute the conventional LB scheme. Thanks to this natural integration of the boundary scheme, the method is second-order accurate in space, compatible with the overall accuracy of the LB method (see [22]). The method handles in a natural way time-dependent inflow conditions for pulsatile flows. The algorithm requires that all nodes of a given inlet or outlet are aligned on a plane which is perpendicular to one of the three main axes, although the injected flow profile and direction can be arbitrary. However, since the inlet section is typically a critical region of simulation in terms of numerical stability due to the high fluid velocities, it is preferable to have an incoming flow direction aligned with one of the Cartesian axes. This requirement can be fulfilled by rotating the artery in such a way as to secure that alignment, the inlet axis with one of the Cartesian axis, which guarantees an exact control of the flow imposed at the inlet. Conversely, the outlet planes are not in general normal to the orientation of the blood vessels. However, this does not lead to noticeable problems, because the pressure drop along typical arterial systems is mild, and the error due to imposing a constant pressure along an inclined plane is negligible.

10.3 Red Blood Cells

RBCs or erythrocytes are globules that present a biconcave discoidal form, and a soft membrane that encloses a high-viscosity liquid made of hemoglobin: they exhibit both rotational and orientational responses that deeply modulate blood rheology. While blood rheology is quasi-Newtonian away from the endothelial region, the presence of RBCs strongly affects blood flow in proximity of the endothelium, where the interplay of RBC crowding for hematocrit levels up to 50%, depletion due to hydrodynamic forces, and RBC arrangement in rouleaux takes place.

In order to consider these different factors, we have recently proposed a model that focuses on three independent components: the far-field hydrodynamic interaction of a RBC in a plasma solvent, the raise of viscosity of the suspension with the hematocrit level, and the many-body collisional contributions to viscosity [26]. These three critical components conspire to produce large-scale hemorheology and the local structuring of RBCs. The underlying idea is to represent the different responses of the suspended bodies, emerging from the rigid body as much as the vesicular nature of the globule, by distinct coupling mechanisms. These mechanisms are entirely handled at kinetic level, that is, the dynamics of plasma and RBC's is governed by appropriate collisional terms that avoid to compute hydrodynamic forces and torques via the Green's function method, as employed in Stokesian dynamics [7]. The fundamental advantage of hydrokinetic modeling is to avoid such an expensive route and, at the same, enabling to handle finite Reynolds conditions and complex boundaries or irregular vessels within the simple collisional approach. At the macroscopic scale, the non-trivial rheological response emerges spontaneously as a result of the underlying microdynamics.

The presence of suspended RBCs is included via the following forcing term [see (10.1)]:

$$F_p = w_p \left[\frac{\mathbf{G} \cdot \mathbf{c}_p}{c_S^2} + \frac{(\mathbf{G} \cdot \mathbf{c}_p)(\mathbf{u} \cdot \mathbf{c}_p) - c_S^2 \mathbf{G} \cdot \mathbf{u}}{c_S^4} \right], \tag{10.6}$$

where $\mathbf{G}(\mathbf{x}, t)$ is a local force-torque. This equation produces first-order accurate body forces within the LB scheme. Higher-order methods, such as Guo's method [16], could be adopted. However, given the non-trivial dependence of the forces and torques on the fluid velocity and vorticity, Guo's method would require an implicit numerical scheme, whereas it is preferable to employ an explicit, first-order accurate numerical scheme.

The fluid-body hydrodynamic interaction is constructed according to the transfer function $\tilde{\delta}(\mathbf{r}_i)$ centered on the i-th particle position $\mathbf{r}_i$ and having ellipsoidal symmetry and compact support. The shape of the suspended body can be smaller than the mesh spacing, allowing to simulate a ratio of order 1 : 1 between suspended bodies and mesh nodes. In addition, the body is scale-adaptive, since it is possible to reproduce from the near-field to the far-field hydrodynamic response with desired accuracy [25]. The fluid-particle coupling requires the computation of the following convolutions over the mesh points and for each configuration of the N suspended bodies:

$$\begin{aligned} \tilde{\mathbf{u}}_i &= \sum\nolimits_{\mathbf{x}} \mathbf{u}(\mathbf{x}) \tilde{\delta}(\mathbf{x} - \mathbf{r}_i), \\ \tilde{\Omega}_i &= \sum\nolimits_{\mathbf{x}} \Omega(\mathbf{x}) \tilde{\delta}(\mathbf{x} - \mathbf{r}_i), \\ \tilde{\mathbf{t}}_i &= \sum\nolimits_{\mathbf{x}} \mathbf{t}(\mathbf{x}) \times (\mathbf{x} - \mathbf{r}_i) \tilde{\delta}(\mathbf{x} - \mathbf{r}_i), \end{aligned} \tag{10.7}$$

where Ω is the fluid vorticity and $\mathbf{t}$ is the fluid traction vector, quantities that are directly obtained from the LB computational core. The three convolutions allow to compute the drag force and drag torque, inclusive of tank trading components. On the fluid side, the body-induced forces are encoded by the term

$$\mathbf{G}(\mathbf{x}) = -\sum_{i=1}^{N} \left[\mathbf{D}_i \tilde{\delta}(\mathbf{x} - \mathbf{r}_i) + \frac{1}{2} \mathbf{T}_i \times \nabla \tilde{\delta}(\mathbf{x} - \mathbf{r}_i) \right],$$

where $\mathbf{D}_i$ and $\mathbf{T}_i$ are the drag forces and torques acting on the particles, constructed starting from the quantities featuring in (10.7). The explicit expression of the drag forces and torques are not given here, and can be found in [25].

Besides hydrodynamic interactions, mechanical forces regulate the direct interactions and the packing attitude of suspended bodies. The interactions are modeled as pairwise by means of the Gay-Berne (GB) potential [14], the pairwise GB energy being a function of the relative distance between pairs of RBCs and their mutual orientation. In addition, the mutual interaction depends on the eccentricity of each interacting particle, so that, as for the hydrodynamic coupling, mixtures of particles of different shapes can be handled within a unified framework. Once the forces and torques standing from both hydrodynamics and direct mechanical forces are computed, the rigid-body dynamics is propagated via a time second-order accurate algorithm [24, 10].

Numerical results have shown that the particulate nature of blood cannot be omitted when studying the non-trivial rheology of the biofluid and the shear stress distribution in complex geometries. Regions of low shear stress can appear as the hematocrit reaches physiological levels as a result of the non-trivial organization of RBCs and the irregular morphology of vessels, with far reaching consequences in real-life cardiovascular applications, where the organization of RBCs impacts both the local flow patterns and the large-scale flow distribution in vascular networks.

A crucial advantage of the hydrokinetic model in the presence of physiological levels of RBCs is its reduced computational cost, thus enabling the investigation of systems of physiological relevance (Fig. 10.2). To a large extent, both the LB method and the RBC dynamics have been proved to scale over traditional CPU-based computers such as on Blue Gene architectures, as much as over massive assemblies of graphic processing units (see [31] and references therein).

10.4 A Closer View to Blood-Wall Interaction

At a lower scale, new intriguing aspects come to light in hemodynamics. For example, the vessel wall surface is covered by endothelial cells (EC), that give a wavy structure, so far neglected (Fig. 10.3): this does not imply a significant variation in the flow field, but it can be relevant in computing ESS, which is constant in a flat-walled artery. Indeed, the ECs (a single EC has been estimated

Fig. 10.2 Snapshot of a multi-branched artery in presence of red blood cells for 50% hematocrit

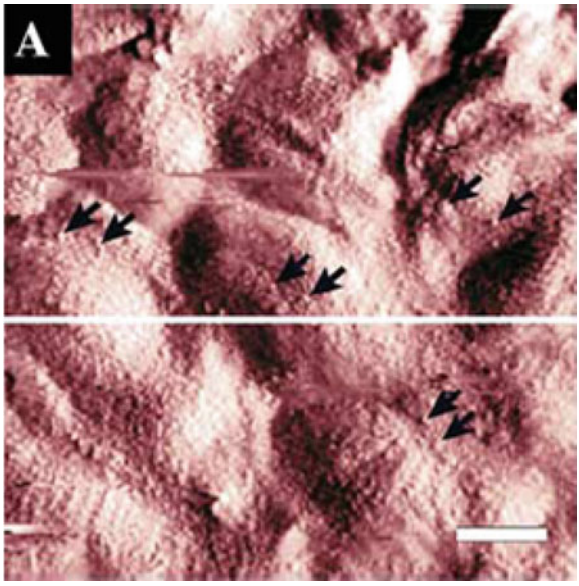

Fig. 10.3 The rough surface of the endothelium as imaged using scanning force microscopy (from [35]). *Arrows* point to granular structures on EC's surfaces, *white line* marks scanning line for height profile evaluation, and *scale bar* corresponds to 5 μm

to be about 15 μm long by 0.5 μm high [35]) form a continuous, undulated wall layer above which blood is flowing. At such mesoscopic scale, the wall may be considered as a smoothly corrugated idealized surface constituted by a regular array

of equal, repeated EC's. The pressure-driven axi-symmetric flow of a continuum fluid over such a surface has been recently modelled by Pontrelli et al. [34]. It was shown that, despite no great change in velocity profiles, there can occur significant ESS variations between the ECs wall peaks and throats, especially in small-sized arteries. Differently than in Sect. 10.3, the mesoscopic particulate nature of the blood is now addressed in the context of a bicomponent fluid model: RBC are here deformable, neutrally buoyant liquid drops constrained by a uniform interfacial tension and suspended in the plasma.

In addition, the endothelial surface is not only wavy in its geometry, but, at a smaller scale, it is covered by fibrous filaments and long protein chains forming a thin layer called the endothelial surface layer (ESL) or glycocalyx [44]. From a fluid-dynamics point of view, the ESL can be modelled as a porous layer of constant thickness which suits the wall undulation, through which the flow of the continuous phase (plasma) is possible. This would alter the boundary condition of the problem, specifically the classical no-slip condition at the vessel wall may have to be replaced to allow for plasma penetration through the ESL. The LB method readily accommodates a model of the glycocalyx itself, as it is particularly well suited to address what would now become a multiscale model. Conceptually, the idea is to solve a two-domain problem, whereby the bulk flow (in the lumen) is governed by the multicomponent Navier–Stokes equations and the near-wall region by a porous-medium Brinkman flow formulation (see below). At the mesoscale, the glycocalyx is not modelled in a detailed form, but its effect on the flow is still properly addressed, using methods which are amenable to coupling other, more detailed, simulations with experiments. We develop here a *two-way coupled* model where the drop interface is forced by compression of the ESL, and the effect of perturbed or compressed glycocalyx is then communicated to the flow [33]. We assume here that the filaments are strongly anchored in the endothelium, where they are most resistant to deformation and that they deform preferably at their tip, that is toward the vessel lumen.

The mesoscale LB method is still used to solve the governing hydrodynamic equations, that involves multicomponent fluid flow, off-lattice, or sub-grid, boundary surfaces and a porous-layer representative of the ESL. The governing hydrodynamic equations for flow in a porous media, with constant or variable porosity ε, are an extension of (10.3) as in [15]:

$$\nabla \cdot \mathbf{u} = 0,$$
$$\frac{\partial \mathbf{u}}{\partial t} + (\mathbf{u} \cdot \nabla)\frac{\mathbf{u}}{\varepsilon} = -\frac{1}{\rho}\nabla(\varepsilon P) + \nu\nabla^2\mathbf{u} + \mathbf{F}. \tag{10.8}$$

Here, $\mathbf{F}$ is the total body force due to the presence of both the porous material (drag) and other external forces:

$$\mathbf{F} = \frac{\varepsilon \nu}{K}\mathbf{u} - \frac{\varepsilon F_\varepsilon}{\sqrt{K}}\mathbf{u}|\mathbf{u}| + \varepsilon\mathbf{H}, \tag{10.9}$$

where **H** is the extra body force that will be used to incorporate further details of the ESL and particulate effects, such as the RBC interface force density (pressure step) defined below. To solve governing Equations (10.8) and (10.9) we combine the LB methods of Guo and Zhao [15] with the model of Halliday et al. [18], that allows for the introduction of two immiscible fluid components and the formation of interfaces that embed correct kinematic and surface tension laws. To complete the algorithm, we must mention that, for multiple fluid LB, the propagation step is augmented by a fluid segregation process that ensures the correct kinematics and dynamics and good integrity for an interface between completely immiscible fluid components, representing RBC and plasma, as discussed above [18]. The propagation step is expressed as:

$$\begin{aligned} R_p(\mathbf{x} + \mathbf{c}_p\Delta t, t + \Delta t) &= \frac{R}{\rho} f_p^+ + w_p \beta \frac{RB}{\rho} \cdot \mathbf{c}_p \cdot \mathbf{n}, \\ B_p(\mathbf{x} + \mathbf{c}_p\Delta t, t + \Delta t) &= \frac{B}{\rho} f_p^+ - w_p \beta \frac{RB}{\rho} \cdot \mathbf{c}_p \cdot \mathbf{n}, \end{aligned} \tag{10.10}$$

where the density of each fluid component is given by $R = \sum_p R_p(\mathbf{x}, t)$ and $B = \sum_p B_p(\mathbf{x}, t)$, the combined particle distribution function is $f_p = R_p + B_p$, and f_p^+ accounts for the propagated combined distribution. In (10.10) β represents an interfacial segregation parameter and **n** the interfacial unit normal vector. We also note that, if only one fluid component exists, (10.10) reduce to the standard LB propagation step (10.1). Returning to the definition of the extra body force term, **H** in (10.9), this incorporates both particulate and glycocalyx forces and is defined as

$$\mathbf{H} = \frac{\sigma}{2\rho} \pi \nabla \rho_N + \mathbf{E}. \tag{10.11}$$

The left-hand side term imposes an interfacial tension σ on multicomponent particles. Here, $\pi = \square \cdot \mathbf{n}$ is the local curvature, and $\rho_N = (R - B)/(R + B)$ is a phase field indicator. The right-hand term **E** is a glycocalyx force that acts upon the particles as defined in the next section.

10.5 The RBC: Glycocalyx Interplay

In the proposed model of the ESL as a porous layer, the porosity is reduced by a compressive encounter with an erythrocyte. As a consequence, the ESL is squashed locally transporting the same mass into a smaller volume and consequently decreasing the porosity in that region. Even in the simplest situation, the ESL-lumen boundary should not be regarded as sharp, and there is an *uncertainty region* between bulk, lumen, and glycocalyx material [33]. Let us define a variable porosity

$\varepsilon(x, y)$ that tends to 1 in the lumen region and gradually reduces, as we enter the glycocalyx region, where it approaches a minimum value, ε_G. This porosity transition is modelled through the increasing smooth function:

$$\varepsilon(\mathbf{x}) = \varepsilon_G + \frac{1 - \varepsilon_G}{2}[1 - \tanh(\xi(s - l))], \tag{10.12}$$

where l is the mean ESL thickness and the parameter $1 \quad \xi$ determines the distribution of (i.e., the effective standard deviation of) protein chain lengths, while $s(\mathbf{x})$ denotes distance measured normally to the endothelial boundary. Note that $\varepsilon_G \leq \varepsilon(\mathbf{x}) \leq 1$ and that, for $\varepsilon \to 1$, we have $\mathbf{F} \to \mathbf{H}$ [see (10.9)], and (10.8)–(10.9) reduce to the multi-component LB Navier–Stokes equations for free multicomponent fluid flows, and the described procedure reduces to the standard LB method for two-component, incompressible fluid. On the other hand, an additional, fictitious, repulsive body force density acts on the drop interface which enters the ESL region, impinging on the lumen. This force distribution is so designed that its accumulation produces an effective Hookean force acting at the center of the local volume. Specifically, the erythrocyte is subjected to a surface force distribution, effective in the ESL only, which is directed everywhere in the drop-surface normal direction. This force device effectively models the glycocalyx as a continuum of elastic springs, with modulus E, gradually decaying from a maximum value, and E_G (in the ESL) to 0 (towards the bulk):

$$E(x) = \frac{E_G}{2}[1 - \tanh(\xi(s - l))], \tag{10.13}$$

where all notations are given in correspondence to (10.12). It is important to note that the above force acts solely on the red fluid (drop) and not upon the plasma. Hence, the relative density of the material which comprises the drop may be modelled by appropriate choice of the spring constant E_G in the above equation.

A number of simulations have been carried out in the case of an axi-symmetric channel having the same corrugation repeated along the length. Its size (of order of μm) is slightly larger than a single RBC flowing through it, driven by a constant pressure gradient with periodic conditions. At such fine scale, for accuracy purposes, the off-lattice non-slip endothelial surface uses continuous bounce-back conditions [4]. The ESL structure has been modelled as a porous layer of constant thickness over the undulated wall. As one may expect, the average velocity of the drop is slower in the presence of the glycocalyx, which constitutes a hindrance for the lumen flow. Also, the mean deformation of the drop is more pronounced with the glycocalyx force (Fig. 10.4). Hence, when the drop is in the ESL influence region, it is subjected to the elastic force which squeezes and lifts it away from the boundary while making its shape more elongated. Considering the action of the glycocalyx as a sensor of mechanical forces, it is worth computing the shear stress at the ESL/lumen boundary. Our results evidence, in the latter case with ESL, a reduction of the shearing stress either at the wall (due to the plasma only) and at the ESL top (due to the particulate fluid) [33]. It is seen that ESL is more likely to protect the endothelial cells from ESS fluctuations associated with particle transits.

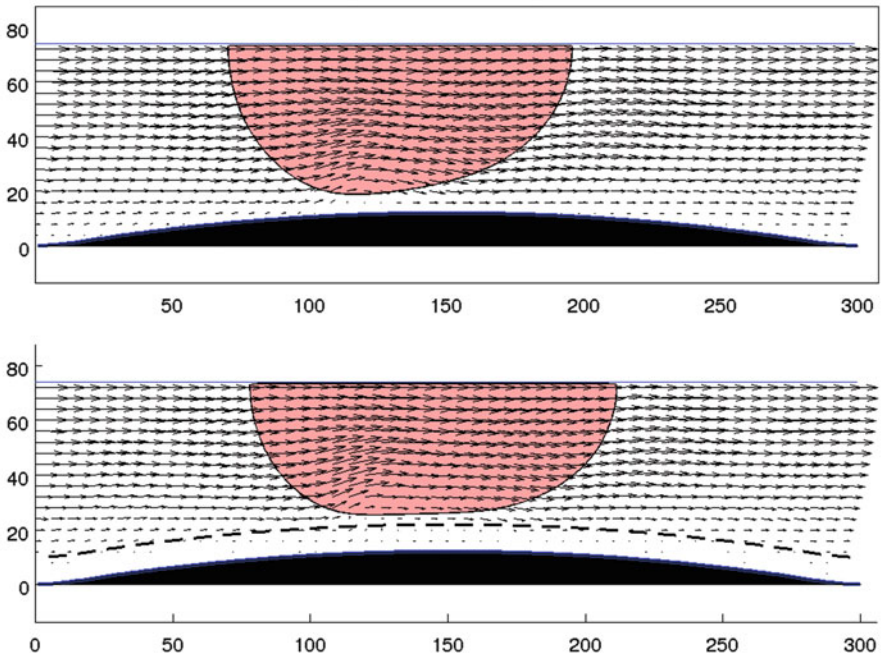

Fig. 10.4 The velocity field for the particulate fluid in the region of the endothelium. The extent of the ESL is indicated by the *broken line*. An enhanced recirculation region is induced by the porous media (*bottom*), with respect to an experiment without glycocalyx (*top*). The single deformable drop has been acted on by encountering the glycocalyx body force field. The flow appears to be deflected up which would tend to protect the endothelial cell surface from increased WSS

10.6 The MUPHY Software

The simulation of real-life blood flows involves five basic steps: (1) acquisition of MDCT data, (2) data segmentation into a stack of slices, (3) mesh generation from the segmented slices, (4) flow simulation; (5) data analysis and visualization. The MUPHY simulation package is designed to handle generic geometries, such as those provided by the MDCT acquisitions, and to run large-scale simulations on commodity or high-performance hardware resources. The major advantage of MUPHY is the possibility of concurrently simulating fluid dynamics together with suspended bodies at cellular and molecular scales. This multi-scale methodology arises from the combined use of LB and molecular dynamics techniques and has been discussed in previous sections and in paper [3].

In the design of MUPHY, we have followed some basic guidelines that allow us to use the software as is, for a number of diverse applications. The cornerstone of our approach is to use an indirect addressing scheme [11, 37]. At variance with most Navier–Stokes solvers, the LB mesh is Cartesian, providing extreme simplicity in

data management and algorithms. At the working resolution, given the size of a reconstructed arterial tree (linear edge $\simeq$ 10 cm), the resulting simulation box would have a size $\sim 10^{11}\Delta x^3$, clearly beyond the capabilities of most commodity and high-end computers. Hence, for the LB simulation and all the ancillary stages of simulation (mesh construction and data analysis), only the active computational nodes, those residing inside the arterial vessel, should be taken into account, resulting in huge savings in memory (about three orders of magnitude) and CPU time. The scheme relies on representing sparse mesh regions as a compact one-dimensional primary array, complemented by a secondary array that contains the Cartesian location of each element. In addition, neighboring mesh points are accessed by constructing a connectivity matrix whose elements are pointers to the primary storage array. For the LB mesh topology, this matrix requires the storage of $18 \times N_{\mathrm{mesh}}$ elements, where N_{mesh} is the number of active computational nodes. The indirect addressing approach demands some extra programming effort and may result in a minor (and very reduced on modern computing platforms) computational penalty in simulating non-sparse geometries. This choice provides strategic advantages in handling sparse and generic systems, allowing us to handle a number of fluid nodes of the order 10^9, a size sufficient to study extended arterial systems with a high degree of ramification. We further mention the possibility of simulating the dynamical trajectories of active and passive tracers. Different ways to exchange hydrodynamic information locally between tracers and mesh nodes can be cast within the indirect addressing framework, without major efficiency penalties [13].

To exploit the features of modern computing platforms, the MUPHY code has been highly tuned and parallelized. The code takes advantage of optimizations like (a) removal of redundant operations; (b) buffering of multiply used operations [45], and (c) fusion of the collision and streaming in a single step. This last technique, already in use in other high-performance LB codes [45], significantly reduces data traffic between main memory and processor. With these optimizations in place, we achieve $\sim$ 30% of the peak performance of a single core of a modern CPU, in line with other highly tuned LB kernels [45]. Indeed, the algorithm for the update of the LB populations has an unfavorable ratio between number of floating point operations and number of memory accesses, no optimized libraries are available as for other computational kernels (e.g., matrix operations or FFTs), and it is not possible to exploit the SIMD-like operations on many modern processors since the LB method has a scattered data access pattern.

10.7 Conclusions

Studying the cardiovascular system and capturing the essence of blood circulation cogently requires to cope with the complexity of such biological fluid, as much as the details of the anatomy under study. From the computational standpoint, taming such complexity is not a trivial task, as it requires to handle several computational actors. Choosing the right computational framework, therefore, is a delicate issue

that has been addressed in the present chapter. It was shown that the LB method is an extremely powerful framework to deal simultaneously with blood plasma, RBCs, and the glycocalyx in a unified and consistent form. The versatility of this framework is such to be a good candidate to study biological fluids of different types and at different scales without major differences.

When dealing specifically with blood and the development of cardiovascular disease, it is key to address the detailed structure and dynamics of blood in the surroundings of the endothelium, as recent work has revealed a correlation between the flow-induced mechano-transduction in the glycocalyx and the development of atherosclerosis. The presence of the glycocalyx is supposed necessary for the endothelial cells to respond to fluid shear, and its role is characterized by studying its response to shear stress. A coarse-grained model and a preliminary numerical simulation of the blood flow over the exact, microscale, corrugated EC shape covered by a prototype ESL have been proposed. Another direction we are undertaking is to enhance our current, simplistic, interfacial tension model with additional stresses and bending properties associated with elastic structures. Our current effort is to modify and extend the behaviour our fluid-fluid interface so as to enrich and adapt its existing mechanical properties, in a manner which mimics the thin membrane of erythrocytes.

If, at one hand, the microscopic blood-wall interaction has a noticeable importance for pathological states, on the other hand, the simulation of large-scale circulatory systems relies on sophisticated imaging techniques and powerful simulation methodologies. Owing to the basic assets of hydrokinetic modeling, the unifying LB methodology provides a reliable and robust approach to the understanding of cardiovascular disease in multiple-scale arterial systems, with great potential for impact on biophysical and biomedical applications. The inclusion of RBCs allows to reproduce non-trivial blood rheology and represents a step forward for clinical purposes, as much as for the basic understanding of biomechanics in model and physiological scenarios.

References

1. Arlsan N (2007) Mathematical solution of the flow field over glycocalyx inside vascular system. Math Comp Appl 12:173–179
2. Benzi R, Succi S, Vergassola M (1992) Theory and application of the lattice boltzmann equation. Phys Rep 222(3):147
3. Bernaschi M, Melchionna S, Succi S, Fyta M, Kaxiras E, Sircar J (2009) MUPHY: a parallel MUlti PHYsics/scale code for high performance bio-fluidic simulations. Comp Phys Comm 180:1495–1502
4. Bouzidi M, Firdaouss M, Lallemand P (2001) Momentum transfer of a boltzmann-lattice fluid with boundaries. Phys Fluids 13(11):3452–3459
5. Boyd J, Buick JM (2008) Three-dimensional modelling of the human carotid artery using the lattice boltzmann method: II. shear analysis. Phys Med Biol 53(20):5781–5795
6. Boyd J, Buick J, Green S (2007) Analysis of the casson and Carreau-Yasuda non-Newtonian models. Phys Fluids 19:032,103

7. Brady JF, Bossis G (1988) Stokesian dynamics. Ann Rev Fluid Mech 20:111, DOI 10.1146/annurev.fl.20.010188.000551, URL http://www.annualreviews.org/doi/abs/10.1146/annurev.fl.20.010188.000551?journalCode=fluid
8. Caro C, Fitzgerald J, Schroter R (1969) Arterial wall shear stress and distribution of early atheroma in man. Nature 223:1159–1161
9. Chatzizisis YS, Jonas M, Coskun AU, Beigel R, Stone BV, Maynard C, Gerrity RG, Daley W, Rogers C, Edelman ER, Feldman CL, Stone PH (2008) Prediction of the localization of high-risk coronary atherosclerotic plaques on the basis of low endothelial shear stress: An intravascular ultrasound and histopathology natural history study. Circ 117(8):993–1002
10. Dullweber A, Leimkuhler B, Mclachlan R (1997) A symplectic splitting method for rigid-body molecular dynamics. J Chem Phys 107:5851
11. Dupuis A, Chopard B (1999) Lattice gas: An efficient and reusable parallel library based on a graph partitioning technique. In: Sloot P, Bubak M, Hoekstra A, Hertzberger (eds) Lattice gas: An efficient and reusable parallel library based on a graph partitioning technique, 1st edn, High-Performance Computing and Networking: 7th International Conference, HPCN Europe 1999, Amsterdam, The Netherlands, April 12-14, 1999 Proceedings, Springer
12. Evans D, Lawford P, Gunn J, Walker D, Hose D, Smallwood R, Chopard B, Krafczyk M, Bernsdorf J, Hoekstra A (2008) The application of multiscale modelling to the process of development and prevention of stenosis in a stented coronary artery. Phil Trans R Soc A 366 (1879):3343–3360
13. Fyta M, Kaxiras E, Melchionna S, Succi S (2008) Multiscale simulation of nanobiological flows. Comput Sci Eng March/April:10
14. Gay JG, Berne BJ (1981) Modification of the overlap potential to mimic a linear site–site potential. J Chem Phys 74:3316, URL http://dx.doi.org/10.1063/1.441483
15. Guo Z, Zhao T (2002) Lattice boltzmann model for incompressible flows through porous media. Phys Rev E 66:036,304
16. Guo Z, Zheng C, Shi B (2002) Discrete lattice effects on the forcing term in the lattice boltzmann method. Phys Rev E 65:046,308
17. Guo Z, Zheng C, Shi B (2002) An extrapolation method for boundary conditions in lattice boltzmann method. Phys Fluids 14:2007
18. Halliday I, Hollis A, Care C (2007) Lattice boltzmann algorithm for continuum multicomponent flow. Phys Rev E 76:026,708
19. Heart and stroke encyclopedia (2009) American Heart Association, http://www.americanheart.org. Accessed 2009
20. Janela J, Pontrelli G, Sequeira A, Succi S, Ubertini S (2010) Unstructured lattice-boltzmann methods for hemodynamics flows with shear-dependent viscosity. Int J Modern Phys 21 (6):1–17
21. Ladd AJC, Verberg R (2001) Lattice-Boltzmann simulations of particle-fluid suspensions. J Stat Phys 104(5):1191–1251
22. Latt J, Chopard B, Malaspinas O, Deville M, Michler A (2008) Straight velocity boundaries in the lattice Boltzmann method. Phys Rev E 77(5):056,703
23. Malek AM, Alper SL, Izumo S (1999) Hemodynamic shear stress and its role in atherosclerosis. J Am Med Assoc 282(21):2035–2042, DOI 10.1001/jama.282.21.2035
24. Melchionna S (2007) Design of quasisymplectic propagators for langevin dynamics. J Chem Phys 127:044,108
25. Melchionna S (2011) Incorporation of smooth spherical bodies in the lattice boltzmann method. J Comput Phys 230(10):3966–3976, DOI 10.1016/j.jcp.2011.02.021, URL http://www.sciencedirect.com/science/article/B6WHY-5281T5X-1/2/c5feae9e1ad72e651d08cf21a575186d
26. Melchionna S (2011b) A model for red blood cells in simulations of large-scale blood flows. Macromol Theory & Sim 20:000, DOI 10.1002/mats.201100012, URL http://onlinelibrary.wiley.com/doi/10.1002/mats.201100012/abstract
27. Melchionna S, Bernaschi M, Succi S, Kaxiras E, Rybicki FJ, Mitsouras D, Coskun AU, Feldman CL (2010) Hydrokinetic approach to large-scale cardiovascular blood flow. Comput Phys Comm 181:462–472

28. Melchionna S, Kaxiras E, Bernaschi M, Succi S (2011) Endothelial shear stress from large-scale blood flow simulations. Phil Trans Royal Soc A: Math, Phys Eng Sci 369(1944):2354–2361, DOI 10.1098/rsta.2011.0042, URL http://rsta.royalsocietypublishing.org/content/369/1944/2354.abstract
29. Ouared R, Chopard B (2005) Lattice boltzmann simulations of blood flow: Non-Newtonian rheology and clotting processes. J Stat Phys 121:209–221
30. Pahakis M, Kosky J, Dull R, Tarbell J (2007) The role of endothelial glycocalyx components in mechanotransduction of fluid shear stress. Biochem Biophys Res Comm 355(1):228–233
31. Peters A, Melchionna S, Kaxiras E, Latt J, Sircar J, Bernaschi M, Bisson M, Succi S (2010) Multiscale simulation of cardiovascular flows on the IBM Bluegene/P: full Heart-Circulation system at Red-Blood cell resolution. In: Proceedings of the 2010 ACM/IEEE international conference for high performance computing, networking, storage and analysis, IEEE Computer Society, pp 1–10
32. Pontrelli G, Ubertini S, Succi S (2009) The unstructured lattice boltzmann method for non-newtonian flows. J Stat Mech Theory & Exp, P06005:1–13
33. Pontrelli G, Halliday I, Spencer T, Care C, Köenig C, Collins M (2011) Near wall hemodynamics: Modelling the glycocalyx and the endothelium surface. Proceedings micro and nano flows conference, MNF2011, CD rom
34. Pontrelli G, Köenig C, Halliday I, Spencer T, Collins M, Long Q, Succi S (2011) Modelling wall shear stress in small arteries using the lattice boltzmann method: Influence of the endothelial wall profile. Med Eng Phys 33(7):832–839
35. Reichlin T, Wild A, Dürrenberger M, Daniels A, Aebi U, Hunziker P, Stolz M (2005) Investigating native coronary artery endothelium in situ and in cell culture by scanning force microscopy. J Structural Biol 152:52–63
36. Rybicki FJ, Otero HJ, Steigner ML, Vorobiof G, Nallamshetty L, Mitsouras D, Ersoy H, Mather RT, Judy PF, Cai T, Coyner K, Schultz K, Whitmore AG, Di Carli MF (2008) Initial evaluation of coronary images from 320-detector row computed tomography. Intl J Cardiovasc Imaging 24(5):535–546
37. Schulz M, Krafczyk M, Tolke J, Rank E (2002) Parallelization strategies and efficiency of CFD computations in complex geometries using the lattice boltzmann methods on high-performance computers. In: Breuer M, Durst F, Zenger C (eds) High performance scientific and engineering computing, Proceedings of the 3rd international Fortwihr conference on HPESC, Erlangen, March 12-14, 2001, vol 21 of Lecture notes in computational science and engineering, Springer
38. Secomb T, Hsu R, Pries A (2002) Blood flow and red blood cell deformation in nonuniform capillaries: Effects of the endothelial surface layer. Microcirculation 9:189–196
39. Shaaban AM, Duerinckx AJ (2000) Wall shear stress and early atherosclerosis: A review. AJR Am J Roentgenol 174(6):1657–1665
40. Sherman TF (1981) On connecting large vessels to small. the meaning of murray's law. J Gen Physiol 78(4):431 –453, DOI 10.1085/jgp.78.4.431, URL http://jgp.rupress.org/content/78/4/431.abstract
41. Succi S (2001) The lattice Boltzmann equation for fluid dynamics and beyond. Oxford University Press, USA
42. Vincent P, Sherwin S, Weinberg P (2008) Viscous flow over outflow slits covered by an anisotropic brinkman medium: A model of flow above interendothelial cell cleft. Phys Fluids 20(6):063,106
43. Vorp DA, Steinman DA, Ethier CR (2001) Computational modeling of arterial biomechanics. Comput Sci Eng pp 51–64
44. Weinbaum S, Tarbell J, Damiano E (2007) The structure and the function of the endothelial glycocalyx layer. Ann Rev Biom Eng 9(6.1):121–167
45. Wellein G, Zeiser T, Hager G, Donath S (2006) On the single processor performance of simple lattice boltzmann kernels. Comput Fluids 35(8-9):910–919
46. Zou Q, He X (1997) On pressure and velocity boundary conditions for the lattice boltzmann BGK model. Phys Fluids 9(6):1591

Chapter 11
Dielectrophoretic Characterization and Continuous Separation of Cells in a PDMS Microfluidic Device with Sidewall Conducting PDMS Composite Electrodes

Nuttawut Lewpiriyawong and Chun Yang

Abstract A complete polymer microfluidic device with sidewall conducting PDMS composite electrodes represents a new class of dielectrophoresis (DEP) devices used for manipulation of cells. This chapter summarizes the key functions of such a novel device for characterization of cells in stagnant flow and for continuous-flow separation of microparticles and cells based on size or electrical polarizability. These novel conducting PDMS composites can be synthesized by mixing 1 μm silver particles into PDMS gel. Unlike other existing fabrication techniques relying heavily on glass and silicon, the proposed technique yields sidewall conducting PDMS electrodes which are strongly bonded to PDMS microfluidic channels and allows for straightforward device assembly with only one-step oxygen plasma treatment.

11.1 Introduction

Separation of target cells in biofluids such as blood or bone marrow is one of the most important bioanalytical tasks for medical practitioners to diagnose patients' pathological states [1]. These complex biofluids usually contain various biosamples such as healthy cells, cancer cells, and even pathogenic microorganisms (e.g., *E. coli* O157:H7). Some of them are of similar sizes but possess different electrical properties; some are of similar electrical properties but have different sizes. For example, MCF10A, MDA-MB-231, and MCF7 human breast cancer cells are of similar sizes but not much difference in electrical properties [2]. Normal erythrocytes become less electrically conductive as they are injected by malaria

N. Lewpiriyawong • C. Yang (✉)
School of Mechanical and Aerospace Engineering, Nanyang Technological University, 50 Nanyang Avenue, Singapore 639798, Singapore
e-mail: lewp0001@e.ntu.edu.sg; mcyang@ntu.edu.sg

M.W. Collins and C.S. König (eds.), *Micro and Nano Flow Systems for Bioanalysis*, Bioanalysis 2, DOI 10.1007/978-1-4614-4376-6_11,

(*Plasmodium falciparum*) [3]. On the other hand, lymphocytes, monocytes, and granulocytes are white blood cells having similar electrical properties but are different in size [4].

Dielectrophoresis field-flow fractionation (DEP-FFF) has been proposed for separating cells in continuous flow [5]. DEP-FFF transports cells with pressure-driven flow in microfluidic channels and separates them using an externally applied DEP force perpendicular to the direction of flow. Under a nonuniform electric field, polarizable cells in a buffer solution can be manipulated by the DEP force as a result of polarization effects [6]. Since the magnitude and the direction of the DEP force is dependent on the polarizability of cell relative to that of buffer solution and its magnitude is also scaled to the cubic power of the cell radius, cells can be separated based on their size or polarizability without any pretreatment [7]. These intriguing benefits enable DEP to be a label-free, inexpensive and versatile separation tool, superior to flow cytometry where modification of samples with expensive reagents is often required [8].

To produce a DEP force, the conventional approach of generating a nonuniform electric field in DEP devices is through planar metallic electrodes deposited on the bottom or/and the top of the separation channel [9–11]. However, the rapid decay of electric field strength from the electrode surface often causes inefficient manipulation of cells at the center of the separation channel [12, 13]. As a result, three dimensional (3-D) or sidewall electrodes have been engineered to generate a 3-D electric field across the channel height. Recently reported 3-D electrodes are made from heavily doped silicon [14], pyrolytic SU-8 photoresist [15], electroplated gold or titanium [16, 17]. Nevertheless, the assembly of these devices is still rather complicated to prevent liquid leakage as the devices are fabricated from glass or silicon.

With the rapid advancement of soft lithography techniques, the use of polydimethylsiloxane (PDMS) as the fabrication material is ubiquitous in microfluidic devices due to its numerous advantages (e.g., ease of fabrication and bonding, low cost, biocompatibility, and optical transparency) [18]. However, a serious challenge is the infeasibility to embed 3-D metallic electrodes in PDMS-based DEP devices, since the adhesion between metallic electrodes and PDMS is extremely weak [19]. Manually embedding copper electrodes into PDMS channel to a certain degree overcomes the problem [20, 21], but this technique is not practical for batch fabrication and also readily causes liquid leakage at high flow rates due to the mismatch between the thickness of copper sheet and that of channel height.

Here we introduce a complete polymer DEP device with sidewall conducting PDMS composite electrodes for manipulating particles and biological cells [22, 23]. The proposed fabrication technique allows for very strong adhesion between the conducting PDMS composite electrodes and PDMS microfluidic channels, thus greatly facilitating the device assembly with only one-step oxygen plasma treatment. This novel device with sidewall conducting PDMS composite electrodes is so versatile that it can be employed for characterizing cells in stagnant flow and separating particles or cells based on their size or their polarizability.

11.2 Basic Theory of Dielectrophoresis

DEP is referred to as the motion of a neutrally charged particle suspended in a dielectric medium under a nonuniform electric field, and physically it results from the interaction between the induced dipoles in the polarized particle and the applied nonuniform electric field [7]. To provide a better understanding of how polarization occurs, two scenarios are described: a neutral particle is placed in both uniform and nonuniform electric fields. As shown in Fig. 11.1a, under an applied electric field, both particle and medium are polarized and dipole charges are induced in the particle. When the electric field is uniform, columbic forces acting on induced net dipole charges (on both sides) are equal in magnitude but opposite in direction. Therefore, the net force is zero and the particle has no movement. This phenomenon

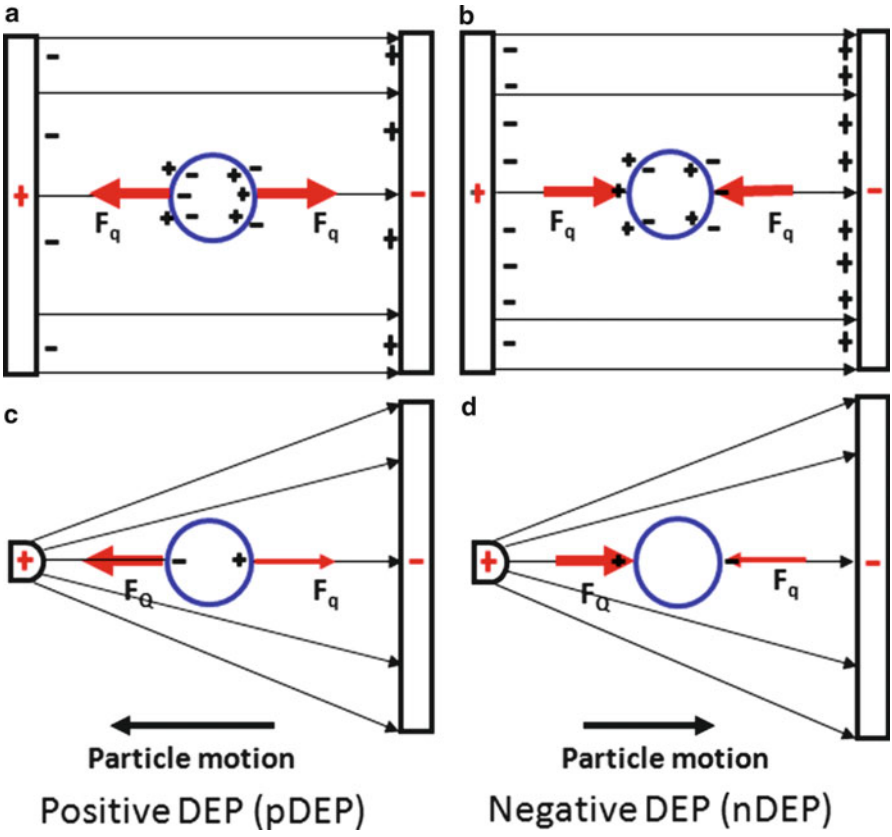

Fig. 11.1 Motion of a neutrally charged particle under an applied electric field [24]. A neutral particle (**a**) more or (**b**) less polarizable than the suspending medium has no movement under an applied uniform electric field due to zero net force. Under a nonuniform electric field the net force acting on the particle however is no longer zero. (**c**) When a particle is more polarizable than the suspending medium, the particle is attracted to the high electric field region as $F_Q > F_q$. (**d**) When a particle is less polarizable than the suspending medium, the particle is repelled from the high electric field region as $F_Q > F_q$

occurs for the particle either more or less polarizable than the suspending medium as shown in Fig. 11.1a, b, respectively. On the other hand, consider a particle more polarizable than the medium in a spatially nonuniform electric field (Fig. 11.1c). Because the electric field near the left electrode is higher, the columbic force on the left side is larger ($F_Q > F_q$). As a result, the net force attracts the particle to the high electric field region. This motion is known as positive DEP (pDEP). In contrast, when a particle is less polarizable than the suspending medium, the net force repels the particle to be away from the high electric field region (Fig. 11.1d). This motion is known as negative DEP (nDEP).

Under an AC electric field, $\vec{E}_{ac}(\vec{r}, t)$, the DEP force acting on a dielectric particle can be quantified by using the effective dipole moment method [25]. Assuming that the particle and suspending medium have dielectric permittivities of ε_p and ε_m, and conductivities of σ_p and σ_m, respectively, the time-average DEP force acting on the particle with radius a can be expressed as

$$\left\langle \vec{F}_{DEP} \right\rangle = 2\pi\varepsilon_m a^3 Re[K^*(\omega)]\nabla\vec{E}^2_{rms} \tag{11.1}$$

where $\langle\,\rangle$ denotes the time-average, $\vec{E}_{rms,ac} = \vec{E}_{ac}/\sqrt{2}$ is the root-mean-square magnitude of the applied AC electric field and ∇ denotes a gradient operator. $Re[K^*(\omega)]$ is the real part of the Clausius-Mossotti (CM) factor and $-0.5 \le Re[K^*(\omega)] \le 1$. $K^*(\omega)$ is a function of electric field frequency and complex permittivities of the particle and the suspending medium, and it can be expressed as

$$K^*(\omega) = \frac{\varepsilon_p^* - \varepsilon_m^*}{\varepsilon_p^* + 2\varepsilon_m^*} \tag{11.2}$$

where $\varepsilon_p^* = \varepsilon_p - i\sigma_p/\omega$ and $\varepsilon_m^* = \varepsilon_m - i\sigma_m/\omega$ are the complex permittivities of the particle and the suspending medium, respectively, $i = \sqrt{-1}$, and $\omega = 2\pi f$ is the radian field frequency. From (11.1), under the same applied electric field condition, the sign and magnitude of the DEP force depends on both $Re[K^*(\omega)]$ and particle size. When $Re[K^*(\omega)]>0$, it is indicated that the particle is more polarizable than the suspending medium and it experiences a pDEP force (Fig. 11.1c). On the other hand, $Re[K^*(\omega)]<0$ indicates that the particle is less polarizable than the suspending medium and it experiences an nDEP force (Fig. 11.1d). Furthermore, as $Re[K^*(\omega)]$ becomes zero, both particle and the suspending medium are equally polarizable and the corresponding frequency is known as the cross-over frequency where the DEP force vanishes. Therefore, cells of the same size possessing distinct polarizabilities (nDEP and pDEP) can be separated from each other. In some cases where cells have the same polarizability but are of different size, larger cells experiencing a stronger nDEP force can be repelled farther away from the high electric field region than the smaller ones, thus achieving separation. In addition, due to the complex structure of biological cells such as yeast and bacterial cells, the CM factor can be determined by modeling the structure of a cell as consisting of three concentric layers. For yeast cells, the three layers are wall, cytoplasm, and nucleus [26]. For bacterial cells, the

three layers are wall, membrane, and cytoplasm [27]. The CM factor is then given by

$$K^*(\omega) = \frac{\varepsilon^*_{\text{cell}} - \varepsilon^*_{\text{m}}}{\varepsilon^*_{\text{cell}} + 2\varepsilon^*_{\text{m}}} \tag{11.3}$$

where $\varepsilon^*_{\text{cell}}$is the effective complex permittivity of the cell. Using the smeared-out sphere approach [28], one can obtain the effective complex permittivity of the cell as

$$\varepsilon^*_{\text{cell}} = \varepsilon^*_1 \left[\frac{\left(\frac{r_1}{r_2}\right)^3 + 2\left(\frac{\varepsilon^*_{23} - \varepsilon^*_1}{\varepsilon^*_{23} + 2\varepsilon^*_1}\right)}{\left(\frac{r_1}{r_2}\right)^3 - \left(\frac{\varepsilon^*_{23} - \varepsilon^*_1}{\varepsilon^*_{23} + 2\varepsilon^*_1}\right)} \right] \tag{11.4}$$

and

$$\varepsilon^*_{23} = \varepsilon^*_2 \left[\frac{\left(\frac{r_2}{r_3}\right)^3 + 2\left(\frac{\varepsilon^*_3 - \varepsilon^*_2}{\varepsilon^*_3 + 2\varepsilon^*_2}\right)}{\left(\frac{r_2}{r_3}\right)^3 - \left(\frac{\varepsilon^*_3 - \varepsilon^*_2}{\varepsilon^*_3 + 2\varepsilon^*_2}\right)} \right] \tag{11.5}$$

where ε^*_1, ε^*_2,ε^*_3,r_1, r_2, and r_3 are the complex permittivities and radii of (1) yeast cells' wall, cytoplasm, and nucleus or (2) bacterial cells' wall, membrane, and cytoplasm, respectively.

11.3 PDMS Microfluidic Device with Sidewall Conducting PDMS Composite Electrodes

Conducting PDMS composites were synthesized by adding 1 μm silver (Ag) particles into PDMS gel and using them as sidewall DEP electrodes in a PDMS-based micro flow device, as shown in Fig. 11.2a. The device fabrication processes were elaborated in detail in our previous work [22]. The device has a 200 μm wide and 1,400 μm long separation channel with four branch channels connected to inlets A and B and outlets C and D. The branch channels A, B, C, and D are 100, 115, 50, and 170 μm wide, respectively. The depth of all channels is 40 μm. Four 100 μm wide AgPDMS electrodes with 100 μm separating gaps apart were embedded along a sidewall of the separation channel.

The following key functions of such a device have been demonstrated: (1) DEP characterization of cells in stagnant flow, (2) continuous-flow separation of cells from latex particles by polarizability, and (3) continuous-flow separation of microparticles by size. The DEP characterization of yeast and bacterial cells was

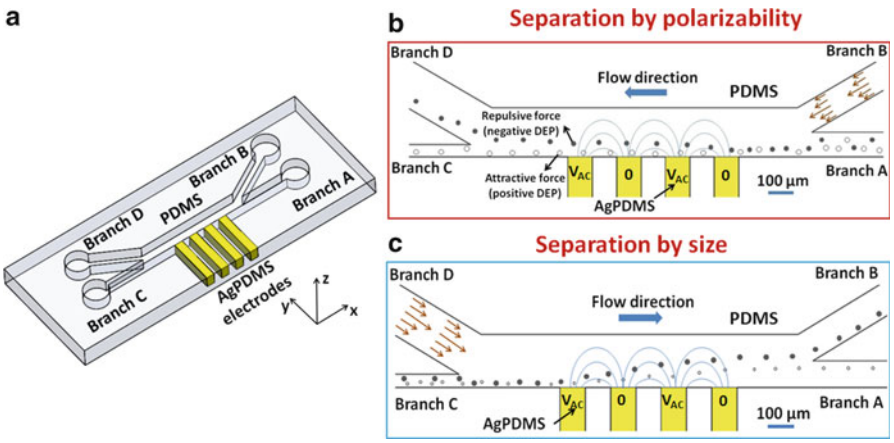

Fig. 11.2 (**a**) Schematic of a PDMS-fabricated microfluidic device with sidewall conducting AgPDMS composite electrodes. (**b**) Schematic of continuous separation of samples of similar sizes by polarizability [23]. In this operation mode, the device separates the samples under pDEP to the lower branch C and the others under nDEP to the upper branch D. (**c**) Schematic of continuous separation of samples of two different sizes but having the same polarizability [22]. The device separates larger samples (undergoing a larger nDEP force) to the upper branch B and smaller samples to the lower branch A ((**a** and **c**) are adapted with permission from Lewpiriyawong et al. (2010). ©2010 WILEY-VCH Verlag GmbH & Co. KGaA; (**b**) is reprinted with permission from Lewpiriyawong et al. (2011). ©2011 American Chemical Society)

performed in stagnant buffer solutions under a broad spectrum of AC electric field frequencies (i.e., 10 kHz to 80 MHz). Accommodating this parameter allows for an investigation of frequency-dependent DEP behaviors of cells, which are useful information for separating different kinds of cells. In addition to the characterization, this device can be operated to separate particles and cells, depending on either their polarizability or size.

11.3.1 Separation of Samples by Polarizability

Figure 11.2b illustrates the separation of cells from particles of similar sizes by pDEP and nDEP forces, respectively, due to their different polarizabilities. In particular, the samples containing a mixture of cells and particles from branch A are first hydrodynamically focused by the flow from branch B such that the focused samples can experience a strong DEP force near the electrodes. Then, the cells undergoing pDEP are attracted to the electrodes and are transported to the lower branch C, while the particles undergoing nDEP are repelled away from the electrodes being transported to the upper branch D.

11.3.2 Separation of Samples by Size

Figure 11.2c illustrates the separation of particles having the same polarizability (i.e., nDEP) by size . As larger particles experience a stronger repulsive nDEP force, they are pushed laterally farther away from the electrodes in comparison to the smaller particles. When the applied voltage is large enough, the larger particles can be transported to the upper branch B separating them from the smaller ones, which are transported to the lower branch A.

11.4 Results and Discussion

11.4.1 Numerical Simulation of Electric Fields and DEP Forces

In a microchannel with sidewall AgPDMS composite electrodes, the electric field $\vec{E} = -\nabla\phi$ associated with the electric potential ϕ is governed by Laplace's equation ($\nabla^2\phi = 0$). The boundary conditions are specified based on the channel configuration shown in Fig. 11.2a. The component of the electric field normal to the nonconducting PDMS walls as well as all inlets and outlets are set to be zero, the first and third electrodes (from the left) are assigned with an electric potential ($\phi = V_{AC}$), and the potentials of the second and fourth electrodes are also set to be zero ($\phi = 0$). The contour electric fields (lines) and DEP forces (arrows) created by the sidewall AgPDMS electrodes are numerically obtained using COMSOL Multiphysics (version 3.4). As shown in Fig. 11.3a, when $Re[K^*(\omega)] < 0$, nDEP forces cause the repulsion of cells away from the sidewall electrodes. The opposite scenario (cell attraction to the electrodes) occurs when $Re[K^*(\omega)] > 0$, as shown in Fig. 11.3b. The magnitude of the DEP forces shown by arrows are proportional to the length of arrows. The simulation results also indicate that highly nonuniform electric fields are induced near the AgPDMS electrode edges as can be seen from the high density of accumulated electric field lines. However, electric field strength rapidly decreases at further distance from the electrodes (along the y direction). Such an electric field distribution results in markedly strong DEP forces near the electrodes. Furthermore, along the horizontal direction, the DEP force is much weaker towards both the center of the electrode and the center of the gap between any two adjacent electrodes. Therefore, for all samples of experiencing dominant DEP force effects, the hydrodynamic focusing is incorporated in our two separation mechanisms to confine the flowing particle stream near the edges of the sidewall electrodes.

11.4.2 DEP Characterization of Yeast and Bacterial Cells

DEP behaviors of yeast and bacterial cells were characterized under various AC electric field frequencies ranging from 10 kHz to 80 MHz in stagnant buffer

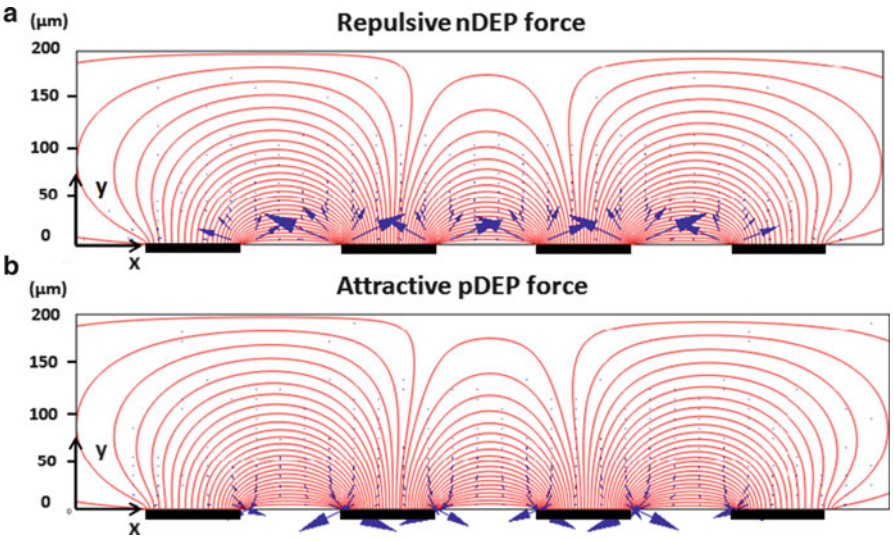

Fig. 11.3 Numerical simulation of the contour electric fields (*lines*) and DEP forces (*arrows*) created by sidewall AgPDMS electrodes (*thick black segments*). (**a**) nDEP forces cause repulsion of cells away from the electrodes, while (**b**) pDEP forces point towards the electrodes resulting in attraction of cells. These DEP forces are shown by *arrows* with their length proportional to the magnitude of force

solutions. The effects of medium conductivity on cellular DEP behavior were investigated by suspending the cells in 2 μs/cm DI water and 380 μs/cm NaCl solution. Based on (11.3) together with (11.4) and (11.5), the real part of the CM factor predicts the frequency-dependent DEP responses of yeast and bacterial cells whether they both experience either pDEP or nDEP, depending on the specific frequency and buffer solution as shown in Fig. 11.4a. These predicted behaviors were computed by basing them on the cell's structural dimensions and dielectric properties taken from the literature [27, 29]; they were verified experimentally through the use of conducting PDMS composite electrodes.

Figure 11.4b presents well dispersed yeast cells in stagnant 380 μS/cm NaCl solution under no applied electric field. With an AC voltage of 10 V at 10 kHz, yeast cells underwent a repulsive nDEP force and were moved away from the electrodes (Fig. 11.4c). This behavior is consistent with the CM factor prediction which explains that yeast cells are less polarizable than the 380 μS/cm NaCl solution at 10 kHz. More findings from the literature [30–32] confirmed that yeast cells tend to exhibit nDEP in the low frequency regime. On the other hand, at 10 MHz, yeast cells underwent an attractive pDEP force, thus being transported towards and accumulating at the electrodes' edges (Fig. 11.4d). Above 80 MHz, no DEP movement of cells could be noticed. This was anticipated, since at very high frequencies the computed effective complex permittivity of yeast cells is rather close to the permittivity of the buffer solution, the resulting CM factor becomes small at 80 MHz (Fig. 11.4a). Hence, the DEP force became insignificant in the experiments. Moreover, the device can

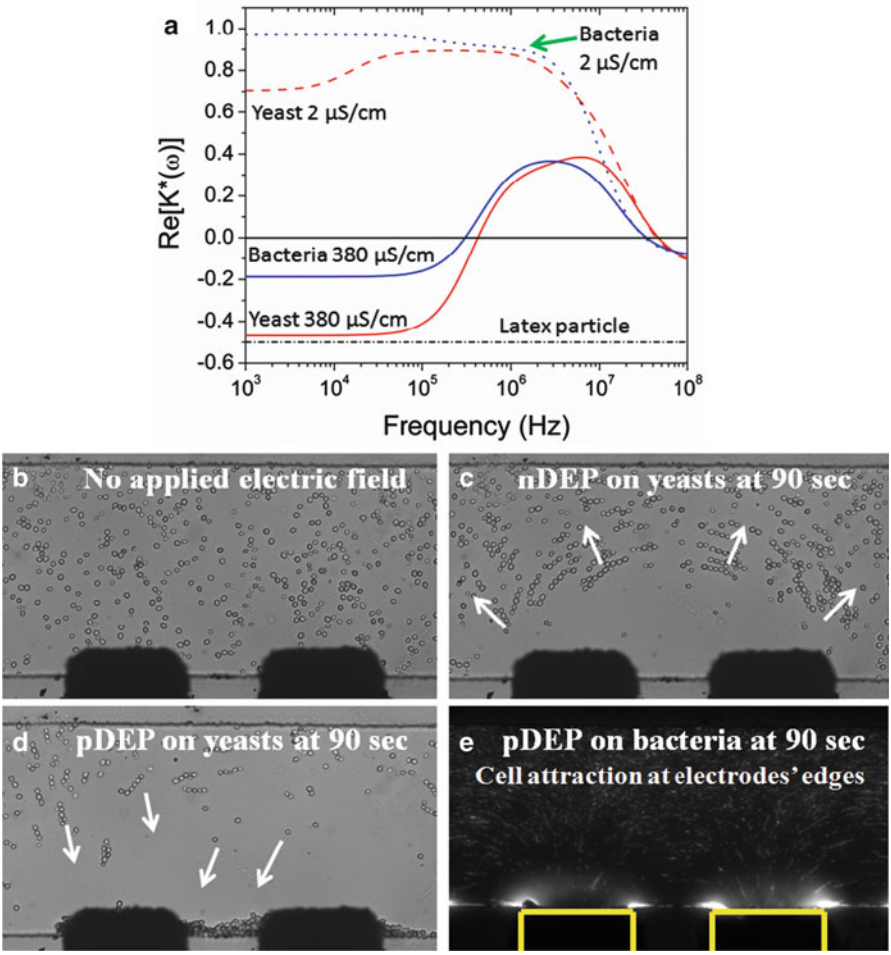

Fig. 11.4 (**a**) CM factor versus electric field frequency for yeast and bacterial cells in 2 μS/cm DI water and 380 μS/cm NaCl solution and for latex particles in 380 μs/cm NaCl solution. The structural dimensions and dielectric properties of these cells are taken from the literature [27, 29]. (**b–e**) DEP behaviors of yeast and bacterial cells in stagnant NaCl solution of 380 μS/cm. (**b**) Well dispersed yeast cell suspension in the absence of applied AC electric field. (**c**) Cells experience a repulsive nDEP force after 90 s under 10 V at 10 kHz [23]. (Reprinted with permission from Lewpiriyawong et al. (2011). ©2011 American Chemical Society). (**d**) Cells experience an attractive pDEP force after 90 s under 10 V at 10 MHz. (**e**) Accumulation of *E. coli* after 90 s by an attractive pDEP force under 15.3 V at 1 MHz. These snapshot images were captured with a 20× objective

reasonably provide the cross-over frequencies as compared to the predicted ones. The DEP behaviour of yeast cells was found to change from nDEP to pDEP at ~300 kHz and from pDEP to no DEP at ~40 MHz. At these applied AC field frequencies, cells could not move due to the DEP force being zero.

Additional experimental findings showed that reducing the medium conductivity from 380 to 2 μS/cm can result in a change from nDEP to pDEP at low frequencies. According to (11.3), such switching of DEP behavior is expected when the medium conductivity is lower than that of the cell (i.e., $\sigma_m < \sigma_{cell}$). Experiments using conducting AgPDMS electrodes clearly confirmed this DEP switching. For all frequencies ranging from 10 kHz up to a cross-over frequency of 40 MHz, yeast cells suspended in 2 μS/cm DI water were observed to experience only a pDEP force, attracting them to the electrodes (images are not shown here but the cell behavior under pDEP are similar to that shown in Fig. 11.4d). Above the cross-over frequency of 40 MHz, cells no longer moved under the applied AC field because the DEP force became very weak (as shown by the red dashed line at 40 MHz shown in Fig. 11.4a). In addition, cells were also observed to form chains in the same direction as the electric field lines as shown in Fig. 11.3. The mechanism of chain formations has been described in the literature [25]. It is also important to note that in DI water, Baker's yeast cells still survive though experiencing a high osmotic pressure[33].

DEP behavior of *E. coli* cells was also obtained through the use of conducting AgPDMS electrodes. Under an AC voltage of 15.3 V at 400 kHz and 30 MHz, *E. coli* cells in 380 μS/cm NaCl solution exhibited weak pDEP but strong pDEP at 1 MHz (Fig. 11.4e). These DEP behaviour regimes are reasonably consistent with the CM factor prediction in Fig. 11.4a, although no DEP movement was experimentally observed below 150 kHz and above 35 MHz. Moreover, two cross-over frequencies were found at 150 kHz (from no DEP to pDEP) and 35 MHz (from pDEP to no DEP). Similar in behavior to the yeast cells, *E. coli* cells suspended in DI water only experienced pDEP at all frequencies from 10 kHz to 30 MHz, even up to a cross-over frequency of 35 MHz. Formation of an *E. coli* chain was noted in that cells aligned along the electric field lines.

In general, the DEP behavior and the cross-over frequencies of yeast and bacterial cells are quite similar. They experienced nDEP in the low frequency regime (e.g., 10–100 kHz) and pDEP in the medium-to-high frequency regime (e.g., 500 kHz to 10 MHz). On one hand, at low frequencies, the CM factor is mainly determined by the conductivity of the cell and the buffer solution. Since their membrane conductivity is very low, biological cells behave like insulating objects under a DC or low frequency electric field, thus experiencing nDEP [30]. On the other hand, at higher frequencies, an electric current can pass through the capacitive membrane and the conductivity of the cells is dominated by the relatively high conductivity of the internal parts of the cells. As a result, the cells tend to exhibit pDEP in the medium-to-high frequency regime. Furthermore, our experiments showed that *E. coli* cells are generally more conductive than yeast cells. This finding is validated from the experimental facts that in the 380 μS/cm NaCl solution, *E. coli cells* experienced pDEP while yeast cells experienced nDEP at 10 kHz.

11.4.3 Continuous Separation of Samples by Polarizability

The separation of samples of similar sizes based on their different polarizabilities is demonstrated by subjecting one type of samples by nDEP and the others by pDEP. This separation mechanism, previously described in Sect. 11.3, is also shown in Fig. 11.2b. Three binary mixtures were prepared: (1) yeast cells and 5 μm fluorescent latex particles, (2) bacterial cells and 3 μm latex particles, and (3) live and dead yeast cells. These latex microspheres (of similar sizes to yeast and bacterial cells) were selected to eliminate the size-dependent effect.

As shown in Fig. 11.4a, the CM factor predicts that yeast cells and latex particles will exhibit distinct DEP polarizabilities at the medium range of the AC electric field frequency (i.e., from 300 kHz to 1 MHz) in 380 μS/cm NaCl solution. The latex particles are predicted to experience nDEP for all frequencies since they are electrically insulating, and the resulting CM factor of latex particles approaches −0.5. Figure 11.5a presents a snapshot image of the continuous-flow separation of yeast cells (black dots) by pDEP and 5 μm fluorescent latex particles (white dots) by nDEP under 31.2 V at 300 kHz (cross-over frequency of yeast cells) after 4 min. Both yeast cells and particles were hydrodynamically focused near the sidewall AgPDMS composite electrodes so as to have a strong DEP force as shown by the distribution of the simulated DEP force (Fig. 11.3). The latex particles were repulsed from the electrodes by the nDEP force and separated to outlet D. In contrast, as the yeast cells underwent a weak pDEP force, most of them ended up preferentially in outlet C, though the others were observed to be attracted to the electrodes. The rationale that yeast cells exhibited the weak pDEP force rather than zero DEP force at 300 kHz results from their DEP polarizability which is highly sensitive to frequency in this frequency regime. In these experiments, the time window defined by the velocity of the fluid flow (306 μm/s) and the separation channel length (1,400 μm) was about 4.6 s, giving rise to an nDEP drift velocity of about 11 μm/s. The separation of yeast cells (with a throughput ~780/min) and 5 μm latex particles (with a throughput ~1,200/min) were reliable for more than 5 min at the flow rate of 0.15 μl/min, and the separation efficiency was up to 97%.

Compared to yeast cells, separation of smaller samples like *E. coli* cells and 2.9 μm latex particles becomes more challenging as the DEP force—scaled to the cubic power of cell size—on these small cells is much weaker. Therefore, strong pDEP and nDEP forces are preferred for separating these two samples. Based on the CM factor shown in Fig. 11.4a, the most suitable AC electric field frequency to separate *E. coli* from the particles is 10 MHz, since it provides a strong pDEP force for *E. coli* and a strong nDEP force for the particles. However, the maximum frequency achievable by our customized amplifier is limited to 1 MHz to generate a higher voltage (40.4 Vac). Under 40.4 Vac at 1 MHz, clear separation of *E. coli* and 2.9 μm latex particles in 380 μS/cm NaCl solution still can be successfully achieved as illustrated in Fig. 11.5b. This separation of *E. coli* (with a throughput ~1,440/min) and 2.9 μm latex particles (with a throughput ~780/min) were reliable at the flow rate of 0.06 μl/min for more than 6.18 min with a separation efficiency

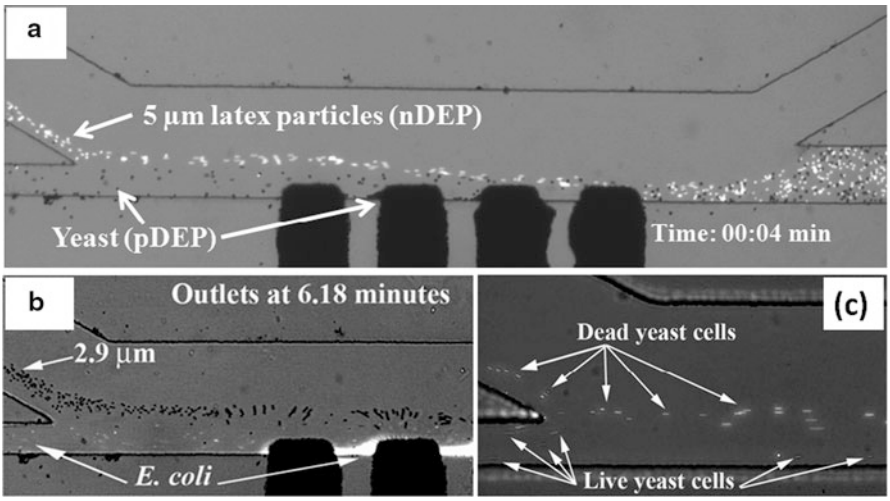

Fig. 11.5 Snapshot images of continuous separation of samples of similar sizes by polarizability [23]. (**a**) Separation of yeast cells (*black dots*) by pDEP from 5 μm fluorescent latex particles (*white dots*) experiencing nDEP under 31.2 Vac at 300 kHz after 4 min. (**b**) Separation of stained *E. coli* cells by pDEP from 2.9 μm latex particles exhibiting nDEP under 40.4 Vac at 1 MHz after 6.18 min. (**c**) Separation of live yeast cells by pDEP from dead yeast cells undergoing nDEP under 26.5 Vac at 1 MHz. The microscopic objective lenses used in (**a**), (**b**), and (**c**) are 5×, 10×, and 20×, respectively (Reprinted with permission from Lewpiriyawong et al. (2011). ©2011 American Chemical Society)

of up to 97%. In these experiments, the time window defined by the velocity of the fluid flow (123 μm/s) and the separation channel length (1,400 μm) was about 11.4 s, thus resulting in an nDEP drift velocity of about 4.4 μm/s.

In addition to the separation of biological cells from latex particles, the device was also tested to separate live and dead yeast cells based on the difference in their electrical properties. The demonstration was performed in a 600 μS/cm NaCl solution. Huang et al. found that the conductivity of the nucleus of live yeast cells dramatically decreased from 0.2 to 7×10^{-3} S/m after they died [28]. The reason the nucleus's conductivity rapidly changes is because the membrane of dead yeast cells becomes more permeable and it permits content inside the cells to exchange with the external liquid medium [34]. Therefore, the dead cells are less conductive and hence are likely to experience nDEP in comparison with the live cells. Consistent with these experimental facts, our characterization results (images not shown here) revealed that at 1 MHz, live cells suspended in a 600 μS/cm NaCl solution underwent pDEP while dead cells underwent nDEP. Figure 11.5c shows continuous-flow separation of live yeast cells (black dots) from dead ones (white dots) under 26.5 V at 1 MHz. Dead cells were repulsed from the electrodes by nDEP and transported to the upper outlet D, while live cells under pDEP were attracted to

the electrodes and ended up in the lower outlet C. The device was operated at a flow rate of 0.087 μl/min with a throughput of 480 cells/min for both samples. The separation efficiency was more than 97%. For these experiments, the time window defined by the velocity of the fluid flow (181 μm/s) and the separation channel length (1,400 μm) was about 7.7 s, thus leading to an nDEP drift velocity of about 6.5 μm/s.

11.4.4 Continuous-Flow Separation of Samples by Size

As elaborated in Sect. 11.3 and illustrated in Fig. 11.2c, samples of different sizes but having the same polarizability (e.g., nDEP) can be separated by size. The DEP force expressed in (11.1) clearly shows that the magnitude of DEP force is proportional to the cubic power of particle radius. Thus, the larger particles attain a stronger nDEP force and can be diverted to the upper branch B, whereas the smaller ones, experiencing a weaker nDEP force, move to the lower branch A. Figure 11.6a shows continuous separation of 5 μm particles from 10 μm particles under 55 Vac at 1 MHz. The separation efficiency for 5 μm particles is 88% at the lower branch A and that for 10 μm particles is 100% at the upper branch B. Moreover, separation of 10 and 15 μm particles was also successfully achieved with a separation efficiency of 100% for both particle sizes as shown in Fig. 11.6b. Both separation experiments were operated at a flow rate of 0.68 μl/min. By assessing the voltages required to achieve the separation of these two cases, the voltage for the second case (with larger particles) is anticipated to be lower than that for the first, since the larger particles attain a stronger DEP force under the same applied voltage.

11.5 Conclusions

This chapter presents manipulation of cells using DEP forces via sidewall PDMS composite electrodes in a complete polymer DEP device. Three main functions of the device are demonstrated, including (1) characterization of cell DEP behavior, (2) separations of cells from latex particles and live and dead cells by polarizability, and (3) separation of microparticles by size. The DEP characterization results reveal the excellent capability of conducting PDMS composite electrodes accurately to provide the desired DEP behavior regimes for both yeast and bacterial cells. Furthermore, the very high separation efficiency of ~97% for all cases (either by polarizability or by size) demonstrates that conducting PDMS composite electrodes have promising performance and versatility to deal with a variety of cells in biofluids.

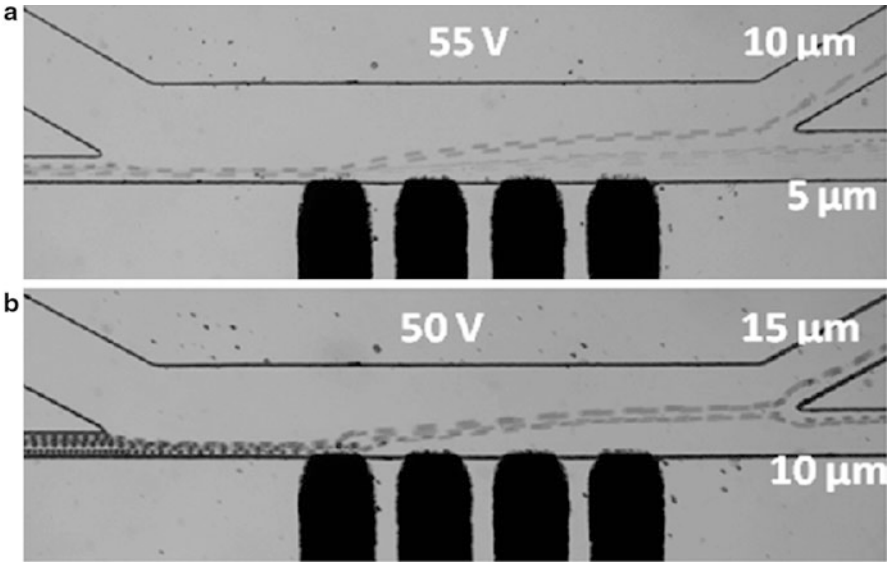

Fig. 11.6 Superimposed images of continuous separation of microparticles according to their size [22]. (**a**) Separation of 5 µm particles from 10 µm particles under 55 Vac at 1 MHz. (**b**) Separation of 10 µm particles from 15 µm particles under 50 Vac at 1 MHz. Both cases are operated at 0.68 µl/min. Separation of larger samples requires lower voltages since they experience a stronger DEP force (Reprinted with permission from Lewpiriyawong et al. (2010). ©2010 WILEY-VCH Verlag GmbH & Co. KGaA)

References

1. Toner M, Irimia D (2005) Blood on a chip. Annu Rev Biomed Eng 7:77–103
2. Henslee EA, Sano MB, Rojas AD, Schmelz EM, Davalos RV (2011) Selective concentration of human cancer cells using contactless dielectrophoresis. Electrophoresis 32:2523–2529
3. Gascoyne P, Mahidol C, Ruchirawat M, Satayavivad J, Watcharasitb P, Beckera FF (2002) Microsample preparation by dielectrophoresis: isolation of malaria. Lab Chip 2:70–75
4. Yang J, Huang Y, Wang X-B, Becker FF, Gascoyne PRC (2000) Differential analysis of human leukocytes by dielectrophoretic field-flow-fractionation. Biophys J 78:2680–2689
5. Schimpf ME, Caldwell K, Giddings JC (2000) Field-flow fractionation handbook. Principle and theory. Wiley, New York
6. Pohl HA (1951) The motion and participation of suspensoids in divergent electric fields. J Appl Phys 22(7):869–871
7. Pohl HA (1978) Dielectrophoresis—the behavior of neutral matter in nonuniform electric fields. Cambridge University Press, Cambridge
8. Lenshof A, Laurell T (2010) Continuous separation of cells and particles in microfluidic systems. Chem Soc Rev 39:1203–1217
9. Yang J, Huang Y, Wang X-B, Becker FF, Gascoyne PRC (1999) Cell separation on microfabricated electrodes using dielectrophoretic/gravitational field-flow fractionation. Anal Chem 71:911–918
10. Wang X-B, Yang J, Huang Y, Vykoukal J, Becker FF, Gascoyne PRC (2000) Cell separation by dielectrophoretic field-flow fractionation. Acc Chem Res 72:832–839
11. Moschallski M, Hausmann M, Posch A, Paulus A, Kunz N, Duong TT, Angres B, Fuchsberger K, Steuer H, Stoll D, Werner S, Hagmeyer B, Stelzle M (2010) MicroPrep: chip-based dielectrophoretic purification of mitochondria. Electrophoresis 31:2655–2663

12. Morgan H, Izquierdo AG, Bakewell D, Green NG, Ramos A (2001) The dielectrophoretic and travelling wave forces generated by interdigitated electrode arrays:analytical solution using Fourier series. J Phys D Appl Phys 34:1553–1561
13. Markx GH, Pethig R, Rousselet J (1997) The dielectrophoretic levitation of latex beads with reference to field-flow fractionation. J Phys D Appl Phys 30:2470–2477
14. Iliescu C, Xu GL, Samper V, Tay FEH (2005) Fabrication of a dielectrophoretic chip with 3D silicon electrodes. J Micromech Microeng 15:494–500
15. Park BY, Madou MJ (2005) 3-D electrode designs for flow-through dielectrophoresis systems. Electrophoresis 26:3745–3757
16. Wang L, Flanagan L, Jeon NL, Monuki E, Lee AP (2007) Dielectrophoresis switching with vertical sidewall electrodes for microfludic flow cytometry. Lab Chip 7:1114–1120
17. Zhang YT, Bottausci F, Rao MP, Parker ER, Mezic I, MacDonald NC (2008) Titanium-based dielectrophoresis devices for microfluidic applications. Biomed Microdevices 10:509–517
18. Xia Y, Whitesides GM (1998) Soft lithography. Annu Rev Mater Sci 28:153–184
19. Niu X, Peng S, Liu L, Wen W, Sheng P (2007) Characterizing and patterning of PDMS-based conducting composites. Adv Mater 19:2682–2686
20. Cetin B, Kang Y, Wu Z, Li D (2009) Continuous particle separation by size via AC-dielectrophoresis using a lab-on-a-chip device with 3-D electrodes. Electrophoresis 30:766–772
21. Kang Y, Cetin B, Wu Z, Li D (2009) Continuous particle separation with localized AC-dielectrophoresis using embedded electrodes and an insulating hurdle. Electrochim Acta 54:1715–1720
22. Lewpiriyawong N, Yang C, Lam YC (2010) Continuous sorting and separation of microparticles by size using AC dielectrophoresis in a PDMS microfluidic device with 3-D conducting PDMS composite electrodes. Electrophoresis 31:2622–2631
23. Lewpiriyawong N, Kandaswamy K, Yang C, Ivanov V, Stocker R (2011) Microfluidic characterization and continuous separation of cells and particles using conducting poly (dimethyl siloxane) electrode induced alternating current-dielectrophoresis. Anal Chem 83:9579–9585
24. Lewpiriyawong N (2011) Continuous separation and manipulation of particles and cells using dielectrophoresis. Nanyang Technological University, Singapore
25. Jones TB (1995) Electromechanics of particles. Cambridge University Press, Cambridge
26. Morgan H, Green NG (2003) AC electrokinetics: colloids and nanoparticles. Research Studies, Philadelphia, PA
27. Suehiro J, Hamada R, Noutomi D, Shutou M, Hara M (2003) Selective detection of viable bacteria using dielectrophoretic impedance measurement method. J Electrostat 57:157–168
28. Wang L, Lu J, Marchenko SA, Monuki ES, Flanagan LA, Lee AP (2009) Dual frequency dielectrophoresis with interdigitated sidewall electrodes for microfluidic flow-through separation of beads and cells. Electrophoresis 30:782–791
29. Huang Y, Holzel R, Pethig R, Wang X-B (1992) Differences in the AC electrodynamics of viable and non-viable yeast cell determined through combined dielectrophoresis and electrorotation studies. Phys Med Biol 37(7):1499–1517
30. Markx GH, Huang Y, Zhou X-F, Pethig R (1994) Dielectrophoretic characterization and separation of micro-organisms. Microbiology 140:585–591
31. Lewpiriyawong N, Yang C, Lam YC (2012) Electrokinetically driven concentration of particles and cells by dielectrophoresis with DC-offset AC electric field. Microfluid Nanofluid 12:723–733
32. Church C, Zhu J, Wang G, Tzeng TJ, Xuan X (2009) Electrokinetic focusing and filtration of cells in a serpentine microchannel. Biomicrofluidics 3:044109
33. Wolfson A, Haddad N, Dlugy C, Tavor D, Shotland Y (2008) Baker's yeast catalyzed asymmetric reduction of methyl acetoacetate in glycerol containing systems. Org Commun 1(2):9–16
34. Tay FEH, Yu L, Panga AJ, Iliescu C (2007) Electrical and thermal characterization of a dielectrophoretic chip with 3D electrodes for cells manipulation. Electrochim Acta 52:2862–2868

Chapter 12
Integrating "Omics" Data for Quantitative and Systems Pharmacology in Translational Oncology

Erica L. Bradshaw Pierce and Aik Choon Tan

Abstract Cancer is the phenotypic end point of multiple genetic aberrations and epigenetic modifications that have accumulated within its genome. These genetic and epigenetic alterations come together to form complex, dynamic, and plastic networks that govern the "hallmarks of cancer." The development of new technologies and powerful computational algorithms to sequence and characterize genomes have enabled researchers to acquire and analyze measurement of tens of thousands of "omic" data points across these genetic and epigenetic changes within cancer genomes. Quantitative and Systems Pharmacology (QSP) represents one of these translational medicine approaches that integrates computational and experimental methods to elucidate, validate, and apply new pharmacological concepts to the development and use of small molecule and biologic drugs. QSP is a promising approach that can provide a scientifically rational approach for defining optimal multidrug regimens, identifying responsive patient populations, identifying translational biomarkers, and designing clinical trials.

E.L. Bradshaw Pierce
Department of Pharmaceutical Science, Skaggs School of Pharmacy, University of Colorado Anschutz Medical Campus, Mail Stop C238, 12850 E. Montview Blvd., Rm 4107, Aurora, CO 80045, USA

University of Colorado Cancer Center, University of Colorado Anschutz Medical Campus, Aurora, CO 80045, USA
e-mail: erica.pierce@ucdenver.edu

A.C. Tan (✉)
Division of Medical Oncology, Department of Medicine, School of Medicine, University of Colorado Anschutz Medical Campus, Mail Stop 8117, 12801 E. 17th Avenue, RC1S-Rm8103, Aurora, CO 80045, USA

Department of Biostatistics and Informatics, Colorado School of Public Health, University of Colorado Anschutz Medical Campus, Aurora, CO 80045, USA

University of Colorado Cancer Center, University of Colorado Anschutz Medical Campus, Aurora, CO 80045, USA
e-mail: aikchoon.tan@ucdenver.edu

M.W. Collins and C.S. König (eds.), *Micro and Nano Flow Systems for Bioanalysis*, Bioanalysis 2, DOI 10.1007/978-1-4614-4376-6_12,

12.1 Introduction

We are entering an important era where cancer medicine is being transformed into personalized medicine. This transformation has been primarily driven by the development of new technologies and powerful computational algorithms to sequence and characterize genomes. These high-throughput and scalable technologies have enabled researchers to acquire and analyze measurement of tens of thousands of "omic" data points across multiple levels (e.g., DNA, RNA, protein) from a single tissue in a reasonable time frame. These massive "omic" data, when analyzed and interpreted by powerful computational methods, reveal new information and knowledge that can be translated to disease treatment and management. Indeed, the application of such technologies in the field of oncology has changed the paradigm of cancer treatment in a manner previously not possible.

Large-scale cancer genome projects such as the Cancer Genome Atlas Research Networks (TCGA) [81,82] and the International Cancer Genome Consortium (ICGC) [38] have identified genes and pathways that drive the initiation in some cancers [81]. Numerous studies have demonstrated that some cancers are dependent on these oncongene driven signals for survival and maintenance [90]. Understanding of these oncogenes is key for developing novel small molecules to inhibit the activity and function of these oncogenes. Targeted cancer therapies have exploited this "oncogene addiction" concept [90] leading to several successful genotype-directed clinical applications of targeted therapies. One of the "best success" examples of exploiting the "oncogenic addiction" concept was the development of Imatinib Mesylate (Gleevec™) in chronic myelogenous leukemia (CML) [19]. CML can be genetically characterized by the formation of the Philadelphia chromosome, which is a result of reciprocal translocation between the long arms of chromosomes 9 and 22 [65]. Consequently, this translocation generates the fusion protein BCR-ABL, a constitutively activated tyrosine kinase, which drives this disease and can be detected in all CML patients. Multiple in vitro and animal model experiments ("bench") have demonstrated that BCR-ABL alone is sufficient to cause CML [15,35,49]. Further mutational analysis has established BCR-ABL protein oncogenic activity is driven by the tyrosine kinase activity. Therefore, efforts have been made to develop an inhibitor of the BCR-ABL tyrosine kinase, with the expectation that this therapeutic should be an effective and selective treatment for CML. Imatinib Mesylate (Gleevec®, Novartis, Inc.), a novel tyrosine kinase inhibitor of BCR-ABL, began Phase I clinical testing ("bedside") in June 1998. The dramatic results obtained from the clinical trials in CML patients led to rapid US Food and Drug Administration (FDA) approval in May 2001 as the first-line treatment for this disease. The success of Imatinib provided the framework for future targeted drug development such as the recent approval of Crizotinib for ALK + patients in non-small cell lung cancer [11] and Vemurafenib for patients with BRAF mutations in advanced melanoma [23].

Over the past decade, DNA-based microarrays have been the assays of choice for high-throughput studies to quantitate and characterize gene expressions.

Microarray-based expression profiling was provided, for the first time, by means of monitoring genome-wide gene expression changes in a single experiment [20,27,75,86,87]. This technology has been widely employed to reveal molecular portraits of gene expression in various cancer subtypes, for correlations with disease progression, as well as response to drug treatments. Recent improvements in the efficiency, quality, and cost of genome-wide sequencing have prompted biologists and biomedical researches to dive into ultra high-throughput, massively parallel genomic sequencing (Next Generation Sequencing, NGS) technology for data acquisition. NGS technology opens up new research avenues for the investigation of a wide range of biological and medical questions across the entire genome at single base resolution. Therefore, NGS technology shifts the bottleneck in sequencing processes from experimental data production to computationally intensive informatics-based data analysis. To gain insights, novel computational algorithms and bioinformatics methods represent a critical component in modern biomedical research to analyze and interpret these massive "omics" data.

As biological systems are complex in nature, merely characterizing individual molecular components (such as genes and proteins) by high-throughput technologies is not sufficient to understand the functional properties of these systems. Classically, efforts have been made to perform linear integration beginning at the level of gene, RNA, and protein to infer function. However, it is becoming clear that to understand the function of the biological systems, integrative approaches are required to delineate the complex interactions both within and across different hierarchical levels of biological organization [6,41]. To exert their functions, individual molecular components interact with each other, which can be located either in the same cell or across cells, and even across organs. Feedback interaction and cross-talk between pathways and networks are common properties in biological systems [57,89]. These complex interactions are fully exerted in cancer cells to provide a robust system under the attack of therapeutics treatment. When cancer cells are exposed to treatment, they can rewire their signaling networks extensively to provide an escape mechanism for the continuation of growth and survival in therapy-specific manner [50]. Therefore, a systems biology approach is required to identify these critical and functional nodes in the oncogenic and escape networks whose inhibition will result in "total systems failure" upon drug treatment.

In this chapter, we will review the technologies and computational algorithms to acquire and analyze these multi-level "omics" data and provide an introduction to systems-based approaches, bridging molecular to cellular to organ to organism scales, in translational research. Here, our emphasis is focusing on quantitative systems pharmacology (QSP), a translational medicine approach that integrates computational and experimental methods to elucidate, validate, and apply new pharmacological concepts to the development and use of small molecule and biologic drugs [74]. In QSP "omics" data can be used to inform molecular model building, which may provide detailed information on drug-target binding, downstream effects, and/or molecular network interactions; that can be incorporated into multi-scale models that describe organism level drug interactions (i.e., pharmacokinetics) and efficacy (Fig. 12.1).

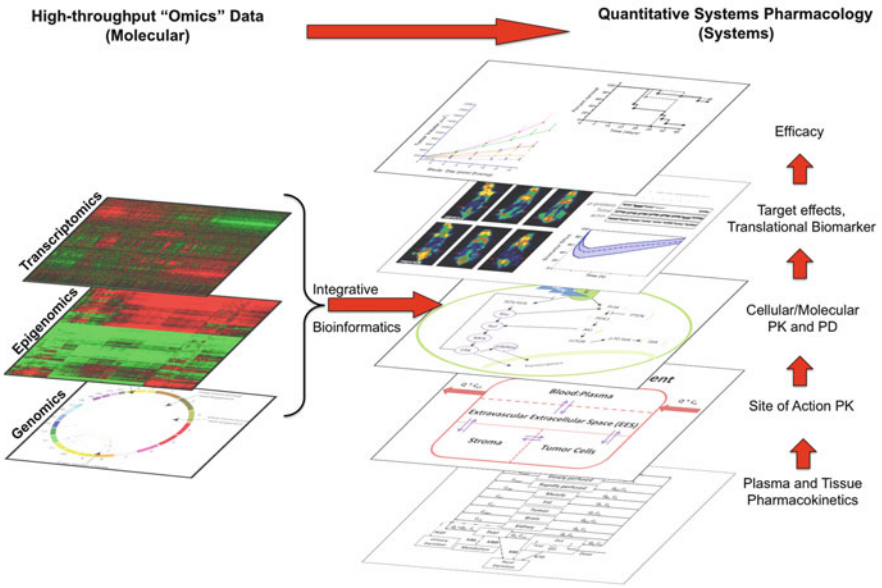

Fig. 12.1 Schematic diagram of integrating "omics" data with multi-scale quantitative systems pharmacology models in cancer research. Cancer is the phenotypic end point of multiple genetic aberrations and epigenetic modifications that have accumulated within its genome. These molecular changes can be measured by high-throughput technologies such as microarray and next-generation sequencing platforms. Using powerful computational algorithms, multiple "omics" data will be integrated at the cellular level for QSP modeling. In QSP modeling, a "middle-out" approach is used to evaluate the concentration–effect relationships of a particular drug. Using mechanistic cellular models derived from "omis" data, detailed modeling can be performed to predict the pharmacokinetics and pharmacodynamics of a drug within the "system." Using these computational approaches, translational biomarkers can be established to predict drug effects. The ultimate goal of QSP is to mechanistically describe drug action of a "system" which should enable better prediction of drug efficacy in patients

12.2 Molecular Levels

Cancer is the phenotypic end point of multiple genetic aberrations and epigenetic modifications that have accumulated within its genome [10]. These genetic and epigenetic alterations come together to form complex, dynamic, and plastic networks that govern the "hallmarks of cancer" [33,34]. The most common genetic alteration is the somatic mutation which is acquired in the origin of cancer development, and this DNA sequence change is different from the normal genome [30]. This genetic event can be accumulated in the life of cancer and propagated to different generations of cancer cells. Mutation can be classified into two classes, "driver" and "passenger" mutations [32]. Driver mutations are the key mutation that drive the development of cancer and provides survival advantage, whereas passenger mutations are "by-stander" alterations that happen to be altered in the primary

cells but do not provide survival advantage of cancer. The identification and characterization of driver mutations and the cancer genes represent a central aim of cancer research [7,8,30]. With the advancement of technologies to sequence multiple cancer genomes and the accumulation of cancer biology knowledge, somatic mutations were identified in about 447 (~2 %) of the ~22,000 human protein-coding genes (COSMIC database, version 3/15/2012) [24].

12.2.1 Genomics

Single nucleotide polymorphisms. The somatic mutations in a cancer cell genome can encompass several distinct classes of DNA sequence change. The most common mutation is the substitutions of one base by another, known as single nucleotide polymorphism (SNP). Some of these SNPs will cause changes in the amino acids (building blocks of proteins) and ultimately alter the function of the encoded proteins. These changes, known as non-synonymous mutations, are critical and may provide insights into mechanisms of oncogenes driving the development of cancer. Some of the cancer cells might acquire non-synonymous mutations to confer resistance to targeted therapies. Other SNPs that do not cause changes at the amino acids are known as synonymous mutations (or "silent mutations"), which may or may not have a functional impact on the survival advantage of the cancer cell.

Insertions or deletions. The second class of somatic mutations is the insertions or deletions of small or large segments of DNA. Similar to SNPs, insertions or deletions in DNA sequence may cause changes in amino acids sequence, therefore, leading to gain or loss of function of the encoded proteins. Insertion of exogeneous DNA into normal cell genome is a common mechanism in virus-associated cancers. For example, integration of the human papillomavirus (HPV) E6 and E7 oncogenes into human genome, which bind and enhance degradation of p53 and RB tumor suppressor genes, respectively, is a predominant mechanism for HPV-induced head and neck cancer [91].

Chromosomal rearrangement. Another class of somatic mutations in cancer cell genome is chromosomal rearrangement. These are large structural alterations in the genome in which DNA has been broken and then rejoined to a DNA segment from elsewhere in the genome. Molecular consequence of these rearrangements is the generation of new fusions genes that drive cancer development. Examples of these are BCR-ABL in CML [65], ALK-EML4 in non-small cell lung cancer [73], and TMPRSS2-ETS family in prostate cancer [83].

Amplifications and deletions. Other common mutations in the cancer cell genome are chromosomal amplifications and deletions. For chromosomal amplification, copy number of a DNA segment or even the whole chromosome can increase from the two copies present in the normal diploid genome to sometimes several hundred copies (known as gene amplification) in the cancer cell genome.

Conversely, chromosomal deletions represent the copy number reductions that may result in the complete absence of a DNA sequence from the cancer genome. Usually, amplifications occur at regions enriched with oncogenes and deletions happen at regions enriched with tumor suppressor genes.

12.2.2 Epigenomics

CpG site methylation. Epigenetic modifications are defined as heritable information other than nucleotide sequences. DNA methylation and histone modifications are the two major classes of epigenetic. Epigenetics are now known to regulate a wide range of physiological and pathological processes, including cancer. DNA methylation is one of the most important epigenetic alterations and plays a critical functional role in development, differentiation, and disease [22,44]. Promoter regions are usually enriched with CpG dinucleotides, known as CpG islands; and hypermethylation of these islands correlates with transcriptional silencing of tumor suppressor genes [36]. Conversely, increased expressions of oncogenes were associated with hypomethylation [13]. This hypomethylation is known to contribute to cancer cell phenotypes through loss of imprinting and genomic instability that characterizes tumors [13]. Furthermore, tumorigenesis of several cancers was also marked by specific methylation changes in their genomes [101]. Therefore, constructing a global methylation profile can lead to the discovery of candidate genes that correlate to therapeutic outcomes [70,80] and patient survival in cancer [64].

12.2.3 Transcriptomics

Gene expression. Each of the genetic and epigenetic changes described previously in cancer genome can alter the expression levels of genes or noncoding RNAs (including both microRNAs and long noncoding RNAs). Some of these modifications can alter the splicing patterns of a gene to generate different variants of transcripts in cancer. These changes ultimately translate into altered functions, leading to the development of cancer.

12.2.4 Translational Bioinformatics for "Omics" Data

The development of powerful and scalable high-throughput methods to interrogate cancer genome has transformed cancer research over the past decade. The application of such technologies coupled with advanced bioinformatics in cancer research has facilitated the discovery of new oncogenes and their associate in various cancers. Many of the gene expression changes can be assessed by microarray analysis. In fact,

quantifying mRNA expression in cancer represents the first application of high-throughput genome-wide of DNA-microarray technology in biomedical research [27,75,86,87]. With the introduction of microarray technology, it is now possible to monitor genome-wide gene expression changes within a sample. Microarrays are also being used to genotype SNPs by hybridizing the DNA of individuals to arrays of oligonucleotides representing different polymorphic alleles. The genome-wide SNP microarray has accelerated genome-wide association studies (GWAS) over the last 5 years, and many loci that are associated with diseases have been discovered and validated [37,96]. Another type of microarray known as array-Comparative Genomic Hybridization (aCGH) is being used to detect genomic structural variations in different cancer genomes [61]. The large-scale, systematic sequencing studies conducted by applying massively parallel, next-generation sequencing technologies open up new research avenues in cancer genomics. Applications of these massively parallel sequencing platforms have led to the identification of the full range of somatically acquired genetic alteration in cancer via whole-genome or exome sequencing [2,72,77,81,82,94]. These include the identification of genome-wide point mutations, insertions, and deletions, copy number changes and genomic rearrangements in various cancers [2,72,77,81,82,94].

New computational and statistical tools are required to analyze and interpret these large-scale data sets. The goal of microarray data analysis is to find the connections between gene expression patterns within cancer cells and their different phenotypes. There are two approaches for analyzing microarray gene expression data: (1) data-driven approach and (2) knowledge-driven approach.

Data-driven approach. The most straightforward method of analyzing microarray gene expression data is the data-driven approach, in which the goal is to correlate gene expression patterns with cancer phenotypes. The gene expression data analyses can be accomplished by either unsupervised (clustering) [20] or supervised (classifying) [85] algorithms. For the unsupervised approaches, computational algorithms are being used to identify substructures of gene expression patterns underlying the data. Some of the most commonly used clustering algorithms include hierarchical, *k*-means, principal component analysis, self-organizing maps, and their variants [14,63,102]. Clustering of gene expression data has identified the intrinsic subtypes of breast cancer, which is currently being used to annotate breast cancer patients in clinic for tailoring their treatments [75]. For the supervised approaches, statistical and machine learning algorithms [45,46,55] are being employed to identify gene features that can distinguish between cancer phenotypes, such as identifying diagnostic, predictive, or prognostic gene markers.

Knowledge-driven approach. With the increasing knowledge of cancer and their underlying biological pathways, several computational methods have improved the ability to identify candidate genes that are correlated with a disease state by exploiting the idea that gene expression alterations might be revealed at the level of biological pathways or co-regulated gene sets, rather than at the level of individual genes [52,62,68,69,78]. Such approaches are more objective and robust in their ability to

discover sets of coordinated differentially expressed genes among pathway members and their association to a specific biological phenotype. These analyses may provide new insights linking biological phenotypes to their underlying molecular mechanisms, as well as suggesting new hypotheses about pathway membership and connectivity. Gene Set Enrichment Analysis (GSEA) [78] represents one of the most commonly used knowledge-driven approaches in microarray data analysis.

12.3 Cellular

As biological systems are complex in nature, the interactions between the components (such as genes and proteins) within a cell form a highly complex network. The human interactome, which is the study of all molecular interactions in a human cell, is made by ~20,000 protein-coding genes, ~1,000 metabolites and a large number of distinct proteins and functional RNA molecules. The total number of molecular components which serve as the nodes of the interactome easily exceeds 100,000, and the number of functional interactions (edges) between these nodes is expected to be much larger. To characterize the interactions in the human interactome, large-scale efforts using the yeast two-hybrid (Y2H) technique have been employed to systematically identify the interacting human protein pairs [66,76]. Massively parallel interactome-mapping strategy, Stitch-seq, that combines PCR stitching and next-generation sequencing technology was recently developed to facilitate the characterization of human interactome [103]. Other sequencing technologies such as ChIP-seq and RNP-seq have been widely used to define protein–DNA and protein–RNA interactions in biological systems, respectively.

Generating the interactions represent the first step in systems biology [40]. These interaction data provide the network topology for a particular biological system. Network-based analysis and modeling can provide insights into the biological properties and potential clinical applications in cancer. Computational cellular models are becoming critical for the analysis of these complex biological systems. Multiple levels of abstraction can be applied to dissect different biological systems, ranging from detailed modeling with differential equations, to intermediate topology inference using Boolean models and Petri Networks to higher level modeling by Bayesian networks. Obviously, for model building the more detailed the model is, the more comprehensive the experimental measurements need to be. These computational tools and methodologies are facilitating the emergence of systems biology [41]. For example, Iadevaia et al. [39] have developed a computational approach that integrates mass action modeling with particle swarm optimization to train on the model against reverse-phase protein array and infer the unknown model parameters in the insulin-signaling growth factor (IGF-1) signaling network in breast cancer cell line. Using this computational model, they can predict how targeting individual signaling proteins alter the rest of the network and identify drug combinations that inhibit cell signaling and proliferation. This model will be useful for generating testable hypotheses that could optimize drug combinations and discover novel pharmacologic targets for cancer therapy.

12.4 System Level

Systems biology employs computational methods to identify networks and to elucidate and interrogate biochemical and molecular interactions. Systems biology models can be useful tools for understanding disease states and for hypothesis generation and testing. However, the link between systems biology in basic science research to translational clinical application lies largely in the application of systems biology models to predict drug efficacy.

Pharmacology is the study of drug action. The primary focus of pharmacology studies is to establish the concentration–effect relationship, which in vivo requires temporal evaluation of concentration and effect through pharmacokinetic (what the body does to the drug) and pharmacodynamic (what the drug does to the body) studies. By default pharmacology is a system-based science since various organs or organ systems contribute to the disposition and dynamics of a compound. Computational modeling of drug effects has traditionally been performed by pharmacokinetic–pharmacodynamic (PK–PD) models. In contrast to the highly mechanistic systems biology models, PK–PD models are typically empiric, relatively easy to construct, data-driven and developed at the organism level. Unfortunately, since PK–PD models frequently lack mechanistic features and are data-based, their ability to scale and predict safety and efficacy is limited.

Quantitative and systems pharmacology (QSP) is an emerging field that aims to incorporate some of the detail and granularity commonly found in network and/or cell-based systems biology models with pharmacology models [1,3,42,74,88]. QSP models offer an intermediate level of detail between systems biology models and PK–PD models which can be "tailored" to the users need, but typically is built at the tissue or organ level with the use of only key network constituents [1].

12.4.1 Organ Level

Systems biology models typically focus on the cellular level of molecular networks and often only account for a single cell or heterogeneous cell populations. However, it is well-understood that the pathophysiology of diseases frequently involves multiple cell types, tissues and/or organs. This has led to the development of complex cell–cell interaction or tissue and organ level models to describe disease states. In oncology, the incorporation of tissue or organ level components is of critical importance given the known influence the tumor microenvironment has on tumor characteristics.

The signal transduction pathways important in cancer progression are largely regulated by autocrine and paracrine signaling which can be greatly affected by the host organ environment in which a tumor grows. The tumor "microenvironment" can be thought of as the biological, biochemical, and genetic characteristics regulated or deregulated by the autocrine and paracrine effects between the host

environment, the tumor, and the tumor vasculature. The expression of cytokines, integrins, and growth factors can vary considerably between organs, resulting in different molecular, biochemical, and physiologic properties of tumors growing in different environments.

A recent study published by Park et al. [59] utilized a "systems" approach to investigate the microenvironmental influence on gene expression profiles of cell-line-based tumors growing either subcutaneously, orthotopically (growing in the appropriate organ) or in the brain. Interestingly, the expression profiles of the tumors growing subcutaneously and orthotopically generally clustered with the original cell line. Yet, the tumors growing in the brain had a significantly different expression pattern than their respective cell lines. The cells from tumors implanted in the brain had neuronal cell characteristics, clustering with normal mouse brain samples, indicating a complete "reprogramming" of the cells.

Additional studies have shown that enzymes critical in the processes of invasion and metastases, such as the extracellular matrix (ECM) degradation enzyme type IV collagenase and plasminogen activators, are regulated by serum factors, growth factors, and tumor cell–ECM matrix interactions [54,58]. Tumor microenvironment is also critical in angiogenesis regulation. cDNA expression profiles of endothelial cells isolated from different organ environments have shown differential expression of RTKs and chemokine receptors [48] and have demonstrated that endothelial cells originating from different organs exhibited marked differences in response to stimulation by different mitogens. Evidence to the effect of tumor organ environment on therapeutic response has been demonstrated in preclinical models [92] and clinical observations also suggest that anatomic location of metastases plays a critical role in determining response to therapy [18].

Despite the known involvement of microenvironment in disease pathophysiology, there are currently only a handful of examples of molecular systems biology models being extended to the tissue, organ, or multi-organ level [4,5,17,29]. The need for integrative multi-scale models for basic and translational cancer research has been recognized. The National Cancer Institute (NCI) established the Integrative Cancer Biology Program which is focused on the development and use of computational models to study prevention, diagnostics, and therapeutics in cancer as a "system" (http://icbp.nci.nih.gov/). As part of this program, the Center for the Development of a Virtual Tumor (CViT) was established and their goal is developing multi-scale models of cancer and the community to carry this out [16].

12.4.2 Organism Level

As stated earlier, the most common type of pharmacology modeling at the organism level is pharmacokinetic or pharmacokinetic–pharmacodynamic modeling. PK–PD models represent valuable tools that allow us to quantitatively relate dose to concentration to effect. However, the vast majority of PK–PD studies conducted assume that the free plasma concentration is reflective of the concentration at the

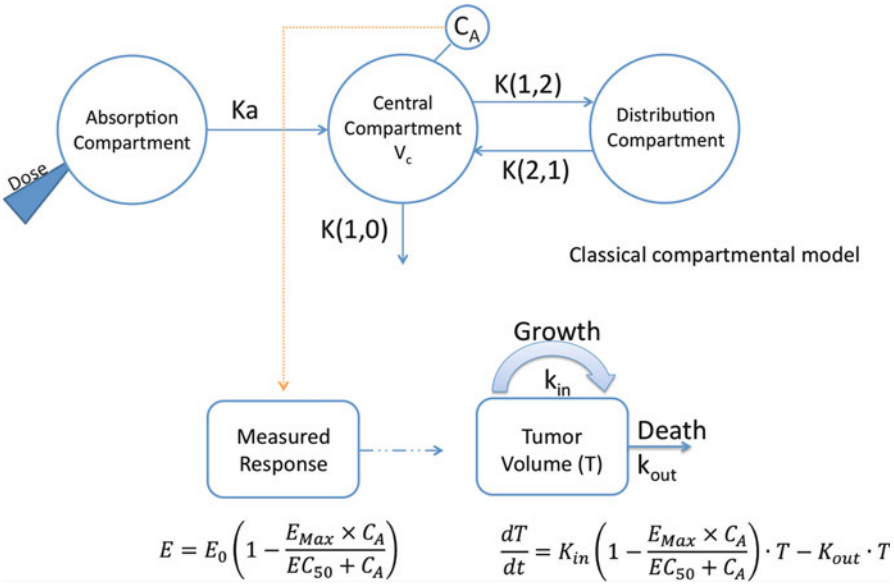

Fig. 12.2 Schematic representation of a typical empiric PK–PD model. Drug concentrations are frequently modeled by classical compartmental PK approaches. The plasma concentration–time profile (C_A) is then used in the biomarker response model and the tumor growth model to determine the concentration–effect relationships

site of action and actual or simulated measures of concentration at the site of action are rarely used. In some indications the plasma PK can be adequately related to target effects [53,104]. However, in oncology, due to the heterogeneous nature of tumors, this is likely to be an inaccurate assumption as we know that there are several barriers to drug delivery in tumors and that these barriers can and will change based on tumor type, location, stage of disease, or even from individual lesion to lesion [51,84]. Tumor molecular, biochemical, and physiologic phenotype can affect the distribution of drugs to tumor cells [51,56,84]. These differences in disposition can lead to non-proportional relationships between plasma concentration and the concentration at the site of action leading to a poor understanding of the concentration–effect relationships. Figure 12.2 is a schematic representation of a PK–PD model structure commonly used in oncology to determine the nonclinical PK–biomarker–tumor growth effect relationships [28,67,71,93,98,99]. Typically, a compartmental model is used to describe the plasma distribution of a drug. It is important to note, that in the classical compartmental pharmacokinetic model the compartments do not carry any anatomic or physiologic meaning, making these types of models data-based, primarily confined to describing plasma concentration and highly limited in the ability to scale between species or extrapolate doses.

To improve the scaling and extrapolation of pharmacokinetics, more complex, mechanistically grounded models can be employed, such as *p*hysiologically *b*ased *p*harmaco*k*inetic (PBPK) models. In contrast to compartmental models, the

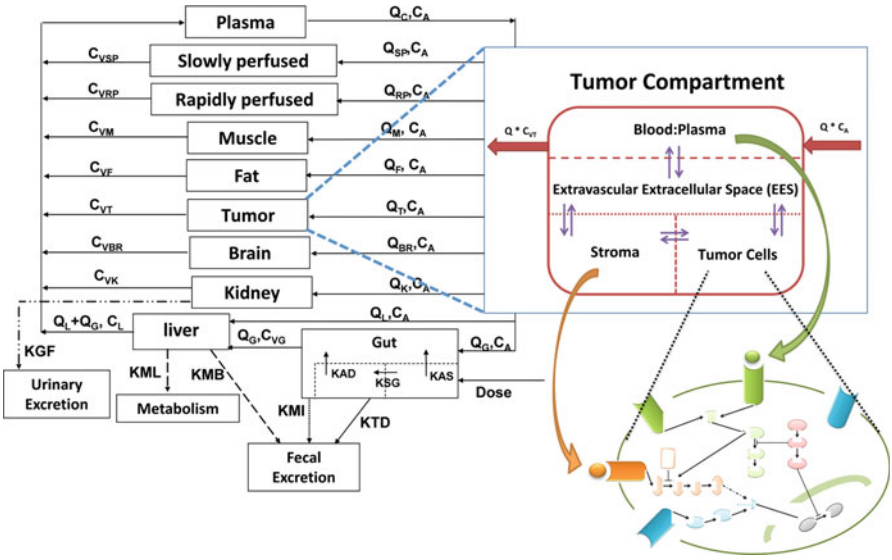

Fig. 12.3 Schematic representation of a hypothetical QSP model. Drug concentration–time profiles in the plasma and tissues are described by a whole-body PBPK model. Drug distribution to tumor is described in greater detail to delineate concentrations in tumor cells, where the drug target is, rather than total tumor concentration. The model incorporates key molecular intermediates in tumor cells, rather than the entire network, which may be useful in understanding temporal delays in downstream signaling events

compartments in PBPK models represent tissues, organs, or groups of tissues that carry anatomic and physiologic meaning. PBPK models are ODE-based models that utilize a large body of physiologic and physiochemical data, allowing for better extrapolation between doses, routes of administration, and species. Additionally, the mechanistic nature of PBPK models allows for a priori prediction of plasma and tissue data. The fundamental objective of PBPK modeling is to identify the principle organs or tissues involved in the disposition of the compound of interest and to correlate absorption, distribution, and elimination within and among these organs and tissues in an integrated and *biologically plausible* manner [9,43,79].

A schematic representation of a QSP model to describe multi-organ and multicellular distribution of a compound is shown in Fig. 12.3. The QSP model incorporates a whole-body PBPK model with a multicellular tumor compartment. Mass-balance differential equations are developed for each individual compartment and are then simultaneously solved. Since equations are developed for each compartment, different levels of complexity can be integrated into specific compartments. For instance, as illustrated in Fig. 12.3, if we decide that the tumor is not a single well-stirred compartment, but made up of tumor cells, stromal cells, and extravascular extracellular space, we can write the mathematical term to describe it. We can establish the distribution of drug (or any other endogenous or exogenous molecule, protein, or antibody) to be perfusion or permeability limited,

or to be mediated, linearly or nonlinearly, by the presence of the target or of other nonspecific binding elements. The model could also be further extended to incorporate specific signaling events in the tumor cell population. The caveat to this, much like developing biochemical or molecular systems-biology model, is that with increasing granularity comes an increase in the assumptions and supportive data necessary for model building and validation.

Until recently, systems biology and pharmacology have existed separately and very little overlap or integration has occurred. QSP is an integrative discipline, incorporating computational data analysis and modeling with molecular and cellular biology. Although QSP modeling is still in its infancy, there are a couple of elegant examples of multi-scale modeling and simulation incorporating biochemical and molecular reaction networks and whole-body models [21,97]. Wu et al. [97] modeled the VEGF system from the molecular level to the cellular level to tissue level to organism and Eissing et al. present a software platform to conduct multi-scale systems modeling. In the work published by Eissing et al., the authors created a virtual patient with a tumor in the pancreas. The tumor was subdivided into proliferating, resting and dead cells and nested a molecular model of the EGFR-MAPK pathway into the cells. They then simulated the treatment effects on the tumor. The drug used in their virtual patient is a prodrug converted to the active metabolite in the liver by CYP2D6, which has known a polymorphism that affects the metabolism rate. They were able to model the effect different phenotypes of CYP2D6 would have on the effect of treatment. They were also able to vary the concentrations of the proteins in the EGFR signal transduction to model the effect that would have on drug treatment. These two examples illustrate the power and utility of multi-scale, mechanistic QSP models.

12.5 Translation

There are significant challenges in the development of novel targeted oncology drugs [31,47,100] and the predictable translation of impressive preclinical activity of agents to successful clinical compounds remains elusive. Recently, greater emphasis has been placed in developing knowledge of the concentration of drugs at the site of action and understanding how this relates to modulation of the target pathway and the measurement of therapeutic effect [12,53,95]. Preclinical QSP studies are of critical importance because they allow us to establish how plasma concentrations relate to target concentrations, target modulation, surrogate biomarkers (a clinical or translational biomarker), and growth effect so we can extrapolate the relationship to patients, where often the only measures obtained are plasma PK and/or a surrogate biomarker (Figs. 12.1 and 12.4).

In clinical studies, tremendous variability is often observed both in the pharmacokinetics and in response to therapy. Recently, efforts have been made to develop "biomarkers" to predict which patients may respond to a given therapy versus those who will not. This has been successfully employed in non-small cell lung cancer,

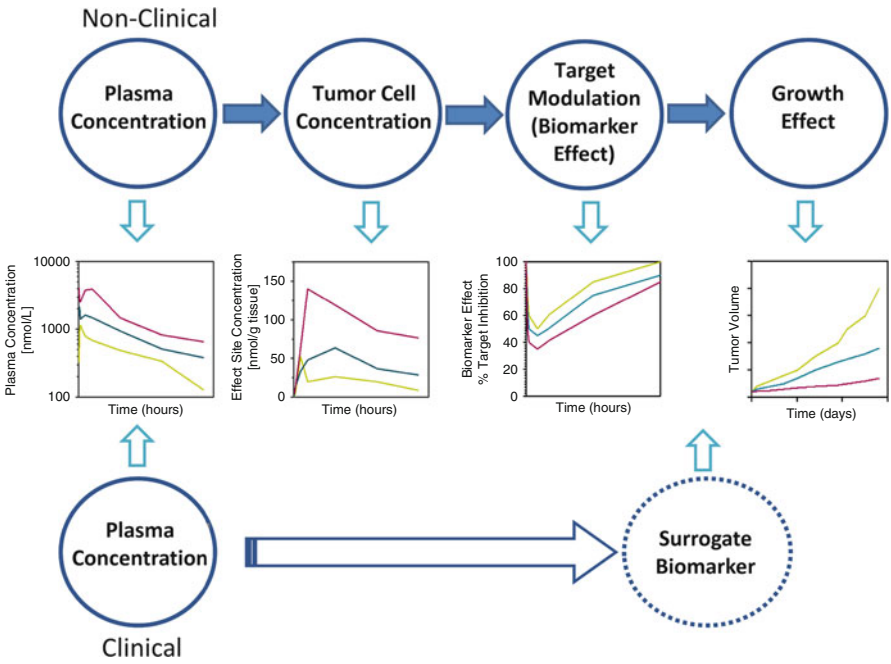

Fig. 12.4 Diagram of nonclinical and clinical data obtained for pharmacokinetic–pharmacodynamic studies. Nonclinical studies in oncology most frequently measure dose and tumor growth inhibitory effects. However, by taking quantitative measurements and establishing mechanistic models to describe the relationships between dose, plasma concentrations, tumor cell concentrations (i.e., site of drug action), target modulation and resultant growth effect, we can better understand clinical effects and may be able to more successfully translate and inform clinical decisions

the selection of patients with certain EGFR mutations predicted to confer sensitivity to small molecule EGFR inhibitors, and in colorectal cancer, where patients with wild-type *KRAS* may be eligible for Cetuximab therapy but not patients with mutant forms of *KRAS*. Pharmacogenomic approaches have also been used in understanding how polymorphisms in drug transporters and drug metabolizing enzymes affect adverse outcomes [60]. Traditionally the understanding of inter-patient variability has been studied by empiric population approaches. QSP approaches have the ability to mechanistically understand how or which variables affect a given outcome. QSP models can incorporate variability in targets, down-stream effectors, disease states, as well as drug metabolizing enzymes and transporters (which can be identified by various omics data) which can provide better prediction of the outcome or effect of a compound in a population of patients rather than a single average. The inclusion of semi-mechanistic to mechanistic pathway models and variability may provide insight to genotypes or phenotypes predictive of response to therapy and may even be useful in elucidating or predicting mechanisms of drug resistance. The implementation of these preclinical and clinical modeling approaches may help to reduce the risk of failure to translate clinically [25,26,53].

Despite the potential QSP models may have in directly impacting drug development and patient care, there are several challenges in the wide-spread development and use of such approaches. The development of detailed, mechanistic models is time-consuming and requires significant, and at times very costly, data to generate and validate. Additionally, the development of such models requires a broad knowledge-base as principles of biology, physiology, biochemistry, pharmacology, are incorporated with engineering, computer science or programming, and statistics, requiring inter-disciplinary teams and training programs. QSP is a promising approach and the utilization of these types of QSP models in conjunction with molecular and genomic information is a scientifically rational approach for defining optimal multidrug regimens, identifying responsive patient populations, identifying translational biomarkers, and designing clinical trials.

References

1. Agoram BM, Demin O (2011) Integration not isolation: arguing the case for quantitative and systems pharmacology in drug discovery and development. Drug Discov Today 16:1031–1036
2. Agrawal N, Frederick MJ, Pickering CR, Bettegowda C, Chang K, Li RJ, Fakhry C, Xie TX, Zhang J, Wang J et al (2011) Exome sequencing of head and neck squamous cell carcinoma reveals inactivating mutations in NOTCH1. Science 333:1154–1157
3. Allerheiligen SR (2010) Next-generation model-based drug discovery and development: quantitative and systems pharmacology. Clin Pharmacol Ther 88:135–137
4. Bassingthwaighte J, Hunter P, Noble D (2009) The cardiac physiome: perspectives for the future. Exp Physiol 94:597–605
5. Bassingthwaighte JB, Raymond GM, Butterworth E, Alessio A, Caldwell JH (2010) Multiscale modeling of metabolism, flows, and exchanges in heterogeneous organs. Ann N Y Acad Sci 1188:111–120
6. Beyer A, Bandyopadhyay S, Ideker T (2007) Integrating physical and genetic maps: from genomes to interaction networks. Nat Rev Genet 8:699–710
7. Bignell GR, Greenman CD, Davies H, Butler AP, Edkins S, Andrews JM, Buck G, Chen L, Beare D, Latimer C et al (2010) Signatures of mutation and selection in the cancer genome. Nature 463:893–898
8. Bozic I, Antal T, Ohtsuki H, Carter H, Kim D, Chen S, Karchin R, Kinzler KW, Vogelstein B, Nowak MA (2010) Accumulation of driver and passenger mutations during tumor progression. Proc Natl Acad Sci U S A 107:18545–18550
9. Bradshaw-Pierce EL, Eckhardt SG, Gustafson DL (2007) A physiologically based pharmacokinetic model of docetaxel disposition: from mouse to man. Clin Cancer Res Off J Am Assoc Cancer Res 13:2768–2776
10. Chin L, Gray JW (2008) Translating insights from the cancer genome into clinical practice. Nature 452:553–563
11. Choi YL, Soda M, Yamashita Y, Ueno T, Takashima J, Nakajima T, Yatabe Y, Takeuchi K, Hamada T, Haruta H et al (2010) EML4-ALK mutations in lung cancer that confer resistance to ALK inhibitors. N Eng J Med 363:1734–1739
12. Cohen A (2008) Pharmacokinetic and pharmacodynamic data to be derived from early-phase drug development: designing informative human pharmacology studies. Clin Pharmacokinet 47:373–381

13. Cui H, Onyango P, Brandenburg S, Wu Y, Hsieh CL, Feinberg AP (2002) Loss of imprinting in colorectal cancer linked to hypomethylation of H19 and IGF2. Cancer Res 62:6442–6446
14. D'Haeseleer P (2005) How does gene expression clustering work? Nat Biotechnol 23:1499–1501
15. Daley GQ, Van Etten RA, Baltimore D (1990) Induction of chronic myelogenous leukemia in mice by the P210bcr/abl gene of the Philadelphia chromosome. Science 247:824–830
16. Deisboeck TS, Zhang L, Martin S (2007) Advancing cancer systems biology: introducing the center for the development of a virtual tumor, CViT. Cancer Inform 5:1–8
17. Dobrin R, Zhu J, Molony C, Argman C, Parrish ML, Carlson S, Allan MF, Pomp D, Schadt EE (2009) Multi-tissue coexpression networks reveal unexpected subnetworks associated with disease. Genome Biol 10:R55
18. Donelli MG, Rosso R, Garattini S (1967) Selective chemotherapy in relation to the site of tumor transplantation. Int J Cancer 2:421–424
19. Druker BJ, Talpaz M, Resta DJ, Peng B, Buchdunger E, Ford JM, Lydon NB, Kantarjian H, Capdeville R, Ohno-Jones S et al (2001) Efficacy and safety of a specific inhibitor of the BCR-ABL tyrosine kinase in chronic myeloid leukemia. N Eng J Med 344:1031–1037
20. Eisen MB, Spellman PT, Brown PO, Botstein D (1998) Cluster analysis and display of genome-wide expression patterns. Proc Natl Acad Sci U S A 95:14863–14868
21. Eissing T, Kuepfer L, Becker C, Block M, Coboeken K, Gaub T, Goerlitz L, Jaeger J, Loosen R, Ludewig B et al (2011) A computational systems biology software platform for multiscale modeling and simulation: integrating whole-body physiology, disease biology, and molecular reaction networks. Front Physiol 2:4
22. Fernandez AF, Assenov Y, Martin-Subero JI, Balint B, Siebert R, Taniguchi H, Yamamoto H, Hidalgo M, Tan AC, Galm O et al (2011) A DNA methylation fingerprint of 1628 human samples. Genome Res 22(2):407–419
23. Flaherty KT, Puzanov I, Kim KB, Ribas A, McArthur GA, Sosman JA, O'Dwyer PJ, Lee RJ, Grippo JF, Nolop K et al (2010) Inhibition of mutated, activated BRAF in metastatic melanoma. N Eng J Med 363:809–819
24. Forbes SA, Bindal N, Bamford S, Cole C, Kok CY, Beare D, Jia M, Shepherd R, Leung K, Menzies A et al (2011) COSMIC: mining complete cancer genomes in the catalogue of somatic mutations in cancer. Nucleic Acids Res 39:D945–D950
25. Gabrielsson J, Green AR (2009) Quantitative pharmacology or pharmacokinetic pharmacodynamic integration should be a vital component in integrative pharmacology. J Pharmacol Exp Ther 331:767–774
26. Gabrielsson J, Green AR, Van der Graaf PH (2010) Optimising in vivo pharmacology studies—practical PKPD considerations. J Pharmacol Toxicol Methods 61:146–156
27. Golub TR, Slonim DK, Tamayo P, Huard C, Gaasenbeek M, Mesirov JP, Coller H, Loh ML, Downing JR, Caligiuri MA et al (1999) Molecular classification of cancer: class discovery and class prediction by gene expression monitoring. Science 286:531–537
28. Goteti K, Garner CE, Utley L, Dai J, Ashwell S, Moustakas DT, Gonen M, Schwartz GK, Kern SE, Zabludoff S et al (2010) Preclinical pharmacokinetic/pharmacodynamic models to predict synergistic effects of co-administered anti-cancer agents. Cancer Chemother Pharmacol 66:245–254
29. Grabe N, Neuber K (2005) A multicellular systems biology model predicts epidermal morphology, kinetics and Ca2+ flow. Bioinformatics 21:3541–3547
30. Greenman C, Stephens P, Smith R, Dalgliesh GL, Hunter C, Bignell G, Davies H, Teague J, Butler A, Stevens C et al (2007) Patterns of somatic mutation in human cancer genomes. Nature 446:153–158
31. Gutierrez ME, Kummar S, Giaccone G (2009) Next generation oncology drug development: opportunities and challenges. Nat Rev Clin Oncol 6:259–265
32. Haber DA, Settleman J (2007) Cancer: drivers and passengers. Nature 446:145–146
33. Hanahan D, Weinberg RA (2000) The hallmarks of cancer. Cell 100:57–70

34. Hanahan D, Weinberg RA (2011) Hallmarks of cancer: the next generation. Cell 144:646–674
35. Heisterkamp N, Jenster G, ten Hoeve J, Zovich D, Pattengale PK, Groffen J (1990) Acute leukaemia in bcr/abl transgenic mice. Nature 344:251–253
36. Herman JG, Baylin SB (2003) Gene silencing in cancer in association with promoter hypermethylation. N Eng J Med 349:2042–2054
37. Hindorff LA, Sethupathy P, Junkins HA, Ramos EM, Mehta JP, Collins FS, Manolio TA (2009) Potential etiologic and functional implications of genome-wide association loci for human diseases and traits. Proc Natl Acad Sci U S A 106:9362–9367
38. Hudson TJ, Anderson W, Artez A, Barker AD, Bell C, Bernabe RR, Bhan MK, Calvo F, Eerola I, Gerhard DS et al (2010) International network of cancer genome projects. Nature 464:993–998
39. Iadevaia S, Lu Y, Morales FC, Mills GB, Ram PT (2010) Identification of optimal drug combinations targeting cellular networks: integrating phospho-proteomics and computational network analysis. Cancer Res 70:6704–6714
40. Ideker T (2004) Systems biology 101—what you need to know. Nat Biotechnol 22:473–475
41. Ideker T, Lauffenburger D (2003) Building with a scaffold: emerging strategies for high- to low-level cellular modeling. Trends Biotechnol 21:255–262
42. Iyengar R, Zhao S, Chung SW, Mager DE, Gallo JM (2012) Merging systems biology with pharmacodynamics. Sci Transl Med 4(126):126ps7
43. Jones HM, Gardner IB, Watson KJ (2009) Modelling and PBPK simulation in drug discovery. AAPS J 11:155–166
44. Jones PA, Baylin SB (2002) The fundamental role of epigenetic events in cancer. Nat Rev Genet 3:415–428
45. Kingsford C, Salzberg SL (2008) What are decision trees? Nat Biotechnol 26:1011–1013
46. Krogh A (2008) What are artificial neural networks? Nat Biotechnol 26:195–197
47. Kummar S, Gutierrez M, Doroshow JH, Murgo AJ (2006) Drug development in oncology: classical cytotoxics and molecularly targeted agents. Br J Clin Pharmacol 62:15–26
48. Langley RR, Ramirez KM, Tsan RZ, Van Arsdall M, Nilsson MB, Fidler IJ (2003) Tissue-specific microvascular endothelial cell lines from H-2K(b)-tsA58 mice for studies of angiogenesis and metastasis. Cancer Res 63:2971–2976
49. Lugo TG, Pendergast AM, Muller AJ, Witte ON (1990) Tyrosine kinase activity and transformation potency of bcr-abl oncogene products. Science 247:1079–1082
50. Luo J, Solimini NL, Elledge SJ (2009) Principles of cancer therapy: oncogene and non-oncogene addiction. Cell 136:823–837
51. Minchinton AI, Tannock IF (2006) Drug penetration in solid tumours. Nat Rev Cancer 6:583–592
52. Mootha VK, Lindgren CM, Eriksson KF, Subramanian A, Sihag S, Lehar J, Puigserver P, Carlsson E, Ridderstrale M, Laurila E et al (2003) PGC-1alpha-responsive genes involved in oxidative phosphorylation are coordinately downregulated in human diabetes. Nat Genet 34:267–273
53. Morgan P, Van Der Graaf PH, Arrowsmith J, Feltner DE, Drummond KS, Wegner CD, Street SD (2011) Can the flow of medicines be improved? Fundamental pharmacokinetic and pharmacological principles toward improving Phase II survival. Drug Discov Today 17(9–10):419–424
54. Nakajima M, Welch DR, Belloni PN, Nicolson GL (1987) Degradation of basement membrane type IV collagen and lung subendothelial matrix by rat mammary adenocarcinoma cell clones of differing metastatic potentials. Cancer Res 47:4869–4876
55. Noble WS (2006) What is a support vector machine? Nat Biotechnol 24:1565–1567
56. Olive KP, Jacobetz MA, Davidson CJ, Gopinathan A, McIntyre D, Honess D, Madhu B, Goldgraben MA, Caldwell ME, Allard D et al (2009) Inhibition of Hedgehog signaling enhances delivery of chemotherapy in a mouse model of pancreatic cancer. Science 324:1457–1461

57. Orton RJ, Adriaens ME, Gormand A, Sturm OE, Kolch W, Gilbert DR (2009) Computational modelling of cancerous mutations in the EGFR/ERK signalling pathway. BMC Syst Biol 3:100
58. Overall CM, Wrana JL, Sodek J (1989) Independent regulation of collagenase, 72-kDa progelatinase, and metalloendoproteinase inhibitor expression in human fibroblasts by transforming growth factor-beta. J Biol Chem 264:1860–1869
59. Park ES, Kim SJ, Kim SW, Yoon SL, Leem SH, Kim SB, Kim SM, Park YY, Cheong JH, Woo HG et al (2011) Cross-species hybridization of microarrays for studying tumor transcriptome of brain metastasis. Proc Natl Acad Sci U S A 108:17456–17461
60. Phillips KA, Veenstra DL, Oren E, Lee JK, Sadee W (2001) Potential role of pharmacogenomics in reducing adverse drug reactions: a systematic review. JAMA 286:2270–2279
61. Pinkel D, Albertson DG (2005) Array comparative genomic hybridization and its applications in cancer. Nat Genet 37(Suppl):S11–S17
62. Rhodes DR, Kalyana-Sundaram S, Mahavisno V, Barrette TR, Ghosh D, Chinnaiyan AM (2005) Mining for regulatory programs in the cancer transcriptome. Nat Genet 37:579–583
63. Ringner M (2008) What is principal component analysis? Nat Biotechnol 26:303–304
64. Rosenbaum E, Hoque MO, Cohen Y, Zahurak M, Eisenberger MA, Epstein JI, Partin AW, Sidransky D (2005) Promoter hypermethylation as an independent prognostic factor for relapse in patients with prostate cancer following radical prostatectomy. Clin Cancer Res Off J Am Assoc Cancer Res 11:8321–8325
65. Rowley JD (1973) Letter: A new consistent chromosomal abnormality in chronic myelogenous leukaemia identified by quinacrine fluorescence and Giemsa staining. Nature 243:290–293
66. Rual JF, Venkatesan K, Hao T, Hirozane-Kishikawa T, Dricot A, Li N, Berriz GF, Gibbons FD, Dreze M, Ayivi-Guedehoussou N et al (2005) Towards a proteome-scale map of the human protein–protein interaction network. Nature 437:1173–1178
67. Salphati L, Pang J, Plise EG, Lee LB, Olivero AG, Prior WW, Sampath D, Wong S, Zhang X (2012) Preclinical assessment of the absorption and disposition of the PI3K/mTOR inhibitor GDC-0980 and prediction of its pharmacokinetics and efficacy in human. Drug Metab Dispos 40(9):1785–96
68. Segal E, Friedman N, Kaminski N, Regev A, Koller D (2005) From signatures to models: understanding cancer using microarrays. Nat Genet 37(Suppl):S38–S45
69. Segal E, Shapira M, Regev A, Pe'er D, Botstein D, Koller D, Friedman N (2003) Module networks: identifying regulatory modules and their condition-specific regulators from gene expression data. Nat Genet 34:166–176
70. Shen L, Kondo Y, Ahmed S, Boumber Y, Konishi K, Guo Y, Chen X, Vilaythong JN, Issa JP (2007) Drug sensitivity prediction by CpG island methylation profile in the NCI-60 cancer cell line panel. Cancer Res 67:11335–11343
71. Simeoni M, Magni P, Cammia C, De Nicolao G, Croci V, Pesenti E, Germani M, Poggesi I, Rocchetti M (2004) Predictive pharmacokinetic-pharmacodynamic modeling of tumor growth kinetics in xenograft models after administration of anticancer agents. Cancer Res 64:1094–1101
72. Sjoblom T, Jones S, Wood LD, Parsons DW, Lin J, Barber TD, Mandelker D, Leary RJ, Ptak J, Silliman N et al (2006) The consensus coding sequences of human breast and colorectal cancers. Science 314:268–274
73. Soda M, Choi YL, Enomoto M, Takada S, Yamashita Y, Ishikawa S, Fujiwara S, Watanabe H, Kurashina K, Hatanaka H et al (2007) Identification of the transforming EML4-ALK fusion gene in non-small-cell lung cancer. Nature 448:561–566
74. Sorger PK, Allerheiligen SRB, Abernethy DR, Altman KL, Brouwer R, Califano A, D'Argenio DZ, Iyengar R, Jusko WJ, Lalonde R et al (2011) Quantitative and systems pharmacology in the post-genomic era: new approaches to discovering drugs and understanding therapeutic mechanisms. In: Ward R (ed) An NIH White Paper by the QSP Workshop Group—October 2011

75. Sorlie T, Perou CM, Tibshirani R, Aas T, Geisler S, Johnsen H, Hastie T, Eisen MB, van de Rijn M, Jeffrey SS et al (2001) Gene expression patterns of breast carcinomas distinguish tumor subclasses with clinical implications. Proc Natl Acad Sci U S A 98:10869–10874
76. Stelzl U, Worm U, Lalowski M, Haenig C, Brembeck FH, Goehler H, Stroedicke M, Zenkner M, Schoenherr A, Koeppen S et al (2005) A human protein-protein interaction network: a resource for annotating the proteome. Cell 122:957–968
77. Stransky N, Egloff AM, Tward AD, Kostic AD, Cibulskis K, Sivachenko A, Kryukov GV, Lawrence M, Sougnez C, McKenna A et al (2011) The mutational landscape of head and neck squamous cell carcinoma. Science 333(6046):1157–1160
78. Subramanian A, Tamayo P, Mootha VK, Mukherjee S, Ebert BL, Gillette MA, Paulovich A, Pomeroy SL, Golub TR, Lander ES et al (2005) Gene set enrichment analysis: a knowledge-based approach for interpreting genome-wide expression profiles. Proc Natl Acad Sci U S A 102:15545–15550
79. Sun W, Pierce E, Vicini P (2011) Development of a physiologically-based pharmacokinetic (PBPK) model of Vandetanib. AAPS J 13:R6353
80. Tan AC, Jimeno A, Lin SH, Wheelhouse J, Chan F, Solomon A, Rajeshkumar NV, Rubio-Viqueira B, Hidalgo M (2009) Characterizing DNA methylation patterns in pancreatic cancer genome. Mol Oncol 3:425–438
81. TCGA (2008) Comprehensive genomic characterization defines human glioblastoma genes and core pathways. Nature 455:1061–1068
82. TCGA (2011) Integrated genomic analyses of ovarian carcinoma. Nature 474:609–615
83. Tomlins SA, Rhodes DR, Perner S, Dhanasekaran SM, Mehra R, Sun XW, Varambally S, Cao X, Tchinda J, Kuefer R et al (2005) Recurrent fusion of TMPRSS2 and ETS transcription factor genes in prostate cancer. Science 310:644–648
84. Tredan O, Galmarini CM, Patel K, Tannock IF (2007) Drug resistance and the solid tumor microenvironment. J Natl Cancer Inst 99:1441–1454
85. Tusher VG, Tibshirani R, Chu G (2001) Significance analysis of microarrays applied to the ionizing radiation response. Proc Natl Acad Sci U S A 98:5116–5121
86. van't Veer LJ, Dai H, van de Vijver MJ, He YD, Hart AA, Mao M, Peterse HL, van der Kooy K, Marton MJ, Witteveen AT et al (2002) Gene expression profiling predicts clinical outcome of breast cancer. Nature 415:530–536
87. van de Vijver MJ, He YD, van't Veer LJ, Dai H, Hart AA, Voskuil DW, Schreiber GJ, Peterse HL, Roberts C, Marton MJ et al (2002) A gene-expression signature as a predictor of survival in breast cancer. N Eng J Med 347:1999–2009
88. van der Graaf PH, Benson N (2011) Systems pharmacology: bridging systems biology and pharmacokinetics-pharmacodynamics (PKPD) in drug discovery and development. Pharm Res 28:1460–1464
89. von Kriegsheim A, Baiocchi D, Birtwistle M, Sumpton D, Bienvenut W, Morrice N, Yamada K, Lamond A, Kalna G, Orton R et al (2009) Cell fate decisions are specified by the dynamic ERK interactome. Nat Cell Biol 11:1458–1464
90. Weinstein IB (2002) Cancer. Addiction to oncogenes—the Achilles heal of cancer. Science 297:63–64
91. Wiest T, Schwarz E, Enders C, Flechtenmacher C, Bosch FX (2002) Involvement of intact HPV16 E6/E7 gene expression in head and neck cancers with unaltered p53 status and perturbed pRb cell cycle control. Oncogene 21:1510–1517
92. Wilmanns C, Fan D, O'Brian CA, Bucana CD, Fidler IJ (1992) Orthotopic and ectopic organ environments differentially influence the sensitivity of murine colon carcinoma cells to doxorubicin and 5-fluorouracil. Int J Cancer 52:98–104
93. Wong H, Choo EF, Alicke B, Ding X, La H, McNamara E, Theil FP, Tibbitts J, Friedman LS, Hop CE et al (2012) Anti-tumor activity of targeted and cytotoxic agents in murine subcutaneous tumor models correlates with clinical response. Clin Cancer Res Off J Am Assoc Cancer Res 18(14):3846–3855

94. Wood LD, Parsons DW, Jones S, Lin J, Sjoblom T, Leary RJ, Shen D, Boca SM, Barber T, Ptak J et al (2007) The genomic landscapes of human breast and colorectal cancers. Science 318:1108–1113
95. Workman P, Aboagye EO, Chung YL, Griffiths JR, Hart R, Leach MO, Maxwell RJ, McSheehy PM, Price PM, Zweit J (2006) Minimally invasive pharmacokinetic and pharmacodynamic technologies in hypothesis-testing clinical trials of innovative therapies. J Natl Cancer Inst 98:580–598
96. WTCCC (2007) Genome-wide association study of 14,000 cases of seven common diseases and 3,000 shared controls. Nature 447:661–678
97. Wu FT, Stefanini MO, Mac Gabhann F, Popel AS (2009) Modeling of growth factor-receptor systems from molecular-level protein interaction networks to whole-body compartment models. Methods Enzymol 467:461–497
98. Yamazaki S, Nguyen L, Vekich S, Shen Z, Yin MJ, Mehta PP, Kung PP, Vicini P (2011) Pharmacokinetic–pharmacodynamic modeling of biomarker response and tumor growth inhibition to an orally available heat shock protein 90 inhibitor in a human tumor xenograft mouse model. J Pharmacol Exp Ther 338:964–973
99. Yamazaki S, Skaptason J, Romero D, Lee JH, Zou HY, Christensen JG, Koup JR, Smith BJ, Koudriakova T (2008) Pharmacokinetic–pharmacodynamic modeling of biomarker response and tumor growth inhibition to an orally available cMet kinase inhibitor in human tumor xenograft mouse models. Drug Metab Dispos Biol Fate Chem 36:1267–1274
100. Yap TA, Sandhu SK, Workman P, de Bono JS (2010) Envisioning the future of early anticancer drug development. Nat Rev Cancer 10:514–523
101. Yegnasubramanian S, Kowalski J, Gonzalgo ML, Zahurak M, Piantadosi S, Walsh PC, Bova GS, De Marzo AM, Isaacs WB, Nelson WG (2004) Hypermethylation of CpG islands in primary and metastatic human prostate cancer. Cancer Res 64:1975–1986
102. Yeung KY, Ruzzo WL (2001) Principal component analysis for clustering gene expression data. Bioinformatics 17:763–774
103. Yu H, Tardivo L, Tam S, Weiner E, Gebreab F, Fan C, Svrzikapa N, Hirozane-Kishikawa T, Rietman E, Yang X et al (2011) Next-generation sequencing to generate interactome datasets. Nat Methods 8:478–480
104. Zhou Q, Gallo JM (2011) The pharmacokinetic/pharmacodynamic pipeline: translating anticancer drug pharmacology to the clinic. AAPS J 13:111–120

Index

M.W. Collins and C.S. König (eds.), *Micro and Nano Flow Systems for Bioanalysis*, Bioanalysis 2, DOI 10.1007/978-1-4614-4376-6,